Characteristics of D-to-Z Diamonds

Emeralds from Swat Valley, Pakistan

History of European Royal Jewel Sales

Turquoise from China with "Raindrop" Pattern

p. 319

p. 337

p. 374

p. 381

p. 421

p. 435

GEMS & GEMOLOGY®

gia.edu/gems-gemology

About the Cover

The three largest fleur-de-lis motifs, decorated with colorless diamonds of various shapes, detach from a diamond tiara crafted in 1912 for Archduchess Marie Anne of the Bourbon-Parma family. The individual fleur-de-lis motifs may be worn as brooches. The tiara was among the 100 lots featured in Sotheby's historic 2018 auction of jewels with royal provenance. Courtesy of Sotheby's.

FSC
www.fsc.org
MIX
Paper from
responsible sources
FSC® C006300

Colorless to Near–Colorless Diamonds, Emeralds from Pakistan, a History of European Royal Jewel Sales, and More...

Welcome to the Fall *Gems & Gemology*! This issue offers an exciting glimpse into the world of D-to-Z diamonds, characterizes the inclusion features and chemical composition of emeralds from Swat Valley, and details the acquisition and auction of crown jewels by European royalty.

In the lead article, a GIA team led by Sally Eaton-Magaña and Christopher M. Breeding examines colorless to light yellow/brown diamonds with a "D-to-Z" color grade, which make up the vast majority of the world's gem diamond trade. Because this group of mostly type Ia diamonds has not been subjected to HPHT decolorizing treatment or laboratory growth, researchers usually investigate their more rare diamond type counterparts. This study evaluates diamond

"An exciting glimpse into the world of D-to-Z diamonds..."

type properties and grading quality factors of D-to-Z diamonds submitted to GIA in 2017 and sheds light on their unique geological formation story.

The second article comes from a team led by Hongshu Guo, a student at the School of Gemology, China University of Geosciences in Beijing. The authors present the gemological and geochemical details of emeralds (including trapiche emeralds) from Swat Valley in Pakistan.

In the third article, Russell Shor examines how European royal families acquired their crown jewels, which were later sold at important auctions. The most recent of these was Sotheby's historic Bourbon-Parma auction in 2018, in which 10 of the lots once belonged to Marie Antoinette.

Next, Ling Liu and colleagues from the Gemmological Institute, China University of Geosciences in Wuhan characterize turquoise from China's Hubei Province with a rare surface pattern of spots resembling raindrops. They identify the color origin and formation mechanism of this distinctive pattern.

The final article is a field report from Hạ Long Bay in northern Vietnam, where in late 2019 Nicholas Sturman and coauthors visited a shell nucleus manufacturing factory and two pearl farms, all managed by Orient Pearls (Bangkok) Ltd. The team observed how high-quality bead nuclei are fabricated and used to produce Vietnamese bead cultured pearls suitable for fine jewelry on a commercial scale.

Our regular features continue to highlight interesting gemological findings from around the world. In *Lab Notes,* discover how gem cutters cleverly use color zoning in alexandrite and closely spaced needles in diaspore to showcase phenomena, and how areas of dramatic fluorescence correspond to diamond defects and produce a "lightsaber" effect. Curiosities abound in the *Micro-World* section: epigenetic residue mimicking a fried egg, metal sulfide inclusions resembling trees, and ferrocolumbite posing as star cruisers. *Gem News International* reports on bead cultured pearls with embedded electronic devices and Maxixe beryl with an unusual violet color, among other exciting topics.

This issue also contains the list of winners from this year's *G&G* Challenge quiz. Congratulations, and our special thanks to everyone who participated!

Duncan Pay | Editor-in-Chief | dpay@gia.edu

NATURAL-COLOR D-TO-Z DIAMONDS: A CRYSTAL-CLEAR PERSPECTIVE

Sally Eaton-Magaña, Troy Ardon, Christopher M. Breeding, and James E. Shigley

Colorless to light yellow or brown diamonds with a "D-to-Z" color grade make up the overwhelming majority of the world's gem diamond trade. Besides clarity features (such as inclusions) and fluorescence observations, however, comparatively little has been explored and published regarding the distinguishing characteristics of these diamonds. The vast majority are type Ia, with infrared spectra showing very high concentrations of nitrogen aggregates. This population of diamonds could not have been subjected to HPHT decolorizing treatment or been laboratory grown, and thus they have been spectroscopically scrutinized in much less detail than the far more rare natural diamonds of types IIa, IIb, and IaB, which need to be investigated as potentially color-treated or synthetic.

This study examines a large sample set comprising the full complement of D-to-Z diamonds submitted to GIA laboratories during a significant portion of 2017. The data were evaluated on the basis of diamond type properties, as well as distribution among various grading quality factors, to provide an unprecedented glimpse into the role of these diamond types and differences in their geologic conditions of formation.

When people hear the word *diamond*, colorless diamonds generally come to mind—not the more exotic colors discussed earlier in this article series. In purchasing a diamond, they are likely to choose one that is colorless to near-colorless. When one thinks of perfection in a diamond, a D-Flawless stone is usually the benchmark. The lack of color, which so inhibits the consumer appeal of many other gemstones, is instead considered a measure of stature for diamonds.

Therefore, we finish this series (Breeding et al., 2018, 2020; Eaton-Magaña et al., 2018a, 2018b, 2019) by examining diamonds with very little to no color at all—those on the D-to-Z grading scale. Although they make up by far the largest proportion of stones submitted to GIA, detailed statistics of D-to-Z diamonds have never been presented before. In each of our previous colored diamond articles, we presented data on stones submitted to GIA from 2008 to 2016. For example, GIA examined more than 15,000 naturally colored blue/gray/violet diamonds in that period (Eaton-Magaña et al., 2018a). During those same years, GIA received millions of D-to-Z diamonds (e.g., figure 1).

For this study, we examined all D-to-Z diamonds submitted for grading reports or dossier reports to any of GIA's laboratories during much of 2017. From our analysis of submissions over the last decade, those from 2017 and used in this study are representative of GIA's current and historical intake. Any diamonds submitted on multiple occasions during this period were identified, and only the most recent data for each stone are included in this study.

In Brief

- D-Z diamonds represent the vast majority of all gem diamonds but have rarely been documented systematically and in detail from a gemological laboratory.
- When D-Z diamonds are distinguished by diamond type, we see distinct trends in their grading quality factors.
- HPHT-treated diamonds have distinct trends in their grading quality factors compared to their natural counterparts.

Additionally, we wish to highlight that these data represent a snapshot for a certain period and only include those diamonds submitted to GIA. They may not represent the entirety of the marketplace, such as some lower-quality diamonds that are not
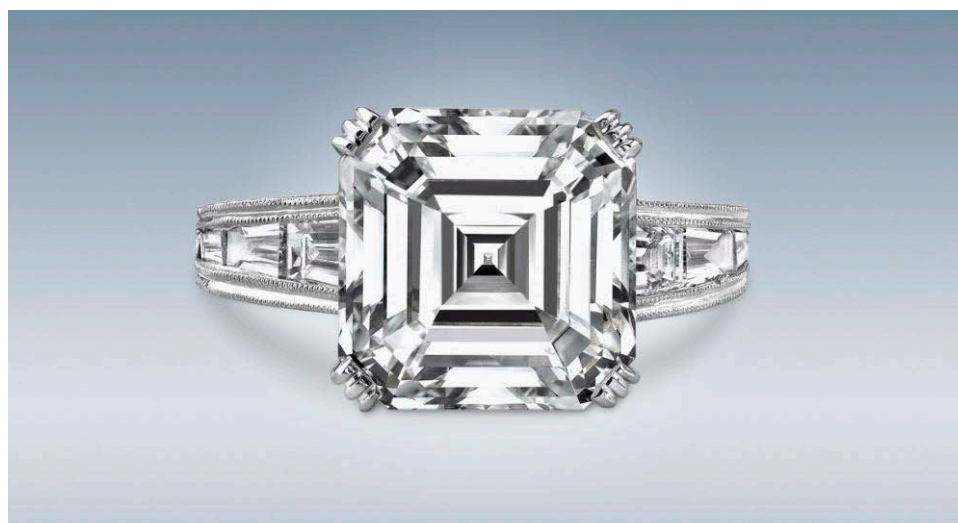
Figure 1. Diamond rings that commemorate a marriage engagement often utilize colorless to near-colorless diamonds and constitute a major sector of the gem and jewelry world. Photo courtesy of Neil Lane.

usually submitted for grading. However, for those in the marketplace that are certified, these results are representative.

The trends presented in this article apply to faceted diamonds. They represent not only the rough selected for manufacturing but also the business and cutting decisions of the polishers. Each faceted diamond is ultimately the culmination and intersection of science, artistry, and commerce.

The GIA system for grading (the absence of) color with the D-to-Z scale has gained worldwide trade and consumer acceptance since its introduction in 1953 by Richard T. Liddicoat and Robert Crowningshield, followed by the first diamond grading reports issued by GIA in 1955 (Dirlam et al., 2002). The grading terminology (though not necessarily the practices) has since been adopted by most other gemological laboratories (King et al., 2008).

Many articles about various aspects of diamond grading have been published regarding color grading (King et al., 2006, 2008), cutting decisions (Caspi, 1997), cut grading of round brilliants (Hemphill et al., 1998; Moses et al., 2004), symmetry (Geurts et al., 2011), crystal inclusions (Koivula, 2000; Kaminsky et al., 2000; Shirey and Shigley, 2013; Smith et al., 2016; Renfro et al., 2018), trends exclusively seen in large diamonds (Smith et al., 2017), and fluorescence (Moses et al., 1997; Luo and Breeding, 2013; Bouman et al., 2018; Breeding and Eaton-Magaña, 2019). Recounting the specifics of the grading process or the mechanics of fluorescence observations is beyond the scope of this article. Instead, we present some statistics of these grading quality factors and other recorded data to illuminate relationships and trends not recognized before.

CAUSES OF COLOR

Only diamonds deemed to be colorless or possessing faint to light yellow or brown color are graded according to the D-to-Z color scale (figure 2). Diamonds with faint to light color saturation of other hues are considered "fancy color" (King et al., 2008), and many of those categories have been described previously in this series. The causes of yellow coloration for D-to-Z diamonds are similar to those for Fancy yellow color (Breeding et al., 2020) and brown coloration (Eaton-Magaña et al., 2018b), but these color causes will be briefly recounted here.

Stones with grayish coloration were discussed in detail in Eaton-Magaña et al. (2018a). In most natural diamonds, the grayish color is produced by clouds of dark (often graphitic) inclusions. For grayish diamonds with a depth of color equivalent to K or greater, the diamond is given a color description of Faint gray, Very Light gray, etc., but without a letter grade (King et al., 2008). Therefore, only D to J diamonds (that is, colorless to near-colorless) with a grayish color contribution would be placed on the D-to-Z scale.

Yellow. The majority (~74%) of Fancy yellow diamonds submitted to GIA are colored by "cape" spectral features (figure 3), which include a combination of absorptions from the N3 defect (three nitrogen atoms adjacent to a vacancy and a zero-phonon line at 415.2 nm), the associated N2 band at 478 nm, and absorptions at 451 and 463 nm (Breeding et al., 2020). The term *cape*, originally used for yellow diamonds from Cape Province in South Africa (the first prominent source of such diamonds), is now used for any yellow diamond colored by N3 and its associated defects.

	E	G	I	K	M	O-P	S-T	W-X
Face-up (yellow)								
Table-down (yellow)								
Face-up (brown)								
Table-down (brown)								

Figure 2. The color grades of D-to-Z diamonds are generally assessed in the table-down position (King et al., 2008) but admired in jewelry in face-up orientation. While most D-to-Z diamonds show a yellow coloration, a small percentage (about 5% overall) show a brown color.

Similarly, among those D-to-Z diamonds with a yellowish tint, that color is predominantly from cape-related defects. However, the defects are at such a low concentration that the diamond cannot attain a Fancy color grade.

Figure 3. The Vis-NIR absorption spectra for two Y-Z diamonds and two D-color diamonds. The type Ia diamonds show cape features that correspond with yellow coloration; the D-color type Ia sample also shows the contribution of N3 fluorescence, which reduces the appearance of the N2 absorption for that sample. The spectra of the two type IIa diamonds show the brown absorption continuum, a relatively featureless absorption that increases toward lower wavelengths and becomes more prominent with stronger brown color.
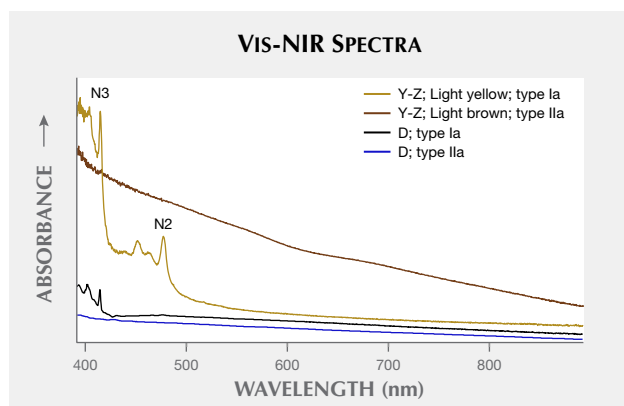
Brown. Though not as common as yellow in submissions to the laboratory, brown is more prevalent than most other diamond colors. The vast majority of D-to-Z diamonds with brownish tints owe their color to selective light absorption due to vacancy clusters (i.e., clusters of vacant carbon-atom positions; see Hounsome et al., 2006; Fisher et al., 2009). These clusters, created through natural plastic deformation of the diamond lattice, are believed to contain approximately 40–60 vacancies that cause a gradually increasing absorption across the visible spectrum toward lower wavelengths (Fisher et al., 2009; Dobrinets et al., 2013; figure 3).

OCCURRENCE AND FORMATION

Yellow. Most diamonds grow within the earth's continental lithosphere (Shirey and Shigley, 2013). By the time they are faceted, there are typically no distinguishing features remaining from the geographic region in which they formed or from their transport to the earth's surface. The yellowish coloration in D-to-Z diamonds generally arises from cape features such as the N3 center, which forms from a high amount of nitrogen incorporation (> 500 ppm) combined with the dual variables of geologic time and high temperature. The presence of nitrogen in the earth's lithosphere where diamonds grow, residence time scales of millions to billions of years, and temperatures of about 1100–1200°C (Shirey and Shigley, 2013) all lead to the

transformation of single nitrogen to more aggregated nitrogen defects, and the accompanying formation of cape spectral features, in the vast majority of natural diamonds. Most of these show intermediate concentrations of color-causing nitrogen incorporation such as N3 and its related absorptions such as N2—neither so small that the diamond is colorless, nor so great that it achieves a Fancy yellow color grade.

Brown. Both brown and pink color in diamonds (due to the formation of the brown absorption continuum and the 550 nm absorption band) are believed to be created by plastic deformation. However, careful high-pressure, high-temperature (HPHT) annealing of brown-pink diamonds can reduce the brown color while preserving the pink color, indicating that the corresponding 550 nm absorption band has higher thermal stability. Therefore, it appears likely that the deformation producing pink color occurs inside the earth's mantle (Smit and Shor, 2017; Eaton-Magaña et al., 2018b), while the more prevalent brown coloration is likely caused by the diamond's rapid ascent to the surface in kimberlite or lamproite vulcanism (Gaillou et al., 2010).

Distinction by Diamond Type. Diamond type has proven to be an important distinguishing characteristic in fancy-color diamonds, and colorless diamonds are no exception (Breeding and Shigley, 2009). Box A illustrates the nitrogen configurations that lead to the different diamond types, as well as the importance of this classification for color origin determination in colorless to near-colorless diamonds.

Recent research on the inclusions contained within type IIa (Smith et al., 2016), type IIb (Smith et al., 2018), and some type IaB diamonds (Kagi et al., 2016; Rudloff-Grund et al., 2016; Gu and Wang, 2017) has demonstrated that many of these stones have a

Figure 4. Recent research has shown that some type IaB, many type IIa, and potentially all type IIb diamonds have superdeep origins below the continental lithosphere, while the majority of the world's diamonds (generally type Ia/IaAB, but also some type IIa) have a more shallow lithospheric origin (~150–200 km depth; Shirey and Shigley, 2013). Most kimberlite pipes are found in geologically ancient and stable portions of the crust that geologists call cratons.
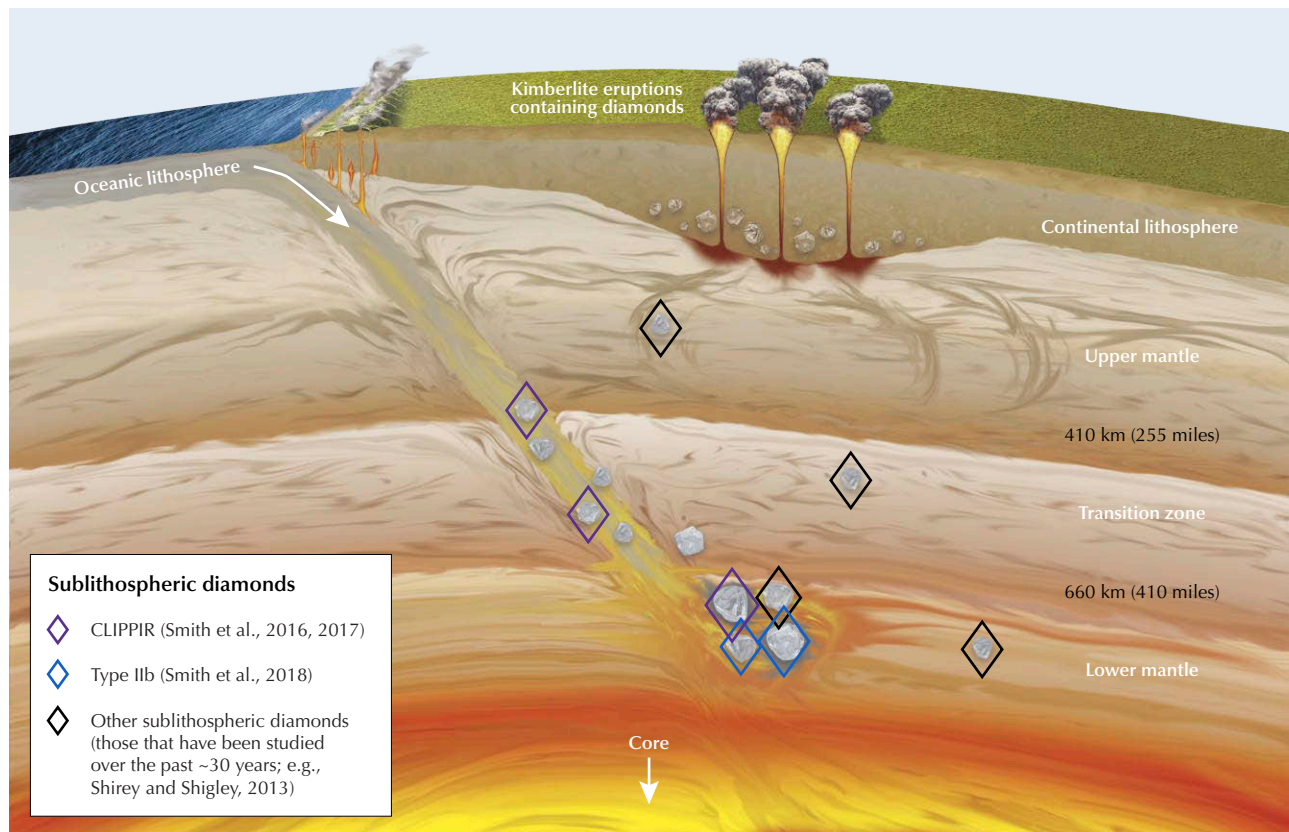
BOX A: A BRIEF SUMMARY OF DIAMOND TYPE

One of the foundations of diamond science is the determination of diamond type. The presence/absence of nitrogen or boron distinguishes the range of color, defects, and potential treatment history. Recent research has also shown that the various diamond types can have very different geological formation methods and depths (Shirey and Shigley, 2013; Smith et al., 2016, 2017, 2018; Kagi et al., 2016; Rudloff-Grund et al., 2016; Gu and Wang, 2017).

The B-aggregate has been identified as four nitrogen atoms surrounding a vacancy (Boyd et al., 1995), and it is generally considered the end product of the nitrogen aggregation process. Geologically young diamonds show nitrogen as single isolated atoms that coalesce over geologic time into pairs (A-aggregates; Kiflawi et al., 1994) and then ultimately into B-aggregates (figure A-1). This pairing of nitrogen atoms (and the subsequent steps of aggregation) involves internal diffusion at relatively high temperature and/or long geologic residence times during which the nitrogen atoms can move through the lattice by filling vacancies or changing places with adjacent car-

bon atoms. During the next stage of aggregation, the A centers form B-aggregates, and there is the side reaction (Woods, 1986) that produces N3 centers (three nitrogen atoms with a vacancy). The A- and B-aggregates are infrared active and produce infrared spectral features but no features in the visible spectrum (i.e., they do not produce any color). Meanwhile, the N3 defect is the opposite—it has no infrared features but possesses visible spectral features that result in yellow coloration.

If all A-aggregates have converted to B-aggregates and formed a type IaB diamond, then generally the diamond is geologically quite old or was subjected either to higher temperatures that encouraged aggregation or a combination of long residence time and high temperature. However, the vast majority of type I diamonds show a combination of A- and B-aggregates, so very few D-to-Z natural diamonds (0.09%) are shown to reach the type IaB endpoint.

Figure A-1 (bottom) shows another example of the importance of diamond types. The natural abundance of D-

Figure A-1. Top: The progression of nitrogen aggregation in natural diamonds. All young diamonds that contain nitrogen have it in the isolated form. Over millions to billions of years of residence in the earth, these isolated atoms find each other and pair to form A-aggregates. These A-aggregates further coalesce to form B-aggregates resulting in a combination of A- and B-aggregates—most natural diamonds are at this point on the A→B pathway. Very few progress to complete aggregation and show only B-aggregates. Bottom: The diamond type distribution for several forms of D-to-Z diamond demonstrates the importance of identifying whether a diamond is type II or type IaB, as these could be laboratory-grown or HPHT-treated.

Type Ib [N]

Type IaA [N-N]

Type IaB [N_4V]

Side reactions: Other defects formed such as N3 [N_3V] and 3107 cm^{-1} [N_3VH]

Time / Temperature

D-to-Z Diamond Type Distribution

Natural
Type IaB, 0.1% — Type II, 0.9%
Type Ia, 99%

HPHT Lab-Grown
Type II, 100%

CVD Lab-Grown
Type II, 100%

HPHT-Treated
Type IaB, 0.5%
Type II, 99.5%

Collect and assess IR spectrum on diamond

Does it contain nitrogen (1400–1100 cm⁻¹)?

Yes → Type I

No → Type II

Is it single nitrogen (peak at 1344 cm⁻¹)? Very, very rare in colorless diamonds

No → Type Ia

Yes → Type Ib

Does it contain boron (2800 cm⁻¹)? Peak will be small in colorless diamonds

Yes → Type IIb

No → Type IIa

Is the feature saturated at 1300–1100 cm⁻¹? Most colorless diamonds will be

Yes → Type Ia

No → Can determine form of aggregates

Feature at 1280 cm⁻¹? Yes → Type IaA

Feature at 1170 cm⁻¹? Yes → Type IaB

Features at both 1280 and 1170 cm⁻¹? Yes → Type IaAB

Type II
Type IIb
Type IIa
ABSORBANCE
4000 3500 3000 2500 2000 1500
WAVENUMBER (cm⁻¹)

Type I
Type IaA
Type Ia
Type IaB
Two-phonon region
Type IaAB
ABSORBANCE
2600 2400 2200 2000 1800 1600 1400 1200 1000
WAVENUMBER (cm⁻¹)

Figure A-2. This flowchart illustrates the identification process for determining diamond type.

to-Z diamonds is heavily skewed toward type Ia/IaAB (99%). Meanwhile, laboratory-grown diamonds in the D-to-Z color range are type II, while HPHT-treated D-to-Z diamonds can be either type II or type IaB (see box B for more regarding HPHT-treated diamonds). However, some reports on treated HPHT-grown diamonds indicate this could change in the future (Fang et al., 2018).

One aspect of comparing the infrared spectra of faceted stones is that the path length through a rough or polished diamond is unknown and rather difficult (or impossible) to determine compared to a double-sided parallel-polished plate, where the path length is simply the plate thickness. Fortunately, we can compare infrared spectra from different diamonds because the absorption coefficient of diamond is generally considered to be constant in the two- and three-phonon regions. For example, at 2000 cm⁻¹ the absorption coefficient is 12.3 cm⁻¹ (Tang et al., 2005; Breeding and Shigley, 2009). Each diamond IR spectrum, regardless of the sample's thickness or path length, can be compared by applying this normalization. As the two-phonon region is often saturated in the IR spectra of faceted diamonds, we generally compare each IR spectrum using the three-phonon region and apply that normalization to determine nitrogen/boron concentrations.

An interesting side note regarding the naming of the N3 and H3 centers (among others) is that the "N" in N3

and the "H" in H3 do not refer to nitrogen or hydrogen. Instead, they refer to "natural" and "heated," (Zaitsev, 2003), as these defect centers were observed and named decades ago in the Vis-NIR absorption spectra of natural and heated diamonds. Researchers at the time designated the peaks across the spectrum as 1, 2, 3, etc. In the years since, diamond scientists have identified these configurations. We now understand their formation process and can also detect H3 in the Vis-NIR absorption and photoluminescence spectra of natural, unheated diamonds. Nevertheless, the defect nomenclature remains. The configuration of the N3 defect is N_3V—it is pure coincidence that this defect contains three nitrogen atoms—and the H3 defect is NVN.

Similarly, type I and type II diamonds were distinguished decades ago, mainly on the basis of UV transparency (Robertson et al., 1933) instead of the detailed analysis of IR spectra used today. In the decades since that initial identification, scientists have recognized that the absence of nitrogen leads to observed UV transparency in type II diamonds, while the presence of nitrogen creates the UV absorption (type I). IR spectroscopy has allowed the distinguishing of the various forms of nitrogen and whether boron is present as the major impurity, to further subcategorize the two diamond types (figure A-2).

"superdeep" origin. These form principally at depths of ~300–800 km, largely within the mantle transition zone and uppermost lower mantle, while the vast majority of diamonds form within the continental lithosphere at depths of 150–200 km (figure 4). The differences in pressure, temperature, and local chemistry at these very distinct formation depths produce many of the differences between these diamond types.

At the greater depths where type II diamonds form, nitrogen is presumably not available in the surrounding geologic environment. Therefore, it cannot be incorporated into the growing diamond as with type I stones. Superdeep type IaB diamonds are exposed to much higher temperatures and pressures than their lithospheric cousins, and those higher temperatures promote complete nitrogen aggregation (again, see box A or Breeding and Shigley, 2009, for more information). While many, if not most, type IIa diamonds may be assumed to have a superdeep origin, there are some known type IIa diamonds that originate from the lithosphere along with type Ia diamonds (Smith et al., 2017). It is important to note that the type classification scheme does not translate directly to a geological classification, even though some notable and meaningful correlations exist between diamond type and the various geological settings of formation.

COMPARISON OF SPECTROSCOPY WITH LABORATORY GRADING

Standard testing conditions and instrumentation are applied to all diamonds submitted to GIA. Some that are potentially treated or laboratory-grown undergo additional testing. The instrumentation has been detailed in other publications (e.g., Smit et al., 2018) and is summarized for this series of articles in Breeding et al. (2018). In this study, diamond type was automatically determined from the IR spectra using a mathematical algorithm similar to the one used by GIA's DiamondCheck instrument, and the result was verified by the technician. Among those determined as type Ia, the calculation of the collected spectra, particularly the nitrogen concentration (in the form of A- and B-centers) and the intensity of the N_3VH defect (3107 cm^{-1} peak), was performed using custom software written by one of the authors (TA). The evaluation of these results was verified by manually calculating the aggregate concentrations on several hundred diamonds using a customized algorithm derived from a spreadsheet provided by Dr.

David Fisher (De Beers Group Technology, Maidenhead, UK) and comparing those results with the software's calculations. After the spectral results of all type Ia diamonds were calculated, the calculations were verified again on several hundred randomly selected diamonds. For the plots in this article, the dataset consisted of D-to-Z diamonds submitted to all GIA labs within a significant portion of 2017, as described above. A different dataset was used for the charts presented in box B, and those specifics are described therein.

Diamond Type and Grading Quality Factors. As noted above, diamond type is an important metric for inferring the likely formation depth of a diamond. It also creates a number of interesting comparisons when evaluating differences in grading quality factors. Box A provides a brief summary of diamond type; Breeding and Shigley (2009) examines this topic in much greater depth.

Because type II and type IaB diamonds comprise such a small percentage of submitted faceted diamonds, the dataset needed to be quite large so that these rare diamond types would have adequate representation, and therefore the dataset is composed of a majority of GIA's 2017 D-to-Z intake. Nevertheless, many of the following figures compare the distribution of grading quality factors for the various diamond types, even though the population within these groups may differ by several orders of magnitude. We show the distribution of the various grading quality factors for type II diamonds (separated into type IIa and boron-containing type IIb) and type I diamonds (separated as type IaB and type Ia/IaAB). To clarify, we use the designation of "type Ia" for all diamonds with saturated nitrogen (i.e., spectral absorption is too great to be quantified by the spectrometer, where we cannot distinguish the nitrogen aggregates more specifically) along with those that have unsaturated nitrogen and are determined to be either type IaA or type IaAB. These are also illustrated in box A. Among the many D-to-Z diamonds used for this study, 99.06% were determined to be type Ia/IaAB, 0.83% type IIa, 0.09% type IaB, and 0.02% type IIb. Figure 5 plots the distribution of various grading quality factors and fluorescence observations for type Ia/IaAB stones, and figure 6 plots the distribution for the remaining diamond types. Type Ib diamonds are not included in these figures, as the isolated nitrogen defect (N) associated with this diamond type generally introduces sufficient color to be classified as fancy color.
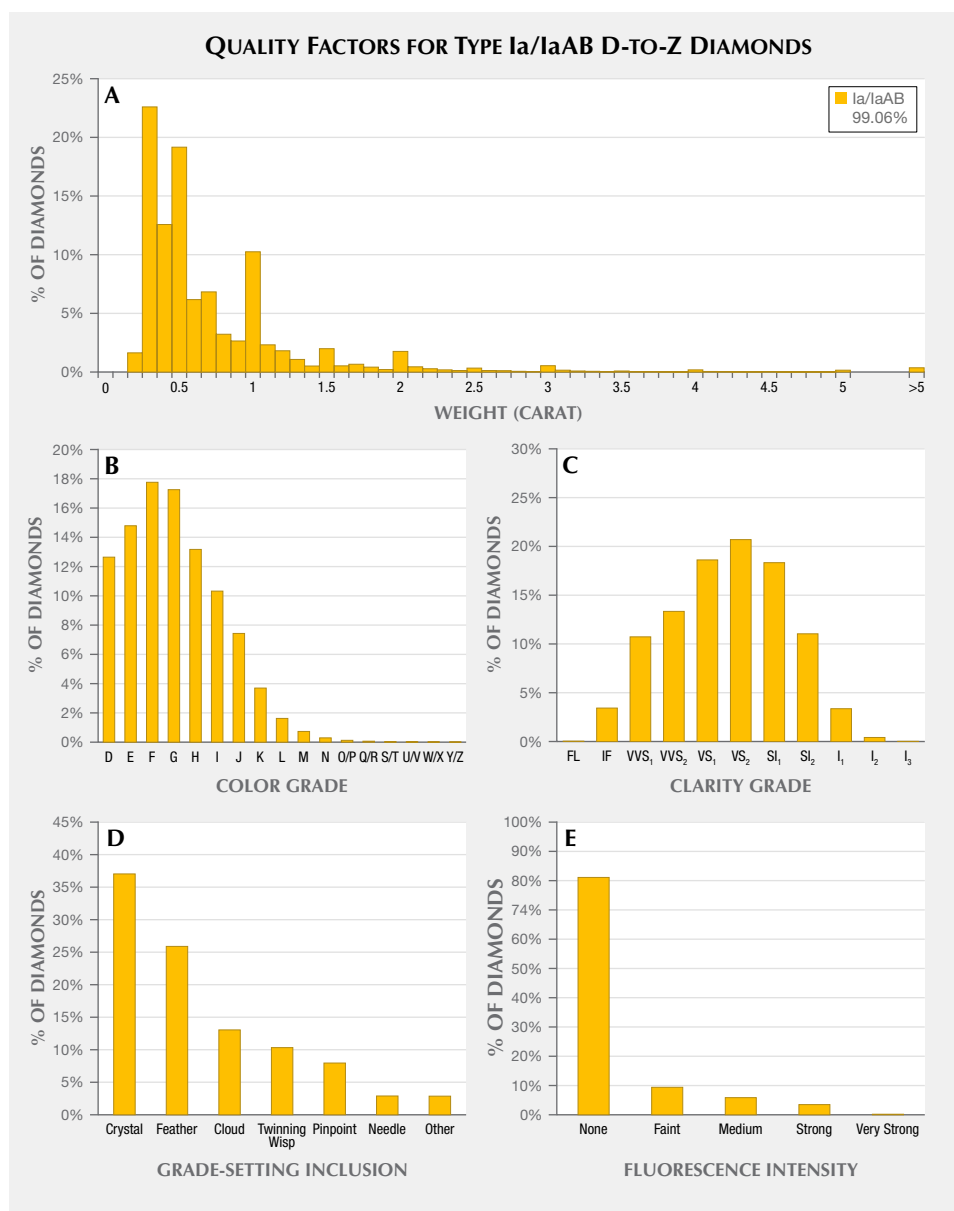
Figure 5. The dataset representing a majority of D-to-Z diamonds submitted to GIA in 2017 was separated according to diamond type and their grading quality factors chronicled accordingly. Here we present data for type Ia/IaAB. A: The weight histogram is divided into 0.1 ct increments between 0 and 5 ct. Also shown are the percentages of the remaining graded diamonds larger than 5 ct. B: Type Ia/IaAB diamonds show a plurality of F and G color grades. The remaining histograms show clarity (C), grade-setting inclusion (D), and fluorescence intensity (E).

Weight. Figures 5A and 6A show the distribution of D-to-Z diamonds across the carat weights for type I and type II. The data are presented in 0.1 ct increments, and noticeable spikes in quantity are observed (not surprisingly) near important carat-weight thresholds (e.g., 0.25, 0.5, 1.0, 1.5, and 2.0 ct), particularly for type I diamonds. These figures also show that type Ia diamonds are more plentiful among the smaller carat weights, while type II are more plentiful at higher weights—a trend consistent with prior observations (Smith et al., 2017). For example, 34% of type IIa diamonds weighed 0.5 ct or less and 60% weighed 1 ct or less. Among type Ia/IaAB diamonds, 49% weighed 0.5 ct or less and 79% weighed 1 ct or less.

Color. Figures 5B and 6B plot the distribution of D-to-Z color grades for the various diamond types. For type II and type IaB diamonds, the most common color is D, and the percentages decrease as the color grade increases. For type IIb, 72% of those within the D-to-Z range are D-color. These stones have a low boron concentration (<100 parts per billion); high boron values would generally place a diamond in the gray-to-blue fancy color range (King et al., 2008; Eaton-Magaña et al., 2017). Since type IIa diamonds have no detectable single nitrogen or nitrogen aggregates in the infrared, which can also correlate with nitrogen-related defects in the visible region, their major cause of color is plastic deformation, which gives a brown coloration.

QUALITY FACTORS FOR TYPE IIa/IIb/IaB D-TO-Z DIAMONDS
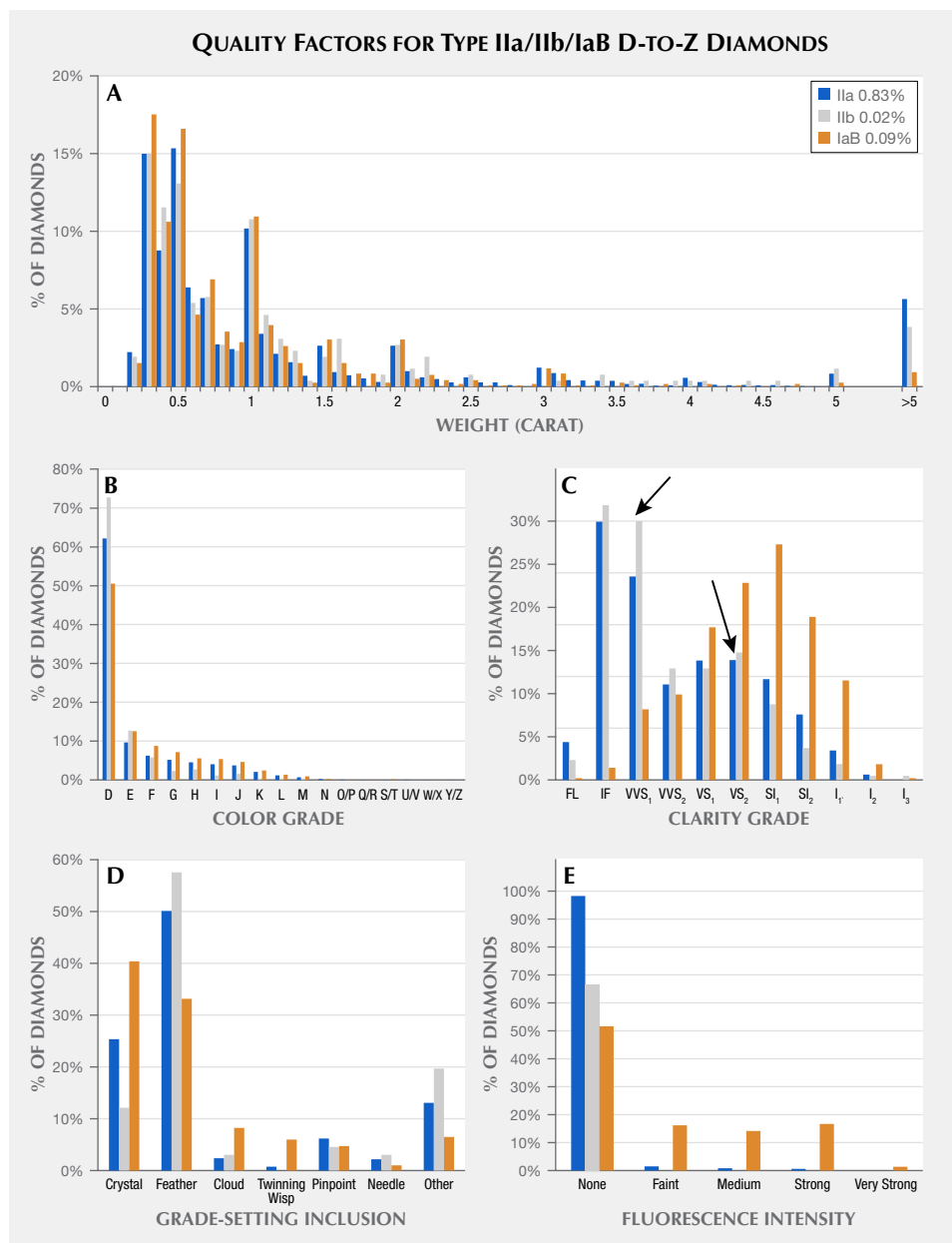
Figure 6. The dataset of D-to-Z diamonds was separated according to diamond type and their grading quality factors chronicled accordingly. Here we present data for type IIa/IIb/IaB. A: The weight histogram is divided into 0.1 ct increments between 0 and 5 ct. Also shown are the percentages of the remaining graded diamonds larger than 5 ct. B: The color distribution for type II and type IaB diamonds shows that the majority are D-color. C: For type IIa and type IIb diamonds, a bimodal distribution is seen with maxima at IF/VVS$_1$ clarity ranges and the VS$_2$ clarity grade (also marked by black arrows). This pattern noticeably contrasts with type I diamonds, which show a single maximum at the VS$_2$/SI$_1$ clarity range. D: For the majority of type II diamonds, the grade-setting inclusion feature is a feather, with a relatively low incidence of both crystals and twinning wisps compared to type I. E: Type II diamonds have the highest number with no fluorescence response, while type IaB show the lowest percentage.

Among type Ia diamonds, the color grades of F and G show the highest population (figure 5B). Since type Ia is by far the most abundant diamond type, this color distribution represents the vast majority of D-to-Z diamonds submitted to GIA for grading. Again, for type Ia diamonds, the major causes of color are higher concentrations of nitrogen-related defects that increase the yellow coloration.

Figure 7A shows the distribution of G to Z grades and the percentages for each color grade for brown versus yellow coloration; the brown/yellow assessment was made using GIA's internal color grading methodology. For G-color diamonds, only 5% had brown coloration. For the combined-grade diamonds (O to Z that are presented as O-P, Q-R, S-T, etc.), the percentage showing brown coloration has increased to 16%. It is interesting to note that for diamonds beyond the D-to-Z scale—that is, unmodified brown or yellow diamonds on the fancy color scale—there is a decidedly reverse trend, as there are far fewer Fancy brown than Fancy yellow diamonds submitted for grading, most likely due to market forces.

This trend in D-to-Z diamonds toward an increasing proportion of brown coloration with higher color saturation is also seen in figure 7B, which plots the

average nitrogen concentration of B-aggregates with color grade in type IaB diamonds. From D to G color, we see an increase in the concentration of B-aggregates, reaching a maximum for G color. For the combined-grade range (O to Z), the average nitrogen concentration (across all diamonds in the dataset) decreases as the percentage of diamonds with brown coloration becomes more prominent.

Figure 7C shows the results of the automatic calculations for nitrogen-aggregate defect concentrations from the infrared spectra for type Ia/IaAB diamonds.

Diamonds on the D-to-Z scale are predominantly type Ia with a mixture of A- and B-aggregates; many of them have such high nitrogen concentrations that we cannot determine the A/B ratio or the exact concentration (because the intensity of the infrared peaks exceeds the vertical scale of the spectrum plot due to very strong absorbance in this region). We generally refer to these as saturated type Ia or often as simply "type Ia." For faceted diamonds analyzed with current infrared spectrometers, those with nitrogen concentrations greater than 500 parts per million generally have infrared spec-

Figure 7. A: The yellow or brown coloration is shown for G to Z color. The percentage of diamonds with brown coloration increases from 5% for G color to 16% for the combined grades (O to Z). B: Among the small quantity of type I diamonds determined as type IaB, the concentration of B-aggregates can be determined and plotted versus color. The quantity increases from D to G color and then decreases as the brown coloration in these type IaB diamonds becomes more pronounced. C: The vast majority of type Ia/IaAB diamonds have IR spectra with a saturated nitrogen region, making it impossible to calculate their nitrogen concentration or A/B aggregate ratio. D: The 3107 cm⁻¹ peak (N_3VH) in the IR spectra can be determined in diamond, even if the nitrogen region is saturated. Here, the calculated median value and the values for the upper and lower quartiles illustrate the range of values for each color grade.

A
BROWN VS. YELLOW COLORATION IN G-Z DIAMONDS

B
AVERAGE NITROGEN B-AGGREGATE CONCENTRATION IN TYPE IaB DIAMONDS VS. COLOR GRADE

C
SATURATED NITROGEN AGGREGATES IN IR SPECTRA

D
NORMALIZED 3107 cm⁻¹ PEAK AREA IN IR SPECTRA FOR TYPE Ia D-TO-Z DIAMONDS
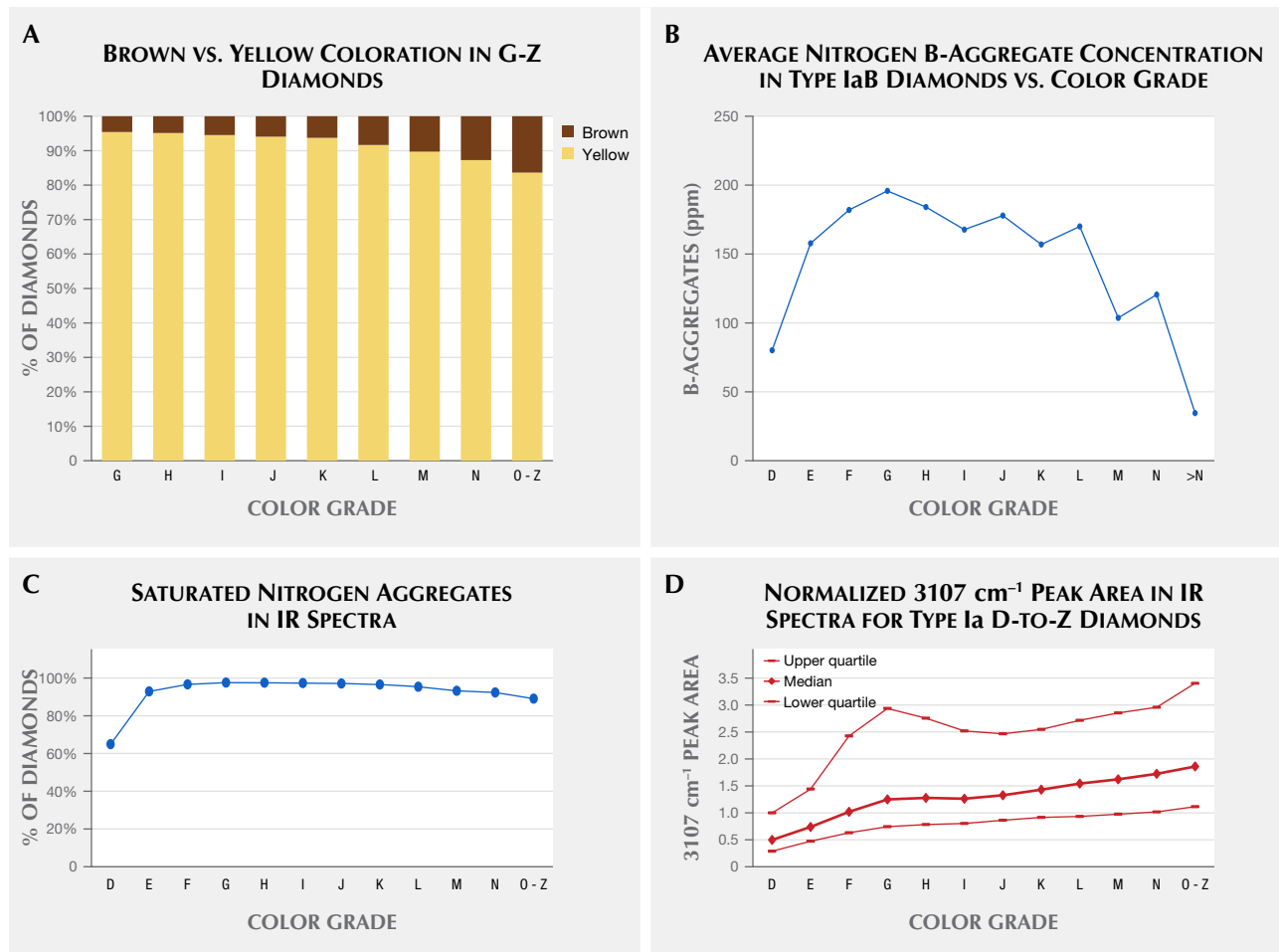
BOX B: GRADING QUALITY FACTORS IN HPHT-TREATED DIAMONDS

We discuss here a dataset that is different from the one in the main body of the article. Here, the dataset consists of HPHT-treated diamonds in the D-to-Z range that have been submitted to all GIA laboratories over the last decade; it includes several thousand stones.

Gemological data have been published on small quantities of stones when this treatment was first seen in the trade (Chalain et al., 1999; Fisher and Spits, 2000) and when notably large diamonds were HPHT treated (e.g., Wang, 2010). As mentioned in the Identification section, only type II and the rare type IaB diamonds may be HPHT treated to remove or reduce brownish or grayish coloration. Most commercial HPHT treatments are conducted in the 1900–2100°C range, as reaching these temperatures is considered relatively inexpensive and reliable for the color treatment of light brown diamonds (Dobrinets et al., 2013).

The spectra and images for our dataset of HPHT-treated diamonds were collected using similar methods to those described above for natural-color D-to-Z diamonds. The same software was used to assist in diamond type determination and nitrogen concentrations for type IaB diamonds. Among this dataset of HPHT-treated diamonds, 0.5% were type IaB, 1.7% were type IIb, and the balance (97.8%) were type IIa. Among the type IaB diamonds chosen for HPHT treatment, the concentration of B-aggregates is considerably lower than among natural, untreated type IaB. The HPHT-treated, type IaB diamonds had B-aggregates ranging from ~1 ppm to 90 ppm, with an average value of <10 ppm. In comparison, the B-aggregates in natural, untreated type IaB ranged from ~1 ppm to 570 ppm, with an average value of ~120 ppm.

Figure B-1 illustrates the distribution of various grading quality factors for these stones. Unlike the data in the main body of this article, these graphs plot the different diamond types together due to the much smaller sample set. A comparatively large percentage of these stones (11%) are greater than 5 ct, almost twice the percentage we see among natural type IIa diamonds (6%; compare figure B-1A with figure 6A). It is possible that the larger-size, off-color diamonds were considered worth the risk and expense of the treatment to improve their color.

Figure B-1B shows the post-treatment color distribution of these HPHT-treated diamonds. The majority are heated to high temperatures (1900–2100°C; Dobrinets et al., 2013) such that the result is in the colorless range (D to F). Figure B-1C shows the shape distribution of HPHT-treated diamonds. Figure B-1D shows the clarity distribution of HPHT-treated diamonds, which, as with natural type II diamonds, skews toward the higher clarity grades but does not show the bimodal distribution seen among the natural type IIa diamonds (figure 6C). Despite the high stabilizing pressures used in HPHT treatment, diamonds with poorer clarity grades and a number of internal clarity features generally do not benefit from HPHT treatment due to discoid fractures that form around crystal inclusions and graphitization of preexisting fractures (Fisher and Spits, 2000). For a majority of these HPHT-treated diamonds, a feather is the grade-setting feature (figure B-1E), which is comparable with the natural distribution of type IIa diamonds (figure 6D). Yet the incidence of crystal inclusions is far lower in HPHT-treated diamonds (10% compared to 25% for IIa natural diamonds), showing that type IIa diamonds are carefully chosen for HPHT processing to minimize the possibility of adverse effects from this treatment process.

---

tra with saturated nitrogen. The likelihood that an IR spectrum will be saturated is also affected by the size of the faceted diamond as the path length approximately increases with size for the same shape. A thin plate fashioned from a type Ia diamond would have a higher threshold for saturation, and these higher nitrogen concentrations could be quantified.

Figure 7C shows that the vast majority, nearly 100% for most color grades, have saturated spectra in which the A- and B-aggregate concentrations cannot be determined. The exceptions are D-color diamonds, in which only 65% have saturated nitrogen. There is a slight decrease in the percentage of lower color grades (moving toward Y-Z color) showing saturated spectra; the higher number of diamonds showing brown coloration decreases the overall average nitrogen concentration.

Since the vast majority of type Ia/IaAB D-to-Z diamonds have saturated nitrogen in their infrared spectra, we are unable to determine their nitrogen concentration or their A/B aggregate ratio. Therefore, any trends in total nitrogen or A/B ratio can include only a small percentage of diamonds where the infrared spectral features fall within the vertical scale of the spectrum plot. In order to observe trends in the infrared spectra of this massive database without being able to look at nitrogen aggregates, we can consider other features in the infrared—most notably the 3107 wavenumber (cm^{-1}) peak. This peak has long been correlated with hydrogen impurity in diamond, and it has been recently attributed to the N_3VH defect—that is, the N3 center plus a hydrogen atom (Goss et al., 2014). N3 is an important color center in D-to-Z diamonds. It is one of the major defects

QUALITY FACTORS FOR HPHT-TREATED D-TO-Z DIAMONDS

Figure B-1. The distribution of grading quality factors in D-to-Z HPHT-treated diamonds are shown for weight (A), color (B), shape (C), clarity (D), and grade-setting clarity characteristic (E).

leading to yellow coloration, and it creates the most commonly observed blue fluorescence. The 3107 cm^{-1} peak rarely saturates within the spectrum, so its intensity can be determined for almost all infrared spectra, including those with saturated nitrogen-aggregate spectral features, although its intensity may not always correlate with other nitrogen defects. Figure 7D presents the results of these calculations for the normalized 3107 cm^{-1} peak area (which is generally proportional to the concentration) plotted versus the graded color (see box A for more detail on this normalization). The values represent the median within each color grade, while the upper and lower quartile values indicate the spread of data for these diamonds. The graph shows that the median value of the 3107 cm^{-1} intensity increases with color. The upper quartile (i.e., those diamonds with values be-

tween the median and the 75th percentile) also shows a high value at around G color, possibly due to the very high nitrogen seen in those diamonds.

Clarity. One interesting trend among the various diamond types (figures 5C and 6C) is that type II diamonds have a bimodal clarity grade distribution—that is, they show a maximum in percentage of diamonds with IF/VVS$_1$ clarity grades and another maximum in VS$_2$ clarity (indicated by arrows on the graph). This pattern is seen independently in both type IIa and type IIb. Meanwhile, type I diamonds (both type Ia/IaAB and type IaB) show one maximum at VS$_2$/SI$_1$ clarity grades. While type IaB diamonds share a similar pattern in color grade distribution with type II diamonds (see again figure 6B), they show a similar clarity grade distribution with type Ia diamonds in figure 5C.

Figures 5D and 6D show the distribution of grade-setting clarity characteristics for the different diamond types. Since many of the type II diamonds skew toward the higher clarity grades, the clarity features are likely smaller and less abundant/noticeable than in their type Ia/IaB counterparts. Nevertheless, the most common clarity characteristic in type II diamonds is feathers, with a much smaller percentage of crystal inclusions than in type I. This comparison is consistent with the prior observation of Smith et al. (2017) regarding superdeep type IIa diamonds, which they termed CLIPPIR diamonds—an acronym that contains the phrase "inclusion-poor." Also, the twinning wisp clarity feature is much less abundant among type II than type I diamonds (10% in type Ia/IaAB diamonds versus 0.7% in type IIa and 0% in type IIb). Twinning wisps are groups of microscopic inclusions formed along an orientation change in the crystal structure (a twin plane) during growth. These are considered unique to natural diamonds and, as seen here, mostly type Ia natural diamonds.

To study the bimodal distribution of clarity grades in type II diamonds in greater detail, we examined the grade-setting inclusions. The results show that among type IIa and type IIb diamonds with VVS_1 clarity, feathers were the most common grade-setting inclusions, while other inclusions such as pinpoints or clouds were seldom the grade setters. At lower clarity grades in type IIa diamonds, feathers or crystals were the most common. For a grade-setting feather to be considered VVS_1, it must be small, located on the pavilion, and most importantly have little to no depth; often these can be improved to IF by repolishing. Therefore, type II diamonds appear to have two distinct clarity populations—about half (48% of type IIa and 53% of type IIb) are FL or IF, or VVS_1 that are potentially improvable to IF. The other half generally have more significantly sized feathers, crystal inclusions, or other features, spanning from VVS_2 to I_1 clarity. Subsequent analysis of the clarity distribution in type II diamonds across the years 2010–2019 showed that this bimodal distribution was consistent and not specific to 2017.

If we limit our examination to only those stones larger than 10 ct, we see other interesting observations and distinctions between type I and type II diamonds. For large type II diamonds, the bimodal distribution does not remain. Instead, the majority of large type II diamonds are FL to VVS_1, which is consistent with figure 2C in Smith et al. (2017). For such large diamonds, cutters are quite diligent in planning around inclusions within the rough. For ex-

ample, the 603 ct Lesotho Promise rough showed several dark and likely metallic eye-visible inclusions and yet, through careful preparation and skilled cutting, yielded 26 D-FL diamonds (0.55–75 ct totaling 224 ct; Krawitz, 2008). Meanwhile, type Ia/IaAB diamonds larger than 10 ct show a clarity distribution similar to the entire dataset with a maximum at VS_2 clarity grades, consistent with figure 2C in Smith et al. (2017).

While planning and cutting decisions help improve the clarity grade of faceted diamonds and guide the polisher to an IF/VVS_1 grade, this does not generally appear to be possible for type Ia, even among higher-weight stones. It appears specific to a significant portion of type II rough.

Fluorescence. While fluorescence is not a grading quality factor, its observation is reported on grading reports and included here as well. Figures 5E and 6E show the distribution of fluorescence intensities among the various diamond types. As expected for type II diamonds, which have no detectable nitrogen in the infrared spectrum, they have very little incidence of fluorescence. In nearly 100% of these, fluorescence is described on the grading report as "None."

In contrast, type IaB diamonds have only ~50% with "None." This is not surprising, as the primary cause of fluorescence is the N3 defect, which is created as A-aggregates progress to B-aggregates (again, see box A). Additionally, type IaB diamonds do not contain A-aggregates that could act to quench (suppress) fluorescence, so type IaB diamonds show the highest incidence of medium to strong fluorescence. In diamonds containing A-aggregates, these interact with N3 defects in such a way that fluorescence may not be observed. The presence of A-aggregates inhibits fluorescence of the N3 center by creating an alternate, non-radiative (i.e., non-fluorescing) pathway for the electron to return from the excited state to the ground state (Collins, 1992; Vasil'ev et al., 2004).

Figure 8 plots the calculated features from the infrared spectra against the fluorescence intensity observations. As mentioned above, the vast majority of type Ia diamonds have saturated response in the nitrogen region of their infrared spectra, which makes it impossible to determine their concentration of nitrogen aggregates. In a small percentage of type Ia diamonds, we can determine the A- and B-aggregates and correlate those with the fluorescence intensity. Figure 8 (left) shows the median values for the A- and B-aggregates (and the upper and lower quartiles) for each fluorescence intensity. As the intensity pro-

A- AND B-AGGREGATE CONCENTRATION VS. FLUORESCENCE INTENSITY (UNSATURATED IR)

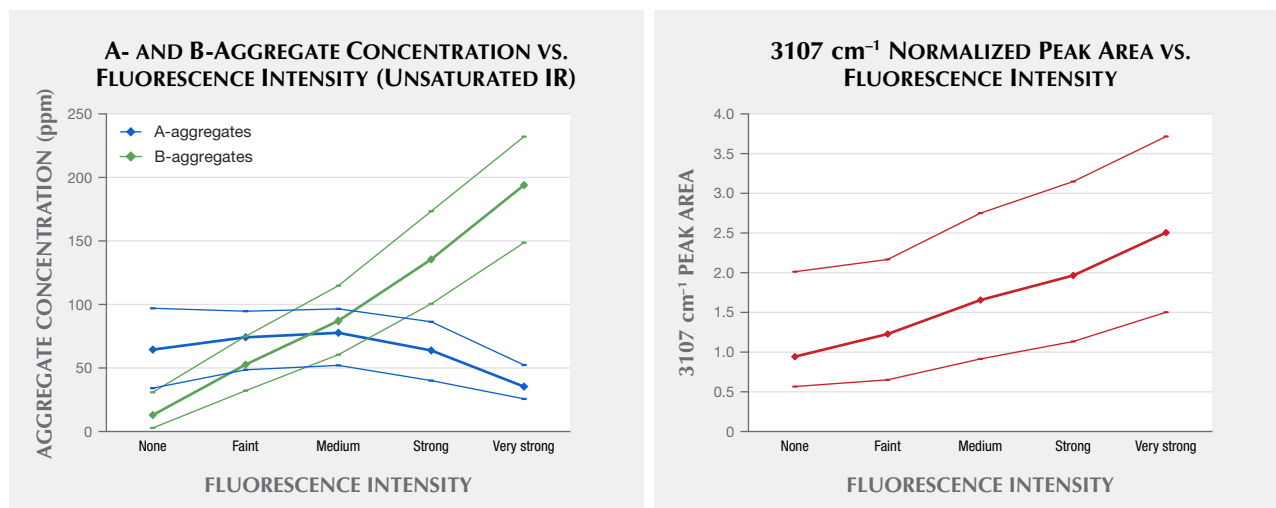**3107 cm⁻¹ NORMALIZED PEAK AREA VS. FLUORESCENCE INTENSITY**

Figure 8. Left: For diamonds with unsaturated nitrogen, the A- and B-aggregates were calculated and plotted according to their fluorescence observations. For both A- and B-aggregates, the median value along with the upper and lower quartile are plotted. Right: For a far higher number of the IR spectra for diamonds, the 3107 cm⁻¹ normalized peak area, the median value, and the upper and lower quartile can be plotted.

gresses, there is a shift from predominantly A-aggregates among the "None" category to predominantly B-aggregates among the "Very strong." Figure 8 (right) shows the increase in the 3107 cm⁻¹ normalized peak area of the infrared spectra (again, the 3107 cm⁻¹ peak is the N3 fluorescence defect associated with hydrogen; see Goss et al., 2014). The median value for the 3107 cm⁻¹ normalized peak area increases from ~1.0 for those showing "None" to ~2.5 for "Very strong."

OTHER FACTORS: SHAPE AND CUT

Software introduced shortly after 2000 has allowed manufacturers to plan the cutting of rough shapes with high color and clarity by mapping their inclusions. Cutters now use sophisticated planning pro-

grams that maximize the cut quality (with specific parameters for various cut shapes) and clarity grades so that the highest-value yield guides the cutting choices. The software lists the options available in value order, and the cutter can then view instructions for where to saw the rough and parameters to cut in order to yield the highest value from the entire piece.

The morphology of the original rough also influences the shapes available to cutters. The octahedron, generally sourced from the continental lithosphere, is the most common shape for diamond rough. Figure 9 (left) shows that two round brilliants are often the best use of the available rough octahedron when planning. In contrast, irregular rough can often present a variety of shapes (such as rounds and a pear in the example in figure 9, right) as the best choices to the cutters.
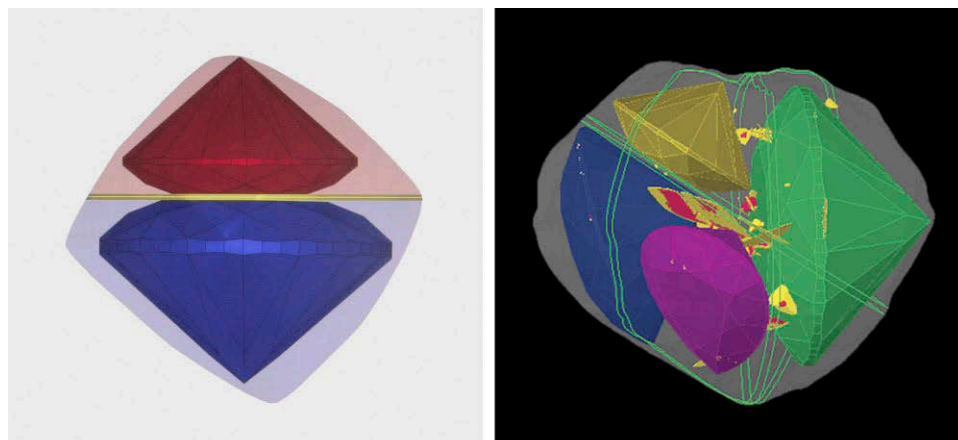

Figure 9. Left: The computer-generated planning solution for faceting a rough diamond octahedron into two rounds. This shape of rough is only expected to occur in diamonds originating from the lithosphere. Right: An irregular rough crystal (generated by Lexus M-Box software) can often lend itself to a variety of resulting shapes.

GEMOLOGICAL OBSERVATIONS

Under magnification, the most prominent visible features in D-to-Z diamonds are mineral inclusions (crystals and clouds), feathers, twinning wisps, and graining. Numerous resources detail the various crystal inclusions and the microscopic world of natural diamonds (e.g., Koivula, 2000; Renfro et al., 2018). Among the most common mineral inclusions are garnets, olivines, clinopyroxenes, and various sulfide minerals, identified by their appearance and distinctive Raman spectra.

Graining, however, is not as widely understood as crystal inclusions. Graining in D-to-Z diamonds—particularly whitish, reflective, and transparent graining—was discussed by King et al. (2006) and includes any planar (or visibly linear and repeating) internal features seen under magnification (figure 10A). These features are widely considered to be planes of misaligned carbon atoms in the crystal structure, usually due to plastic deformation. In its more extreme forms, graining is associated with vacancy clusters that absorb light and produce a brown color (figure 10B). Brown graining is common in type Ia brownish diamonds in the G to Z range, but not as prevalent in type IIa diamonds with similar colors. When vacancy clusters are not sufficiently concentrated in the grain lines to produce brown color, the graining appears transparent or colorless and may be whitish or reflective, or even exhibit interference colors in rare instances due to distortion of the light by the planar features (figure 10, C and D). Even HPHT-processed diamonds that have been decolorized often retain clearly visible transparent graining that was once brown before the vacancy clusters were destroyed by the treatment (figure 10E).

IDENTIFICATION CONCERNS

The vast majority of natural D-to-Z diamonds are type Ia/IaAB (99%; figure A-1) and cannot be decolorized by HPHT processing. Natural diamonds in the D-to-Z range that are type IIa (0.83%), type IIb (0.02%), or type IaB (0.09%) can be subjected to HPHT processing to reduce a brownish or grayish appearance, and the color origin of such diamonds should be confirmed by a gemological laboratory (Chalain et al., 1999; Fisher and Spits, 2000). More information regarding HPHT-treated diamonds is discussed in box B.

For a colorless diamond to be grown by chemical vapor deposition (CVD) or HPHT methods, its diamond type must be type II (e.g., see figure A-1, top). An infrared spectrometer can quickly determine diamond type, helping to separate the vast population of colorless natural type Ia diamonds from the much smaller population of those that might have been treated or laboratory grown, but IR analysis cannot determine the color origin of a diamond. Many types of detection equipment based upon other methods, such as Vis-NIR absorption spectroscopy or fluorescence spectroscopy, indirectly ascertain the diamond type. The assessment of such detection methods is beyond the scope of this article; however, third-party testing and evaluation of common laboratory-grown diamond detection equipment is available (e.g., https://www.naturaldiamonds.com/council/assure-testing-program/). More details regarding growth methods and identification criteria of CVD- and HPHT-grown diamonds with D-to-Z color have been previously documented (Wang et al., 2012; D'Haenens-Johansson et al., 2015; Eaton-Magaña and Shigley, 2016; Eaton-Magaña et al., 2017).

Figure 10. Graining in D-to-Z diamond is relatively common and related to displaced planes of carbon atoms in the atomic lattice (A). Brown graining indicates vacancy cluster defects along the areas of distortion (B), while reflective or interference (rainbow) graining is a product of light interaction with the grainlines (C and D). Even after HPHT treatment has removed the brown color to decolorize a diamond, remnant transparent graining can often still be seen (E). Photomicrographs by Kyaw Soe Moe (A), Vincent Cracco (B and C), and John I. Koivula (D and E).
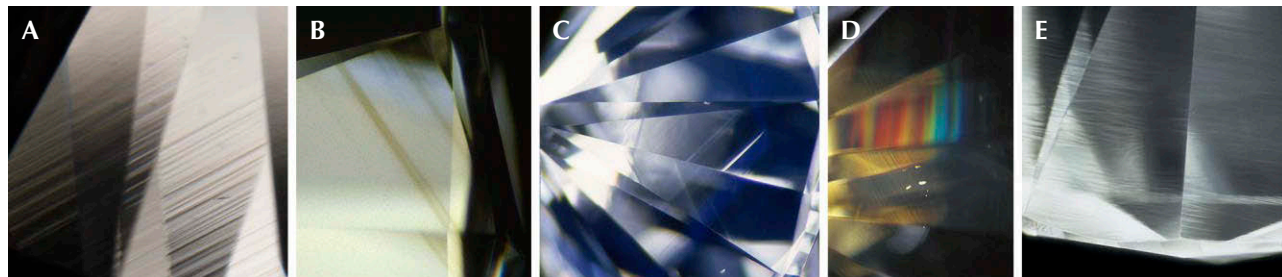
Figure 11. Colorless diamonds are a cornerstone of the gem trade. Photo by Robert Weldon.

CONCLUSIONS

Previous research has shown that most type I and type II diamonds (distinguished by the presence/absence of detectable nitrogen in their IR spectra) formed under very different conditions (Shirey and Shigley, 2013; Smith et al., 2016, 2018). These differences extend to the faceted diamonds studied here. We examined the grading quality factors (among other properties) on all diamonds submitted to all GIA laboratories during much of 2017, and these showed quite distinct distri-

butions. A majority of type II and type IaB diamonds show D color. For type II diamonds, the average carat weight is greater and the cut grades are higher. Additionally, type II diamonds show a bimodal clarity distribution, with a significant percentage of both type IIa and type IIb showing IF clarity (or VVS_1 clarity that is perhaps improvable to IF), while the remaining type II diamonds more closely resemble the clarity distribution of type I.

In a separate examination, we looked at the distribution of grading quality factors for HPHT-treated diamond (box B). The vast majority of these are large type IIa diamonds, treated at a sufficiently high temperature to become colorless. Due to the adverse effects of HPHT treatment on lower-clarity diamonds, the majority of the stones chosen are in the VVS range.

Most people are familiar with colorless to near-colorless diamonds and GIA's 4Cs grading system for evaluating them. However, analyzing the distribution across the grading range for such a large sample set illuminated some heretofore unseen trends. The majority of the world's diamonds that have been submitted to GIA—type Ia/IaAB that likely formed in the continental lithosphere—generally show high quantities of nitrogen and often have no observable fluorescence. Type II diamonds show some distinctly different patterns in grading quality factors that likely correspond with their unique formation, along with cutting decisions stemming from those differences.

Although this article compiles and combines data for an enormous dataset of the world's diamonds (figure 11), each stone remains unique. No two natural diamonds are alike. Each has its own specific clarity plot, IR spectrum, faceting pattern, and formation story.

ABOUT THE AUTHORS
Dr. Eaton-Magaña is a senior manager of diamond identification, Mr. Ardon is a research associate, Dr. Breeding is a senior manager of analytics, and Dr. Shigley is a distinguished research fellow, at GIA in Carlsbad, California.

REFERENCES

Bouman M., Anthonis A., Chapman J., Smans S., De Corte K. (2018) The effect of blue fluorescence on the colour appearance of round-brilliant-cut diamonds. *Journal of Gemmology*, Vol. 36, No. 4, pp. 298–315.

Boyd S.R., Kiflawi I., Woods G.S. (1995) Infrared absorption by the B nitrogen aggregate in diamond. *Philosophical Magazine B*, Vol. 72, No. 3, pp. 351–361, http://dx.doi.org/10.1080/13642819508239089

Breeding C.M., Eaton-Magaña S.C. (2019) Fluorescence of natural and synthetic gem diamond: Mechanism and applications. *Encyclopedia of Analytical Chemistry*, John Wiley & Sons, Ltd.

Breeding C.M., Shigley J.E. (2009) The "type" classification system of diamonds and its importance in gemology. *G&G*, Vol. 45, No. 2, pp. 96–111, http://dx.doi.org/10.5741/GEMS.45.2.96

Breeding C.M., Eaton-Magaña S.C., Shigley J.E. (2018) Natural-color green diamonds: A beautiful conundrum. *G&G*, Vol. 54, No. 1, pp. 2–27, http://dx.doi.org/10.5741/GEMS.54.1.2

Breeding C.M., Eaton-Magaña S.C., Shigley J.E. (2020) Naturally colored yellow and orange gem diamonds: The nitrogen factor. *G&G*, Vol. 56, No. 2, pp. 194–219, http://dx.doi.org/10.5741/GEMS.56.2.194

Caspi A. (1997) Modern diamond cutting and polishing. *G&G*, Vol. 33, No. 2, pp. 103–121, http://dx.doi.org/10.5741/GEMS.33.2.102

Chalain J.P., Fritsch E., Hänni H.A. (1999) Detection of GEPOL diamonds, a first stage. *Revue de. Gemmologie*, No. 138–139, pp. 30–33.

Collins A.T. (1992) The characterisation of point defects in diamond by luminescence spectroscopy. *Diamond and Related Materials*, Vol. 1, No. 5/6, pp. 457–469, http://dx.doi.org/10.1016/0925-9635(92)90146-F

Davies G., Crossfield M. (1973) Luminescence quenching and zero-phonon line broadening associated with defect interactions in diamond. *Journal of Physics C: Solid State Physics*, Vol. 6, No. 5, L104-L108, http://dx.doi.org/10.1088/0022-3719/6/5/007

D'Haenens-Johansson U.F., Katrusha A., Johnson P., Wang W. (2015) Large colorless HPHT-grown synthetic gem diamonds from New Diamond Technology, Russia. *G&G*, Vol. 51, No. 3, pp. 260–279, http://dx.doi.org/10.5741/GEMS.51.3.260

Dirlam D.M., Shigley J.E., Overlin S.D. (2002) The ultimate gemologist: A tribute to Richard T. Liddicoat. *G&G*, Vol. 38, No. 1, pp. 2–13, http://dx.doi.org/10.5741/GEMS.38.1.2

Dobrinets I.A., Vins V.G., Zaitsev A.M. (2013) *HPHT-Treated Diamonds: Diamonds Forever.* Springer, Heidelberg.

Eaton-Magaña S.C., Shigley J.E. (2016) Observations on CVD-grown synthetic diamonds: A review. *G&G*, Vol. 52, No. 3, pp. 222–245, http://dx.doi.org/10.5741/GEMS.52.3.222

Eaton-Magaña S.C., Shigley J.E., Breeding C.M. (2017) Observations on HPHT-grown synthetic diamonds: A review. G&G, Vol. 53, No. 3, pp. 262–284, http://dx.doi.org/10.5741/GEMS.53.3.262

Eaton-Magaña S.C., Breeding C.M., Shigley J.E. (2018a) Natural-color blue, gray, and violet diamonds: Allure of the deep. G&G, Vol. 54, No. 2, pp. 112–131, http://dx.doi.org/10.5741/GEMS.54.2.112

Eaton-Magaña S.C., Ardon, T., Smit K.V., Breeding C.M., Shigley J.E. (2018b) Natural-color pink, purple, red, and brown diamonds: Band of many colors. G&G, Vol. 54, No. 4, pp. 352–377, http://dx.doi.org/10.5741/GEMS.54.2.352

Eaton-Magaña S.C., Ardon T., Breeding C.M., Shigley J.E. (2019) Natural-color fancy white and fancy black diamonds: Where color and clarity converge. G&G, Vol. 55, No. 3, pp. 320–327, http://dx.doi.org/10.5741/GEMS.55.3.320

Fang C., Zhang Y., Zhang Z., Shan C., Shen W., Jia X. (2018) Preparation of "natural" diamonds by HPHT annealing of synthetic diamonds. Crystal Engineering Communications, Vol. 20, No. 4, pp. 505–511, http://dx.doi.org/10.1039/C7CE02013A

Fisher D., Spits R.A. (2000) Spectroscopic evidence of GE POL HPHT-treated natural type IIa diamonds. G&G, Vol. 36, No. 1, pp. 42–49, http://dx.doi.org/10.5741/GEMS.36.1.42

Fisher D., Sibley S.J., Kelly C.J. (2009) Brown colour in natural diamond and interaction between the brown related and other colour-inducing defects. Journal of Physics: Condensed Matter, Vol. 21, No. 36, Article 364213, 10 pp., http://dx.doi.org/10.1088/0953-8984/21/36/364213

Gaillou E., Post J.E., Bassim N.D., Zaitsev A.M., Rose T., Fries M.D., Stroud R.M., Steele A., Butler J.E. (2010) Spectroscopic and microscopic characterizations of color lamellae in natural pink diamonds. Diamond and Related Materials, Vol. 19, No. 10, pp. 1207–1220, http://dx.doi.org/10.1016/j.diamond.2010.06.015

Geurts R.H., Reinitz I.M., Blodgett T., Gilbertson A.M. (2011) GIA's symmetry grading boundaries for round brilliant cut diamonds. G&G, Vol. 47, No. 4, pp. 286–295, http://dx.doi.org/10.5741/GEMS.47.4.286

Goss J.P., Briddon P.R., Hill V., Jones R., Rayson M.J. (2014) Identification of the structure of the 3107 cm^{-1} H-related defect in diamond. Journal of Physics: Condensed Matter, Vol. 26, No. 14, pp. 1–6, http://dx.doi.org/10.1088/0953-8984/26/14/145801

Gu T., Wang W. (2017) IaB diamond and its geological implications. International Kimberlite Conference: Extended Abstracts, Vol. 11.

Hemphill T.S., Reinitz I.M., Johnson M.L., Shigley J.E. (1998) Modeling the appearance of the round brilliant cut diamond: An analysis of brilliance. G&G, Vol. 34, No. 3, pp. 158–183, http://dx.doi.org/10.5741/GEMS.34.3.158

Hounsome L.S., Jones R., Martineau P.M., Fisher D., Shaw M.J., Briddon P.R., Oberg S. (2006) Origin of brown coloration in diamond. Physical Review B, Vol. 73, No. 12, Article 125203, http://dx.doi.org/10.1103/PhysRevB.73.125203

Kagi H., Zedgenizov D.A., Ohfuji H., Ishibashi H. (2016) Micro- and nano-inclusions in a superdeep diamond from São Luiz, Brazil. Geochemistry International, Vol. 54, No. 10, pp. 834–838, http://dx.doi.org/10.1134/S0016702916100062

Kaminsky F.V., Zakharchenko O.D., Griffin W.L., Channer D.M.D., Khachatryan-Blinova G.K. (2000) Diamond from the Guaniamo area, Venezuela. The Canadian Mineralogist, Vol. 38, No. 6, pp. 1347–1370, http://dx.doi.org/10.2113/gscanmin.38.6.1347

Kiflawi I., Mayer A.E., Spear P.M., Van Wyk J.A., Woods G.S. (1994) Infrared absorption by the single nitrogen and A defect centres in diamond. Philosophical Magazine B, Vol. 69, No. 6, pp. 1141–1147, http://dx.doi.org/10.1080/01418639408240184

King J.M., Moses T.M., Wang W. (2006) The impact of internal whitish and reflective graining on the clarity grading of D-to-Z color diamonds at the GIA Laboratory. G&G, Vol. 42, No. 4, pp. 206–220, http://dx.doi.org/10.5741/GEMS.42.4.206

King J.M., Geurts R.H., Gilbertson A.M., Shigley J.E. (2008) Color grading "D-to-Z" diamonds at the GIA Laboratory. G&G, Vol. 44, No. 4, pp. 296–321, http://dx.doi.org/10.5741/GEMS.44.4.296

Koivula J.I. (2000) The Microworld of Diamonds: A Visual Reference Guide. Gemworld International, Inc., Northbrook, IL, 157 pp.

Krawitz A. (2008) Graff unveils Lesotho Promise necklace. https://www.diamonds.net/news/NewsItem.aspx?ArticleID=22702 [Accessed: 2/19/2020]

Luo Y., Breeding C.M. (2013) Fluorescence produced by optical defects in diamond: Measurement, characterization, and challenges. G&G, Vol. 49, No. 2, pp. 82–97, http://dx.doi.org/10.5741/GEMS.49.2.82

Moses T.M., Reinitz I.M., Johnson M.L., King J.M., Shigley J.E. (1997) A contribution to understanding the effect of blue fluorescence on the appearance of diamonds. G&G, Vol. 33, No. 4, pp. 244–259, http://dx.doi.org/10.5741/GEMS.33.4.244

Moses T.M., Johnson M.L., Green B., Blodgett T., Cino K., Geurts R.H., Gilbertson A.M., Hemphill T.S., King J.M., Kornylak L., Reinitz I.M., Shigley J.E. (2004) A foundation for grading the overall cut quality of round brilliant cut diamonds. G&G, Vol. 40, No. 3, pp. 202–229, http://dx.doi.org/10.5741/GEMS.40.3.202

Renfro N.D., Koivula J.I., Muyal J., McClure S.F., Schumacher K., Shigley J.E. (2018) Inclusions in natural, synthetic, and treated diamond. G&G, Vol. 54, No. 4, pp. 428–429, http://dx.doi.org/10.5741/GEMS.54.4.428

Robertson R., Fox J.J., Martin A.E. (1933) Two types of diamonds. Philosophical Transactions of the Royal Society A, Vol. 232, No. 707-720, pp. 463–535, http://dx.doi.org/10.1098/rsta.1934.0013

Rudloff-Grund J., Brenker F.E., Marquardt K., Howell D., Schreiber A., O'Reilly S.Y., Griffin W.L., Kaminsky F.V. (2016) Nitrogen nanoinclusions in milky diamonds from Juina area, Mato Grosso State, Brazil. Lithos, Vol. 265, pp. 57–67, http://dx.doi.org/10.1016/j.lithos.2016.09.022

Shirey S.B., Shigley J.E. (2013) Recent advances in understanding the geology of diamonds. G&G, Vol. 49, No. 4, pp. 188–222, http://dx.doi.org/10.5741/GEMS.49.4.188

Smit K.V., Shor R. (2017) Geology and development of the Lomonosov diamond deposit, northwestern Russia. G&G, Vol. 53, No. 2, pp. 144–167, http://dx.doi.org/10.5741/GEMS.53.2.144

Smit K.V., Myagkaya E., Persaud S., Wang W. (2018) Black diamonds from Marange (Zimbabwe): A result of natural irradiation and graphite inclusions. G&G, Vol. 54, No. 2, pp. 132–148, http://dx.doi.org/10.5741/GEMS.54.2.132

Smith E.M., Shirey S.B., Nestola F., Bullock E.S., Wang J., Richardson S.H., Wang W. (2016) Large gem diamonds from metallic liquid in Earth's deep mantle. Science, Vol. 354, No. 6318, pp. 1403–1405, http://dx.doi.org/10.1126/science.aal1303

Smith E.M., Shirey S.B., Wang W. (2017) The very deep origin of the world's biggest diamonds. G&G, Vol. 53, No. 4, pp. 388–403, http://dx.doi.org/10.5741/GEMS.53.4.388

Smith E.M., Shirey S.B., Richardson S.H., Nestola F., Bullock E.S., Wang J., Wang W. (2018) Blue boron-bearing diamonds from Earth's lower mantle. Nature, Vol. 560, No. 7716, pp. 84–87, http://dx.doi.org/10.1038/s41586-018-0334-5

Tang C.J., Neves A.J., Carmo M.C. (2005) On the two-phonon absorption of CVD diamond films. Diamond and Related Materials, Vol. 14, No. 11/12, pp. 1943–1949, http://dx.doi.org/10.1016/j.diamond.2005.08.060

Vasil'ev E.A., Ivanov-Omskii V.I., Pomazanskii B.S., Bogush I.N. (2004) The N3 center luminescence quenched by nitrogen impurity in natural diamond. Technical Physics Letters, Vol. 30, No. 10, pp. 802–803, http://dx.doi.org/10.1134/1.1813714

Wang W. (2010) Lab Notes: Lab sees increasing number of large HPHT-treated type IIa diamonds. G&G, Vol. 46, No. 4, p. 298.

Wang W., D'Haenens-Johansson U.F., Johnson P., Moe K.S., Emerson E., Newton M.E., Moses T.M. (2012) CVD synthetic diamonds from Gemesis Corp. G&G, Vol. 48, No. 2, pp. 80–97, http://dx.doi.org/10.5741/GEMS.48.2.80

Woods G.S. (1986) Platelets and the infrared absorption of type Ia diamonds. Proceedings of the Royal Society of London A, Vol. 407, No. 1832, pp. 219–238, http://dx.doi.org/10.1098/rspa.1986.0094

Zaitsev A.M. (2003) Optical Properties of Diamond: A Data Handbook. Springer, Berlin.

INCLUSION AND TRACE ELEMENT CHARACTERISTICS OF EMERALDS FROM SWAT VALLEY, PAKISTAN

Hongshu Guo, Xiaoyan Yu, Yuyu Zheng, Zhulin Sun, and Miro Fei-Yeung Ng

Swat Valley has become an important source of emeralds, including recently discovered trapiche-type crystals. In this study, emerald samples from Swat were examined by standard gemological testing, UV-Vis-NIR, FTIR, Raman analysis, EDXRF, and LA-ICP-MS. The study found three-phase hexagonal inclusions consisting of water, gaseous carbon dioxide and nitrogen, and a magnesite crystal. The gaseous mixture in two-phase inclusions is characteristic in both trapiche-type ($CO_2 + N_2$) and non-trapiche samples ($CO_2 + N_2 + CH_4$). Mineral inclusions of hematite, magnetite, rutile, graphite, and siderite are reported for the first time. Regular non-trapiche-type Swat emeralds contain high chromium (avg. 7471 ppmw), alkali metal (avg. 21040 ppmw), magnesium (avg. 34263 ppmw), and iron (avg. 9265 ppmw), as well as scandium (avg. 633 ppmw). Infrared spectra show that the absorption of type II H_2O is stronger than that of type I H_2O. Logarithm plots of trace elements appear to be diagnostic. Based on Raman spectroscopy, the trapiche-type emeralds' colorless core, light green hexagonal growth zone area, and green rim are emerald, while the six black arms are a mixture of hematite and graphite.

Pakistan's production of emeralds has been increasing in recent years, and reserves are estimated at almost 70 million carats (Jamal-ud-Din, 2014; Makki and Ali, 2019). Swat Valley is known for small stones with saturated color (figure 1). Mineralogical curiosities include three-phase fluid inclusions (Gübelin, 1982) and newly discovered trapiche-type emeralds (Khan, 2018). Photomicrographs of three-phase inclusions in Swat emeralds are provided for the first time in this study.

The history and geology of the Swat deposit were comprehensively reported by Arif et al. (2011) and Giuliani et al. (2019) and are summarized here. However, a detailed study of the inclusions and trace elements of Swat emeralds has not been published despite analytical and geological advances (Bowersox and Anwar, 1989; Gao et al., 2019).

Therefore, we present results from a detailed study of gemological properties, inclusions, spectroscopy, and chemical composition to characterize the emeralds from Swat Valley. Our findings provide insights that can be used for understanding the gen-

In Brief

- Emerald rough from Swat Valley in Pakistan shows a rather bright green color for melee. The rough is typically small and contains high Cr and Fe and low V contents. Relatively high-alkali metal (especially Li), Mg, Fe, and Sc contents separate them from other sources.

- Colorless solid minerals such as magnesite, quartz, talc, and dolomite, as well as black graphite, are common in regular non-trapiche-type Swat emeralds and surrounding rocks.

- Three-phase inclusions are rare and hexagonal. Trapiche-type emeralds from Swat Valley contain water, gaseous carbon dioxide and nitrogen, and a magnesite crystal.

- Trapiche-type emeralds from Swat Valley generally have four parts: one or two colorless cores, six arms or two sets of six arms (hematite + graphite), a light green area, and a green rim; these show a low-to-high content trend of Fe, Cr, Sc, and V.

esis of the emeralds in this deposit while shedding light on the geographic origin determination of emerald.

Figure 1. Swat emeralds are internationally renowned for their bright colors, even in small stones such as these, ranging from 0.3 to 0.8 ct. Photo by Hongshu Guo.

HISTORY AND GEOLOGY

Pakistan's emeralds have been found in four deposits, including Swat Valley in Swat District, Gandao in Mohmand Agency, Barang in Bajaur Agency, and Khaltaro in Gilgit-Baltistan (Khan, 2018). The Swat deposit is the largest of the four. The emerald mining area of Swat Valley is in northern Khyber Pakhtunkhwa and enclosed by the northwestern end of the Himalayan mountain range. To date, there are five mines in Swat Valley: Shamozai, Mingora, Gujar Killi, Charbagh, and Makhad (figure 2).

Mingora, Pakistan's earliest emerald mine, was discovered in 1958 (Khan, 2018). Initially, the Mingora, Gujar Killi, Charbagh, and Makhad mines in Swat Valley (figure 3) were explored, mined, and regulated by a state-owned company, Gemstone Corporation of Pakistan (GEMCP). From the early 1970s to the present, these four mines and the Shamozai mine have been taken over by different private companies. In 1981, Swat emeralds made their first appearance in the world market at the Tucson Gem and Mineral Show (Kazmi et al., 1986). Gübelin
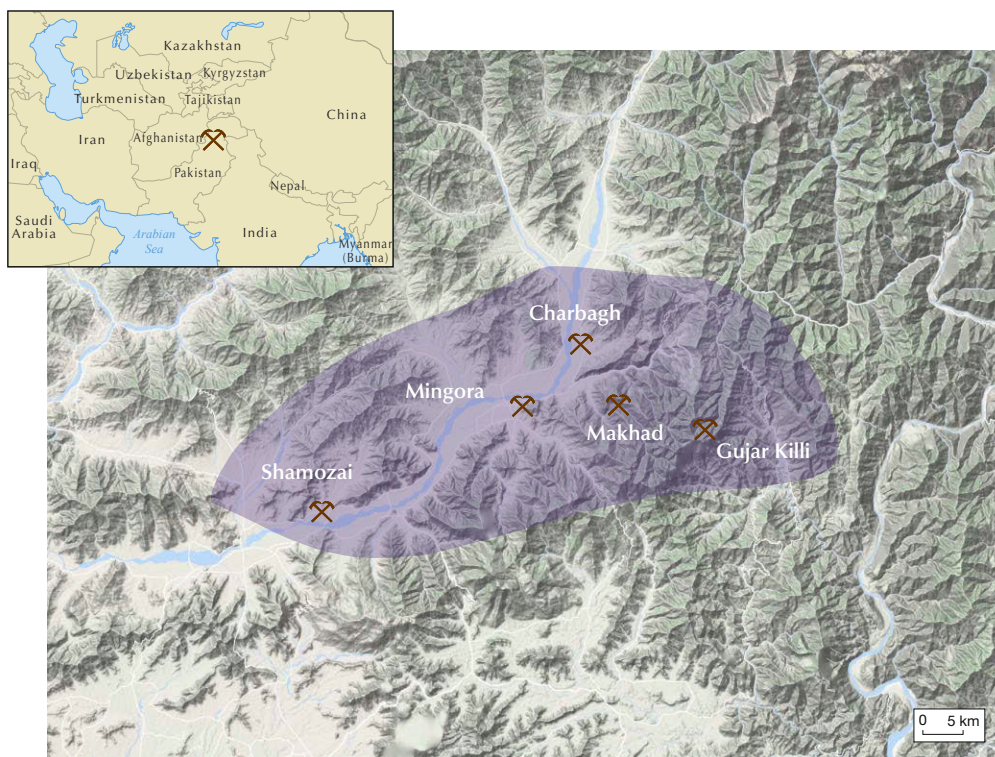
Figure 2. The Swat emerald deposit has five major mines. Gujar Killi is the most important source of high-quality emeralds, followed by Mingora.

Figure 3. En route to mining areas along the ridge of Shangla Peaks (top) and the Swat River (bottom) in the Swat Valley are beautiful villages and terrain. The miners are panning emeralds by the Swat River. Photos courtesy of Cloud Walker Jewel, Inc.

(1982) first described the gemology of the Swat emeralds and their commercial value. At present, the Barang deposit and the Gujar Killi and Mingora mines in the Swat Valley deposit are the main producers of Pakistani emeralds.

The Swat Valley deposit occurs in the Indus suture zone mélange (Arif et al., 2011; Rehman et al., 2011). The Indus suture zone, extending eastward to the Yarlung Zangbo suture zone in Tibet, represents fragments of the Neo-Tethyan upper mantle and the oceanic crust, which were emplaced on the continental margin and separate the Kohistan Arc sequence and the Eurasian plate to the north from the Indo-Pakistan plate to the south (Xu et al., 2015). In the Kohistan region, the Indus suture zone comprises Shangla blueschist mélange, the Charbagh greenschist
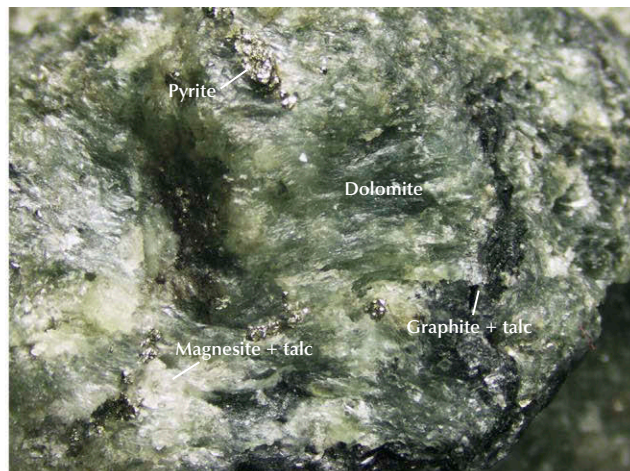
Figure 4. An emerald crystal specimen in matrix from the Mingora mine in Swat Valley. The emerald crystal measures about 7 × 7 × 8 mm (left). The matrix (right) mainly consists of dolomite (light green), magnesite + talc (white), graphite + talc (grayish black), and pyrite (pale brass-yellow), identified by Raman analysis. Photos by Hongshu Guo (left) and Xiaoyan Yu (right).

mélange, and the Mingora ophiolitic mélange (Arif et al., 2011). The ophiolitic rocks occur as lens-shaped bodies of various sizes distributed along the Main Mantle Thrust and are well exposed in the Barkotkai-Lilaunai area, the Gujar Killi village, the Spin Obo-Kuh area, and the town of Mingora.

Emerald deposits in Swat Valley are exposed in carbonate-magnesite-talc-altered ultramafic rocks, which also host high-Cr magnesian tourmaline (Giuliani et al., 2019). These emeralds formed during the Cenozoic era (23 Ma) (Dilles et al., 1994) and exist in magnesite-rich rocks (magnesite ± talc ± quartz ± dolomite), as part of the Indus suture zone mélange, distributed mostly along contacts of serpentinized ultramafic rocks with carbonate ± graphite-bearing metasedimentary rocks (Arif et al., 2011). Additionally, Groat et al. (2008) suggested that carbonate-altered ultramafic rocks hosting high-Cr magnesian tourmaline may be indicator minerals for emerald exploration.

Figure 4 shows an emerald crystal (about 7 × 7 × 8 mm) in matrix from the Mingora mine in the Swat deposit. The matrix is composed mainly of light green dolomite, white magnesite + talc, grayish black graphite + talc, and pale brass-yellow pyrite, suggesting that this Swat emerald occurs in contact with serpentinized ultramafic rocks.

Chromium originates from the dissolution of chromite crystals in the serpentinites, and beryllium and boron from a leucogranite that may be hidden at depth (Lawrence et al., 1989; Arif et al., 1996,

2011). However, the source of vanadium remains uncertain.

Trapiche-type emeralds, containing a green rim, light green areas, six magnetite arms extending perpendicular to the outer crystal faces, and a colorless core (Gao et al., 2019), were found in the Fizzaghat mine near Mingora (Khan, 2018). However, the chemical composition and spectroscopy were not studied further. For more on trapiche-type emeralds from Swat Valley, see Schmetzer (2020), p. 438 of this issue.

By interviewing mine owners, we gained mine-to-market information on Swat emerald. The emeralds are mined by traditional tunneling techniques. There are 30 active tunnels in the Mingora mine at about 1400 m elevation. Most have electricity but no ventilation. These tunnels were dug in a horizontal or slightly downward direction and were reported to be tens of meters to more than one kilometer long (figure 5, top and bottom left). The miners collect the emeralds using hydraulic jackhammers and handpicks along the white quartz vein (figure 5, bottom right). Mild winters, even in the snow, allow for continual mining though production may be reduced.

Emerald trading in Pakistan is traditional, without the use of the internet. Most transactions consist of local brokers buying rough stones from the mine owners, but there are also some foreign buyers. Some Swat emeralds are sold to the Indian and Bangkok markets, while other top-quality emeralds are sold to the Euro-
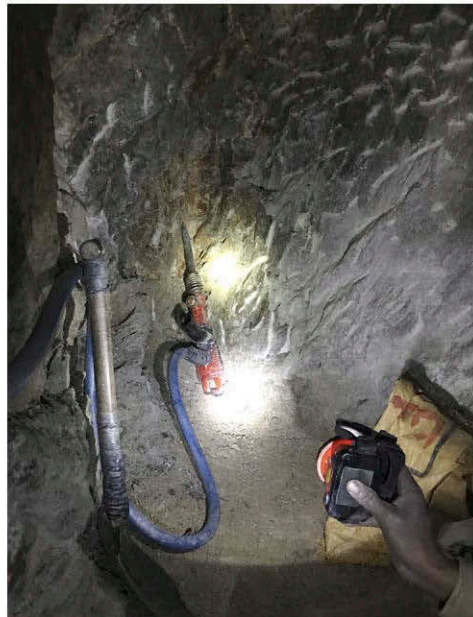
Figure 5. Top: The Mingora mine now has 30 active tunnels. Bottom left: The tunnels are dug in horizontal and slightly downward directions. Bottom right: The miners collect emeralds with hydraulic jackhammers and handpicks. Photos courtesy of Cloud Walker Jewel, Inc.

pean and Middle Eastern markets. Swat emerald rough can range in price from a few dollars to thousands of dollars per carat.

In the international market, Swat emeralds have been favored by many jewelry and luxury watch brands. However, Swat emeralds have only become
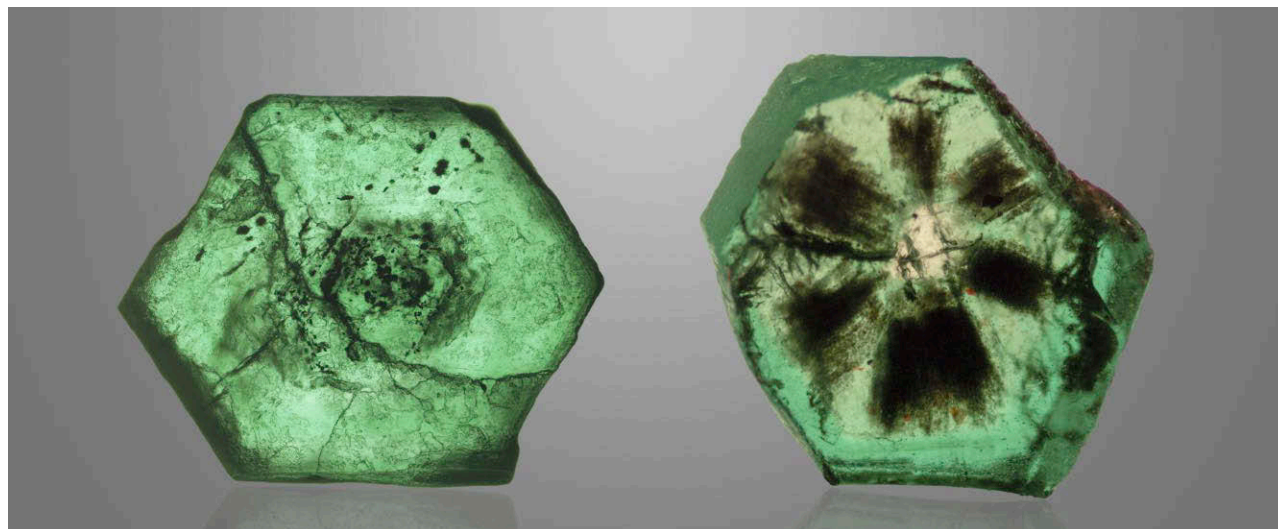
Figure 6. Double-sided emerald wafers from Swat Valley (about 5 mm in diameter) show the original hexagonal crystal habit and a trapiche-type pattern. Photo by Xiaoyan Yu.

widely known in the Chinese market in recent years and Swat is still considered a niche origin. More and more Chinese merchants go to Swat, Peshawar, and Islamabad in Pakistan to buy rough stones from local brokers for processing in China.

MATERIALS AND METHODS

A total of 37 regular emeralds and 16 trapiche-type emeralds from Swat Valley, ranging from 0.06 to 2.88 ct, were analyzed for the study: 26 were double-sided wafers or rough crystals with polished windows; 16 were hexagonal trapiche-type crystals fashioned as double-sided wafers (figure 6); and 11 were unfinished rough crystals. The "regular' or "non-trapiche-type"

samples were selected from more than 700 rough emeralds weighing more than 550 ct (figure 7), obtained from a gem merchant in Swat Valley. The trapiche-type samples, ranging from 0.25 to 0.85 ct with a size of 4 to 5 mm, were provided by Miro Fei-Yeung Ng. The analytical results of regular Swat emeralds and trapiche-type emeralds are presented separately.

Standard gemological properties of all the samples were determined with a refractometer, a Chelsea filter, long-wave (365 nm) and short-wave (254 nm) UV lamps, and an apparatus for hydrostatic specific gravity testing.

Internal features were observed with a binocular gemological microscope and an Olympus polarizing

Figure 7. The 37 Swat emerald specimens for this study were selected from 700 rough stones that ranged from 3 to 15 mm and 0.05 to 17.0 ct. Photos by Xiaoyan Yu.

TABLE 1. Gemological properties of regular emeralds from Swat Valley, Pakistan.[a]

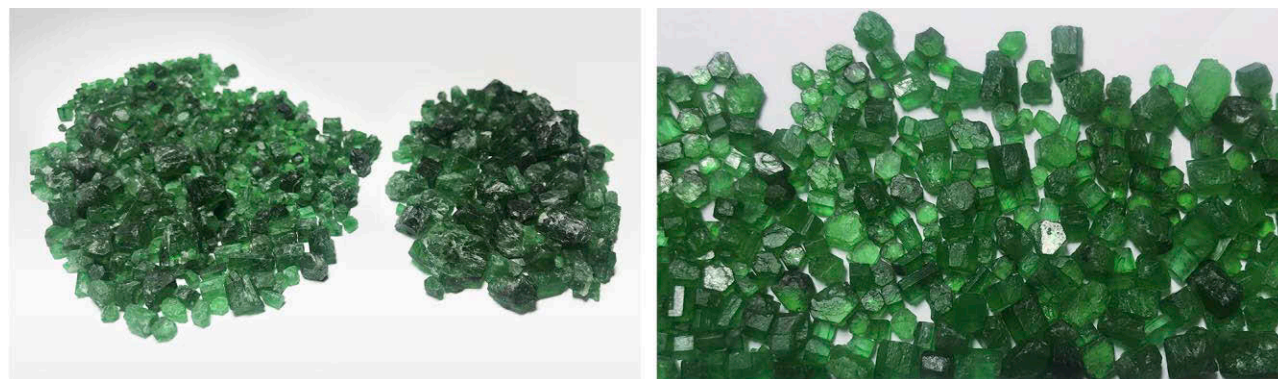|	
Color	Light to medium-dark slightly bluish green; typically a saturated green with a dark tone
Clarity	Very slightly to heavily included
Refractive indices	n_o = 1.587–1.600; n_e = 1.580–1.589 n_o = 1.596; n_e = 1.591[b] n_o = 1.599; n_e = 1.589[c]
Birefringence	0.006–0.011(0.007[b], 0.010[c])
Specific gravity	2.70–2.82 (2.78[b], 2.72[c])
Pleochroism	Strong to medium yellowish green or green (o-ray) and bluish green (e-ray)
Fluorescence	Typically inert to long- and short-wave UV radiation; sometimes faint yellowish green to long-wave UV
Chelsea filter	Pink to red (stones with saturated colors) or no reaction
Visible spectrum	Distinct lines at ~680 nm; partial absorption between 550 and 630 nm; and complete absorption <460 nm
Internal features	• Partially healed fissures with two-phase inclusions—typically elongated, necked-down, or irregular • Three-phase inclusions containing a gas bubble and a colorless crystal, usually with a hexagon outline, are uncommon • Hexagonal color zoning or core partially occurs on planar zones oriented perpendicular to the prism faces • Mineral inclusions: clusters of minute grains of magnesite and hematite; rounded crystals of dolomite, quartz, and fluorite; blocks of siderite and talc; platelets of muscovite and rutile

[a]All data are from the present study unless otherwise noted.
[b]Data from Gübelin (1982), given mean from 70 samples.
[c]Data from Bowersox and Anwar (1989), obtained from eight faceted samples.

microscope objective using darkfield, brightfield, and fiber-optic illumination. Photomicrographs were captured with an Olympus DP2-TWAIN system at 10× to 400× magnification.

UV-Vis-NIR spectra were recorded on a QSPEC GEM-3000 spectrophotometer in the range of 200–950 nm with a 0.5 nm spectral resolution and 180–200 ms integral time. When possible, polarized spectra of oriented samples were collected for obtaining ordinary ray (o-ray) and extraordinary ray (e-ray) absorption spectra.

Infrared spectroscopy was performed by a Bruker Tensor 27 Fourier-transform infrared spectrometer (FTIR) in transmission mode and resolution set at 4 cm^{-1}. The scanning ranges were 7200–2000 cm^{-1}.

Inclusions were identified using a Horiba LabRAM HR-Evolution Raman spectrometer with an Ar-ion laser operating at 532 nm excitation, between 4000 and 100 cm^{-1}, and accumulating up to two scans.

The elemental concentrations of trapiche-type emeralds were determined by the energy-dispersive X-ray fluorescence (EDXRF) technique using a Shimadzu EDX-7000 (15–50 kV, 1000 μA, 0–40 acquisitions, atmospheric conditions, and 1 mm scanning cores).

Trace element chemistry was performed using a Thermo X-Series ICP-MS fitted with a 343 nm femtosecond laser ablation system (Applied Spectra J100), at the National Research Center for Geoanalysis, Chinese Academy of Geological Sciences (CAGS), Beijing. We used a laser repetition rate of 8 Hz at 8 J/cm^2 and spot diameters of ~20 μm. A baffled smoothing device was used in front of the ICP-MS to reduce fluctuation effects induced by laser-ablation pulses and improve the quality of measurement data (Li et al., 2018). Each analysis consisted of ~10 seconds of background acquisition of gas blank measurement followed by 20 seconds of data acquisition from the sample. NIST SRM 610 and NIST SRM 612 were used as calibration reference materials for every 10 analyses to correct the time-dependent drift of sensitivity and mass discrimination. Data reduction was carried out with ICPMS Data Cal 10.8 software and specific analytical procedures and calibration methods (see Liu et al., 2008).

RESULTS

Gemological Properties. The gemological properties of regular emeralds from Swat Valley are summarized in table 1 and discussed in detail below.
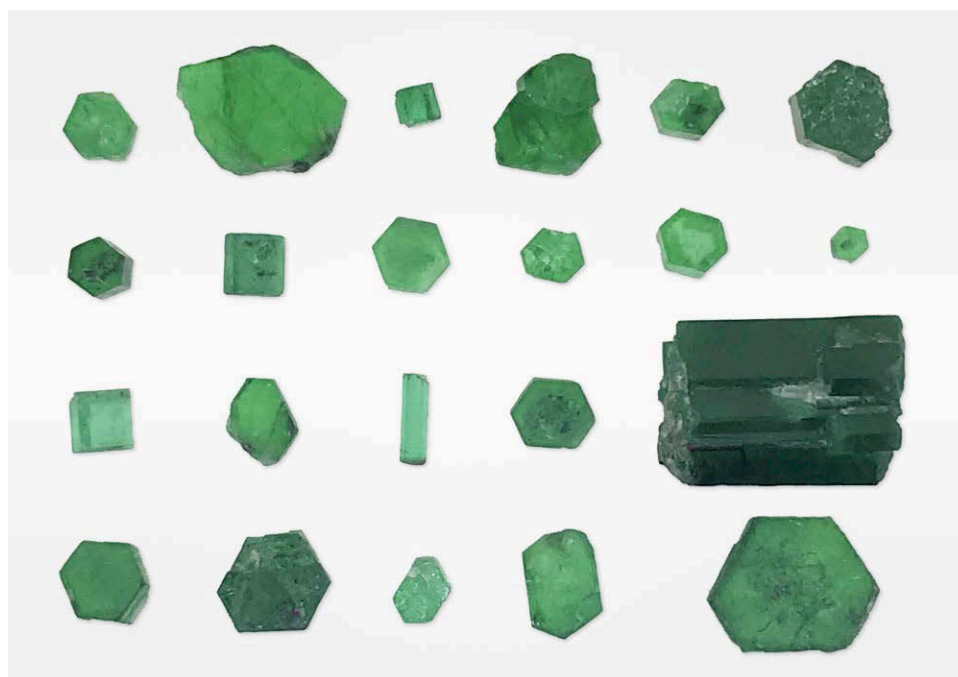
Figure 8. Swat emerald crystals (ranging from 0.05 to 7.60 ct in this photo) typically consist of hexagonal prisms or slabs. Photo by Xiaoyan Yu.

The rough emeralds from Swat Valley were typically small (<1.00 ct), but some weighed over 15 ct. The rough appeared as prisms, slabs, or fragments. Well-formed crystals typically showed short hexagonal prisms or slabs (figure 8). The majority ranged from 3 to 15 mm, but some were a few centimeters long. Larger crystals appeared to be translucent to opaque, whereas smaller crystals (< 4 mm) were transparent. Polished regular emeralds typically showed a dark slightly bluish green color, and others were medium to light green. The color was evenly distributed, while moderate hexagonal color zones or cores were observed in the flat terminations.

Similarly, trapiche-type emeralds ranging from 0.25 ct to 0.85 ct showed an intense to vivid green color in our study. There were four parts from the core to rim: a colorless core, six arms, a light green hexagonal growth zone area, and a green rim, while some had two colorless hexagonal cores (figure 9). In one sample, a colorless core was divided into two parts, indicating that this trapiche-type emerald went through different growth periods (figure 10). The colorless core formed as a completely hexagonal crystal before the green rims and black arms formed.

The regular emeralds from Swat Valley had a refractive index of 1.580–1.600, with birefringence be-

Figure 9. The structure of the trapiche-type emeralds was observed in visible light. They displayed black arms (left and center, transmitted light) with metallic luster (right, reflected light), and the emerald host showed hexagonal symmetrical patterns. The left and right samples have a hexagonal core, a hexagonal growth zone, and six arms, respectively. The middle emerald has two cores and two sets of six arms. Photos by Xiaoyan Yu; field of view 6.0 mm.
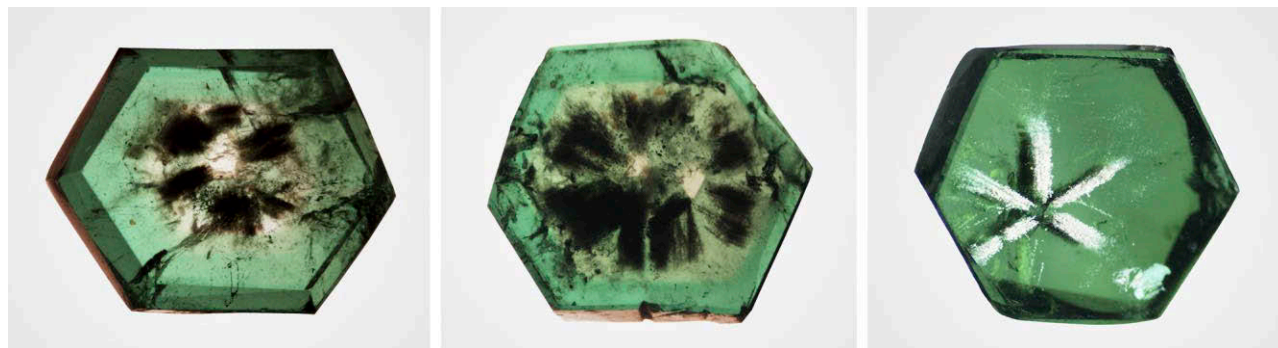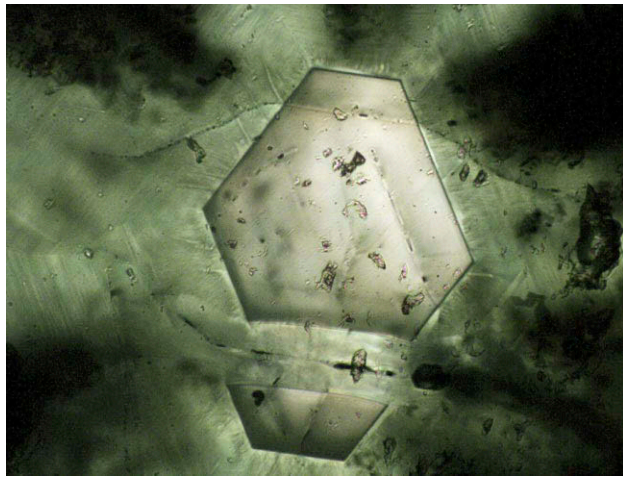
Figure 10. Separate parts in a hexagonal colorless core show multiple growth periods for a trapiche-type emerald. Photomicrograph by Hongshu Guo; field of view 0.6 mm.

birefringence between 0.009 and 0.011. Specific gravity varied from 2.70 to 2.82, including the trapiche-type emerald values of 2.74–2.77.

Pleochroism was strong to medium yellowish green or green (o-ray) and bluish green (e-ray). The regular emeralds were typically inert to long- and short-wave UV radiation, but some had faint yellowish green fluorescence under long-wave radiation. Through the Chelsea filter, the more saturated samples appeared pink to red, while the less saturated samples showed no response. The visible spectrum of most emeralds from the spectroscope had distinct lines at ~680 nm, partial absorption between 550 and 630 nm, and complete absorption in the violet range (<460 nm). Small or light green emeralds showed a weaker spectrum, with two clear lines at about 650 and 680 nm, and a weak band below 460 nm.

tween 0.006 and 0.011. Meanwhile, the trapiche-type emeralds had a refractive index of 1.589–1.601, with

Microscopic Characteristics. The most common inclusions in the regular Swat emeralds were partially
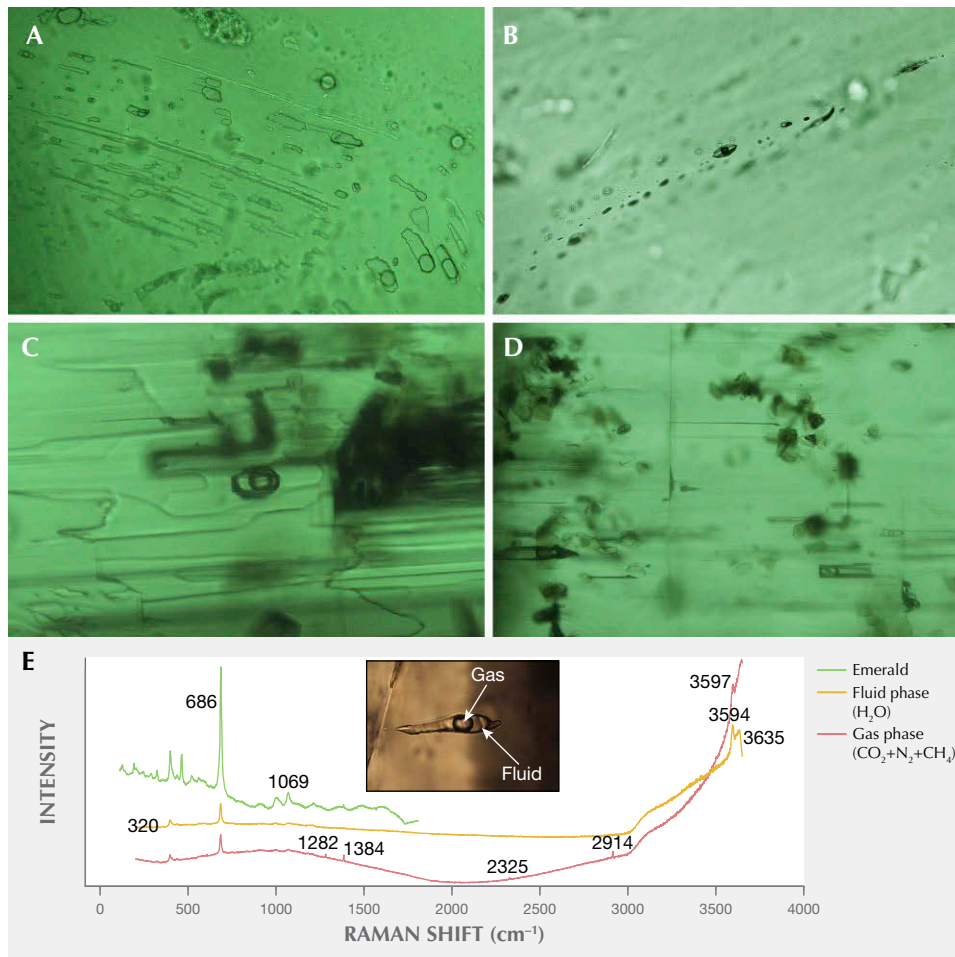
Figure 11. Multi-phase inclusions are commonly observed in regular Swat emeralds. They typically show necked-down, irregular, and elongated shapes (A and B). Two-phase inclusions with a negative crystal shape are rare in the regular emeralds (C). Two-phase primary inclusions oriented parallel to the c-axis and platelets of muscovite were commonly seen in thin and moderately green emeralds (D). Raman spectroscopy (E) was used to identify the host emerald (green), the aqueous fluid phase (orange), and the CO_2 + N_2 + CH_4 gas bubble (red). Photomicrographs by Hongshu Guo; fields of view 0.30, 0.40, 0.48, 0.40, and 0.12 mm, respectively.
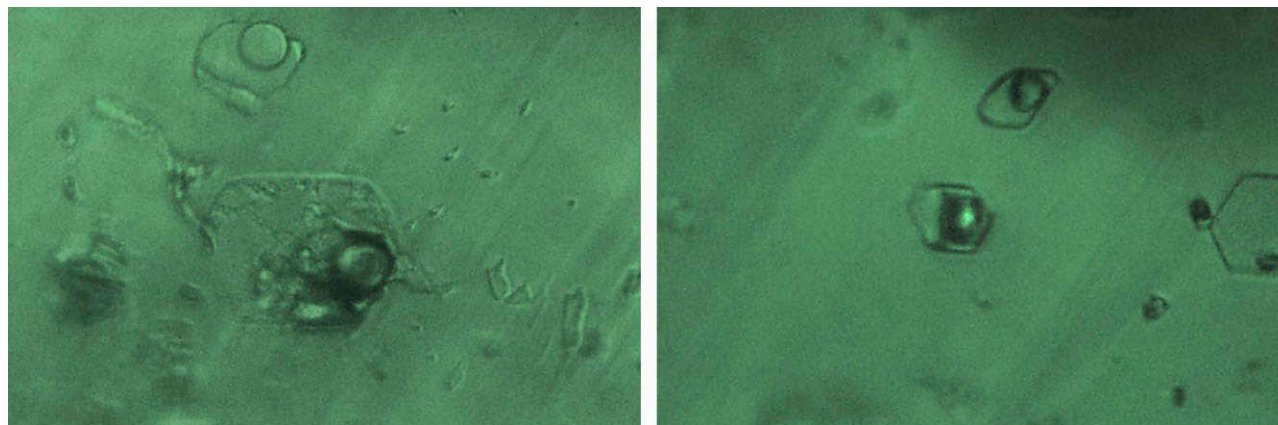
Figure 12. Three-phase inclusions showed a hexagonal outline in the regular Swat emeralds. Photomicrographs by Hongshu Guo; field of view 0.4 mm.

healed fissures with two-phase inclusions. Two-phase inclusions were typically elongated, necked-down, or of irregular shape (figure 11, A and B) and contained a gas bubble ($CO_2 + N_2 + CH_4$, identified by Raman). At room temperature, the gaseous bubbles in the multi-phase fluid inclusions appeared to account for one-third to one-half of the volume of the multi-phase inclusion; sometimes they were even larger than the present irregular mineral inclusions. Unlike pseudo-secondary fluid inclusions commonly found in healed fissures, two-phase primary inclusions were rarely observed. The primary two-phase inclusions occurred as isolated negative crystals with an approximate hexagonal profile and high relief (figure 11C). Two-phase primary inclusions oriented parallel to the c-axis were commonly seen in thin emeralds with medium green color (figure 11D). Hexagonal three-phase inclusions were rare in the regular emeralds (figure 12). They contained a gas bubble and a crystal in an aqueous solu-

tion, but the composition could not be identified by Raman analysis.

Solid inclusions were common in the regular Swat emeralds. Clusters of magnesite grains occurred in most of the emeralds. Rounded crystals of dolomite, quartz, and fluorite (figure 13, left) were found in some samples. Crystals of siderite and talc were generally found to be slightly rounded. Dark minerals included platelets of muscovite (figure 11D) and light to deep brown rutile (figure 13, center). Black magnetite and carbon inclusions were also visible on emerald surfaces and ridgelines (figure 13, right).

Trapiche-type emeralds from Swat Valley contained abundant two- and three-phase inclusions and solid inclusions. Three-phase inclusions were more common in the trapiche-type emeralds than in the regular Swat emeralds. In one sample, the solid was identified by Raman analysis as magnesite, indicating that multi-phase inclusions had captured sur-

Figure 13. Rounded colorless fluorite (left), brown rutile (center), and a mixture of black magnetite + graphite (right) were identified by Raman analysis in the regular Swat emeralds. Photomicrographs by Hongshu Guo; field of view 0.48, 0.48, and 2 mm, respectively.
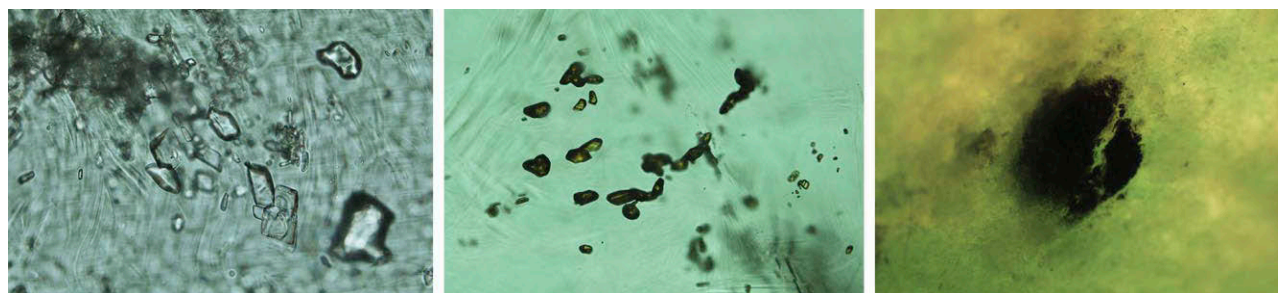
rounding minerals (figure 14). Gas mixtures of CO_2 + N_2 in two- and three-phase inclusions in trapiche-type emeralds (identified by Raman analysis) were different from those in regular Swat emeralds.

The structural components and solid inclusions of the trapiche-type emeralds were identified by Raman analysis. The colorless core, light green area, and green rim were emerald. Meanwhile, the six black arms were a mixture of hematite and graphite. Hematite showed a skeleton-like pattern, with metallic luster and was opaque under reflected light (figure 15A). Trapiche-type emeralds containing only a colorless core and a green rim and no light green areas were observed (figure 15B). A series of black graphite needles were along the fracture direction (figure 15C), and colorless needles intersected vertically with short tubular multi-phase fluid inclusions in the colorless core (figure 15D). Brown minerals of hexagonal and triangular shape were identified as hematite (figure 15E). Irregular or triangular plates of brown rutile and colorless crystal inclusions (figure 15F) were observed in the trapiche-type emeralds.

Spectroscopy. *UV-Vis-NIR.* A representative UV-Vis-NIR e-ray spectrum of the regular Swat emeralds is shown in figure 16 (blue line). There are four characteristic absorption bands: wide bands at 425 and 600–680 nm, a strong band at 850 nm, and a narrow band at 370 nm. Compared to Wood and Nassau (1968) and Schmetzer et al. (1974), the most prominent features in this group were the Cr^{3+} bands at 425, 610, 637, 660, and 681 nm. In addition, the narrow band at around 370 nm indicated the presence of Fe^{3+}, and a strong Fe^{2+} band at 850 nm was recorded. But in some samples, a weak Fe^{2+} band was present at 830 nm.

As figure 16 (red line) shows, the e-ray spectrum of Swat trapiche-type emerald is different from that of regular emeralds. A significant Fe^{3+} absorption band was observed at 370 nm. The difference in Fe peaks may be attributed to the Fe-rich metallogenic fluid of trapiche-type emeralds. Moreover, significant Cr^{3+} bands at about 430, 610, 635, and 681 nm and the Fe^{2+} band at 850 nm were similar to those in regular emeralds.

UV-Vis-NIR spectroscopy shows differences between trapiche-type and regular emeralds. The chemistry in figure 18 agrees well with UV-Vis-NIR spectra. The concentrations of Fe in trapiche-type emeralds (17801 ppmw) are over four times as much as those in regular Swat emeralds (3825 ppmw).
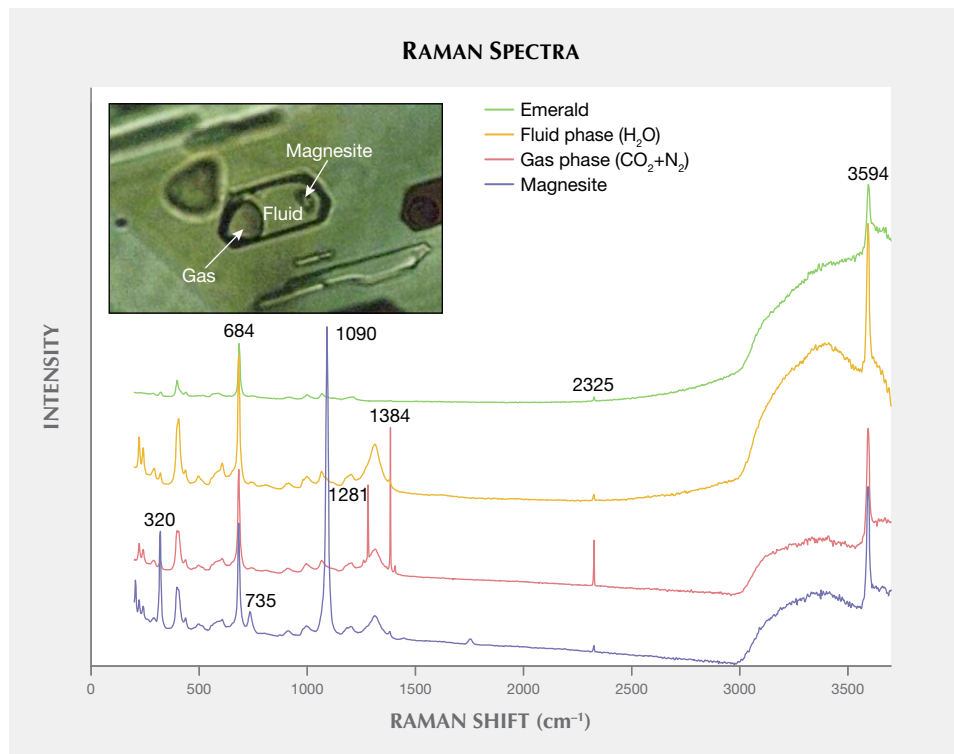
RAMAN SPECTRA

Figure 14. This hexagonal inclusion in Swat trapiche-type emerald clearly displays a gas bubble and a colorless crystal. Raman spectroscopy was used to identify the host emerald (green), the CO_2 + N_2 gas bubble (pink), the aqueous fluid phase (orange), and the magnesite crystal (blue). Photomicrograph by Hongshu Guo; field of view 0.08 mm. The spectra are stacked for clarity.
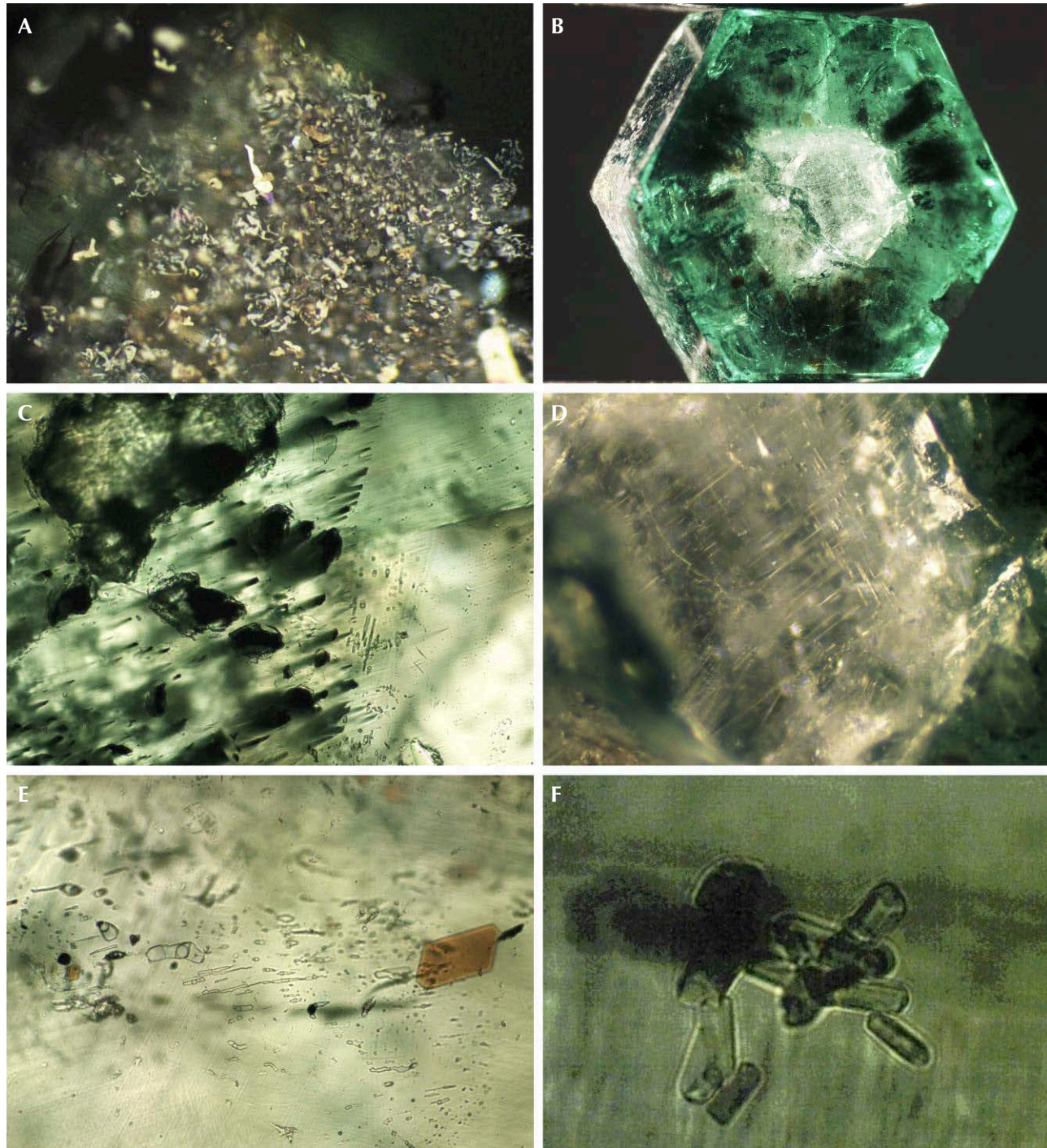
Figure 15. The six black arms in the trapiche-type emeralds were a mixture of hematite and graphite. Skeleton-like hematite arms showed bright metallic luster and were opaque under reflected light (A). A few trapiche-type emeralds had no light green area, only colorless and green parts (B). A cluster of black graphite needles along the fracture (C). Colorless needle-shaped inclusions and short tubular multi-phase fluid inclusions were vertically crossed in the colorless core (D). The two-phase inclusion was composed of a mixture of $CO_2 + N_2$ gas and liquid water. The brown hexagonal mineral was identified as hematite (E). A cluster of colorless crystal inclusions (F). Photomicrographs by Xiaoyan Yu (B, C, and D) and Hongshu Guo (A, E, and F); fields of view 0.7, 5.0, 0.6, 2.2, 0.7, and 0.08 mm, respectively.

UV-VIS-NIR SPECTRA

E || c
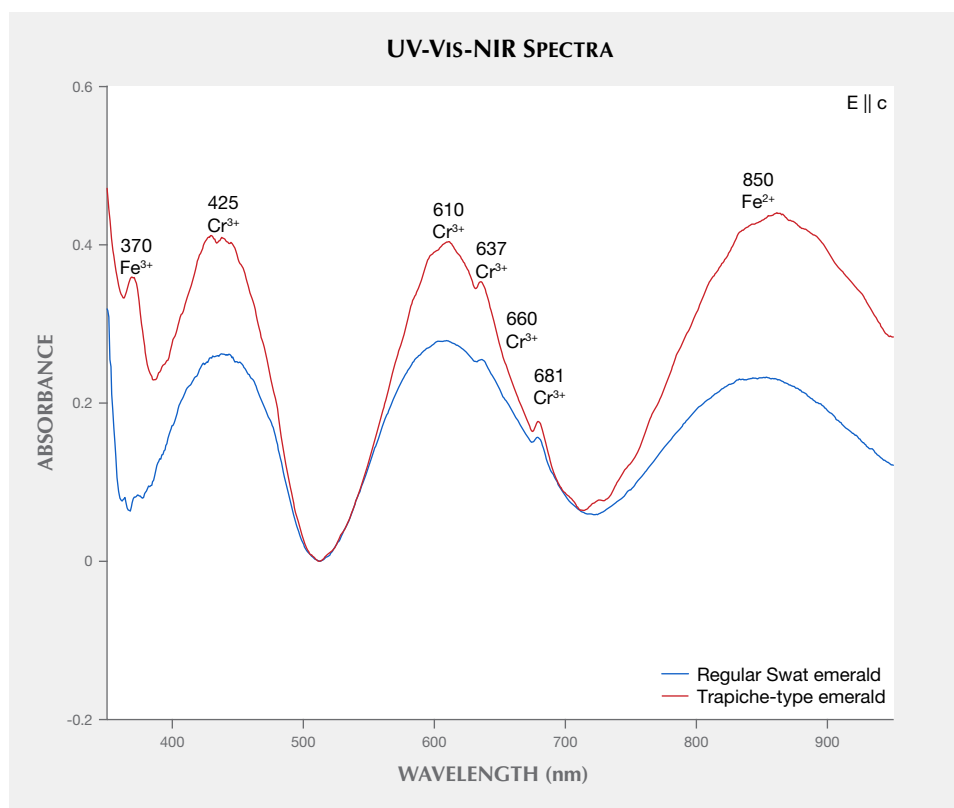
Figure 16. These UV-Vis-NIR absorption spectra are representative of regular Swat emeralds (blue line) and trapiche-type Swat emeralds (red line) in this study. Note: LA-ICP-MS and EDXRF analysis gave values corresponding to the different emeralds. Regular: 4618 ppmw Cr, 764 ppmw V, and 3825 ppmw Fe. Trapiche-type: 4789 ppmw Cr, 272 ppmw V, and 18045 ppmw Fe.

Infrared. Figure 17 (left) shows typical FTIR spectra (e-ray) in the range of 7200–2000 cm^{-1}. There is absorption of H_2O in the channels of the emerald structure. The peaks at 7095 and 5267 cm^{-1} of type II H_2O are sharp and strong, while the peak at 6843 cm^{-1} of type I is sharp but weak. According to Saeseaw et al. (2014), these three characteristic peaks of the Swat emeralds correspond to the vibration of type I and type II H_2O molecules. The significant peak at 2356 cm^{-1} corresponds to CO_2, which was present in all the samples.

Figure 17. The representative FTIR spectrum (E || c) illustrating type I and type II H_2O was observed in Swat emeralds (left). Peaks in the 3200–2500 cm^{-1} range were seen in some of the stones (right), suggesting a mixture of cedarwood oil and Araldite 6010.

FTIR SPECTRUM

E || c

FTIR SPECTRUM

E || c
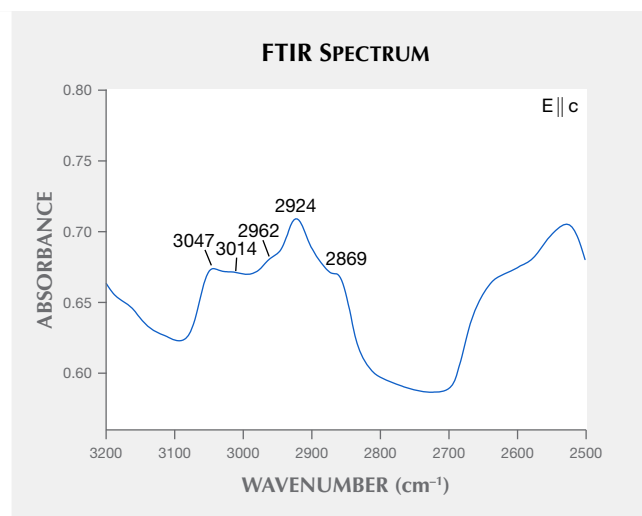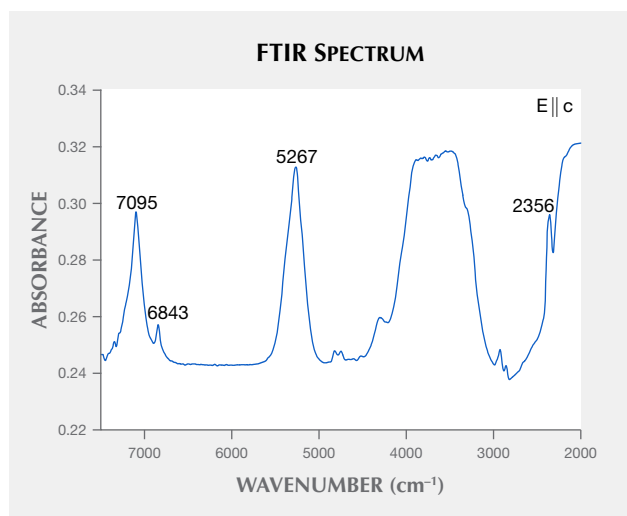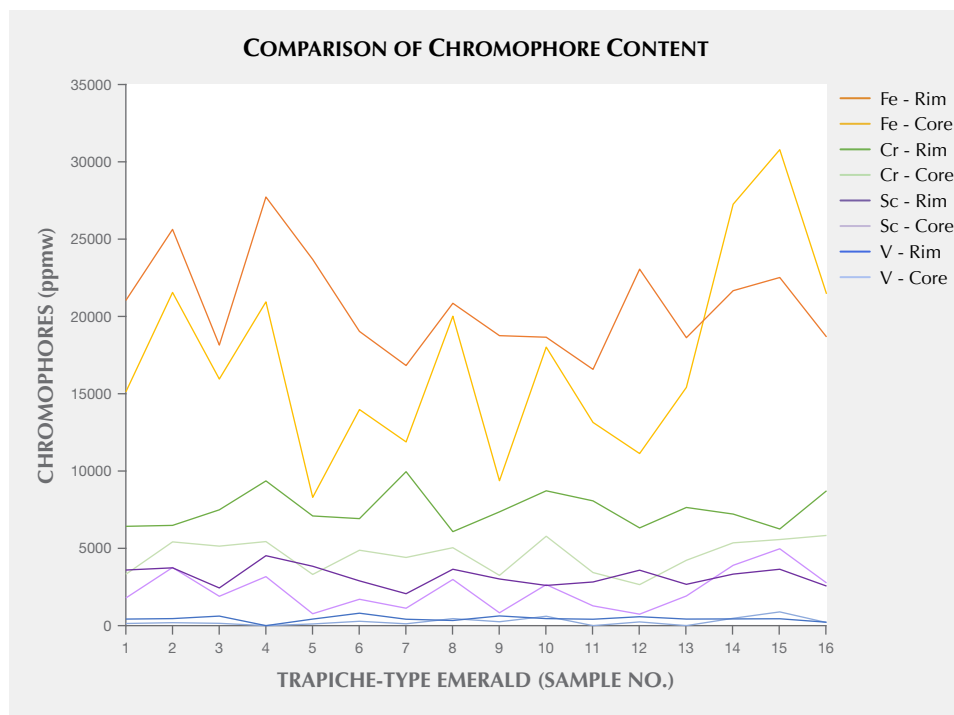
Figure 18. Trapiche-type emeralds from Swat Valley showed the low to high content of Fe, Cr, Sc, and V from the core (colorless) to rim (green), except samples 14–16, whose cores were too small.

The infrared spectroscopy in the 3200–2500 cm⁻¹ range is helpful to identify possible fillers used for clarity enhancement. None of the green fillers were seen in any samples, but some of the stones containing a near-colorless filler showed infrared spectra (figure 17, right) typical of cedarwood oil and Araldite 6010, as indicated by absorptions at 3047, 3014, 2962, 2924, and 2869 cm⁻¹ (Johnson et al., 1999).

Main and Trace Element Analysis. Eleven fabricated regular emerald samples were analyzed using LA-ICP-MS (table 2) and sixteen trapiche-type samples were measured by EDXRF (table 3).

Regular Swat emeralds tended to have high concentrations of Li, Na, Rb, Cs, Mg, and Fe, as well as Sc. Total alkali ion concentrations ranged from 16850 to 24475 ppmw (avg. 21040 ppmw); Mg contents ranged from 15149 to 226396 ppmw (avg. 34263 ppmw), while Fe ranged from 2533 to 59538 ppmw (avg. 9265 ppmw). Sc ranged from 254 to 1408 ppmw (avg. 633 ppmw). The concentrations of Cr (459–23041 ppmw, avg. 7471 ppmw) were greater than V (297–802 ppmw, avg. 565 ppmw), and the Cr/V ratio ranged from 0.8 to 42.

The results of EDXRF from the trapiche-type emeralds showed high contents of Fe (avg. 17801 ppmw), Cr (avg. 5795 ppmw), and Sc (avg. 2367 ppmw). Figure 18 indicated the low-to-high content trend of Fe (14968–20633 ppmw), Cr (4235–7362

ppmw), Sc (1767–2966 ppmw), and V (190–442 ppmw). From the green rim to colorless core, the charts showed a positive correlation between these elements and the green color. However, three samples (14–16) showed an opposite trend of Fe, Sc, and V, because the colorless core was too small.

DISCUSSION

Variations in Properties. The RI, SG, pleochroism, and fluorescence of the samples were consistent with the properties of the Swat emeralds studied by Gübelin (1982) and Bowersox and Anwar (1989). Compared with Afghan emeralds (n_o =1.572–1.580, n_e=1.580–1.590, and SG=2.68–2.74; Bowersox et al., 1991; Saeseaw et al., 2014), Swat emeralds have higher values of RI and SG, which may be explained by the fact that Swat emeralds have higher alkali metal content (avg. 21040 ppmw) than Afghan emeralds (avg.10780 ppmw; Saeseaw et al., 2014). Meanwhile, trapiche-type emeralds from Swat Valley showed higher RI than regular Swat emeralds, possibly because their Fe content was higher (avg. 17801 ppmw) than that in other Swat emeralds (avg. 9265 ppmw).

Microscopic Inclusions. Swat trapiche-type emeralds are different from Colombian trapiche emeralds in their structural characteristics and chemical composition. The black arms of Colombian trapiche

TABLE 2. Chemical composition of 11 regular Swat emeralds, obtained by LA-ICP-MS.[a]

Element (ppmw)	YE-1 Range	Average	YE-2 Range	Average	YE-3 Range	Average	YE-5 Range	Average	YE-8 Range	Average	YE-9 Range
Li	465–495	480	453–472	462	363–401	382	426–677	559	279–416	319	261–342
Be	144484–154269	149376	143110–144562	143836	143128–153712	148420	126409–148358	136710	137721–156481	148007	134890–140497
B	10–16	13	8–10	9	5–7	6	0–7	4	5–7	6	8–9
Na	19924–22394	21159	19142–19445	19294	20853–21369	21111	19752–22291	21076	19267–20316	19909	19582–20080
Mg	23784–27404	25594	22683–23644	23164	26187–27782	26985	21022–26056	23882	21362–25091	23486	25327–75919
Al	186416–208015	197216	63644–190831	127237	196367–221695	209031	26056–193631	112319	174942–200915	189729	183375–184196
Si	581535–588087	584811	600199–606942	603571	564235–596050	580143	605682–622151	616073	580772–607906	593350	559408–614869
P	147–187	167	204–223	214	347–480	414	145–186	173	171–225	204	185–210
Sc	1092–1282	1187	503–508	506	548–639	594	254–377	309	590–1169	851	390–523
Ti	93–106	99	139–141	140	231–300	265	94–116	104	99–505	295	203–280
V	564–576	570	480–520	500	698–703	700	297–608	448	641–796	716	576–802
Cr	580–8831	4706	3454–6655	5054	1257–3537	2397	459–23041	8646	3248–20353	10251	2554–2813
Mn	7–9	8	1	1	3	3	0–11	5	1–3	2	1–306
Fe	9809–10190	9999	4185–4241	4213	5559–6891	6225	3847–5568	4873	4385–7787	6204	7871–18432
Co	1	1	1	1	1–2	1	1	1	1	1	1–10
Zn	3–5	4	4	4	7–8	8	3–6	5	2–4	3	2–9
Ga	6	6	3–4	4	5–6	6	5–6	6	4–6	5	4–5
Rb	10–12	11	12	12	11–18	14	9–11	10	9–13	11	10–11
Cs	157–161	159	120–131	125	418–793	605	98–138	114	128–219	182	110–196
Th	0–0.01	0.005	nd	nd	nd	nd	0–0.028	0.013	0–0.011	0.006	nd
U	nd	nd	nd	nd	0–0.027	0.014	0–0.011	0.003	nd	nd	0–0.014

[a]Ca, Ni, Cu, Ge, As, Sr, Y, Zr, Nb, Mo, Cd, In, Sn, Sb, Ba, La, Ce, Pr, Nd, Sm, Eu, Gd, Tb, Dy, Ho, Er, Tm, Yb, Lu, Hf, Ta, W, Bi, and Pb could not be analyzed correctly by this technique. Abbreviations: nd = not detected.

emeralds are composed mainly of carbonaceous material and albite (Ohnenstetter et al., 1998), while the arms of Swat trapiche-type emeralds are a mixture of hematite and graphite. Gao et al. (2019) identified the black arms as magnetite, while the mixture of hematite and graphite was identified in this study. Hematite (Fe_2O_3) indicates oxidation conditions, while the magnetite (Fe_3O_4) is formed under reducing conditions. Thus, there is a transformation between magnetite and hematite under different redox conditions.

Swat emeralds appear to have characteristic multiphase inclusions. Descriptions of multi-phase inclusions in Swat emeralds are available in the gemological literature (Gübelin, 1982; Bowersox and Anwar, 1989), but with few details. Three-phase inclusions in Swat emeralds were rather rare. Three-phase inclusions occur in emeralds from Colombia, Panjshir (Afghanistan), Davdar (China), and Kafubu and Musakashi (Zambia). But this is the first time that specific components of three-phase inclusions have been reported in Swat Valley emeralds from Pakistan, which are different from the jagged three-phase inclusions in

TABLE 3. Chemical composition (average) of trapiche-type emeralds from Swat Valley, analyzed by EDXRF.

Element (ppmw)	Fe	Cr	Sc	V
Core (colorless)	8288–21529 (14968)	2593–5652 (4235)	691–3501 (1767)	bdl–591 (190)
Rim (green)	16556–27691 (20633)	5939–9729 (7362)	1923–4212 (2966)	bdl–782 (442)
Average	17801	5795	2367	319
Det. limit	21	4.8	20	2.1

YE-9	YE-11		YE-12		YE-13	YE-14		YE-16		Detection limit (ppmw)
Average	Range	Average	Range	Average	Value	Range	Average	Range	Average	
301	309–581	445	83–95	89	478	247–614	425	315–343	329	2.3
137694	111068–121629	116349	126819–134255	130537	159847	155724–165842	160826	152503–154254	153378	9.8
8	1–6	4	10–14	12	10	8–16	12	10–11	11	2.9
19831	16370–21636	19003	23213–23269	23241	17695	19597–21452	20338	20041–20461	20251	128
50623	26502–226396	126449	27908–28974	28441	15149	15786–28550	20136	26572–35393	30982	24
183786	122485–211335	166910	63644–67908	65776	160092	149723–162515	156364	192267–193961	193114	18
587139	444875–594926	519901	603075–603763	603419	636495	608483–624603	616343	580977–582667	581822	1150
198	307–485	396	196–197	197	143	72–171	145	191–193	192	60
456	556–583	570	1325–1408	1366	340	327–464	381	553–576	564	1.7
242	123–150	137	107–149	128	93	86–124	102	148–174	161	24
689	331–342	337	324–378	351	509	549–604	576	649–700	675	0.9
2683	8667–9029	8848	5029–9212	7121	3415	8329–18982	13243	1862–8633	5247	2.3
153	4–1187	595	23–34	29	2	3–10	5	5–67	36	1.8
13151	7623–59538	33580	14491–19188	16840	2757	2533–5717	3429	7672–10444	9058	230
5	1–29	15	1–3	2	1	1–6	2	1–2	2	1.0
5	5–27	16	14	14	3	4–10	7	5–14	10	1.9
4	5–6	5	13	13	3	3–8	5	3–4	4	0.4
11	12	12	40–71	55	6	9–12	11	12	12	1.1
153	144–159	151	868–1096	982	94	67–103	85	138–141	139	0.5
nd	0–0.029	0.014	nd	nd	nd	nd	nd	0–0.003	0.001	0.01
0.007	nd	nd	nd	nd	nd	nd	nd	nd	nd	0.001

Colombian emeralds. The outlines of the cavities of the three-phase inclusions are typically hexagonal and regular, suggesting that they were formed at the same time as the emerald host. The solid phase is magnesite, unlike three-phase inclusions from any other source (Saeseaw et al., 2014). Furthermore, the mixed gas of three-phase inclusions ($CO_2 + N_2$) in trapiche-type emeralds is different from that in regular Swat emeralds ($CO_2 + N_2 + CH_4$), which shows some different conditions of formation in trapiche-type emeralds. The solid inclusions hematite, magnetite, rutile, graphite, and siderite identified in this study are new for emeralds from Swat Valley.

Trace-Element Variations. Several published studies represent an early attempt to use trace elements for provenance purposes (Saeseaw et al., 2014, 2019; Carlo et al., 2018), but the data for Swat emeralds is scarce. In this study, 27 spots on 11 regular Swat emeralds were analyzed via LA-ICP-MS. Logarithm plots of trace elements were applied to detect possible correlations when distinguishing geographic origin, so adding LA-ICP-MS data from other main emerald deposits in the world is necessary, such as Colombia, Kafubu from Zambia, Brazil (Zwaan et al., 2012), Panjshir from Afghanistan, Swat from Pakistan (Carlo et al., 2018), Khaltaro from Pakistan (Laurs et al., 1996), Russia (Saeseaw et al., 2019; Carlo et al., 2018; Karampelas et al., 2019; all averages), Ethiopia (Saeseaw et al., 2019; Carlo et al., 2018; Karampelas et al., 2019; all averages), Egypt (Carlo et al., 2018), India (Carlo et al., 2018), and Malipo from China (Zheng et al., 2019). The inclusions of Ethiopian and Russian emeralds (Saeseaw et al., 2019) are very similar to those in Swat emeralds. But the high Cr (avg. 7471 ppmw), high V (avg. 565 ppmw), and high Fe (avg.

Figure 19. A log-log plot of Cs versus Rb concentrations from LA-ICP-MS analyses clearly shows a positive correlation in emeralds from Swat and other localities. Other sources are from Saeseaw et al. (2019) (average), Carlo et al. (2018), Karampelas et al. (2019) (average), Laurs et al. (1996), Zwaan et al. (2012), and Zheng et al. (2019).

9265 ppmw) content can clearly separate the Swat emeralds from Ethiopian (avg. 3655 ppmw Cr; avg. 112.70 ppmw V; avg. 4867 ppmw Fe) and Russian (avg. 905.27 ppmw Cr; avg. 80.64 ppmw V; avg. 1600.67 ppmw Fe) emeralds (Karampelas et al., 2019).

The plots of Cs versus Rb and Li versus Cs showed a positive correlation (figure 19 and 20), but there is some overlap for emeralds from Swat Valley, Russia, Ethiopia, India, Egypt, and Zambia. The plot of Li versus Sc proved useful in separating Swat Valley from
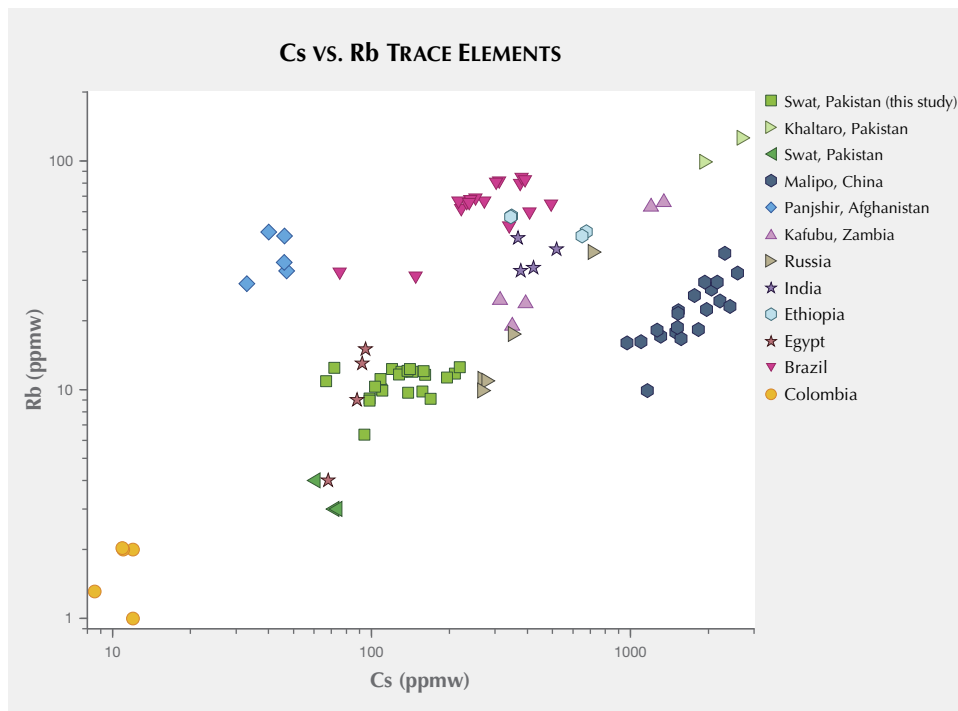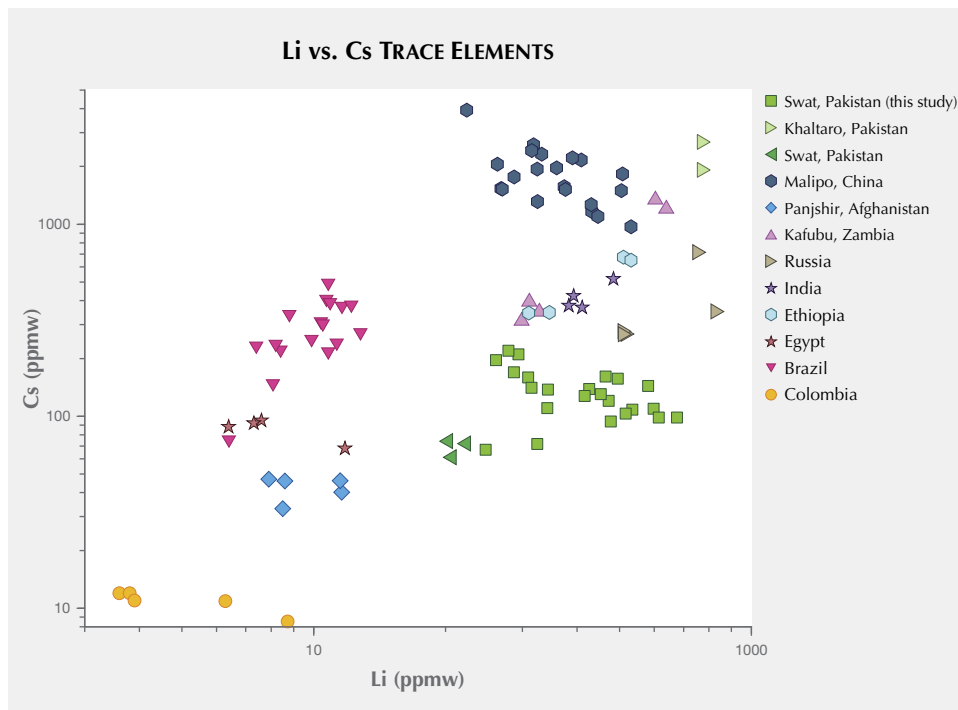

Figure 20. A log-log plot of Li versus Cs concentrations from LA-ICP-MS analyses clearly shows a positive correlation in Swat and other localities emeralds. Sources of data are the same as in figure 19.

most occurrences (figure 21), but there is a small overlap for emeralds from Pakistan, Egypt, and Afghanistan. It also showed Swat emeralds contained high Cs and Li, which can be used to distinguish among Swat, Egyptian, and Afghani emeralds. Particularly, the average of Mg concentrations (34263 ppmw) in Swat emeralds is the highest among worldwide sources.

CONCLUSIONS

Overall, the gemological properties of Swat samples are distinct and can be used in origin determination. Relatively higher values of RI and SG are related to rich alkali metal contents in Swat emeralds. The main chromophores in Swat emeralds are Cr^{3+}, V^{3+}, Fe^{3+}, and Fe^{2+}, of which Cr^{3+} is the most important cause for green color (figure 22). But the spectrum of the trapiche-type emerald illustrates the strong Fe^{3+} band at 370 nm, different from regular Swat emeralds.

This is the first time that the gemological and geochemical details of trapiche-type emeralds from Swat Valley have been published. Compared with regular Swat emeralds, trapiche-type emeralds show higher RI because of higher Fe content. There are four parts: one or two colorless beryl cores, a light green hexagonal growth zone area, a green rim, and six (or two sets of six) black hematite and graphite arms. The

Figure 22. Emerald crystals from the Mingora mine in Swat Valley typically show good color saturation. Photo by Andrew Lucas/GIA.

chemical contents of Fe, Cr, Sc, and V in trapiche-type emeralds have a trend from low to high going from the colorless core to the green rim.

Some typical inclusions are present in Swat emeralds. First, one solid magnesite, one $CO_2 + N_2$ bubble and liquid phase were identified in three-phase inclu-
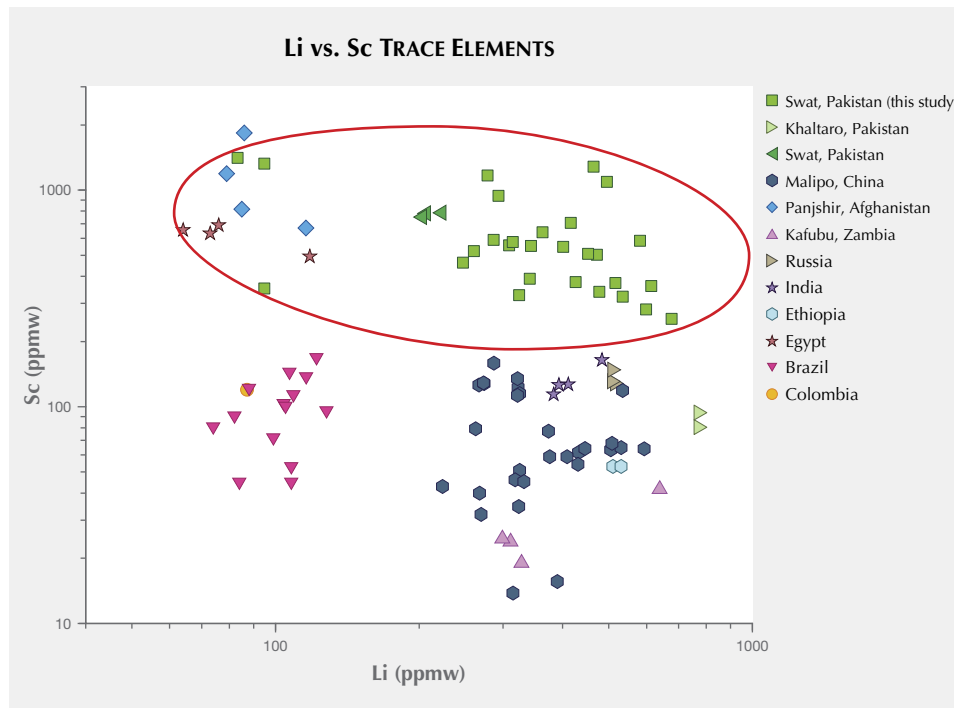

Figure 21. A log-log plot of Li versus Sc concentrations from LA-ICP-MS analyses is useful in separating between Swat emeralds and those from other occurrences. Sources of data are the same as in figure 19.

sions. Second, the gaseous mixture ($CO_2 + N_2 + CH_4$ or $CO_2 + N_2$) in necked-down, elongated, or irregular two-phase inclusions is not identical to other origins. Third, the solid mineral inclusions in regular Swat emeralds typically included magnesite, dolomite, quartz, fluorite, siderite, talc, muscovite, rutile, hematite, magnetite, and graphite. In the trapiche-type emeralds, hematite, graphite, and two-phase inclusions were commonly observed.

The infrared spectrum illustrates the typical features that the absorption of the type II H_2O (7095 and 5267 cm^{-1}) is stronger than that of the peak of type I H_2O (6843 cm^{-1}). The significant peak at 2356 cm^{-1} corresponds to CO_2. Some of the samples are filled with mixtures of cedarwood oil and Araldite 6010.

Trace-element chemistry can provide additional valuable tools for origin determination. The logarithmic plots of trace element data from LA-ICP-MS analyses such as Li versus Sc, Cs versus Rb, and Li versus Cs are distinct for this locality. These emeralds contain relatively high chromium (avg. 7471 ppmw), alkali metal (avg. 21040 ppmw), magnesium (avg. 34263 ppmw) and iron (avg. 9265 ppmw), as well as scandium (avg. 633 ppmw). Based on the identification criteria discussed above, especially microscopic and chemical analysis, separating Swat emeralds from other sources is possible.

ABOUT THE AUTHORS
Hongshu Guo, Yuyu Zheng, and Zhulin Sun are obtaining master's degrees in gemology, and Dr. Xiaoyan Yu (yuxy@cugb.edu.cn, cor-responding author) is director of the gemology teaching and research group and a professor of gemology and mineralogy, at the School of Gemmology, China University of Geosciences in Beijing. Dr. Ng is the founder of the Centre for Gemmological Research in Hong Kong.

REFERENCES

Arif M., Fallick A.E., Moon C.J. (1996) The genesis of emeralds and their host rocks from Swat, northwestern Pakistan: A stable-isotope investigation. *Mineralium Deposita*, Vol. 31, No. 4, pp. 255–268, http://dx.doi.org/10.1007/BF02280790

Arif M., Henry D.J., Moon C.J. (2011) Host rock characteristics and source of chromium and beryllium for emerald mineralization in the ophiolitic rocks of the Indus Suture Zone in Swat, NW Pakistan. *Ore Geology Reviews*, Vol. 39, No. 1-2, pp. 1–20, http://dx.doi.org/10.1016/j.oregeorev.2010.11.006

Bowersox G.W., Anwar J. (1989) The Gujar Killi emerald deposit, Northwest Frontier Province, Pakistan. *G&G*, Vol. 25, No. 1, pp. 16–24, http://dx.doi.org/10.5741/GEMS.25.1.16

Bowersox G.W., Snee L.W., Foord E.E., Seal II R.R. (1991) Emeralds of the Panjshir Valley, Afghanistan. *G&G*, Vol. 27, No. 1, pp. 26–39, http://dx.doi.org/10.5741/GEMS.27.1.26

Carlo A., Conte A.M., Medeghini L., Ottolini L., De Vito C. (2018) Major and trace element geochemistry of emerald from several deposits: Implications for genetic models and classification schemes. *Ore Geology Reviews*, Vol. 94, pp. 351–366, http://dx.doi.org/10.1016/j.oregeorev.2018.02.001

Dilles J.H., Snee L.W., Laurs B.M. (1994) Geology, Ar-Ar age and stable isotopes geochemistry of suture-related emerald mineralization, Swat, Pakistan, Himalayas. In *Proceedings of the Geological Society of America, Annual Meeting*, Seattle, Washington. Abstracts. Vol. 26, pp. A–311.

Gao Y., Sun X., Shan M. (2019) Gem News International: Trapiche emerald from Swat Valley, Pakistan. *G&G*, Vol. 55, No. 3, pp. 441–442.

Giuliani G., Groat L.A., Marshall D., Fallick A.E. (2019) Emerald deposits: A review and enhanced classification. *Minerals*, Vol. 9, No. 2, pp. 105–168, http://dx.doi.org/10.3390/min9020105

Groat L.A., Giuliani G., Marshall D.D., Turner D.B. (2008) Emerald deposits and occurrences: A review. *Ore Geology Reviews*, Vol. 34, No. 1-2, pp. 87–112, http://dx.doi.org/10.1016/j.oregeorev.2007.09.003.

Gübelin E.J. (1982) Gemstones of Pakistan: Emerald, ruby, and spinel. *G&G*, Vol. 18, No. 3, pp. 123–139, http://dx.doi.org/10.5741/GEMS.18.3.123

Jamal-ud-Din (2014) The neglected emerald mines of Swat. *Dawn*, August 3, https://www.dawn.com/news/1122968.

Johnson M.L., Elen S., Muhlmeister S. (1999) On the identification of various emerald filling substances. *G&G*, Vol. 35, No. 2, pp. 82–107, http://dx.doi.org/10.5741/GEMS.35.2.82.

Karampelas S., Al-Shaybani B., Mohamed F., Sangsawong S., Al-Alawi A. (2019) Emeralds from the most important occurrences: Chemical and spectroscopic data. *Minerals*, Vol. 9, No. 9, p. 561, http://dx.doi.org/10.3390/min9090561

Kazmi A.H., Lawrence R.D., Anwar J., Snee L.W., Hussain S.S. (1986) Mingora emerald deposits (Pakistan): suture associated gem mineralization. *Economic Geology*, Vol. 81, No. 8, pp. 2022–2028.

Khan B. (2018) Emerald occurrences in Pakistan. *InColor*, No. 40, pp. 80–84.

Laurs B.M., Dilles J.H., Snee L.W. (1996) Emerald mineralization and metasomatism of amphibolite, Khaltaro granitic pegmatite

– hydrothermal vein system, Haramosh Mountains, northern Pakistan. *Canadian Mineralogist*, Vol. 34, No. 6, pp. 1253–1286.

Lawrence R.D., Kazmi A.H., Snee L.W. (1989) Geological setting of the emerald deposits. In A.H. Kazmi and L.W. Snee, Eds., *Emeralds of Pakistan*. Van Nostrand Reinhold, New York, pp. 13–38.

Li C., Zhou L., Zhao Z., Zhiyuan Z., Zhao H., Li X., Qu W. (2018) In-situ Sr isotopic measurement of scheelite using fs-LA-MC-ICPMS. *Journal of Asian Earth Sciences*, Vol. 160, pp. 38–47, http://dx.doi.org/10.1016/j.jseaes.2018.03.025

Liu Y., Hu Z., Gao S., Günther D., Xu J., Gao C., Chen H. (2008) In situ analysis of major and trace elements of anhydrous minerals by LA-ICP-MS without applying an internal standard. *Chemical Geology*, Vol. 257, No. 1-2, pp. 34–43, http://dx.doi.org/10.1016/j.chemgeo.2008.08.004

Makki M., Ali S.H. (2019) Gemstone supply chains and development in Pakistan: Analyzing the post-Taliban emerald economy in the Swat Valley. *Geoforum*, Vol. 100, pp. 166–175, http://dx.doi.org/10.1016/j.geoforum.2019.01.005.

Ohnenstetter D., Giuliani G., Bustos O. (1998) Emeraudes trapiches colombiennes. In *L'émeraude. Connaissances actuelles et prospective*. Association Française de Gemmologie, pp. 119–124 (in French).

Rehman H.U, Seno T., Yamamoto H., Khan T. (2011) Timing of collision of the Kohistan-Ladakh Arc with India and Asia: Debate. *Island Arc*, Vol. 20, No. 3, pp. 308–328, http://dx.doi.org/10.1111/j.1440-1738.2011.00774.x

Saeseaw S., Pardieu V., Sangsawong S. (2014) Three-phase inclusions in emerald and their impact on origin determination. *G&G*, Vol. 50, No. 2, pp. 114–133, http://dx.doi.org/10.5741/GEMS.50.2.114

Saeseaw S., Renfro N.D., Palke A.C., Sun Z., McClure S.F. (2019) Geographic origin determination of emerald. *G&G*, Vol. 55, No. 4, pp. 614–646, http://dx.doi.org/10.5741/GEMS.55.4.614

Schmetzer K. (2020) Gem News International: Trapiche-type emeralds from Pakistan. *G&G*, Vol. 56, No. 3, p. 438.

Schmetzer K., Berdesinski W., Bank H. (1974) Über die Mineralart Beryll, ihre Farben und Absorptionsspektren. *Zeitschrift der Deutschen Gemmologischen Gesellschaft*, Vol. 23, No. 1, pp. 5–39 (in German).

Wood D.L., Nassau K. (1968) The characterization of beryl and emerald by visible and infrared absorption spectroscopy. *American Mineralogist*, Vol. 53, No. 5-6, pp. 777–800.

Xu Z., Dilek Y., Yang J., Liang F., Liu F., Ba D., Cai Z., Li G., Dong H., Ji S. (2015) Crustal structure of the Indus–Tsangpo suture zone and its ophiolites in southern Tibet. *Gondwana Research*, Vol. 27, No. 2, pp. 507–524, http://dx.doi.org/10.1016/j.gr.2014.08.001

Zheng Y., Yu X., Guo H. (2019) Major and trace element geochemistry of Dayakou vanadium-dominant emerald from Malipo (Yunnan, China): Genetic model and geographic origin determination. *Minerals*, Vol. 9, No. 12, pp. 777–807, http://dx.doi.org/10.3390/min9120777

Zwaan J.C., Jacob D.E., Häger T., Cavalcanti Neto M.T.O., Kanis J. (2012) Emeralds from the Fazenda Bonfim region, Rio Grande do Norte, Brazil. *G&G*, Vol. 48, No. 1, pp. 2–17, http://dx.doi.org/10.5741/GEMS.48.1.2

For online access to all issues of GEMS & GEMOLOGY from 1934 to the present, visit:

gia.edu/gems-gemology

A History of European Royal Jewel Sales, Including Sotheby's 2018 Auction of Marie Antoinette's Jewels

Russell Shor

On November 14, 2018, Sotheby's Geneva sold 100 lots from the House of Bourbon-Parma, including 10 items from Queen Marie Antoinette. The venerable auction house claimed it was one of the largest sales of jewels with royal provenance in modern history. The key word from Sotheby's statement is "modern," because there have been other major sales of jewels from both crown jewels (owned by the state) and the personal property of royalty since 1795. The first section of this article describes how the most prominent European royal houses—particularly the Habsburgs, the Bourbons, and their predecessors—acquired their jewels and then details the most significant auctions of these items, starting with the collection of Madame du Barry in 1795 and the French crown jewels in 1887. The second part chronicles the historic Bourbon-Parma auction in 2018. The Sotheby's sale was extraordinary in its scope because a vast majority of the jewels collected by European royals, mainly in the eighteenth and nineteenth centuries, had been widely scattered over the past two centuries by sale, confiscation, theft, residence in museums, and reworking. With 10 of the lots traced back to France's most famous royal, Marie Antoinette, the auction attracted worldwide attention and exceptional prices—her signature drop-shaped natural pearl pendant alone sold for US$36 million. The 100 lots sold for a total of US$53 million. In recent years, jewels with royal provenance have fetched high premiums at auction, and this was no exception. However, early sales of royal jewels—when monarchies were losing favor throughout Europe—often carried little or no premium for this pedigree. Indeed, contemporaneous accounts of these sales often complained that prices were disappointing.

For more than a millennium, Europe's royal families accumulated jewels and gemstones for their kingdom's treasuries and for their own adornment. By the end of the eighteenth century, they had amassed vast fortunes but the monarchies themselves were weakening. The first documented major sale of jewels of royal provenance—belonging to Madame du Barry, consort of French King Louis XV—was conducted by James Christie in London in 1795, during the French Revolution. This article will chronicle the major sales from European royal houses and detail how Sotheby's experts researched, assembled, and sold the Bourbon-Parma collection in 2018.

BACKGROUND

Gemstones and jewels have long symbolized power and wealth among royal houses worldwide. The earliest known European crown, the Iron Crown of Lombardy, was fashioned in the sixth century (with additions made in the ninth century). It contained seven blue sapphires, seven reddish brown garnets, four amethysts (described as rock crystals), and four pieces made of green glass set in gold (Twining, 1960; Brus, 2011). The second oldest known jeweled crown is the Imperial Crown of the Holy Roman Empire, or Crown of Charlemagne, named for the first Holy Roman Emperor (r. 800–814 CE). The empire was a medieval consolidation of dozens of principalities centered in what are now modern-day Germany and large parts of Austria, Hungary, Poland, Italy, and France. The crown, made for Emperor Otto the Great (r. 962–973 CE), was ornamented with 144 gemstones, including sapphire, amethyst, emerald, and pearls. The 12 largest gems represented the 12 apos-

tles of Christ. The sapphires symbolized strength and protection against disease, while a large center opal (since lost) represented honor. Other surviving regalia from the medieval period, including scepters, swords, crosses, orbs, and of course crowns, were also studded or topped with various types of gemstones to symbolize the royal office (Prince Michael of Greece, 1983).

Until the late Middle Ages, gemstones were quite rare in Europe, hard won across the arduous, predominantly overland trade routes of the Silk Road. These trade routes, established about 100 BCE, invariably began in India, though stones such as sapphires and rubies originally came from Ceylon and Burma (modern-day Sri Lanka and Myanmar, respectively). The gems passed through China, overland from trader to trader through the Himalayas and Persia, and then to the Syrian port of Aleppo near the Mediterranean. From there, they traveled to Venice and the trading center of Pavia, where Emperor Charlemagne had stationed buying agents (Sevillano-Lopez and Gonzalez, 2011; Bycroft and Dupré, 2019). Gemstones of any type were very costly by the time they reached Europe, with traders at every stop along the Silk Road adding in their profit.

As Europe's principalities began consolidating into nascent nation-states, seafaring explorers helped open trade routes between Asia, Europe, and the Western Hemisphere. Vasco da Gama, who discovered the sea route from Europe to India in 1498, brought quantities of gems back to his home port in Portugal. Diamonds from India and emeralds from South America were an important part of this trade (Shor, 2004; Bycroft and Dupré, 2019). Within a decade of da Gama's voyage to India, Portuguese traders had established a trading port in Goa and regular trade routes that imported diamonds through Lisbon and then to the trading centers of Bruges, Antwerp, and Amsterdam. Toward the end of the sixteenth century, a number of Europe's rulers attempted to monopolize trade with India through state trading companies. The British East India Company, the Dutch Vereenigde Oostindische Compagnie, the Portuguese Estado da Índia, and the French Compagnie Française des Indes Orientales established trading bases along western India in Goa, Bombay, and Surat. Gemstones were an important part of these companies' trade, and for the next several centuries monarchs continued to acquire them to fill their treasuries and adorn their families ("Dutch East India Company…," 2017; Ogden, 2018b).

By the mid-sixteenth century, gemstones had become a significant part of Europe's royal treasuries. Rulers often pledged their crown jewels to wealthy merchants or lenders to raise money to pay their armies to fight near-constant wars on the continent. Henry IV of France famously pledged a number of large diamonds to pay 12,000 Swiss mercenaries to protect him after his father was assassinated in 1595. In addition, royal families began amassing collections of diamonds and gemstones for themselves. In 1530, Francis I saw the need to distinguish those owned by the treasury by formalizing the state title over the French crown jewels. He ordered detailed inventories, including records of value, weight, and each alteration, to ensure the jewels' succession to subsequent kings by declaring them property of the state (Twining, 1960).

The best-known gemstone trader of the period, Jean-Baptiste Tavernier, was well connected to roy-

In Brief

- European royal families amassed large collections of jewels and gemstones, symbols of wealth and power, for personal adornment and for their state treasuries.

- Since 1795, there have been a number of significant auction sales from crown jewels and royal collections, including the sale of Madame du Barry, the French crown jewels in 1887, and a portion of the Russian crown jewels in 1926.

- The most recent occurred in 2018 with a sale of 100 items from the Bourbon-Parma royal family, including 10 jewels that once belonged to Marie Antoinette.

- The prices realized from these jewels reflected their extraordinary provenance and history.

alty and also to Cardinal Richelieu, the French regent when Louis XIV was still a child. He was also related by marriage to two prominent Parisian jewelers, Jean Pitau and later Jean Goisse, whose daughter he married in 1662. Tavernier received a commission in 1631 to travel to Constantinople and Persia. This was the first of six voyages he made to acquire gemstones and other rare treasures from the East. On his five subsequent voyages, he made trading visits to India, the source of most of the world's diamonds at the time and a repository of treasures held by the Mughal rulers. Tavernier sketched meticulous drawings of large diamonds he purchased and detailed his dealings with India's rulers
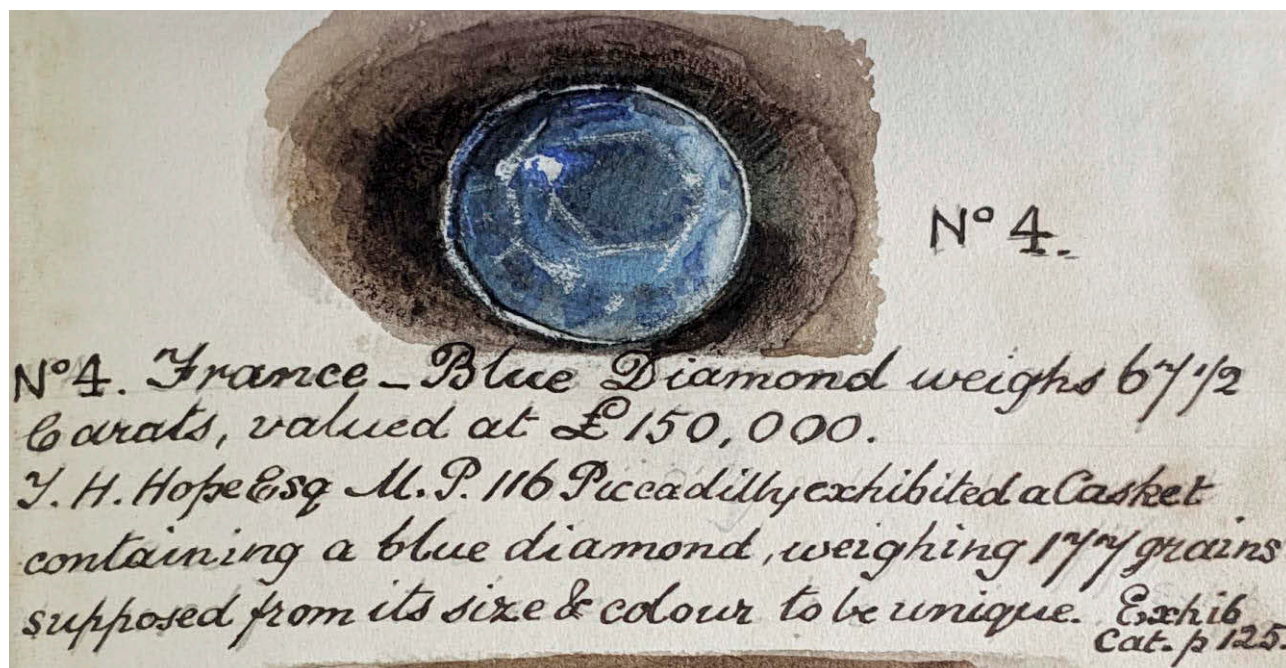
Figure 1. A drawing of the glass model of the 67.12 ct French Blue diamond made for the Great Exhibition of 1851 in London. However, the shape depicted is that of the smaller recut Hope diamond. Courtesy of Jack Ogden.

and gem merchants. On his sixth voyage (1664–1668), he made his most noteworthy purchase, spending 70,000 livres[1] (approximately US$1 million today) for a "roughly cut" blue diamond of 112 ^{3}/$_{16}$ ct[2] (115.28 metric carats), which he subsequently sold to Louis XIV for 220,000 livres (nearly US$3.3 million).

The king entrusted the blue diamond to Pitau, who recut it to 67.12 ct (figure 1). The diamond remained in the royal family until 1792, when it was stolen during a burglary of the French treasury. It reappeared in London 20 years later, this time recut to 45.52 ct as the Hope diamond.

All told, the king paid Tavernier 879,731 livres (US$13.2 million) for the 67.12 ct blue diamond plus 1,134 diamonds of various weights (Ogden, 2017, 2018b).

European royal jewel collections reached their peak in the mid-eighteenth century as an abundance of diamonds emerged from a new source, Brazil, while emeralds continued to flow from Colombia. In addition, British traders grew more active in Asia, bringing back sapphires, rubies, and pearls. These were sold to rulers of Britain; the dukes within the Habsburg realm of the Holy Roman Empire; and royalty of Russia, Italy, Spain, Scandinavia, and France. The Habsburg dynasty accumulated immense wealth and extended its European domain through intermarriage (Ogden, 2018a).

By the late eighteenth century, royal extravagances were taking their toll on the reputations of the monarchs, especially in France, where intrigue over a costly necklace proved to be one of the catalysts for the French Revolution. In 1782, the jewelers to the French crown, Boehmer et Bassenge, created a necklace featuring 650 diamonds weighing a total of 2,500 carats. They presented it to Louis XVI and his wife, Marie Antoinette, who turned it down, citing the high price of 2 million livres (US$8 million). The jewelers then offered the necklace to Madame du Barry, consort to Louis XV, but she also declined. Two years later, the disgraced courtier Cardinal de Rohan was approached by Countess de La Motte,

---

[1]The livre preceded the franc as the French unit of currency. In the seventeenth century, a livre was worth approximately $15 in today's U.S. dollars. By the late eighteenth century, one livre was valued at slightly more than $4 in today's U.S. dollars.

[2]While the term "carat" was used to describe gemstone weight from the fourteenth century onward, its weight was not standardized at 0.2 grams until the early twentieth century, so there are discrepancies in published sources.

who posed as a friend of the queen. La Motte offered to serve as an intermediary to buy the necklace and thus restore Rohan to the queen's good graces. The cardinal eventually arranged a sale price of 1.6 million livres (US$6.5 million). Upon receipt of the necklace, Countess de La Motte promptly disappeared ("The affair of the diamond necklace, 1784-1785," 2017). Cardinal de Rohan and Countess de La Motte were eventually arrested. The cardinal was acquitted in a sensational trial during which allegations of Marie Antoinette's extravagance were constantly brought before the public. The countess was convicted but escaped from prison and made her way to London, where she wrote scathing (and probably untrue) accounts of the queen's sexual liaisons, which became popular reading in France. Europe's leading power had fallen on hard times: The government was nearly bankrupt, and there was widespread poverty. The publicity from the case brought an unprecedented contempt for the royal family and helped bring about the revolution four years later ("The diamond necklace affair," 2009).

NOTABLE SALES OF ROYAL JEWELS

The du Barry Auction of 1795. Christie's 1795 auction of the jewels of Madame du Barry occurred during the height of European royalty's quest for wealth. The title page of the catalog listed her as "deceased," but the auction house's euphemistic description of her fate (a tradition continuing to this day) mentioned little about what actually happened to her (Meylan, 2016).

Born Jeanne Bécu to commoner parents, she gained access to the French court through Jean-Baptiste du Barry, whose brother, Guillaume du Barry, she eventually married. The du Barrys were well connected and introduced her to Louis XV, who took her as his mistress. For five years, the king showered her with jewels. He gave her an estimated 100,000 livres (approximately US$400,000) worth of diamonds to wear upon her presentation to court in 1769 (Meylan, 2016). Louis XV reportedly sent her jewels nearly every week, in addition to furniture and porcelains. By 1774, she had amassed nearly 3 million livres[3] (nearly US$12 million today) worth in her safe boxes (Meylan, 2016).

Louis XV died on May 10, 1774. His son, Louis XVI, whose bride was Marie Antoinette, ordered du

---

[3]The value of the livre had deteriorated by a factor of four in the ensuing 110 years since Tavernier's purchases.

Barry exiled. She led a quiet life until January 10, 1791, when thieves stole an estimated 1.5 million livres (US$6.5 million) worth of diamonds from her chateau (Meylan, 2016). The thieves were caught in London several months later. Du Barry traveled to London several times over the next two years to recover the diamonds—to no avail. In the meantime, with anti-royalist sentiment building in France, she hid her remaining jewels and precious possessions in various places on the grounds of her estate.

As her native land entered the bloody aftermath of the French Revolution (known today as the Reign of Terror), Jeanne du Barry was arrested on November 19, 1793. She was eventually placed in the same cell in La Conciergerie prison as her court rival Marie Antoinette, who had been executed seven weeks earlier. On the day of her own execution, December 8, 1793, Madame du Barry managed to delay the inevitable more than four hours by slowly revealing the hiding places of her treasures. Upon revealing the last of the hiding places, as the guards closed in to take her to the guillotine, she pleaded in vain for yet more time to return to London to retrieve her stolen diamonds (Meylan, 2016).

The audit and appraisal of her jewels, both the stolen pieces and those she had hidden, took some two years amid the chaos of post-revolutionary France. By 1795, the inventory was complete. Her jewels totaled 400,000 livres (US$1.2 million), and the rest of her possessions—paintings, gold *objets d'art*, sculptures, and furniture—were valued at 1.4 million livres (US$5.6 million). British authorities kept some of her jewels to satisfy creditors' claims and assigned the remainder to James Christie, founder of Christie's auction house (Meylan, 2016).

The title page of the catalog promoted the sale as a "Most capital and superb assemblage of valuable jewels, of most singular excellence, beauty and perfection, late the property of Madame La Comtesse du Barry" (figure 2, left). Held on February 19, 1795, the auction consisted of 65 lots, including 1,000 pearls, 150 brilliant-cut diamonds weighing between one and 12 ct, 1,200 smaller diamonds, and some colored gems (Christie's, 1795). None of the gemstones were mounted, as the thieves had apparently broken up the pieces to make identification difficult (Meylan, 2016).

The largest diamond sold for 910 British pounds (approximately US$135,000 today). In addition, the catalog listed several hundred pearls not given in the initial inventory of stolen gems. The entire collection realized 8,788 British pounds (approximately
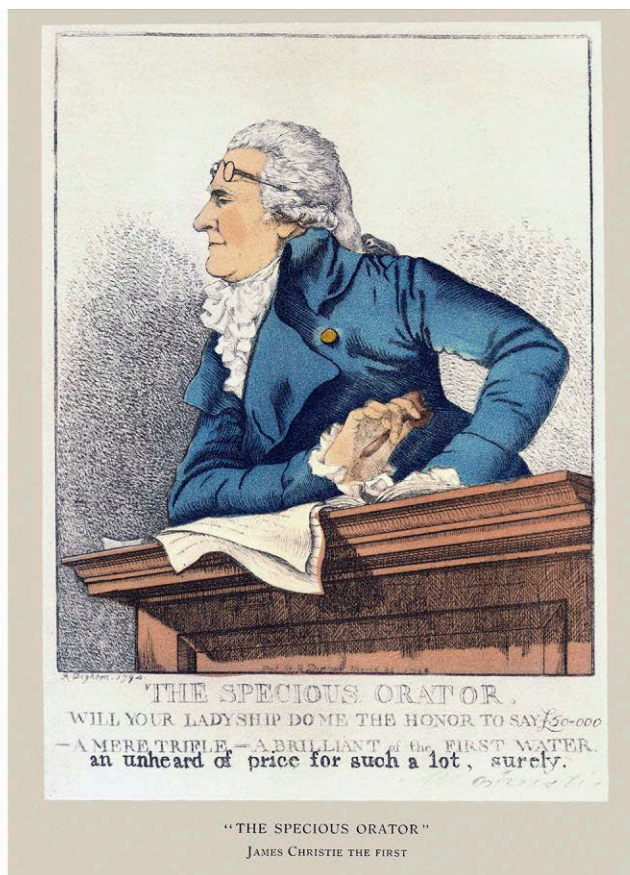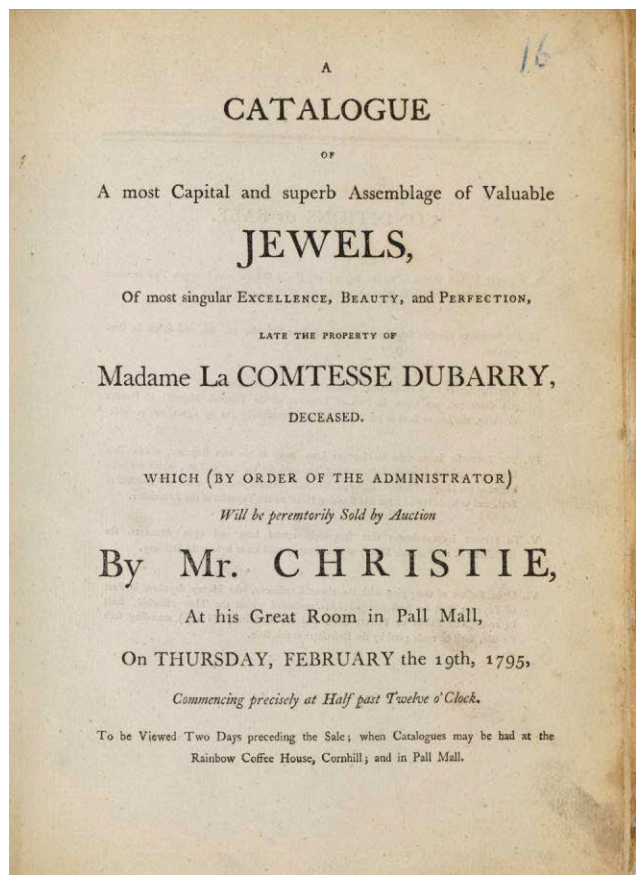
Figure 2. Left: The cover of Christie's 1795 auction catalog featuring Madame du Barry's jewels. Right: A contemporary illustration by Robert Dighton of James Christie conducting the auction: "Will your ladyship do me the honour to say 50,000? A mere trifle. A brilliant of the first water. An unheard of price for such a lot, surely." Images courtesy of Christie's.

US$1.1 million)—far below its appraised value. A satirical illustration, titled the *Specious Orator*, shows James Christie at a podium trying to coax an extra few pounds from a reluctant bidder (figure 2, right).

Meylan speculates that the disappointing prices occurred because many wealthy French citizens had fled to London and sold their jewels cheaply to live in exile as the revolution in their homeland unraveled into violence. However, large diamonds were a difficult sell even before the Christie's auction (Ogden, 2009).

The 1887 Sale of the French Crown Jewels. The French royal line traced its history back to 495 CE, shortly after the demise of the Western Roman empire but long before the establishment of France. The earliest dynasties, the Merovingian and the Carolingian, ruled the Frankish kingdom in what is now northeastern France and established their capital at Reims, a town founded by the Romans in about 80 BCE. The scepter, ring, and the jeweled Crown of Charlemagne were held at the Abbey of St. Denis near Paris, which became the repository for all French royal regalia until the 1789 revolution (Twining, 1960).

When the House of Valois ascended to the French throne in 1328, the rulers began accumulating jewels and gold as a reserve of wealth. The gems served dual purposes, as they could be worn in peacetime and pledged as collateral in times of war. An inventory of Charles V's assets at his death in 1380 included eight jeweled crowns for him, nine for his queen, and 26 other jewel-encrusted pieces. The main crown featured the subsequently recarved Côte de Bretagne, a 262.5 ct round cabochon "Balas ruby" (red spinel from Afghanistan), and two other "Balas rubies": a 93 ct cabochon and an 80 ct square cut. Other "Balas

rubies" in the inventory included a 414.5 ct stone and 261 cabochons. A second crown made for the king was called the Crown of the Five Emeralds, while a third was said to contain diamonds, pearls, and sapphires (Twining, 1960).

As European royal houses began intermarrying to seal alliances, expand their domains (and wealth), and perpetuate heirs to their thrones, the French crowns and accoutrements of rule grew more elaborate, as did the need for more gemstones after the House of Bourbon ascended in 1593. It was during the next 100 years that the French crown jewels grew to become perhaps the greatest treasure house in Europe (Twining, 1960).

Cardinal Mazarin, once a papal envoy sent to mediate various conflicts in Europe, became de facto ruler of France after the death of Louis XIII in 1643. He was appointed as chief minister and regent to Louis XIV, who was four years old at the time of his father's death. The cardinal was immensely wealthy and understood the necessity of accumulating jewels for the royal coffers. Upon his death in 1661, he bequeathed his collection of 18 large diamonds ranging from 8.75 to more than 55 ct to the national treasury. These included the 55.23 ct Grand Sancy and the 19.07 ct Fancy Light pink Grand Mazarin (figure 3), valued at 1.9 million livres (US$28.5 million) (Twining, 1960; Truong, 2017). The state inventory of crown jewels, including the diamonds he bequeathed, totaled 7.4 million livres (US$111.1 million). Louis XIV continued to amass gemstones despite running up significant debts to fund various wars (Twining, 1960).

In 1791, as the French Revolution continued, the government made a detailed inventory of all of the crown jewels and ordered them to be kept in the Garde-Meuble de la Couronne, the royal treasury in the Place de la Concorde in Paris. The royal family was executed in 1793 after two years of imprisonment. Many of the crowns and royal regalia were removed from the repository at the Abbey of St. Denis and melted down (Twining, 1960).

In September 1792, thieves broke into the Garde-Meuble and stole most of the crown jewels, including the Mazarin diamonds. Within a week of the crime, the superintendent of the treasury and several accomplices were arrested. One of the thieves facing the guillotine revealed where his share of the gems was hidden. While a number of diamonds and gems were recovered, all but five of the Mazarin diamonds were still missing (Truong, 2017). Also missing were the Regent and French Blue diamonds. The Regent, the largest diamond in the crown jewels, was located

in an attic shortly afterward, but the blue diamond, as noted previously, remained missing for some 20 years before resurfacing in London as the Hope diamond (Ogden, 2018b). The large "Balas ruby" spinel, which had been documented in the fourteenth-century inventories, was returned to the French treasury after three years. The 55 ct Sancy diamond was also stolen and remained missing for nearly two centuries. During that time, it made its way through a Russian owner and then to India, before the grandson of the maharajah who had purchased the diamond returned it to France in 1978 (Morel, 1988).

When Napoleon became emperor of France in 1804, he and his wife, Josephine, set about rebuilding the collection of crown jewels that had been pledged to creditors or stolen during the revolution, commissioning a new crown for himself (but still named for

Figure 3. The Grand Mazarin diamond is a 19.07 ct Fancy Light pink diamond acquired by Cardinal Mazarin. Bequeathed to Louis XIV in 1661, the diamond remained part of the French crown jewels until it was sold in 1887. It reappeared in 2017 and sold to an undisclosed buyer at Christie's for US$14.46 million. Photo courtesy of Christie's.

Charlemagne) and acquiring more diamonds, gemstones, and jewels from the leading houses of Paris. After his reign ended in 1815, the monarchy was restored until the Second Republic (1848–1852), followed by the Napoleonic Empire (1852–1870), which lasted until the Third Republic (1870–1940) (Twining, 1960; Fasel, 2019).

For 16 years, the new republic deliberated the fate of the French crown jewels. While there was strong sentiment to preserve the collection for its rich history and expert craftsmanship, the country's parliament eventually decided to sell the jewels, in large part to deter any future return to a monarchy (Morel, 1988). A law enacted in December 1886 authorized their sale, with the exception of historical pieces such as the 140.64 ct Regent diamond, which was the centerpiece of Louis XV's crown and later mounted in Napoleon's sword (Twining, 1960).

The sale of the jewels commenced on May 12, 1887, at the Louvre and proceeded in nine sessions to May 23. The Ministry of Finance oversaw the operation. In response to critics who did not want to see a millennium's worth of their national history sold off, the ministry reserved a number of significant pieces to be preserved in the Louvre. This included the Regent diamond, which had comprised about half the appraised value of the entire collection; the 20 ct Hortense diamond, which had been purchased from Tavernier; a large diamond brooch that had belonged to Louis XIV; and, among other regalia, Napoleon's crown and "Joyeuse," the Sword of Charlemagne, which had been fashioned in the eleventh and twelfth centuries, with elements added later (Twining, 1960; Fasel, 2019).

Many of the remaining jewels were broken up and the diamonds and gemstones assembled into large lots for sale (Fasel, 2019). According to Morel (1988), similar pieces were grouped together: "Seven aiguillettes [gem set cords] set with 222 brilliants [diamonds], weighing 215 $^{25}/_{32}$ carats hanging from a foundation ornament set with 59 brilliants 18 $^9/_{16}$ carats and 8 rose diamonds. Estimated value 15,000 francs." Buyers, however, could bid on individual pieces within each grouping.

The most significant grouping (lot 46) included what was described as seven Mazarin diamonds, including a 24 $^{27}/_{32}$ ct rose-colored stone (estimated 70,000 francs[4], about US$1 million), and a 22 ½ ct

white pear shape estimated to sell for 80,000 francs (about US$1.15 million). However, only the Grand Mazarin, listed as 18 $^9/_{32}$ ct, was an actual Mazarin diamond, the others having been misidentified (Morel, 1988). In addition, the catalog did not note the Grand Mazarin's light pink color. Despite the fact that the diamonds were included in a single lot number (46), buyers could bid on individual stones (Twining, 1960; Truong, 2017).

After the first day of the sale, the *New York Times* reported that the auction "seemed to have excited more interest in America than here." The audience of about 600 was primarily made up of "either foreigners or *petit bourgeois* who went to satisfy their curiosity but without any idea of bidding for a single article…knowing that everything would be done to protect the interests of dealers, who, as always happens at the Hotel Drouot [a Parisian auction house], combine systematically to run up prices whenever an outsider presumes on competition."

The correspondent went on to report that the sellers could not guarantee the weight of the mounted diamonds or verify that all the pieces contained their original diamonds. The writer also speculated that many of the buyers were acting as agents for private buyers, including "Orleans princes," referring to the recently deposed royal family ("The French crown jewels…," 1887).

The sale realized 7,221,560 francs (approximately US$107 million today): 6,864,050 francs for the gemstones and jewels, and the remainder for the melted gold and commissions to the sellers. As the *Times* predicted, dealers did dominate the buying (Twining, 1960). Tiffany & Co. purchased more than two-thirds of the lots, later packaging them in special red and gold boxes for sale to American clients.

Frederic Boucheron, founder of the famed Parisian jewelry house, acquired the Grand Mazarin and two other Mazarin diamonds for 101,000 francs (approximately US$1.5 million). The story of that diamond has recently been documented (Truong, 2017). Boucheron eventually resold the Grand Mazarin to a member of the Russian royal family, who later sold it to an unnamed European buyer. The owners lent the diamond to the Louvre for an exhibition of French crown jewels in 1962. But the diamond remained out of sight until 2017, when Christie's Geneva received a call from its owner (Lunel, 2017).

Christie's dispatched two jewelry experts to view the diamond in a private house in Europe. "When the client unwrapped a piece of old parcel paper to reveal this beautiful pink diamond in front of [jewelry ex-

---

[4]A French franc at that time was equivalent to 0.0102408248 ounces of gold, or nearly $15 in today's dollars.

Figure 4. The complete array of Russian crown ceremonial jewels confiscated from royal families and assembled in 1925 by the Soviet government for cataloging and potential sale. This did not include loose gemstones from the royals' personal collections. From Fersman (1925-1926).

perts) Jessica Koers and Max Fawcett, they were stunned" (Lunel, 2017).

Auction house historians authenticated the diamond and its history before it went up for sale on November 14, 2017, in Geneva with a presale estimate of US$4 million. Because estimating the value of such a historic diamond is difficult, Christie's included a US$1 million premium in their estimate (Christie's, 2017), which was considered conservative. At the time "it was the diamond with the most prestigious and historic provenance still in private hands," in the words of Rahul Kadakia, Christie's international head of jewelry. The auction hammer came down at more than US$13 million, adding in the house premium, for a total of US$14,463,493 (Shor, 2019).

The Grand Mazarin is one of the very few pieces from the 1887 French crown jewels sale to have come back to the market—at least publicly—and the only diamond from the original Mazarin collection to do so (R. Kadakia, pers. comm., 2019).

Sales of Other Royal Jewels. Twining and others have noted that other European royal families amassed large gem and jewelry collections, both for the crown and among their members, but the majority of these have been sold off privately in small increments, held in museums, or possibly still kept by family, such as the Bourbon-Parma collection that is the subject of the second section of this article. In addition, there have been, over the years, several smaller sales of royal jewels or sales from royal-titled individuals selling their personal pieces.

Only the Russian crown jewels rivaled the French for the quantity of diamonds and jewelry held in royal coffers, but the plan to sell off the entire collection en masse never materialized. After the 1917 Russian Revolution, the new Soviet government seized the collection and meticulously cataloged it for potential sale, finally completing the job in 1925 (figure 4). Despite the revolutionary zeal of the Bolshevik Party, the government decided against selling the entire collection as the French had (Meylan, 2018), instead depositing many pieces back into the Kremlin Armory Museum and offering others in private or limited sales, including one well-publicized offering.

Early in 1926, the Soviet government conducted a tender auction through Christie Manson & Woods (known as Christie's today) for 124 lots, including

several diadems (smaller ceremonial crowns), the nuptial crown of the last czarina, 30,000 carats of loose diamonds, and "many emeralds and sapphires," according to a February 23 *New York Times* article ("French outbid all for Czar's jewels," 1926). Potential buyers complained that grouping all of the pieces into a relatively small number of costly lots made buying difficult for individuals. In the end, the competition fell between two consortia, one headed by a French dealer and the other by an Anglo-American group. The French won the majority of lots, with total bids topping US$3 million in 1926 dollars. The article noted that the sale prices did not recognize the historical value of the items. Thirty items failed to sell, including two diamond tiaras and a diamond brooch (Twining, 1960).

The French consortium, represented by M. Frankiano, who was working with a Hungarian jeweler named Norman Weisz, subsequently auctioned the collection at Christie's London in March 1927 (McCanless and Wintraecken, 2010). No other major public sales of the Russian collection were reported (Twining, 1960).

Five other major collections with European royal connections have come up for auction: a 1931 Christie's sale of loose gemstones from the Bavarian crown jewels, including nine large emeralds and the Wittelsbach Blue diamond, the latter of which failed to sell; the 1987 Duchess of Windsor collection at Sotheby's; the 1989 Countess du Boisrouvray collection at Sotheby's; the 1992 Collection of Thurn und Taxis at Sotheby's; and the 2006 Princess Margaret, Countess of Snowden auction at Christie's.

The Duchess of Windsor collection was perhaps the most celebrated auction of modern times, touching off a wave of interest in jewelry around the world (Shor, 2013). While the Duke of Windsor had once been King Edward VIII—he famously abdicated the throne to marry Wallis Simpson in 1937—the jewelry collection was considered personal property since it had been acquired with his own funds. The auction, initially valued at a total of $7 to $8 million, realized $50.3 million, a record for an individual sale at the time.

Similarly, the auctions of the three other royally connected jewels (Princess Margaret, Thurn und Taxis, and du Boisrouvray) were primarily the sellers' personal property. With few exceptions, the items were of relatively recent vintage (D. Mascetti, pers. comm., 2019).

In June 2006, Christie's London auctioned 800 items, including 192 pieces of jewelry, belonging to the sister of Queen Elizabeth II, Princess Margaret, who died in 2002. The majority were pieces she acquired as gifts at and during her marriage to Antony Armstrong-Jones, Earl of Snowdon. However, several pieces offered at the sale came from the British royal collection, including the Poltimore Tiara, made in 1870 and worn at her wedding 90 years later. Her children reportedly placed the items up for sale to pay some US$5.5 million in inheritance taxes. The queen is said to have demanded that her portion of the proceeds be given to charity. This was one of the few occasions that jewels from the British royal collection have left the family (Alderson, 2006). The sale realized US$17.7 million, nearly double the high presale estimate. The tiara, set with small diamonds, sold for US$1.7 million against a presale estimate of US$370,000. Another significant piece from the British royal collection, Queen Mary's diamond rivière necklace, brought US$1.8 million against a presale estimate of US$550,000. The Princess Margaret sale also included approximately 15 smaller jewelry items dating back to the eighteenth century (Christie's, 2006).

THE BOURBON-PARMA SALE OF 2018

The Bourbon-Parma dynasty is descended from royal houses in France, Spain, and Italy and related by marriage to the House of Habsburg. Its lineage is the longest of any European ruling family, descended from France's House of Capet (987–1328), and reigning in some capacity since 1572. Bourbon-Parma descendants today include King Felipe VI of Spain and Henri, Duke of Luxembourg.

The Bourbon line ruled France from 1572 to 1792, then for one year in 1814, and again from late 1815 until 1830. The first Bourbon king of Spain was Philip V (the second son of France's Louis XIV), who ascended to the throne in 1700. Fourteen years later, he married Elisabeth Farnese, daughter of Oduardo Farnese, Duke of Parma, whose family had ruled the northern Italian city since 1545. This gave the family dominion over several Italian principalities, which expanded in ensuing centuries until Italian unification in 1867. The Spanish Bourbons still occupy the throne, though their reign was interrupted during the years 1808–1814, 1868–1874, and 1931–1974 (Royde-Smith, 2019).

The House of Habsburg, once Europe's most dominant royal house, was based in Austria. The two families formed a powerful union when Marie Antoinette, Archduchess of Austria and a Habsburg, married the Bourbon and future King Louis XVI in

1770. Louis XVI took the throne of France in 1774 and ruled with Marie Antoinette until they were deposed during the French Revolution.

By 1791, the uneasy arrangement that allowed Louis XVI and Marie Antoinette to remain on the throne began to unravel, and the royal family prepared to flee into exile. In March, Marie Antoinette entrusted her favorite jewels to a loyal retainer, Count Mercy d'Argenteau, who packed them into a wooden chest and spirited them to Brussels for safekeeping. By the end of June, Louis XVI and Marie Antoinette had been imprisoned and her jewelry collection was on its way from Brussels to Austria. The collection eventually went to the queen's eldest and only surviving daughter, Marie Thèrése (1778–1851), who had been imprisoned with other family members on August 13, 1792. During her three years of captivity, both of her parents were led to the guillotine: Louis XVI on January 21, 1793, and Marie Antoinette on October 16, 1793 (Meylan, 2018; Vachandez, 2018).

Marie Thèrése was released from prison in December 1795, just as she turned 17 years old, and taken to Vienna. While she lived in other European capitals throughout much of her life, her jewels, including those she inherited from her mother, remained on deposit in the Imperial Treasury of Vienna.

After her death in 1851, Marie Thèrése left one-third of her jewels to her niece, Louise de Bourbon-Parma, the Duchess of Parma, then an autonomous duchy in what is now Italy (Meylan, 2018). In 1859, however, Italy fell into upheaval with the armies of King Victor Emmanuel battling to unite the various Italian principalities into one nation, causing Louise de Bourbon-Parma to flee to Venice with the collection of jewels. After Louise died in 1864, the jewels were further divided between her brother, Henri, Count of Chambord (who received two-thirds), and three nieces and nephews (Louise, Henri, and Marie Thèrése), though the collection remained in the vault in Vienna. However, war broke out between Austria and Prussia in 1866, forcing family members to entrust the collection to a Rothschild-owned bank, and then it was sent to a family compound at Frohsdorf Palace in eastern Austria. After the Countess of Chambord died, she left her inherited portion of the collection to Louise's son Robert, Duke of Parma. Robert received additional inheritances before he died in 1907. After his death, the collection was passed to Marie Anne, Archduchess of Austria, who in 1903 had married Prince Elias de Bourbon-Parma, son of Robert and Duke of Parma (Vachandez, 2018).

Marie Anne took a keen personal interest in the collection she inherited. In 1907, she made a detailed inventory of each piece, noting from whom it was inherited and the important occasions on which it was worn. Many of these records were on small pieces of paper tucked into the boxes, according to Daniela Mascetti, former chairman of Sotheby's Jewellery Europe.

"Such detail was unusual because Marie Anne made these records herself instead of leaving them to an estate administrator to do," said Mascetti. "This shows the interest she took in the jewels."

The archduchess completed a second inventory of the collection in 1932, which chronicled how some of the pieces had been altered over the years. She died in 1940 at age 58, and her husband lived another 19 years. In the ensuing 60 years since his death, their direct descendants (numbering more than 120 family members) scattered throughout Europe. After the 1907 inventory, the collection remained mostly locked away for over a century, unknown to anyone outside the family.

Well over a decade prior to the auction, family members contacted Sotheby's to carry out a valuation for the collection. (The auction house would not provide specifics of the consignors because of client privacy agreements.)

"The family members were all part owners and widely scattered, so some of them felt they could no longer keep the collection together," said Mascetti (figure 5). Some, but not all. It took nearly a decade to convince all family members to sell. "It's a delicate process. You have to contact them at the right moment and not press them at the wrong time."

All the while, Sotheby's staff was at work producing valuations and sales estimates for each piece. After finally obtaining clearance from all of the family members who had a claim to the jewels, Sotheby's was nearly ready to begin cataloging the collection. Because of the detailed inventories, there was little doubt about the provenance of each piece. Sotheby's experts still had to research and verify each piece where possible because, with such history involved, prices would likely far exceed the value of the gemstones and gold. This process took nearly a full year.

As a tantalizing preview, Sotheby's offered the 6.16 ct Farnese Blue diamond, graded Fancy dark gray-blue by GIA, at its spring 2018 Geneva auction. The diamond took its name from Elisabeth Farnese (1692–1766), queen of Spain, wife of Philippe V, and a member of the Parma family before it became allied with the Bourbons. Inside the box with the diamond

Figure 5. Daniela Mascetti, Sotheby's former chairman of jewelry for Europe, holding the Royal Jewels from the Bourbon-Parma Family *catalog. The auction took place November 14, 2018. Photo by Russell Shor.*

was an engraved silver plaque that read (in French) "Remarkable blue brilliant. This historical stone was offered by the Philippine Islands to Elisabeth Farnese, Queen of Spain, wife of Philippe V, great grandfather of the Comte of Villafranca, current owner of that stone." Count of Villafranca was the title taken in 1849 by Charles II of Bourbon (Meylan, 2018). Sotheby's auctioned the diamond in May 2018 for US$6.7 million, against a presale estimate between $3.7 and $5.2 million (DeMarco, 2018).

Like the other Bourbon-Parma jewels, the Farnese Blue diamond had been handed down through the family to become part of the collection of Archduchess Marie Anne of Austria, which she noted in her 1907 inventory as being mounted on a tiara. Mascetti pointed out that the sale of this blue diamond

was unrelated to the Bourbon-Parma collection that took place six months later.

The royal jewels from the Bourbon-Parma collection, auctioned on November 14, 2018, consisted of 100 lots (see box A). The first 26 featured royal orders, badges, and medals presented to various family members from the 1770s to the 1930s. The middle of the sale offered jewelry items ranging from small wedding gifts to Elias and Marie Anne Bourbon-Parma to diamond tiaras and fancy-color diamonds owed by various royals in the Bourbon-Parma line. The final 10 lots consisted of items that had once belonged to Marie Antoinette.

CONCLUSIONS

Over the centuries, European royal families amassed large collections of gemstones and jewels, both for the state as crown jewels and for their personal adornment. Despite the dissolution of most European monarchies in the early twentieth century, gems and jewels with true royal provenance have occasionally come up for public sale, either kept by descendants, held in museums, or sold off privately. Even rarer have been large collections of jewels entering the market that can be traced directly to kings and queens. Among these were the 1795 sale of Madame du Barry's jewels, the 1887 auction of the French crown jewels, several pieces from Princess Margaret in 2006, and most recently the auction of 100 jewels and badges from the Bourbon-Parma family, which included 10 items that belonged to Marie Antoinette. The history behind these jewels—particularly those pieces connected to the ill-fated queen—caused prices to soar far beyond the value of the gems and gold.

BOX A: HIGHLIGHTS FROM THE 2018 BOURBON-PARMA AUCTION

Significant lots are summarized below, with Archduchess Marie Anne's 1907 inventory notes in quotation marks. All photos courtesy of Sotheby's.

Lot 48: Diamond earrings from the first half of the nineteenth century. "A pair of large diamond earrings (of girandole design), each composed of five large diamonds and three large drops. In a dark blue leather case. These earrings come from Marie Thérèse de Savoie, Duchess of Parma, wife of Duke Charles II of Parma, and given to her grandson, Robert I Duke of Parma." Sotheby's sold the pair for $730,000 against a presale estimate of $150,000 to $250,000.

Lot 65: A pair of late nineteenth-century ruby and diamond earrings, with an early twentieth-century ruby and diamond brooch. Each earring is set with a Burmese ruby, 4.52 and 5.05 ct, respectively. The brooch is set with a 23.76 ct Burmese ruby. "Ruby parure comprising a brooch set with a large ruby framed with large diamonds, and a pair of earrings, large rubies surrounded by large diamonds. Inheritance from my mother. From a sale of the Queen Isabelle of Spain." Sotheby's sold this set for $192,350 against a presale estimate of $150,000 to $250,000.

Lot 76: Diamond tiara by Köchert, ca. 1901, given to Archduchess Marie Anne in 1903. "A beige leather case with a small diamond tiara or bandeau by Köchert. This tiara was given by Emperor François Joseph as a wedding gift." Sotheby's sold this tiara for $248,000 against a presale estimate of $80,000 to $120,000.

**Lot 77:** An eighteenth-century diamond bow brooch. "Large diamond bow set with 7 largest diamonds (to be worn with the Order of the Starry Cross). Inheritance from my mother. From the estate of Archduchess Marie (Ranier). Formerly from the collection of Empress Marie Thérèse." The brooch sold for $186,000 against a presale estimate of $75,000 to $110,000.

Lot 79: A brooch with a 30.70 ct cushion-cut Ceylon sapphire surrounded by brilliant-cut diamonds, ca. 1900. "…a large sapphire framed with 12 nice diamonds. This brooch can be worn as the clasp of the large pearl necklace. This was given to me as a wedding gift by my mother, Archduchess Isabelle of Austria." Sotheby's sold the sapphire brooch for $551,000 against a presale estimate of $150,000 to $250,000.


Lot 80: A ruby and diamond brooch/hair ornament, ca. 1900. The 6.89 ct ruby is from Burma. "A white leather case with a large diamond bow, a large ruby at the centre (from Bachruch). This bow was a gift from my father for the birth of my son, Charles." Sotheby's sold the brooch for $372,000 against a presale estimate of $200,000 to $300,000.
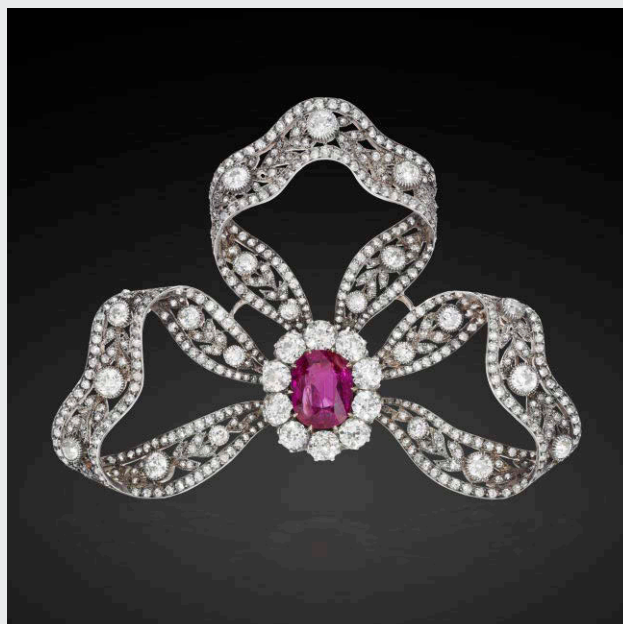
Lot 81: Ring, ca. 1909, featuring a 2.44 ct Fancy orangy pink diamond graded by GIA. Case stamped Schwartz und Steiner. "Given by Archduke Frédéric of Austria (1856–1936) to his daughter, Archduchess Marie Anne of Austria, Princess Elie de Bourbon Parme (1882–1940), on the occasion of the birth of her son, Robert, in 1909." Sotheby's sold the diamond for $575,000 against a presale estimate of $120,000 to $180,000.
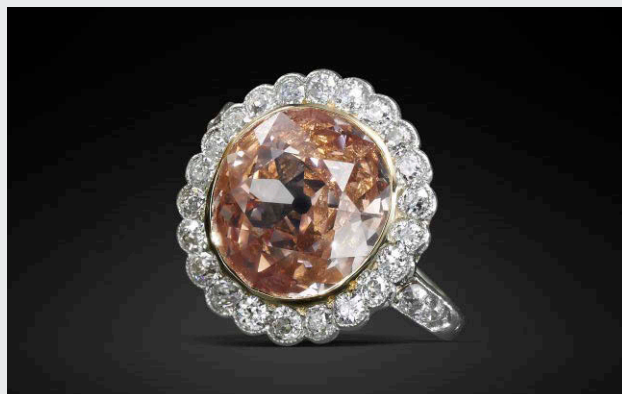
Lot 86: Three diamond pieces, including a diamond parure, comprising a slightly graduated diamond necklace of 40 cushion-shaped diamonds supporting 39 detachable pear-shaped diamond pendants. A brooch set with cushion-shaped diamonds and detachable pear-shaped diamonds. "A large diamond parure, in a dark blue velvet case, composed of two rows of diamonds, a row with drops, a brooch (13 diamonds including a very large one and three drops), a clasp (a large one and 10 smaller diamonds) and a pair of earrings. The parure comes from the sword of the Duke of Berry and was given by his daughter, Louis de France, Mademoiselle Duchess de Parme, to her son Robert I, Duc de Parme 15 March 1932: The diamonds of the first row, 38, and the clasp (large diamond framed with 10 smaller ones) are part of a large rivière with pendants. The 5 large diamonds (from Queen Marie Antoinette) and the pendant (large pear-shaped diamond, estate of my mother) can be worn independently."

   Sotheby's jewelry experts determined that the five diamonds the archduchess noted as coming from Marie Antoinette probably came from a tiara made for her daughter, Marie Thérèse de France (1778–1851). The Duke of Berry (Charles Ferdinand, 1776–1820) was a nephew of Louis XVI and brother-in-law of Marie Thérèse, Marie Antoinette's daughter. The duke was assassinated in 1820 by an opponent of the restoration of the French monarchy. The Duke of Berry's daughter, Louise, married the future Duke of Parma, Charles III, in 1845. For the wedding, the family took the diamonds from a sword owned by the duke. The five diamonds, which Henri presented to the Duke and Duchess of Parma as a wedding present in 1869, were taken from a very elaborate tiara that had come from Marie Thérèse after the restoration of the Bourbon monarchy in 1815. Four years later, Marie Thérèse petitioned her uncle, now King Louis XVIII, to keep the tiara. He allowed her to keep the frame but asked that the diamonds be removed and lodged in the French treasury since they had been part of the crown jewels. Later, the king provided the money to purchase replacement diamonds for the tiara, but they were again removed by his descendants to give as wedding presents. The original tiara frame was later acquired by Greek collector Dimitri Mavrommatis and sold at auction in 2008 (Meylan, 2018). Presale estimate $300,000–$500,000. Sale price $855,000.

Lot 88: A fleur-de-lis motif tiara set with cushion-cut, pear-shaped, rose-cut, and round diamonds, fashioned by Hübner of Vienna in May 1912. This piece was created for Archduchess Marie Anne five years after her 1907 inventory. The diamonds were taken from a large breast star, the Order of the Holy Spirit, worn by Charles X of France (1757–1836). The skeletal base for the breast star remained in the collection as well. The tiara sold for $968,000 against a presale estimate of $350,000 to $500,000. The skeletal frame of the Order sold for $40,000.

The final 10 lots in the sale came from Marie Antoinette's personal collection.

Lot 91: Late eighteenth-century diamond ring set with a miniature depicting Marie Antoinette and small, circular-cut diamonds. "A large ring with a miniature and diamonds. Miniature of Queen Marie Antoinette, according to the will of the Duchess d'Angoulême, Comtesse de Marnes…. The three rings [with lots 92 and 93] come from Queen Marie Antoinette and were given by her daughter, Madame la Duchesse d'Angoulême, Comtesse de Marnes, to her niece and adoptive daughter Louise de France, Duchesse de Parme, who then gave them to her son Robert I Duc de Parme." The ring sold for $248,000 against a presale estimate of $8,000 to $12,000.

Lots 92 and 93: Diamond and woven hair rings, eighteenth century. Enhanced with rose-cut diamond monogram MA for Marie Antoinette (92) and MD for Monseigneur le Dauphin, Louis de Bourbon (93). Lot 92: "Ring with hair and monogram (M.A. set with diamonds), hair of Queen Marie Antoinette." Lot 93 (not shown): "Ring with hair and monogram (M.D. set with diamonds) of Monseigneur Dauphin, Louis XVI's father."


The ring with a lock of the queen's hair, lot 92, sold for $444,000 against a presale estimate of $8,000 to $10,000. Lot 93 sold for $124,000 against a presale estimate of $8,000 to $10,000.

Lot 94: Blue and white enamel and seed pearl pocket watch, eighteenth century and later, opening to reveal a dial and Arabic numbers. "A red leather case containing a blue enamel and pearl watch which belonged to Queen Marie Antoinette, and coming from Duchess d'Angoulême (the movement was changed). This watch was given as a wedding gift by my husband, Prince Elie, who received it from his mother." The watch sold for $250,000 against a presale estimate of $8,000 to $10,000.

Lot 95: Double-ribbon diamond bow brooch from the second half of the eighteenth century featuring a yellow pear-shaped diamond pendant. "A scarlet red case, containing a diamond bow supporting a pendant set with a large yellow diamond, the bow was formerly part of the tiara or belt here above, and has the same provenance." The bow brooch sold for nearly $2.1 million, against a presale estimate of $50,000 to $80,000.
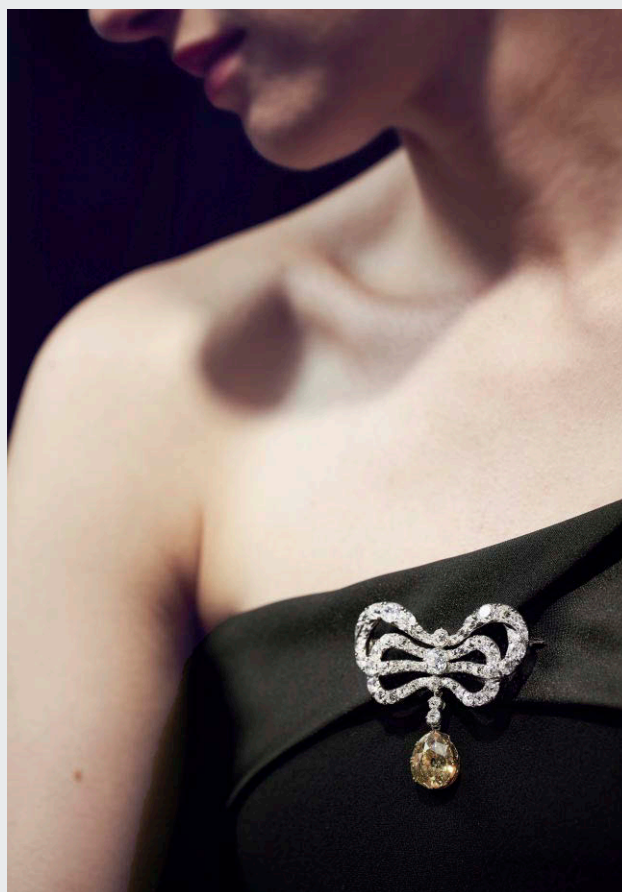
Lot 96: Diamond bow brooch, late nineteenth century, featuring a central cushion-shaped yellow diamond. The fitted leather case is stamped Hübner and has a crowned monogram M.A. for Marie Anne of Austria. "A dark red leather case with monogram M.A. containing a diamond bow, large yellow diamond at the centre. The stones are meant to come from the jewels of Marie Antoinette. (I have been told by my father-in-law but I could not find any written confirmation in the existing wills. This bow was probably a new jewel or it was part of a parure and was therefore not mentioned.) The bow was given to me as an engagement gift by my father-in-law, Duke Robert I de Parme." The diamond brooch sold for $273,000 against a presale estimate of $95,000 to $140,000.

Lot 97: Necklace consisting of three rows of slightly graduated natural pearls, approximately 7.30 to 9.30 mm. The clasp is set with cushion, circular, and rose-cut diamonds in a star motif. Length approximately 380 mm. These pearls were originally strung in a larger three-row necklace, together with lots 98 and 100, that belonged to Marie Antoinette (see Archduchess Marie Anne's 1907 inventory notes for lot 100). The pearl necklace sold for $2.278 million against a presale estimate of $200,000 to $300,000.

Lot 98: Single-strand necklace of slightly graduated natural pearls ranging from 7.30 to 9.40 mm. Cushion-shape diamonds adorn the detachable clasp. Length approximately 380 mm. These pearls originally were strung in a three-row pearl necklace, together with lots 97 and 100, that belonged to Marie Antoinette. The single-strand pearl necklace sold for $444,000 against a presale estimate of $40,000 to $70,000.

Lot 99: Late eighteenth century pair of natural pearl and diamond pendant earrings. The upper portions feature button-shaped natural pearls measuring approximately 12.65 × 12.95 × 15.60 mm and 12.95 × 13.10 × 16.00 mm, respectively. Below them are detachable pendants set with oval pearls measuring approximately 10.50 × 10.50 × 8.55 mm and 10.15 × 10.20 × 7.70 mm, respectively, capped with rose-cut diamonds, and a pinched collet-set cushion-shaped diamond. The hook and hinge back fittings were added in the early nineteenth century. "This parure comes as it is from Queen Marie Antoinette and was inherited by Marie Thérèse de France, Duchess d'Angoulême, Countesse de Marne, then to her niece and adoptive daughter, Louise Marie Thérèse de France, Mademoiselle Duchesse de Parme." The earrings sold for $444,000 against a pre-sale estimate of $200,000 to $300,000.

Lot 100: The final piece was Marie Antoinette's pendant featuring a slightly baroque drop pearl (15.90 × 18.35 × 25.85 mm), probably found in the Persian Gulf, attached below a diamond-set bow with an oval-cut diamond of about 5 ct. "A large drop with a small diamond bow and a large diamond. The drop was originally, together with the diamond bow, part of the third row of large pearls. The diamond was originally the clasp of the large necklace… This parure comes as it is from Queen Marie Antoinette and was inherited by Marie Thérèse de France, Duchess d'Angoulême, Countesse de Marne, then to her niece and adoptive daughter, Louise Marie Thérèse de France, Mademoiselle Duchesse de Parme."

David Bennett, chairman of Sotheby's international jewelry division at the time, began the auction of the pendant at 900,000 Swiss francs. Bidding proceeded methodically up to 6.5 million francs. However, a buyer on the telephone put in a bid of US$29 million, and then another bidder in the room quickly escalated it past US$30 million to the final bid of US$32 million, where Bennett brought the hammer down to the applause of the room. The winner, noted as a private European buyer, paid a total price of 36 million francs (US$36.1 million), after the auction house commission. The presale estimate was $1 million to $2 million (Shor, 2018). (At the time of the auction, the U.S. dollar and Swiss franc were nearly equal.)

REFERENCES

The affair of the diamond necklace, 1784-1785 (2017) Chateau de Versailles, http://en.chateauversailles.fr/discover/history/key-dates/affair-diamond-necklace-1784-1785

Alderson A. (2006) Queen urges Margaret's heirs to avoid another royal gift scandal. *The Telegraph*, June 11, https://www.telegraph.co.uk/news/uknews/1520956/Queen-urges-Margarets-heirs-to-avoid-another-royal-gift-scandal.html

Brus R. (2011) *Crown Jewellery and Regalia of the World*. Pepin Press, Amsterdam, p. 28.

Bycroft M., Dupré S. (2019) Introduction: Gems in the early modern world. In M. Bycroft and S. Dupré, Eds., *Gems in the Early Modern World: Materials, Knowledge & Global Trade, 1450–1800*. Palgrave-Macmillan, London, pp. 1–33.

Christie's (1795) Jewels of Countess du Barry. Auction catalog, February 19.

Christie's (2006) *Jewellery and Faberge from the Collection of HRH The Princess Margaret, Countess of Snowden*, https://www.christies.com/jewellery-and-faberge--20703.aspx?saletitle=)

Christie's (2017) Le Grand Mazarin, the diamond in the crown, https://www.christies.com/features/Le-Grand-Mazarin-Diamond-in-the-Crown-8625-3.aspx

DeMarco A. (2018) Farnese Blue diamond fetches $6.7 million but two white diamonds top all sales. *Forbes*, May 15, https://www.forbes.com/sites/anthonydemarco/2018/05/15/farnese-blue-diamond-fetches-6-7-million-but-two-white-diamonds-top-all-sales/#44016fb64ef7

The diamond necklace affair (2009) Marie Antoinette Online, January 10, https://www.marie-antoinette.org/articles/diamond-necklace/

Dutch East Indian Company, trade network, 18th century (2017) The Geography of Transport Systems, https://transportgeography.org/?page_id=1089

Fasel M. (2019) When and why the French sold the crown jewels. *The Adventurine*, https://theadventurine.com/culture/jewelry-history/when-and-why-the-french-sold-the-crown-jewels/

Fersman A.E. (1925-1926) *Russia's Treasure of Diamonds and Precious Stones*. The People's Commissariat of Finances, Moscow.

The French crown jewels; opening of the auction sale in Paris (1887) *The New York Times*, May 13, https://www.nytimes.com/1887/05/13/archives/the-french-crown-jewels-opening-of-the-auction-sale-in-paris-ten.html

French outbid all for Czar's jewels (1926) *The New York Times*, February 23, https://timesmachine.nytimes.com/timesmachine/1926/02/23/100052090.html?action=click&contentCollection=Archives&module=ArticleEndCTA&region=ArchiveBody&pgtype=article&pageNumber=1

Lunel J.M. (2017) My highlight of 2017 – Le Grand Mazarin. https://www.christies.com/features/2017-highlight-The-Grand-Mazarin-8780-1.aspx

McCanless C.L., Wintraecken A. (2010) Fersman portfolio – Fabergé jewels – Nuptial crown. *Faberge Research Newsletter*, Fall, https://fabergeresearch.com/newsletter-2010-fall/

Meylan V. (2016) *Christie's: The Jewellery Archives Revealed*. ACC Art Books, Woodbridge, UK, pp. 19–26.

——— (2018) Queen Marie Antoinette's Jewels. In *Royal Jewels from the Bourbon-Parma Family*, Sotheby's catalog, November 14.

Morel B. (1988) *The French Crown Jewels*. Fonds Mercator, Antwerp, Belgium.

Ogden J. (2009) England's largest diamond. *Gems & Jewellery*, Vol. 18, No. 2, pp. 30–33.

——— (2017) Camels, courts and financing the French Blue diamond: Tavernier's sixth voyage. *Journal of Gemmology*, Vol. 35, No. 7, pp. 640–650.

——— (2018a) *Diamonds: An Early History of the King of Gems*. Yale University Press, New Haven, CT.

——— (2018b) Out of the blue: The Hope diamond in London. *Journal of Gemmology*, Vol. 36, No. 4, pp. 316–331.

Prince Michael of Greece (1983) *Crown Jewels of Europe*. Harper & Row, Cambridge, UK.

Royde-Smith J.G. (2019) House of Bourbon. *Encyclopædia Britannica*. https://www.britannica.com/topic/house-of-Bourbon

Sevillano-Lopez D., Gonzalez F.J. (2011) Mining and minerals trade on the Silk Road to the ancient literary sources: 2 BC to 10 AD centuries. In J. E. Ortiz, O. Puche, I. Rábano and L. F. Mazadiego, Eds., *History of Research in Mineral Resources*. Instituto Geológico y Minero de España, Madrid, pp. 43–60.

Shor R. (2004) *The New Moghuls: The Remarkable Story of India's Diamond People*. Publ. by the author, pp. 9–20.

——— (2013) Auction houses: A powerful influence on major diamonds and colored gemstones. *G&G*, Vol. 49, No. 1, pp. 2–15, http://dx.doi.org/10.5741/GEMS.49.1.2

——— (2018) Marie Antoinette's jewels: How can you put a price on such history? https://www.gia.edu/gia-news-research/marie-antoinettes-jewels-how-can-you-put-price-history, December 7.

——— (2019) Spring 2019 auctions: Premium prices for historic pieces, https://www.gia.edu/gia-news-research/spring-2019-auctions-premium-prices-historic-pieces, June 14.

Sotheby's (2018) *Royal Jewels from the Bourbon-Parma Family*. Auction catalog, November 14.

Truong A.R. (2017) Le Grande Mazarin. An historic coloured diamond, October 29, http://www.alaintruong.com/archives/2017/10/29/35816152.html

Twining E.F. (1960) *A History of the Crown Jewels of Europe*. B.T. Batsford Ltd., London.

——— (1967) *European Regalia*. B.T. Batsford, London.

Vachandez C. (2018) An introduction. Jewels from the Bourbon-Parma family. In *Royal Jewels from the Bourbon-Parma Family*, Sotheby's catalog, November 14.

Unique Raindrop Pattern of Turquoise from Hubei, China

Ling Liu, Mingxing Yang, and Yan Li

"Raindrop" turquoise is a recently recognized and characterized pattern with a saturated coloration resembling raindrops. This material is very rare but popular in the Chinese gem trade. This paper investigates the differences among the raindrops, veins, and substrates (the matrix portion) of turquoise with this unique pattern using X-ray diffraction, electron probe micro-analysis, laser ablation–inductively coupled plasma–mass spectrometry, and micro-spectroscopic techniques (Raman, FTIR, and UV-Vis). The raindrops and veins were identified as mixtures of turquoise and fluorapatite, which were distinct from the substrates. Nearly pure fluorapatite and turquoise were also discovered in the veins. The color origin of the brownish yellow raindrops and substrates are discussed, as well as the formation mechanism of the raindrop pattern.

T urquoise has been widely used in jewelry and artifacts because of its attractive color. It has a very long history and has played a crucial role in various cultures worldwide (Khazeni, 2014; Kostov, 2019), such as ancient Egypt (Mansour, 2014), Iran (Beale, 1973; Ovissi et al., 2017), Mexico, and the Americas (Harbottle and Weigand, 1992; Weigand and Harbottle, 1993; Hedquist, 2016). Turquoise was used even earlier in Eurasia, between 8000 and 7000 BCE (Kostov, 2019). Turquoise is also closely interwoven with Chinese culture and civilization (Hao and Hao, 2002). Archaeologists proved that the Chinese used it for decoration in Peilligang culture beginning in the Neolithic age (Pang, 2014). The earliest turquoise artifacts in China were found at the Jiahu site in Wuyang County, Henan Province, and traced back to 7000–5800 BCE (Zhang and Pan, 2002; Yang et al., 2017). Their origin has not been confirmed yet (Feng et al., 2003; Mao et al., 2005; Wang et al., 2007). Throughout the long development of Chinese culture and history, turquoise has been endowed with abundant connotations and functions related to political, decorative, economic, and religious aspects. It has always been regarded as a unique and precious gemstone in China, especially in Tibet and Inner Mongolia. Turquoise artifacts not only recorded the development of human society but also reflected exchanges between cultures.

Researchers have succeeded in developing methods of origin traceability of turquoise in the southwestern United States and northern Mexico using hydrogen and copper isotopes (Hull et al., 2008; Hull and Fayek, 2012; Hull et al., 2014) as well as lead and strontium isotopes (Thibodeau et al., 2012; Thibodeau et al., 2015; Thibodeau et al., 2018) to identify the source of turquoise artifacts. Similar approaches were applied to investigate the turquoise artifacts from different regions of China (Ye et al., 2014; Li et al., 2018; Xian et al., 2018).

Turquoise deposits are widespread in China, including Zhushan County (Chen et al., 2012) in Hubei Province; the cities of Ma'anshan (Chen and Qi, 2007) and Tongling (Zuo et al., 2018) in Anhui Province, Baihe County (Shi and Cai, 2008; Zhao et al., 2017) and the city of Shangluo (Luo et al., 2017) in Shanxi Province, Xichuan area of Henan Province (Zhou and Jiang, 2005); and the city of Kumul (or Hami in Chinese) in Xinjiang Uyghur Autonomous Region (Luan, 2001; Liu et al., 2018). Numerous detailed characteristics of turquoise from these locations have been reported in recent years, including its spectra, structure, and chemical and mineral compositions (Chen and Qi, 2007; Chen et al., 2012; Luo et al., 2017; Zhao et al., 2017; Liu et al., 2018; Xian et al., 2018; Zuo et al., 2018; Li et al., 2019; Liu et al., 2019a).

However, Hubei Province is the largest commercial source in the world. Turquoise (a supergene mineral) from this province occurs mainly in the carbon-bearing siliceous rocks, siliceous rocks, and schist of the Lower Cambrian (Tu, 1996). Rich phosphate, iron, and copper
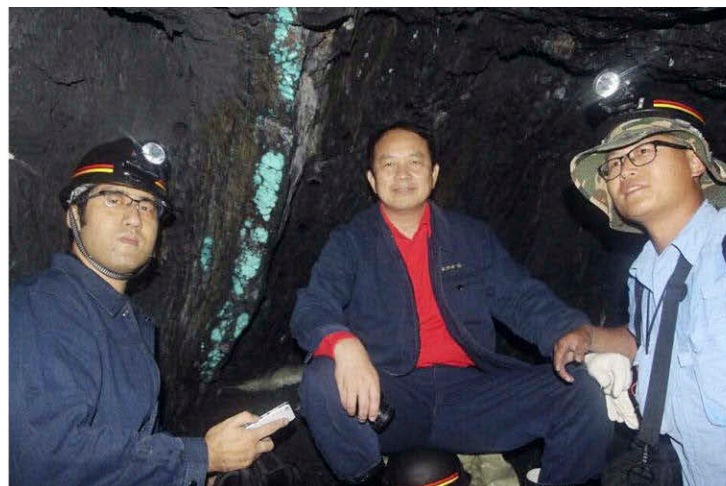
Figure 1. Massive blue turquoise from the mine in Zhushan County, Hubei Province. Photos by Mingxing Yang.

ores are the main sources for turquoise formation (Tu, 1997a). Most of the rough turquoise mined from these deposits is surrounded by black rocks that easily distinguish them from those mined in other locations. In 2015, a massive blue rough turquoise, together with its enclosing rocks weighing more than 11 tons, was extracted in Zhushan County, Hubei Province (figure 1). Consequently, miners had to divide it into two parts to transfer them out of the mine. The mines located in Hubei Province have produced many high-quality (fig-

In Brief

- Currently, about 70% of the turquoise in the Chinese gem trade is sourced from Hubei Province, China, where many different types have been mined.

- Nondestructive and microanalytical techniques were effectively employed to characterize a special raindrop pattern in turquoise.

- The raindrops and substrates are of different mineral assemblages, with Ca and F enrichment from the presence of fluorapatite in the raindrops.

ure 2) and unique turquoise with special patterns (detailed in box A) that were interpreted in Turquoise Grading, National Standard of the People's Republic of China, GB/T36169-2018 (see He et al., 2018).

In China, rough turquoise was traditionally treated with wax, resin, or polymers due to its high porosity. However, Chinese consumers prefer natural turquoise rather than artificially treated and syn-

thetic counterparts. Thus, resin and polymer treatments are not as acceptable in the Chinese turquoise trade or as common as in the past. The most popular treatment is "porcelain enhancement," designed to improve the compactness, densification, and luster of turquoise. Its key techniques are still confidential and not publicly available. The identification characteristics of this porcelain-enhanced turquoise and the fillers used were investigated by Deng et al. (2019) and Liu et al. (2019b).

Recently, the authors discovered a particular surface pattern of turquoise (figure 3, A–C) in the Hubei market. Material with this pattern displays blue and blue-green color spots resembling raindrops, occasionally accompanied by veins (figure 3, B and C). This pattern is called "raindrop" turquoise in the trade.

Researchers have made great effort to investigate gem turquoise's gemological and mineralogical characteristics (Abdu et al., 2011; Chen et al., 2012; Čejka et al., 2015; Rossi et al., 2017), color origin (Zhang et al., 1982; Luan et al., 2004; Reddy et al., 2006), and concentration of trace elements and rare earth elements (Wang et al., 2007; She et al., 2009; He et al., 2011; Rossi et al., 2017; Shirdam and Aslani, 2017). Additionally, the identification characteristics of treated and imitation turquoise have drawn many researchers' attention (Moe et al., 2007; Krzemnicki et al., 2011; Bernardino et al., 2016; Schwarzinger and Schwarzinger, 2017; Xu and Di, 2018; Liu et al., 2019b). However, previous research has paid little attention to this unique raindrop pattern. The authors collected samples displaying this pattern to investigate their gemological and mineralogical characteristics.

Figure 2. A variety of high-quality turquoise products from Hubei Province. A: An 18.5 kg polished ornament. B: An exquisite 0.96 kg carving. C: A 13.9 g carved pendant. D: A 24 g turquoise bead with raindrop pattern. Photos by Ling Liu (A–C) and courtesy of Fei Huang (D).

MATERIALS AND METHODS

Specimens. Three representative specimens of raindrop turquoise were collected from the Hubei market, chosen for the color of the raindrops and the presence of veins. Local gem dealers informed the authors that the raindrop turquoise was mined in Zhushan. Specimens B-1 and B-2 were medium greenish blue and blue, respectively, while specimen B-3 was multicolored, including yellowish green, brownish yellow, and brownish red (figure 4). Specimens B-2 and B-3 contained veins in addition to raindrops, whereas specimen B-1 contained only raindrops.

Figure 3. A: Examples of "raindrop" turquoise from Hubei Province, China (left to right: 0.70 g, 3.32 g, and 3.88 g). B and C: Saturated raindrops of various sizes, as well as veins distributed in the substrates. Photos by Ling Liu; fields of view 3.2 mm (B) and 3 mm (C).
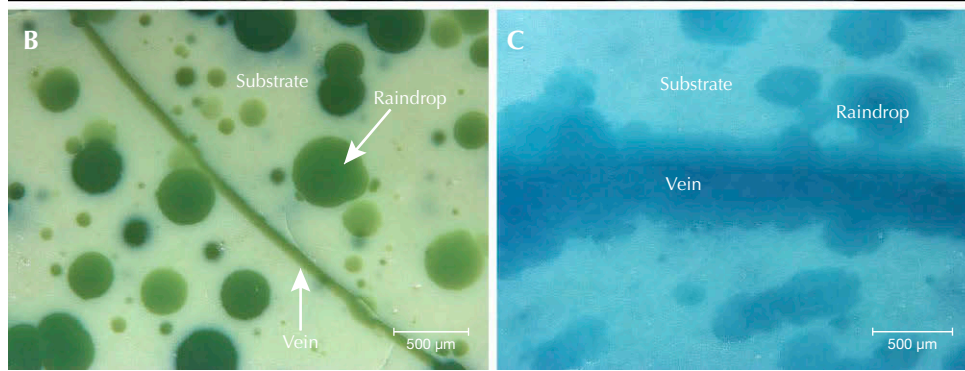
Standard Gemological Testing. Specific gravity of the three specimens was determined hydrostatically. All three specimens were tested for fluorescence reactions under short-wave (254 nm) and long-wave (365 nm) UV. Microscopic observations were performed with a Leica M205A at the Gemmological Institute, China University of Geosciences, Wuhan.

X-Ray Diffraction (XRD). XRD analysis was performed on a micro X-ray diffractometer (Rigaku Rapid IIR) using a collimator 0.1 mm in diameter and Cu-Kα radiation at a voltage of 40 kV and current of 250 mA with a scan step size of 1°/second. The XRD data obtained was analyzed by MDI Jade5.0 software (Materials Data, Inc., Livermore, California). Micro

Figure 4. Three specimens of raindrop turquoise from this study. Shown from left to right are specimens B-1 (1.84 g), B-2 (2.91 g), and B-3 (6.61 g). Photos by Ling Liu.

Box A: Unique Patterns of Turquoise from Hubei Province

Growth layer pattern: A pattern in which the regular color-zoning bands of turquoise resemble water ripples (Ku and Yang, 2021) (see image A in figures A-1 and A-2).

Raindrop pattern: A rare turquoise pattern with a distribution of numerous drop-shaped spots (image B in figures A-1 and A-2).

Spiderweb pattern: This type has fine and uniform black net veins, usually referred to as "iron lines" in Chinese, that resemble a spiderweb (image C in figures A-1 and A-2). Spiderweb turquoise can display a wide range of color, including light to deep blue, green-blue, and green.

Tang tricolor pattern: A term used to describe multicolored turquoise with typically blue, green, and yellow colors (image D in figures A-1 and A-2). The term was originally applied to a kind of multicolored glazed pottery prevalent in the Tang Dynasty (Yu and Zhang, 1994; Zhang, 2008; Ma et al., 2014).

Ulan flower pattern: An extremely valuable subtype of spiderweb turquoise. It shows similar uniform black net veins but possesses a much deeper and more saturated blue color ("Ulan") (image E in figures A-1 and A-2). "Flower" refers to the pattern formed by the fine black veins.

Water grass vein pattern: The iron lines of this turquoise resemble waterweeds (image F in figures A-1 and A-2).
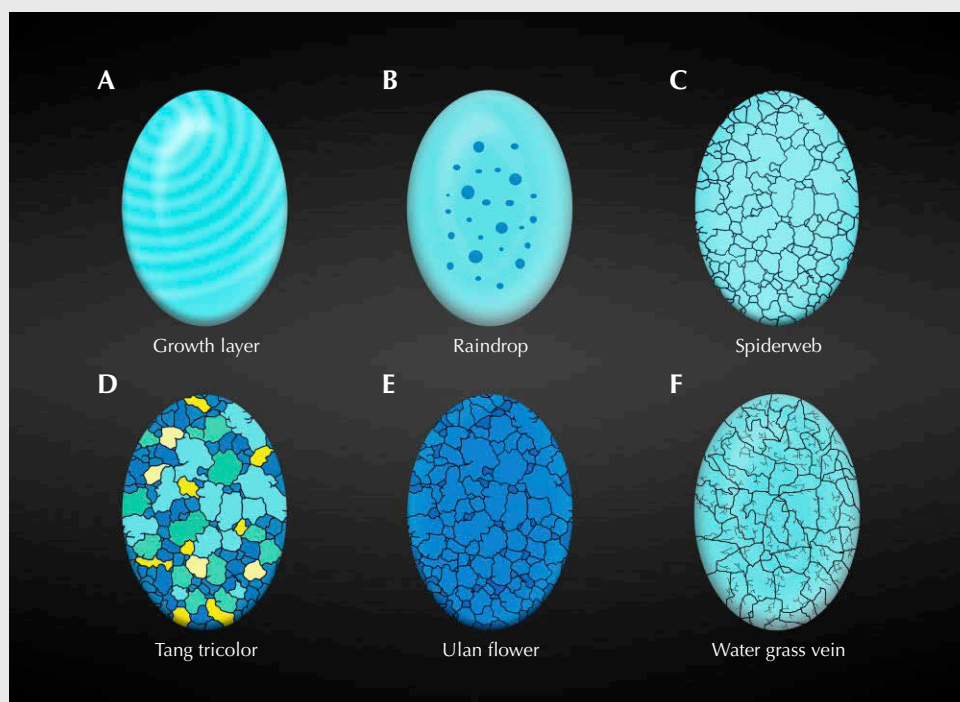

Figure A-1. Schematic of turquoise patterns. Illustrated by Ling Liu.

XRD is a nondestructive technique to characterize a mineral's crystalline structure for phase identification and quantification. Each mineral has its own characteristic diffraction angles and intensities, and the microstructural parameters can be provided by interpretation of the XRD pattern (Lavina et al., 2014).

Electron Probe Micro-Analyzer. Backscattered electron (BSE) imaging and electron probe micro-analysis (EPMA) were carried out by a JEOL JXA-8230 on differently colored areas of two specimens (B-2 and B-3). BSE imaging can reveal differences in the components according to the brightness displayed, since the contrast is determined by the mean atomic number Z or chemical composition of the studied sample. It can also display the topographical contrast, but its resolution is poorer than that of secondary electron images. Thus, EPMA was performed and BSE images were generated to investigate the composition variation of the raindrops and substrates. The operating conditions were: 15 kV accelerating voltage, 20 nA cup current, and a 1-micron beam diameter. A series of natural and synthetic standards was utilized for
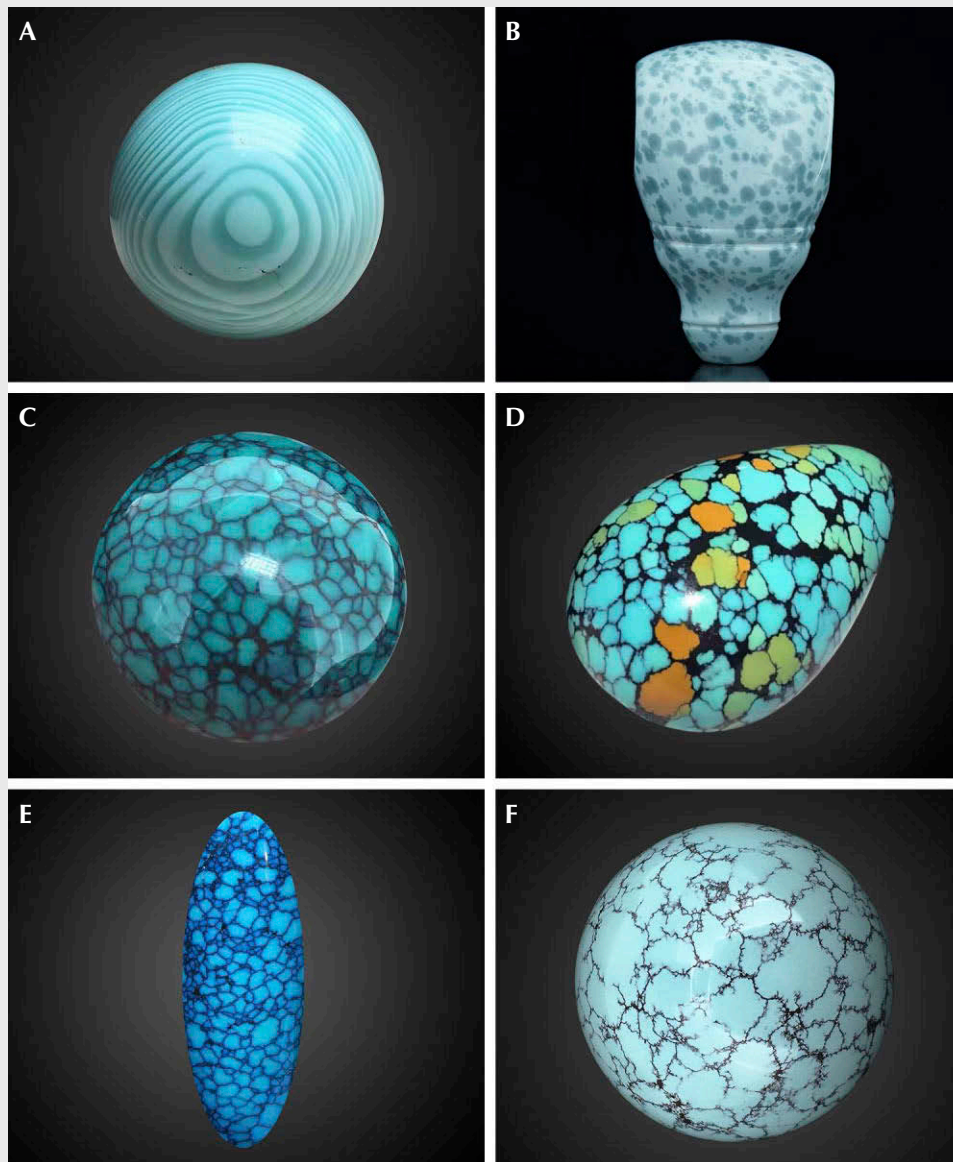
Figure A-2. Turquoise patterns from Hubei Province: growth layer (A), raindrop (B), spiderweb (C), Tang tricolor (D), Ulan flower (E), and water grass vein (F). Photos by Ling Liu (B, C, and F); courtesy of Jiang Li (A), an anonymous jewelry dealer (D), and Mingxing Yang (E).

calibration (i.e., apatite for P, magnetite for Fe, orthoclase for Si and K, pyrope for Al and Mg, diopside for Ca, jadeite for Na, sphalerite for Zn, and chalcopyrite for Cu). Raw X-ray intensities were corrected using a ZAF algorithm (Schiffman et al., 2013). Compositional ranges and mean values of the tested substrates, raindrops, and veins were reported.

Spectroscopy. Micro-Raman spectroscopy (Bruker Optics Senterra R200L) was utilized with a 532 nm laser, an aperture of 50 µm, and spectral resolution of 9–15 cm^{-1}. The laser power was 20 mW, and 10 scans were set with a 5 s integration time for each scan. Baseline correction was performed with OPUS spectroscopic software (Wartewig, 2003). Raman spectra were normalized to the intensity of the ~1041 cm^{-1} band. Fourier-transform infrared (FTIR) spectra were recorded in the 400–4000 cm^{-1} range by a Bruker Optics Hyperion 3000 micro-infrared spectrometer with 64 scans and 4 cm^{-1} spectral resolution. Data were smoothed and Kramers-Kronig transformed using OPUS spectroscopic software. FTIR spectra were normalized to ~1112 cm^{-1}. Micro-ultraviolet-visible spectroscopy (Jasco MSV-5200)
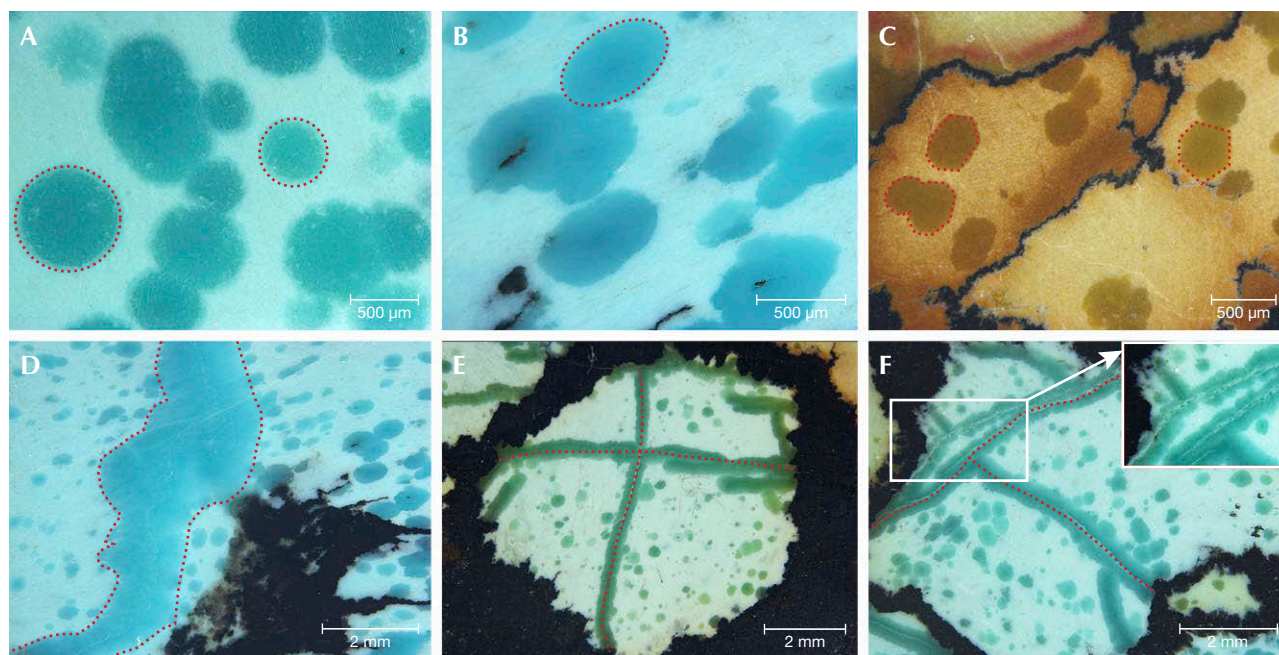
Figure 5. Various shapes of the raindrops and veins, outlined with red dashed lines for clarity. A–C: Round, nearly elliptical, and hexagonal raindrops. D: Curved vein. E and F: Two straight veins crossed in "X" and "Y" patterns. An inset image of whitish cracks at the center of veins is shown in figure F. Photos by Ling Liu.

was performed on different color areas using an aperture of 50 μm, medium response, and a scan speed of 200 nm/min with the photometric mode of %R. The UV-Vis and NIR bandwidths were 5.0 nm and 20.0 nm, respectively. Spectra were carried out from 200 to 850 nm with a data interval of 0.2 nm.

Laser Ablation–Inductively Coupled Plasma–Mass Spectrometry (LA-ICP-MS). Some color-causing transition metal and other trace elements were analyzed by LA-ICP-MS (Agilent 7700e) combined with a GeolasPro laser ablation system consisting of a COMPexPro 102 ArF excimer laser (wavelength of 193 nm and maximum energy of 200 mJ) and a MicroLas optical system. Analytical conditions were as follows: a 44 μm diameter laser spot size, laser frequency of 6 Hz, 80 mJ laser energy, and an energy density of 5.5 J/cm^2. NIST glass standard SRM 610 and USGS glass standards BHVO-2G, BCR-2G, and BIR-1G were used for external standardization. Due to the lack of a phosphate standard, a specimen of turquoise, the element homogeneity and stability of which was evaluated, was selected as a measurement standard (not a calibration standard) to monitor the drift of the instrument and ensure the quality of the data in the whole experiment.

RESULTS

Gemological Properties. The SG values of the three specimens ranged from 2.59 to 2.67 (table 1). The substrates of the specimens were all opaque, while the raindrops and veins appeared slightly translucent. The luster of the raindrops was glassy, while that of the substrate was waxy. However, the luster of the brownish yellow raindrops and substrate was earthy (dull) in this study. All three specimens exhibited medium to strong yellowish green fluorescence under long-wave UV radiation but weak yellowish green fluorescence under short-wave UV. In addition, the scratch hardness of the raindrops and veins was relatively higher than that of the substrates.

Morphological Characteristics. Most of the saturated raindrops of the turquoise specimens were isolated or in clusters. The raindrops displayed approximately round, elliptical, and hexagonal shapes under magnification (figure 5, A–C), ranging from 0.1 to 0.8 mm in length. The boundaries between raindrops and lighter-colored substrates were clear. Furthermore, the saturated veins with different sizes (0.4–2.8 mm in width) occurred in specimens B-2 and B-3 (figure 5, D–F). The veins were typically curved but sometimes nearly straight. The appearance of the veins and raindrops

TABLE 1. Standard gemological properties of the studied turquoise specimens.

Property		B-1	B-2	B-3
SG		2.66	2.59	2.67
Transparency		Opaque	Opaque	Opaque
Luster		Waxy to glas	Waxy to glassy	Glassy to earthy
Fluorescence under UV radiation	LW	Medium to strong yellowish green	Medium to strong yellowish green	Medium to strong yellowish green
	SW	Weak yellowish green	Weak yellowish green	Weak yellowish green

was extremely similar in terms of color, luster, and transparency. When one vein was interspersed by the other, they formed an "X" or "Y" shape (figure 5, E–F). The veins often had a whitish crack at the center (figure 5F, inset). In addition, black irregular veins and patches, often the primary indications of turquoise from around Hubei Province, were noticeable in specimens B-2 and B-3 (again, see figure 4).

X-Ray Diffraction. All specimens were identified as predominantly turquoise by the XRD patterns of the substrates. However, the diffraction patterns of the veins and raindrops had some differences from those of the substrates. The diffraction patterns of the veins and raindrops showed additional diffraction lines that were easy to distinguish from those of turquoise, especially in a vein of sample B-3 (figure 6). These strong lines aligned well with the diffraction lines of the mineral fluorapatite (http://rruff.info/R050529). Therefore, the XRD patterns demonstrated that the veins and raindrops were both composed of turquoise and fluorapatite. The intensity of the fluorapatite diffraction lines varied when XRD was performed on different areas of the veins and raindrops, indicating that their relative proportions of turquoise and fluorapatite also varied.
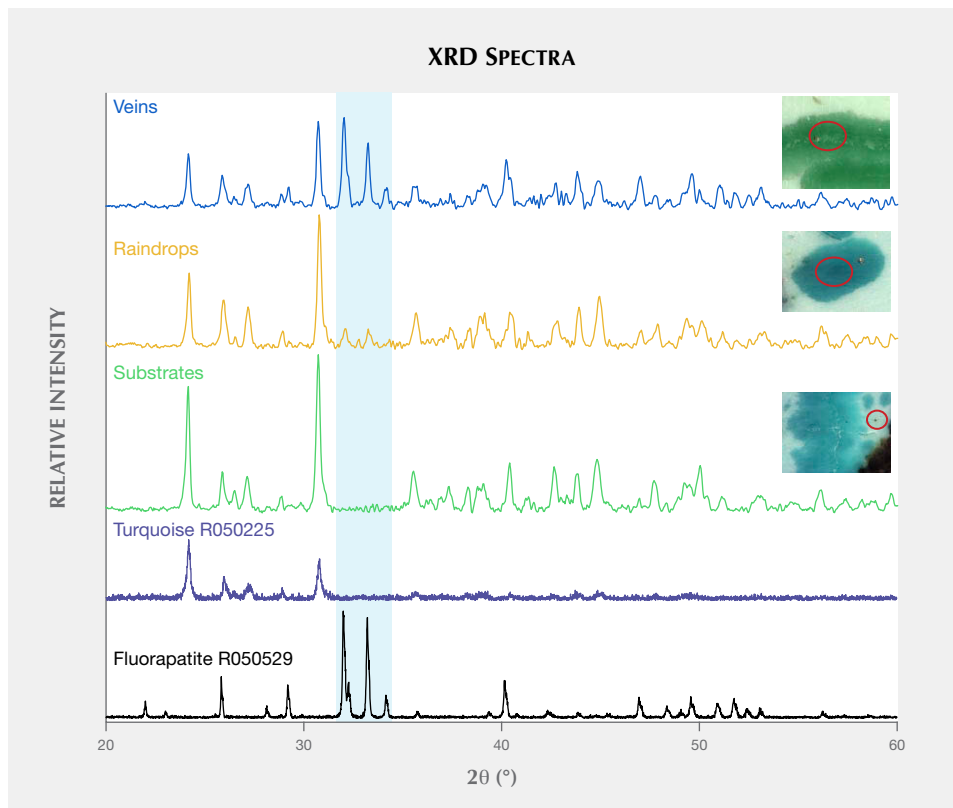

Figure 6. Comparative XRD patterns of the veins, raindrops, and substrates stacked for clarity, with XRD patterns of standard turquoise (http://rruff. info/R050225) and fluorapatite (http://rruff.info/ R050529) included for comparison. Note that additional diffraction lines belonging to the mineral fluorapatite were observed in the XRD patterns of the raindrops and veins.
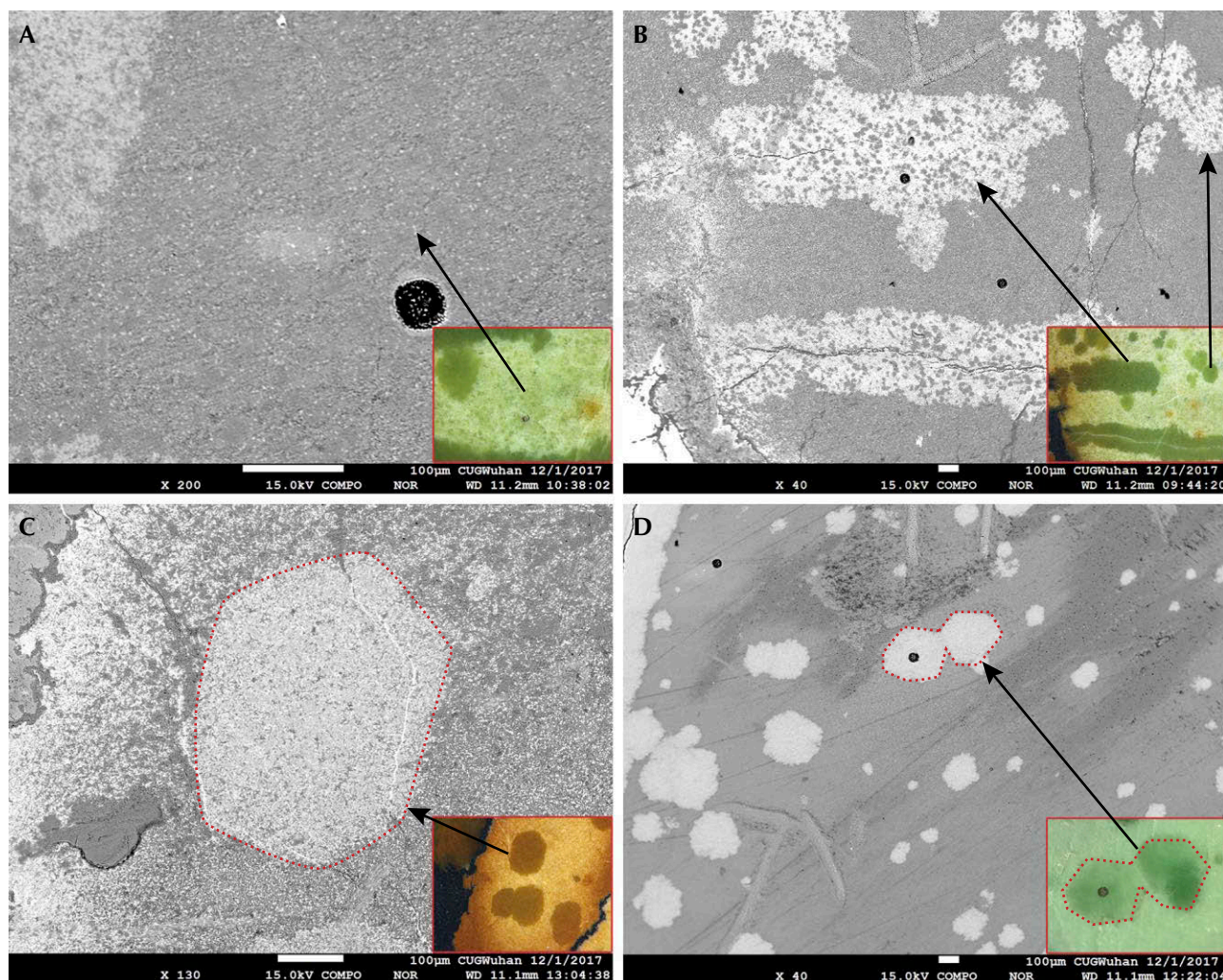
Figure 7. Backscattered electron images showed differences in chemical composition, as indicated by the darker substrate areas (A) and the brighter areas corresponding to raindrops and veins (B, C, and D). C: Individual hexagonal raindrops. D: Conjoined hexagonal raindrops. The black rounded dots in images A, B, and D are laser ablation craters. Photos by Ling Liu; fields of view: 0.6 mm, 3 mm, 0.9 mm, and 3 mm.

Backscattered Electron Imaging. The substrates were dark overall but showed tiny bright grains when examined under high-contrast BSE imaging (figure 7A). However, the raindrops and veins (figure 7B) tended to be brighter than the substrates in specimens B-2 and B-3. There were still numerous small dark grains unevenly distributed in the raindrops and veins (figure 7B), and the gray value of these dark grains was similar to that of the substrates. Meanwhile, some individual or adjacent raindrops were approximately hexagonal in shape, similar to the habit of apatite, under high-contrast BSE imaging (figure 7, C and D). The difference in gray value between the raindrops and the substrates revealed a difference in their min-

eral phases. The gray values of the raindrops and veins were comparable, indicating a similar chemical composition.

Chemical Composition. Quantitative chemical compositions of the substrates, raindrops, and veins, obtained by EPMA and LA-ICP-MS, are summarized below and in tables 2 and 3, respectively.

Substrates. The major components of the substrates (the blue, yellowish green, brownish yellow, and light green areas in samples B-2 and B-3) were Al_2O_3 (27.11–37.981 wt.%), P_2O_5 (26.446–31.791 wt.%), and CuO (5.615–6.636 wt.%). The real content of major

components was slightly inconsistent with those of ideal turquoise, which has a chemical formula of [$CuAl_6(PO_4)_4(OH)_8 \cdot 4H_2O$] (Foord and Taggart, 1998; Čejka et al., 2015). The substrates also contained SiO_2 and FeO, in addition to Al_2O_3, P_2O_5, and CuO. The contents of SiO_2 and FeO were relatively high in several of the testing areas, ranging from 0.252 wt.% to 14.288 wt.% for SiO_2 and from 2.274 wt.% to 19.586 wt.% for FeO. The enrichment of SiO_2 in the substrates of all samples might result from the substitution of P by Si in the turquoise structure and the existence of clay minerals (e.g., kaolinite). Clay minerals often occur together with turquoise (Tu, 1996; Huang, 2003; Abdu et al., 2011). Trace element data of the substrates demonstrated that V (86.0–810 ppm), Ni (44.0–1458 ppm), and Mo (0.71–2124 ppm) had a wide range of concentrations (table 3). The brownish yellow substrate resulted in the high contents of V (810 ppm), Ni (1458 ppm), and Mo (2124 ppm). The substrates contained abundant Ba (570–626 ppm) but low Sr (9.61–17.2 ppm) and U (4.53–16.6 ppm).

TABLE 2. Compositional ranges and mean values of the substrates, raindrops, and veins by EPMA.

Oxides (wt.%)	Substrates (5 spots) Min-Max (avg.)	Raindrops[a] (5 spots) Min-Max (avg.)	Veins[a] (4 spots) Min-Max (avg.)	Turquoise Ideal (Čejka et al., 2015)	Detection limits Min-Max
SiO_2	0.252–14.288 (6.585)	0.864–4.000 (1.954)	0.922–1.752 (1.287)		0.025–0.031
Al_2O_3	27.11–37.981 (35.042)	24.058–27.919 (26.824)	24.163–29.165 (27.645)	37.60	0.019–0.022
P_2O_5	26.446–31.791 (28.632)	33.096–34.813 (33.959)	32.488–34.498 (33.686)	34.90	0.021–0.026
CuO	5.615–6.636 (6.333)	5.436–6.644 (6.087)	5.6–6.701 (6.258)	9.78	0.036–0.040
FeO[b]	2.274–19.586 (6.064)	1.694–4.481 (2.765)	1.647–2.211 (1.935)		0.028–0.037
CaO	0.162–0.587 (0.347)	8.487–14.747 (10.355)	8.023–14.354 (9.882)		0.016–0.019
K_2O	0.013–0.048 (0.027)	bdl–0.02 (0.014)	bdl–0.022 (0.0163)		0.012–0.013
Na_2O	0.029–0.049 (0.04)	0.025–0.069 (0.039)	bdl–0.043 (0.0215)		0.012–0.015
MgO	0.021–0.229 (0.111)	0.047–0.09 (0.057)	0.03–0.072 (0.06)		0.015–0.017
ZnO	0.373–0.549 (0.451)	0.451–0.611 (0.519)	0.366–0.536 (0.463)		0.022–0.027
F	0.14–0.243 (0.184)	0.584–0.753 (0.681)	0.53–0.878 (0.660)		0.016–0.024
TiO_2	bdl–0.104 (0.0494)	bdl	bdl		0.031–0.044
H_2O+[c]	15.87–20.047 (16.134)	n.a.	n.a.	17.72	
Total	100	82.682–84.379 (83.261)	81.13–82.94 (81.913)	100	

[a]The given totals of the raindrops and veins did not include the contents of H_2O and CO_2, which were the components of turquoise and fluorapatite, respectively, but could not be detected by EPMA and analyzed. bdl = below detection limit; n.a. = not analyzed
[b]All Fe was analyzed as FeO by EPMA.
[c]H_2O+ was calculated by the difference from 100%.

Raindrops and Veins. Conversely, the values of Al_2O_3 (24.058–27.919 wt.%) and SiO_2 (0.864–4.000 wt.%) were lower in the raindrops than in the substrates. The CuO value had similar ranges in the raindrops and substrates. The raindrops had significantly higher contents of CaO (8.487–14.747 wt.%) and P_2O_5 (33.096–34.813 wt.%) than the substrates, as well as enriched F (0.584–0.753 wt.%), a consequence of the presence of fluorapatite [$Ca_5(PO_4)_3F$]. And the FeO content, from a minimum value of 1.694 wt.% to a maximum of 4.481 wt.%, was correlated to the color of the raindrops. The major components of the veins were essentially identical to that of the raindrops. Compared to the substrates, the raindrops and veins had lower concentrations of Ni (13.9–408 ppm) and Mo (2.33–532 ppm), but higher concentrations of Sr (98.8–478 ppm), Ba (782–945 ppm), and U (30.2–187 ppm).

Raman and FTIR Spectroscopy. Although the characteristic bands of turquoise related to phosphate, hydroxyl, and water units (Čejka et al., 2015) could be observed in the Raman and FTIR spectra of raindrops, veins, and substrates, there were still significant differences.

Raman Peak at Approximately 966 cm⁻¹ and Shoulder at 1070 cm⁻¹. A strong and sharp peak at 965–968 cm⁻¹ in the Raman spectra of the raindrops and

veins (figure 8) has not been reported in previous studies of turquoise. Based on the XRD and EPMA results, the tested spectra were compared with the spectra of fluorapatite from the RRUFF database (http://rruff.info/R050529) for peak assignment and matched well. This significant peak was attributed to the ν_1 symmetrical stretching vibration of the phosphate group $(PO_4)^{3-}$ in the fluorapatite structure (Penel et al., 1997). The ν_4 $(PO_4)^{3-}$ bending vibrations of fluorapatite (Penel et al., 1997), which occurred at approximately 594 cm⁻¹, strongly overlapped with the band at 593 cm⁻¹ related to the $(PO_4)^{3-}$ group in turquoise (Frost et al., 2006; Čejka et al., 2015).

Another important feature in the Raman spectra of the raindrops and veins was that the band at ~1041 cm⁻¹ was more asymmetric than that of the substrates (figure 8). The peak at 1041 cm⁻¹, assigned to the ν_1 $(PO_4)^{3-}$ symmetric stretching vibrations (Čejka et al., 2015), appeared to consist of more than one band and had a weak shoulder at 1070 cm⁻¹. This shoulder was assigned to ν_1 carbonate bands associated with the substitution of the $(PO_4)^{3-}$ group by $(CO_3)^{2-}$ in the fluorapatite structure (Awonusi et al., 2007). With increasing CaO, the relative intensity of the bands at 1070 and ~966 cm⁻¹ became stronger (figure 8). For example, when the CaO value in a vein reached 14.354 wt.% and the F value was high (up to 0.878 wt.%), the Raman spectrum showed a distinct shoulder at 1070 cm⁻¹. The band at 966 cm⁻¹ was even more intense than the band at 1041 cm⁻¹, implying a high concentration of fluorapatite in this vein. Furthermore, the Raman spectra of the raindrops and veins had a slightly broader band, shifting at the 420–429 cm⁻¹ region in different analyzed areas. This band was unresolved due to a combination of the ν_2 $(PO_4)^{3-}$ bending vibrations at 432 cm⁻¹ (Penel et al., 1997) for fluorapatite and 421 cm⁻¹ for turquoise (Chen et al., 2009; Čejka et al., 2015), respectively. The position and shape of this band, a consequence of the same $(PO_4)^{3-}$ unit in the structure of both fluorapatite and turquoise, also appeared to be linked to the value of CaO.

In conclusion, the distinguishing features of the Raman spectra in the raindrops and veins were the presence of the sharp peak at 965–968 cm⁻¹ and a weak but significant shoulder at 1070 cm⁻¹, both of which became more intense with increasing CaO when compared to the bands at ~1041 cm⁻¹.

Double FTIR Absorption Bands Near 1460 and 1430 cm⁻¹. The FTIR absorption spectra of veins, raindrops, and substrates were similar, all characterized

TABLE 3. Element concentrations of the substrates, raindrops, and veins by LA-ICP-MS.

| Trace elements (ppm)	Substrates (5 spots) Min-Max (avg.)	Raindrops (4 spots) Min-Max (avg.)	Veins (4 spots) Min-Max (avg.)	Detection limits Min-Max
Fe	21779–186608 (57893)	17278–49076 (33639)	16058–21887 (19934)	35.5-78.1
V	86.0–810 (293)	135–329 (230)	143–226 (185)	0.12–0.46
Ni	44.0–1458 (475)	13.9–408 (203)	17.4–188 (64)	1.90–3.80
Sr	9.61–17.2 (13.1)	98.8–154 (119)	105–478 (286)	0.091–0.13
Mo	0.71–2124 (714)	2.33–532 (253)	2.96–365 (97)	0.34–0.72
Ba	570–626 (597)	782–945 (859)	803–846 (816)	0.72–0.99
U	4.53–16.6 (9.7)	30.2–44.7 (37)	44.8–187 (102)	0.020–0.027
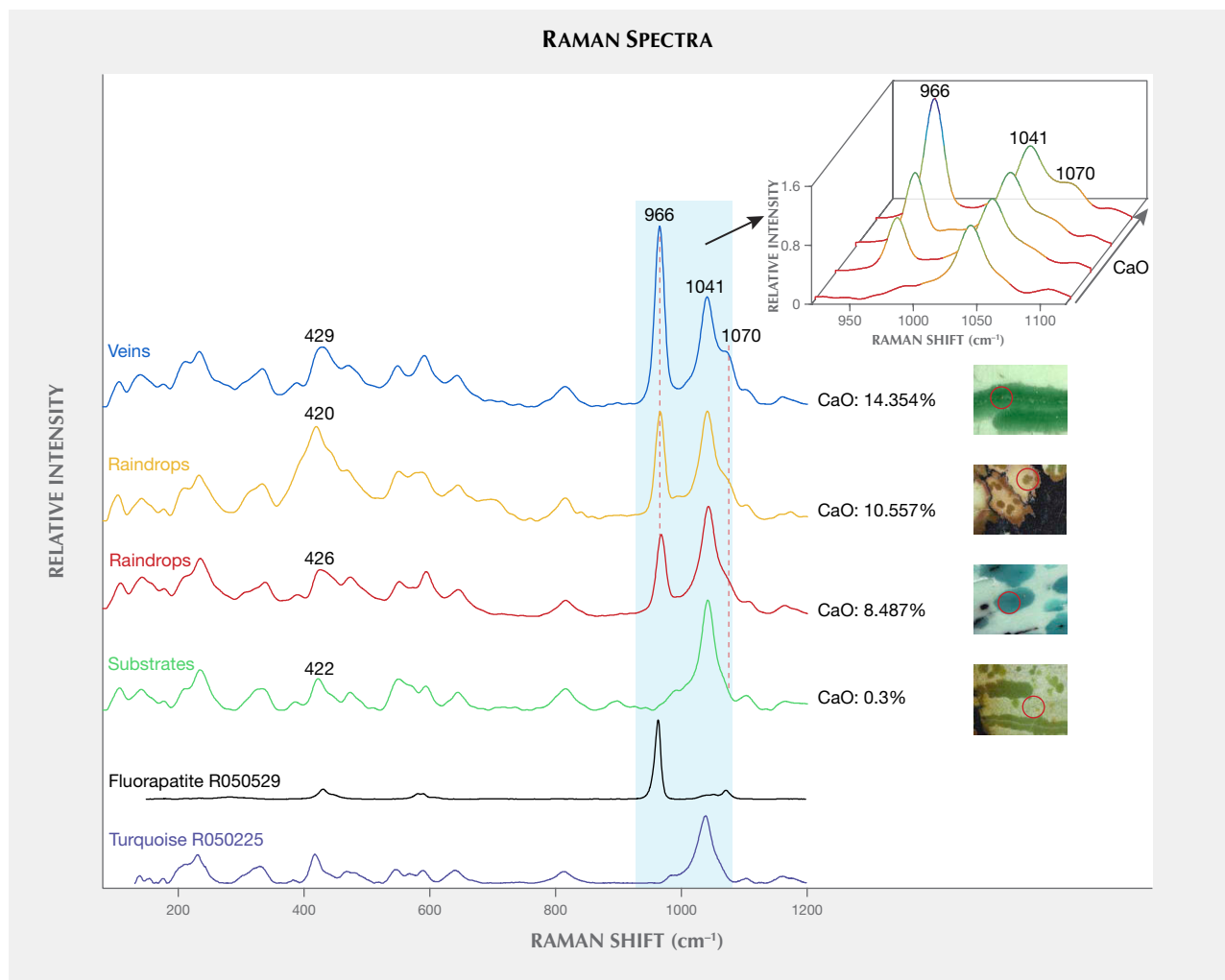
Figure 8. Raman spectra of the veins, raindrops, and substrates of the turquoise, normalized to 1041 cm⁻¹ and stacked for clarity, with Raman spectra of standard fluorapatite (http://rruff.info/R050529) and turquoise (http://rruff.info/R050225) at the bottom for comparison. The 920–1120 cm⁻¹ range of the Raman spectra is shown in the three-dimensional plot in the top right corner, clearly indicating that the relative intensity of the bands at 1070 and ~966 cm⁻¹ became stronger with increasing CaO when the spectra were normalized to ~1041 cm⁻¹.

by the stretching and bending vibrations of water molecules, hydroxyl ions, and tetrahedral phosphate (Chen and Qi, 2007; Čejka et al., 2015). One significant exception was the occurrence of additional double weak bands near 1460 and 1430 cm⁻¹ in the FTIR absorption spectra of all raindrops and veins but not in the substrates (figure 9). Similar double weak bands were also observed in two altered turquoise samples mixed with calcium carbonate, as in the study of Abdu et al. (2011). However, the double weak bands near 1460 and 1430 cm⁻¹ in this study were assigned to ν_3 $(CO_3)^2$, and the asymmetric stretching vibration was due to the substitution of the $(PO_4)^{3-}$ group by $(CO_3)^{2-}$ in the fluorapatite structure (Fleet, 2009). Other very weak bands at 962, 870,

and 608 cm⁻¹ related to ν_1 $(PO_4)^{3-}$ symmetrical stretching vibration, ν_4 $(PO_4)^{3-}$ bending vibration (Penel et al., 1997), and ν_2 $(CO_3)^{2-}$ bending vibration (Fleet, 2009) of fluorapatite, respectively, were also observed in the vein of sample B-3.

Spectral Comparisons Between Raindrops (Veins) and Substrates of Different Colors. In the visible range (figure 10), the absorption from the color-causing elements of turquoise was different for each color. For a specific color, the absorption bands of the raindrops (veins) and substrates had approximately similar positions and shapes. The most significant difference between them was the overall weaker reflectance intensity of the raindrops (veins),
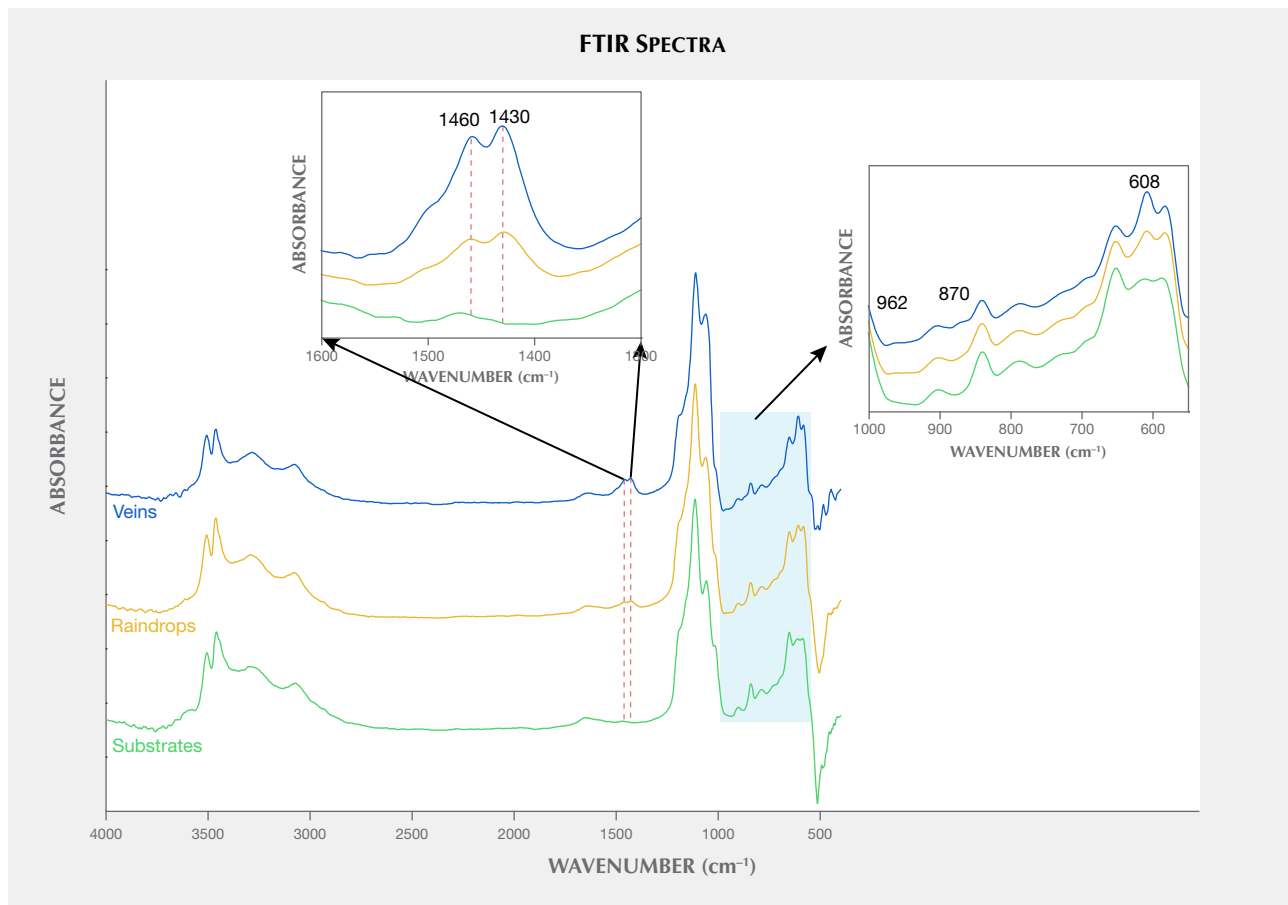
FTIR Spectra

Figure 9. FTIR spectra of the veins, raindrops, and substrates, stacked for clarity. Two ranges (1600–1300 cm⁻¹ and 1000–550 cm⁻¹) of FTIR spectra are enlarged to show the distinct differences of the spectra among the veins, raindrops, and substrates. Additional double bands near 1460 and 1430 cm⁻¹, as well as other weak bands at 962, 870, and 608 cm⁻¹ occurred in the FTIR absorption spectra of raindrops and veins but not in the substrates.

corresponding to their deeper color. The two combined effects caused the raindrops (veins) and substrates to vary in saturation while always being consistent in hue.

Figure 10. The UV-Vis reflectance spectra of the raindrops (veins) and substrates of different colors.
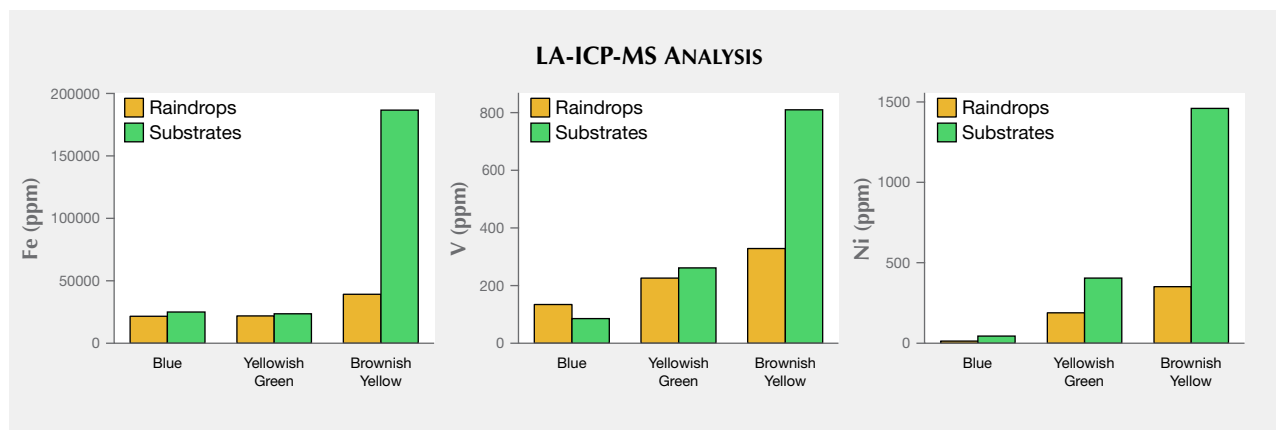

UV-Vis Spectra
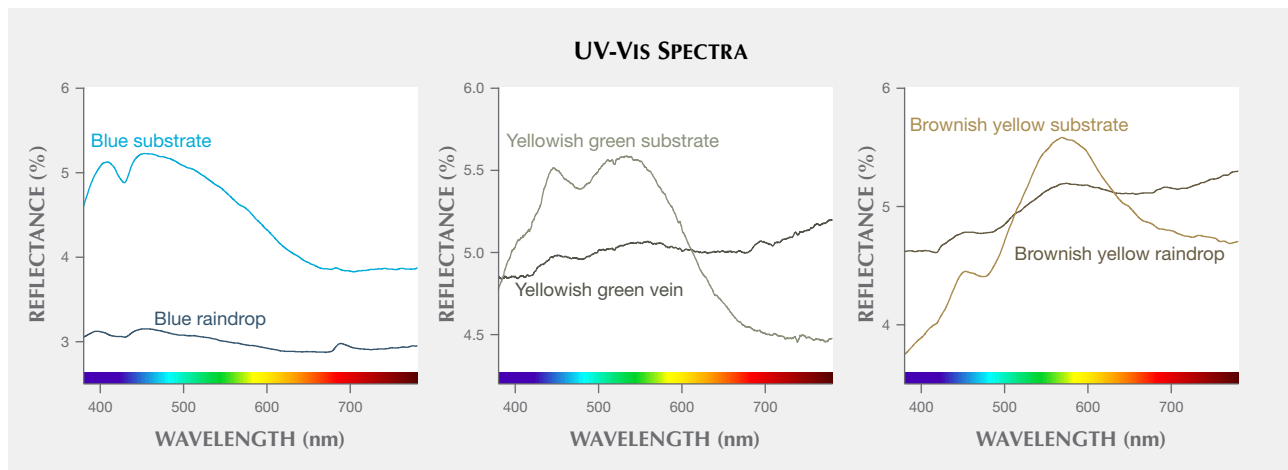
Figure 11. The comparison of Fe (left), V (center), and Ni (right) contents analyzed by LA-ICP-MS between raindrops and substrates with different colors.

DISCUSSION

Color Origin of Brownish Yellow Raindrops and Substrates. The amounts of Fe, V, and Ni analyzed by LA-ICP-MS were higher in the brownish yellow raindrop and substrate than in the blue and yellowish green raindrops and substrates (figure 11). Previous work on color origin concluded that the brownish yellow color of turquoise with high Fe and low Al_2O_3 content was associated with the substitution of Al^{3+} by Fe^{3+} in the turquoise structure (Zhang et al., 1982;

Luan et al., 2004). However, the authors assumed that the existence of secondary iron-bearing minerals in the pores was responsible for the brownish yellow tone. As expected, significant spectral signals for iron minerals only occurred in the Raman spectra of brownish yellow raindrops and substrates.

For instance, when the value of FeO increased to 4.481 wt.% analyzed by EPMA in brownish yellow raindrops, its Raman spectra (figure 12) showed strong bands centered at 416 cm⁻¹, which enveloped
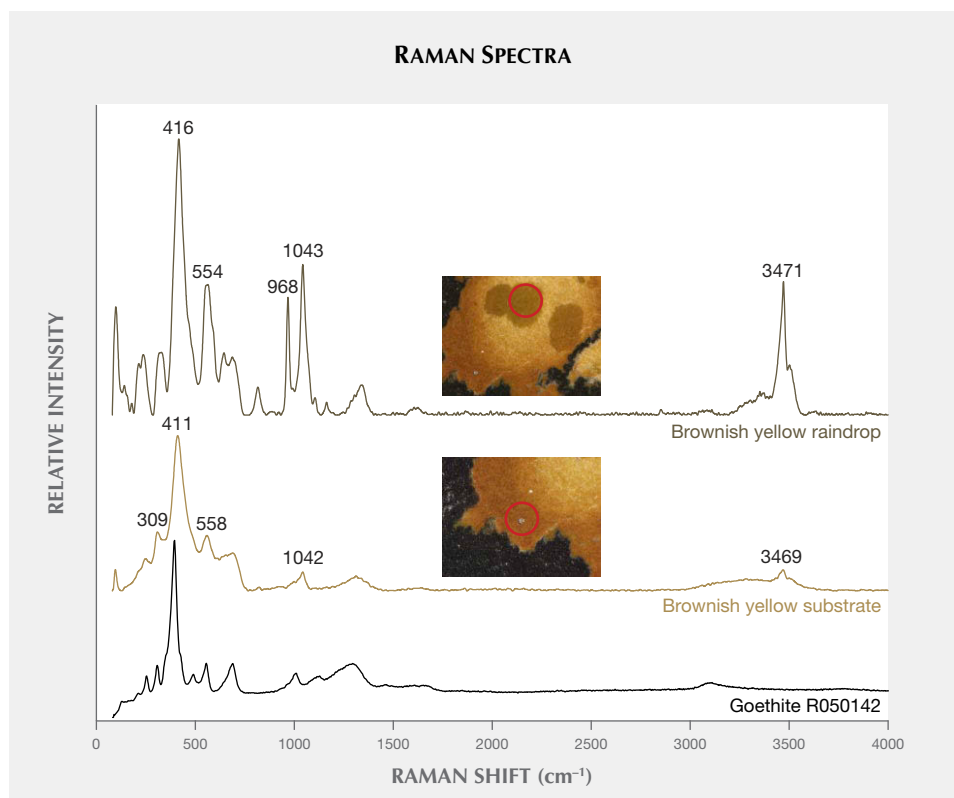

Figure 12. The band at 411–416 cm⁻¹ related to goethite was obvious in the Raman spectra of the brownish yellow raindrop and the substrate. The Raman spectra of standard goethite (http://rruff.info/R050142) is also shown for comparison, stacked for clarity.

the bands in the 420–429 cm⁻¹ range, and was even stronger than the peaks at 1043 and 968 cm⁻¹. Similarly, a strong band at 411 cm⁻¹, accompanied by bands at 309 and 558 cm⁻¹, was observed in the Raman spectrum of brownish yellow substrate due to rich Fe (FeO up to 19.586 wt.% analyzed by EPMA). But other bands of turquoise in the Raman spectrum of the brownish yellow substrate were very weak, such as the ones at 1042 and 3469 cm⁻¹. The band at 411–416 cm⁻¹ was related to goethite (Hanesch, 2009; Liu, 2018). It was very distinct in the Raman spectra of the brownish yellow raindrops and substrates, suggesting the existence of numerous secondary iron minerals in the pores. The brownish yellow or red hue of the raindrops and substrates was presumably generated by the alteration of secondary iron minerals.

Discovery of Nearly Pure Fluorapatite and Turquoise in the Raindrops and Veins. Interestingly, a bright and narrow line (~20 µm in width) was observed in the middle of the vein when specimen B-3 was observed under high-contrast BSE imaging (figure 13, inset). And its Raman spectrum showed strong characteristics of fluorapatite (figure 13). However, only very weak bands at 3455, 3474, and 3499 cm⁻¹, were assigned to the ν(OH) stretching vibrations of turquoise, with weaker bands over the 3000–3300 cm⁻¹ range attributed to the ν(OH) stretching vibrations of water molecules in turquoise. In addition, the bright and narrow line mainly consisted of CaO, P_2O_5, and F with minor Al_2O_3, CuO, and FeO, which were consistent with the Raman results. The mean values for CaO (up to 48.159 wt.%) and F (up to 1.988 wt.%) analyzed from the bright and narrow line were notably higher than those of other areas (table 4). The P_2O_5 content was 28.323–28.975 wt.%, while the contents of other important elements including Al, Cu, and Fe were all below 0.640 wt.% and greatly distinct from the substrates, raindrops, and veins.

Hence, both the Raman spectra and the chemical compositions proved that the bright and narrow line was indeed nearly pure fluorapatite. And there were at least three mineral assemblages (turquoise, fluorapatite, and a mixture of the two) occurring simultaneously in the raindrop turquoise. Yang et al. (2003) and Hull et al. (2008) discovered apatite inclusions in turquoise from Ma'anshan in Anhui Province and the Castilian mine in New Mexico, respectively. Additionally, fluorapatite also occurred in turquoise from Nishapur, Iran (Rossi et al., 2017). However, this study was the first to find fluorapatite coexisting with turquoise from Hubei Province,
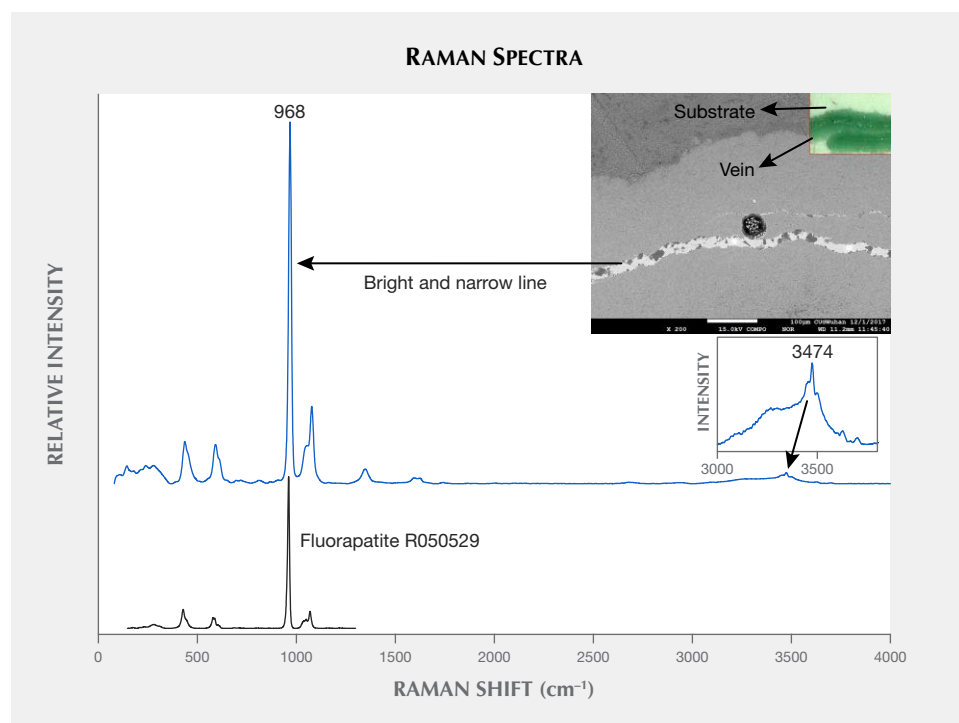

Figure 13. The Raman spectrum of the bright and narrow line in the middle of a vein showed dominant characteristics of fluorapatite and only a very weak signal of the hydroxyl and water units of turquoise. The Raman spectrum of standard fluorapatite (http://rruff.info/R050529) is also shown for comparison. The 3000–3800 cm⁻¹ range is enlarged to show the weak signal of the hydroxyl and water units of turquoise. The inset shows the distribution of lines, veins, and substrates under BSE imaging (field of view 0.6 mm) and the corresponding microscopic image (field of view 2.1 mm).
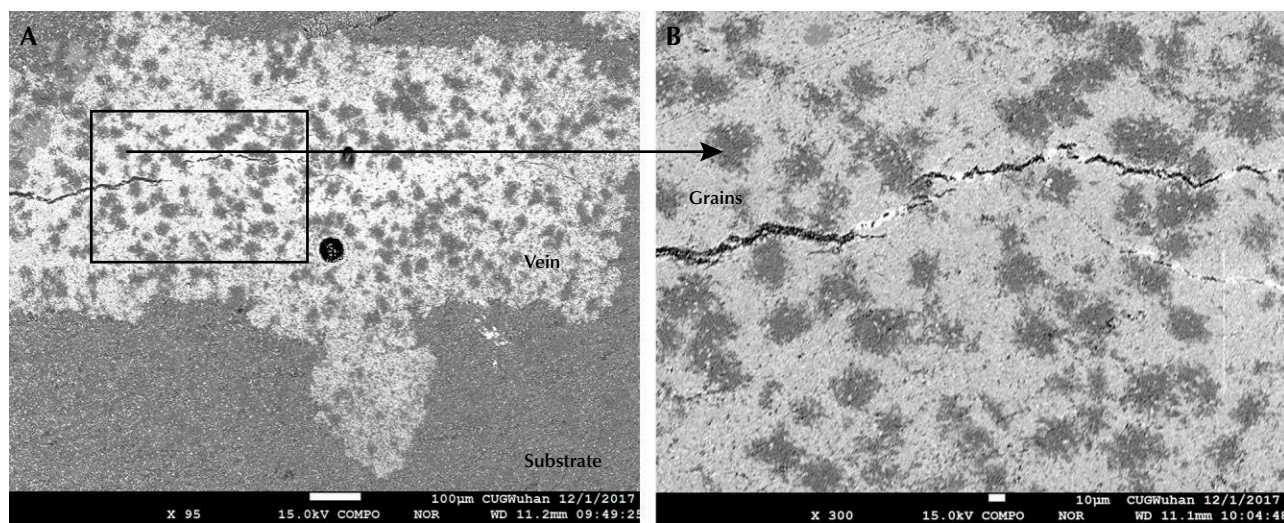
Figure 14. Numerous small dark grains distributed in the raindrops and veins corresponding to turquoise were seen under high-contrast BSE imaging. Images by Ling Liu; fields of view 1.25 mm (left) and 0.39 mm (right).

forming a distinct raindrop pattern. Previous studies have made it clear that a turquoise-blue material, odontolite, which was also fluorapatite [$Ca_5(PO_4)_3F$], was an occasional turquoise imitation used in art objects or historical jewels and previously considered turquoise (Reiche et al., 2001; Krzemnicki et al., 2011).

Moreover, numerous small dark grains were distributed in the raindrops and veins under high-contrast BSE imaging (figure 14). According to the EPMA results, their major chemical compositions were Al_2O_3 (38.25–39.566 wt.%), P_2O_5 (30.144–31.273 wt.%), CuO (6.464–6.896 wt.%), and FeO (2.051–2.613 wt.%), with minor contents of SiO_2, CaO, and F (table 4), corresponding to turquoise.

Speculation about the Formation Mechanism of Raindrop Turquoise. The raindrops and veins may be the byproducts of weathering and leaching. As suggested by Jiang et al. (1983) and Tu (1996), the turquoise deposits in Shaanxi and Hubei areas resulted from leaching and mineralization. The mineralization of turquoise was controlled by tectonic movement and could be achieved through weathering, erosion, transportation, leaching, and deposition. Most of the turquoise orebodies occur in fissures and pores of carbon-bearing silicic rocks as veinlets, lentoid and massive (Tu, 1996, 1997a, b). Rainwater is active along tectonic fractures, creating favorable conditions for leaching and mineralization. And it must dissolve the ore-forming elements of Cu, P, and

Al in bedrock and host rocks. Turquoise tends to be deposited in fracture zones under the high Eh and low pH environment (Tu, 1997a).

When phosphorites are exposed to an acidic environment, their components such as carbonate can be easily dissolved. Then, the secondary apatite mineral can be formed (Huang, 1991; Liu et al., 1994; Tian, 1995). Moreover, the original phosphate minerals were dissolved and migrated after strong weathering and leaching. The secondary mineral fluorapatite can be redeposited under appropriate conditions. And it was usually accompanied by some supergene weathered minerals, such as wavellite, variscite, woodhouseite, and limonite (Liu et al., 1994). These mineral assemblages also occurred in the turquoise deposits of Hubei and Shaanxi Province, indicating secondary genesis (Jiang et al., 1983). The formation and enrichment of fluorapatite bore similarities to the turquoise from Hubei.

Accordingly, the formation mechanism of raindrop turquoise can be speculated as follows: The freely soluble substances of the carbonaceous phosphate rocks were lost under acidic conditions, while the relatively insoluble phosphate was left in-situ and then formed the mixtures of fluorapatite and turquoise. On the other hand, after the phosphate nodules and phosphate minerals of the ore-bearing rock series were strongly weathered and leached, they experienced dissolution, migration, and redeposition (Tu, 1996, 1997a). The secondary phosphate enriched, and then solutions formed the mixed aggregates of

TABLE 4. EPMA data of the bright and narrow line and small dark grains in the turquoise veins.

Oxides (wt.%)	Bright and narrow line[a] (2 spots) Min-Max (avg.)	Small dark grains[a] (2 spots) Min-Max (avg.)	Detection limits Min-Max
SiO_2	bdl	0.772–0.848 (0.810)	0.025–0.039
Al_2O_3	0.292–0.300 (0.296)	38.25–39.566 (38.908)	0.020–0.021
P_2O_5	28.323–28.975 (28.649)	30.144–31.273 (30.709)	0.019–0.025
CuO	0.544–0.640 (0.592)	6.464–6.896 (6.680)	0.037–0.042
FeO^b	0.114–0.188 (0.151)	2.051–2.613 (2.332)	0.031–0.035
CaO	47.426–48.891 (48.159)	0.175–0.191 (0.183)	0.017–0.020
K_2O	bdl	0.023–0.027 (0.025)	0.010–0.014
Na_2O	0.126–0.231 (0.179)	0.018–0.046 (0.032)	0.014–0.017
MgO	0.239–0.259 (0.249)	0.018–0.025 (0.022)	0.015–0.017
ZnO	0.292–0.404 (0.348)	0.434–0.443 (0.439)	0.025–0.031
TiO_2	bdl–0.043	bdl	0.035–0.037
F	1.733–2.242 (1.988)	0.229–0.270 (0.250)	0.016–0.021
H_2O+^c	n.a.	19.244–19.94 (19.592)	
Total	79.91–81.386 (80.648)	100	

[a]Note: The bright line and dark grains can be found in figures 10 and 11, respectively. The given totals of the bright and narrow line did not include the CO_2, which was a component of fluorapatite but could not be detected by EPMA. bdl = below detection limit; n.a. = not analyzed
[b]All Fe was analyzed as FeO by EPMA.
[c]H_2O+ was calculated by the difference from 100%.

turquoise and apatite under appropriate physical and chemical conditions. The similar formation of turquoise and apatite was referred to by Jiang et al. (1983) and Tian (1995), respectively. After the phosphate solutions migrated, they might have been precipitated in the pores and recrystallized as raindrops. They would appear as veins if the phosphate solutions were precipitated in the cracks or fissures. The formed veins could be ruptured by tectonic activities, then providing space for pure apatite crystallizing. The pure apatite filling in the veins was the last phase of mineralization in raindrop turquoise.

In addition, the approximately hexagonal shapes of the raindrops may have been determined by the well-developed hexagonal crystal shapes of apatite. In the Ma'anshan areas of Anhui Province, there is a rare variety of pseudomorphic turquoise (figure 15) of metasomatic origin (Yue, 1995). In these specimens, the primary apatite prepared the matrix for the formation of pseudomorphic turquoise. And the strong alteration of the metallogenic mother rock is beneficial to the participation of surface water (Yue, 1995). Under the actions of alkalescent surface solution containing copper, aluminum, iron, and other elements, apatite metasomatism occurs, generating the pseudomorphic turquoise that inherits the original shape of apatite. Similarly, some raindrops adopt the hexagonal habit of the apatite crystals.
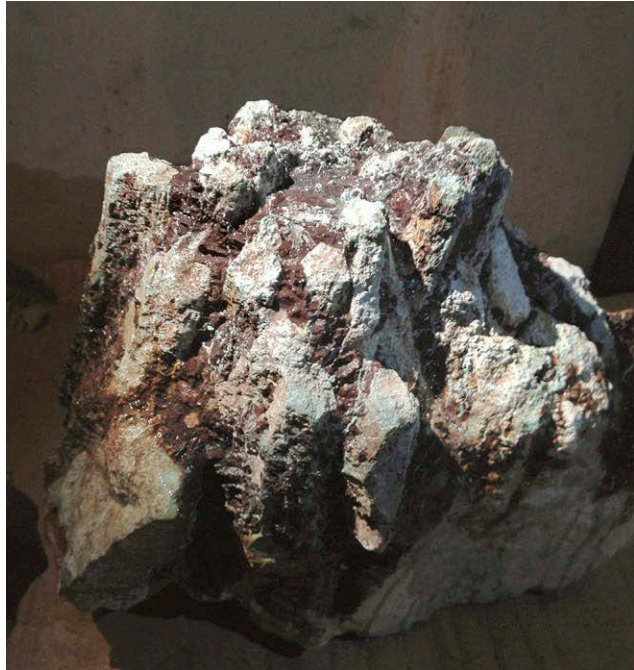
Figure 15. Pseudomorphic turquoise specimens from the Bijiashan mine located in the Ma'anshan area of Anhui Province preserve the original hexagonal shape of the apatite crystal. Photos by Ling Liu.

CONCLUSIONS

The saturated raindrops and veins of turquoise from Hubei Province (figure 16) were characterized by the presence of both turquoise and fluorapatite. In addition to Al_2O_3, P_2O_5, CuO, FeO, and SiO_2, the rain-drops and veins had other major chemical compositions of CaO and F differing from the substrates. Raman spectra of raindrops and veins showed intense peaks at ~966 cm^{-1} related to the v_1 symmetrical stretching vibration of the phosphate group

Figure 16. Raindrop turquoise from Hubei Province. Photos by Yang Xu (left; He et al., 2018) and Qiang Gao (right).
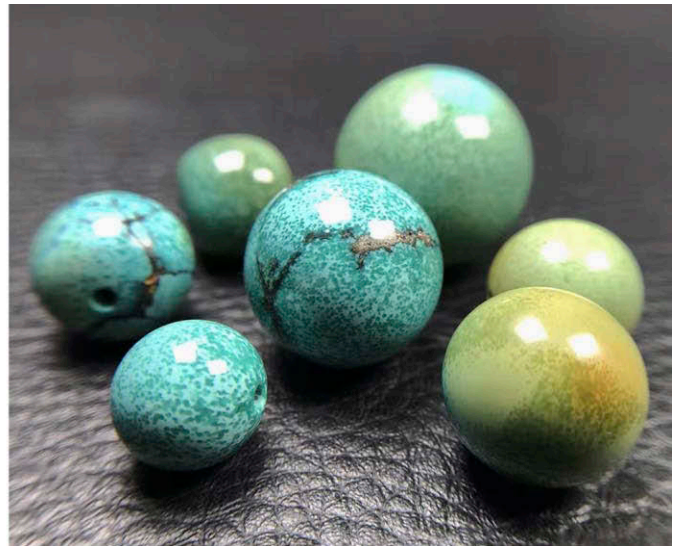
$(PO_4)^{3-}$ in fluorapatite. Moreover, the bands at 1070 cm^{-1} for Raman spectra and double weak bands near 1460 and 1430 cm^{-1} for FTIR spectra attributed to $(CO_3)^{2-}$ confirmed that $(PO_4)^{3-}$ was replaced by $(CO_3)^{2-}$ in the fluorapatite structure. The brownish yellow color present in some of the raindrop turquoise was caused by goethite. The raindrops and veins were potentially the byproducts of weathering and leaching because of similar enrichment and formation of fluorapatite and turquoise. Pure apatite found in the veins formed after the raindrops and veins.

ABOUT THE AUTHORS

Ms. Liu (lingliu0928@163.com) is a PhD candidate at the Gemmological Institute, China University of Geosciences in Wuhan. Prof. Yang (yangc@cug.edu.cn, corresponding author) is the dean of the Gemmological Institute, China University of Geosciences in Wuhan. Dr. Li (yanli@cug.edu.cn) is an associate professor at the Gemmological Institute and Advanced Manufacturing Centre, China University of Geosciences in Wuhan.

REFERENCES

Abdu Y.A., Hull S.K., Fayek M., Hawthorne F.C. (2011) The turquoise-chalcosiderite $Cu(Al,Fe^{3+})_6(PO_4)_4(OH)_8 \cdot 4H_2O$ solid-solution series: A Mössbauer spectroscopy, XRD, EMPA, and FTIR study. *American Mineralogist*, Vol. 96, No. 10, pp. 1433–1442, http://dx.doi.org/10.2138/am.2011.3658

Awonusi A., Morris M.D., Tecklenburg M.M.J. (2007) Carbonate assignment and calibration in the Raman spectrum of apatite. *Calcified Tissue International*, Vol. 81, No. 1, pp. 46–52, http://dx.doi.org/10.1007/s00223-007-9034-0

Beale T.W. (1973) Early trade in highland Iran: A view from a source area. *World Archaeology*, Vol. 5, No. 2, pp. 133–148, http://dx.doi.org/10.1080/00438243.1973.9979561

Bernardino N.D.E., Izumi C.M.S., de Faria D.L.A. (2016) Fake turquoises investigated by Raman microscopy. *Forensic Science International*, Vol. 262, pp. 196–200, http://dx.doi.org/10.1016/j.forsciint.2016.03.041

Čejka J., Sejkora J., Macek I., Malíková R., Wang L., Scholz R., Xi Y., Frost R.L. (2015) Raman and infrared spectroscopic study of turquoise minerals. *Spectrochimica Acta Part A: Molecular and Biomolecular Spectroscopy*, Vol. 149, pp. 173–182, http://dx.doi.org/10.1016/j.saa.2015.04.029

Chen Q.L., Qi L.J. (2007) Study on the vibrational spectra characters of water in turquoise from Ma'anshan. *Journal of Mineralogy and Petrology*, Vol. 27, No. 1, pp. 30–35 [in Chinese].

Chen Q.L., Qi L.J., Chen J.Z. (2009) Raman spectrum study on turquoise. *Spectroscopy and Spectral Analysis*, Vol. 29, No. 2, pp. 406–409 [in Chinese].

Chen Q.L., Yin Z.W., Qi L.J., Xiong Y. (2012) Turquoise from Zhushan County, Hubei Province, China. *G&G*, Vol. 48, No. 3, pp. 198–204, http://dx.doi.org/10.5741/GEMS.48.3.198

Deng Q., Hu J.M., Wang X., Cao Y., Yang W. (2019) Identification of turquoise with "Jia Ci" treatment. *Proceedings China International Gems & Jewelry Academic Conference, Beijing, China, 2019*, pp. 263–267, http://dx.doi.org/10.26914/c.cnkihy.2019.013579 [in Chinese].

Feng M., Mao Z.W., Pan W.B., Zhang S.D. (2003) Preliminary research on turquoise in Jiahu site. *Sciences of Conservation and Archaeology*, Vol. 15, No. 3, pp. 9–12 [in Chinese].

Fleet M.E. (2009) Infrared spectra of carbonate apatites: v_2-region bands. *Biomaterials*, Vol. 30, No. 8, pp. 1473–1481, http://dx.doi.org/10.1016/j.biomaterials.2008.12.007

Foord E., Taggart J. (1998) A reexamination of the turquoise group: The mineral aheylite, planerite (redefined), turquoise and coeruleolactite. *Mineralogical Magazine*, Vol. 62, No. 1, pp. 93–111, http://dx.doi.org/10.1180/002646198547495

Frost R.L., Reddy B.J., Martens W.N., Weier M.L. (2006) The molecular structure of the phosphate mineral turquoise—A Raman spectroscopic study. *Journal of Molecular Structure*, Vol. 788, No. 1, pp. 224–231, https://doi.org/10.1016/j.molstruc.2005.12.003

Hanesch M. (2009) Raman spectroscopy of iron oxides and (oxy)hydroxides at low laser power and possible applications in environmental magnetic studies. *Geophysical Journal International*, Vol. 177, No. 3, pp. 941–948, http://dx.doi.org/10.1111/j.1365-246X.2009.04122.x

Hao Y.W., Hao F.Z. (2002) Chinese turquoise culture of the New Stone Age. *Acta Petrologica et Mineralogica*, Vol. 21, No. z1, pp. 147–150 [in Chinese].

Harbottle G., Weigand P. (1992) Turquoise in Pre-Columbian America. *Scientific American*, Vol. 266, No. 2, pp. 78–85, http://www.jstor.org/stable/24938943

He C., Cao F.F., Di J.R., Yang M.X., Lu R., Liu L. (2018) Interpretation of national standard turquoise grading. *Journal of Gems and Gemmology*, Vol. 20, No. 6, pp. 7–17, http://dx.doi.org/10.15964/j.cnki.027jgg.2018.06.002 [in Chinese].

He X., Chen L., Li Q.H., Gu D.H., Gan F.X., Li F., Li Z. (2011) Trace elements and rare earth elements characteristics of turquoise from Zhushan and Ma'anshan area. *Rock and Mineral Analysis*, Vol. 30, No. 6, pp. 709–713, http://dx.doi.org/10.3969/j.issn.0254-5357.2011.06.011 [in Chinese].

Hedquist S. (2016) Ritual practice and exchange in the late prehispanic Western Pueblo Region: Insights from the distribution and deposition of turquoise at Homol'ovi I. *KIVA*, Vol. 82, No. 3, pp. 209–231, http://dx.doi.org/10.1080/00231940.2016.1214056

Huang F.R. (1991) Secondary enrichment of phosphorite in eastern Yunnan and its formation mechanism. *Mineral Deposits*, Vol. 10, No. 2, pp. 179–186 [in Chinese].

Huang X.Z. (2003) Ore-forming characteristics and prospecting di-

rection of agaphite deposits. China *Non-Metallic Mining Industry Herald*, No. 6, pp. 50–51 [in Chinese].

Hull S., Fayek M. (2012) Cracking the code of Pre-Columbian turquoise trade and procurement strategies. In J.C.H. King et al., Eds., *Turquoise in Mexico and North America: Science, Conservation, Culture and Collec*tions, Archetype Publications, London, pp. 29–40.

Hull S., Fayek M., Mathien F.J., Shelley P., Durand K.R. (2008) A new approach to determining the geological provenance of turquoise artifacts using hydrogen and copper stable isotopes. *Journal of Archaeological Science*, Vol. 35, No. 5, pp. 1355–1369, http://dx.doi.org/10.1016/j.jas.2007.10.001

Hull S., Fayek M., Mathien F.J., Roberts H. (2014) Turquoise trade of the Ancestral Puebloan: Chaco and beyond. *Journal of Archaeological Science*, Vol. 45, pp. 187–195, http://dx.doi.org/10.1016/j.jas.2014.02.016

Jiang Z.C., Chen D.M., Wang F.Y., Li W.Y., Cao X.Q., Wu Q.X. (1983) Thermal properties of turquoise and its intergrowing minerals in a certain district of China. *Acta Mineralogica Sinica*, No. 3, pp. 198–206, 247 [in Chinese].

Khazeni A. (2014) *Sky Blue Stone: The Turquoise Trade in World History*. University of California Press, Berkeley, https://muse.jhu.edu/book/35627

Kostov, R.I. (2019) Archaeomineralogy of turquoise in Eurasia. In G. Querré et al., *La parure en callaïs du Néolithique européen*, Archaeopress, Oxford, pp. 387–396.

Krzemnicki M.S., Herzog F., Zhou W. (2011) A historic turquoise jewelry set containing fossilized dentine (odontolite) and glass. *G&G*, Vol. 47, No. 4, pp. 296–301, http://dx.doi.org/10.5741/GEMS.47.4.296

Ku Y.L., Yang M.X. (2021) Study on the spectral characteristics of blue turquoise with growth layers from Hubei province. *Spectroscopy and Spectral Analysis*, Vol. 41, No. 5 [in Chinese].

Lavina B., Dera P., Downs R.T. (2014) Modern X-ray diffraction methods in mineralogy and geosciences. *Reviews in Mineralogy and Geochemistry*, Vol. 78, No. 1, pp. 1–31, http://dx.doi.org/10.2138/rmg.2014.78.1

Li X.T., Xian Y.H., Fan J.Y., Zhang L.F., Guo J.W., Gao Z.Y., Wen R. (2019) Application of XRD-SEM-XRD-EMPA to study the mineralogical characteristics of turquoise from Xichuan, Henan Province. *Rock and Mineral Analysis*, Vol. 38, No. 4, pp. 373–381, http://dx.doi.org/10.15898/j.cnki.11-2131/td.201809090102 [in Chinese].

Li Y.X., Zhang D.Y., He N., Guo Z.Y., Guo Y.T. (2018) Exploring the origin characteristics of turquoise products unearthed from the pre-Qin site in Shanxi. *Chinese Cultural Relics*, No. 2, pp. 86–91 [in Chinese].

Liu J., Wang Y.M., Liu F.L., He C., Liu F. (2019a) Gemmological and mineralogical characteristics of turquoise from Tongling, Ahui Province. *Journal of Gems and Gemmology*, Vol. 21, No. 6, pp. 58–65 [in Chinese].

Liu J., Yang M.X., He C., Cao F.F. (2019b) Filled turquoise and its corresponding filling solution. *Journal of Gems and Gemmology*, Vol. 21, No. 5, pp. 56–64 [in Chinese].

Liu L. (2018) Study on origin, factors and grading of the color of turquoise from China. Master's thesis, China University of Geosciences [in Chinese].

Liu X.F., Lin C.L., Li D.D., Zhu L., Song S., Liu Y., Shen C.H. (2018) Study on mineralogy and spectroscopy of turquoises from Hami, Xinjiang. *Spectroscopy and Spectral Analysis*, Vol. 38, No. 4, pp. 1231–1239 [in Chinese].

Liu Y.X., Ge D.Y., Zeng Y.F., Dai C.F. (1994) Enrichment characteristics of apatite in the Diandong phosphate deposit. *Journal of Mineralogy and Petrology*, No. 4, pp. 17–36 [in Chinese].

Luan B.A. (2001) The ancient turquoise mine investigating in Xinjiang area. *China Gems & Jades*, No. 4, pp. 66–67 [in Chinese].

Luan L.J., Han Z.X., Wang C.Y., Zhang Y.W. (2004) Elementary research on color-forming mechanism of turquoise. *Northwestern Geology*, Vol. 37, No. 3, pp. 77–82 [in Chinese].

Luo Y.F., Yu X.Y., Zhou Y.G., Yang X.G. (2017) A study of texture and structure of turquoise from Luonan, Shaanxi Province. *Acta Petrologica et Mineralogica*, Vol. 36, No. 1, pp. 115–123, http://dx.doi.org/10.3969/j.issn.1000-6524.2017.01.012 [in Chinese].

Ma B., Liu L., Feng S.-L., Xu Q., Feng X.-Q. (2014) Analysis of the elemental composition of Tang Sancai from the four major kilns in China using EDXRF. *Nuclear Instruments and Methods in Physics Research Section B: Beam Interactions with Materials and Atoms*, Vol. 319, pp. 95–99, http://dx.doi.org/10.1016/j.nimb.2013.11.011

Mansour A.M.A. (2014) *Turquoise in Ancient Egypt: Concept and Role*. British Archaeological Reports.

Mao Z.W., Feng M., Zhang S.D., Zhang J.Z., Wang C.S. (2005) A nondestructive test of the turquoise from the Jiahu site and a preliminary study of its source. *Huaxia Archaeology*, No. 1, pp. 55–61, http://dx.doi.org/10.3969/j.issn.1001-9928.2005.01.006 [in Chinese].

Moe K.S., Moses T.M., Johnson P. (2007) Polymer-impregnated turquoise. *G&G*, Vol. 43, No. 2, pp. 149–151, http://dx.doi.org/10.5741/GEMS.43.2.149

Ovissi M., Yazdi M., Ghorbani M. (2017) Turquoise; a gemstone that relates geology to archaeology and anthropology. *The First Symposium of Turquoise: Industry and Culture* [in Persian].

Pang X.X. (2014) The researches on the turquoise objects of the Neolithic age unearthed in China. *Acta Archaeologica Sinica*, No. 2, pp. 139–168 [in Chinese].

Penel G., Leroy G., Rey C., Sombret B., Huvenne J.P., Bres E. (1997) Infrared and Raman microspectrometry study of fluor-fluor-hydroxy and hydroxy-apatite powders. *Journal of Materials Science: Materials in Medicine*, Vol. 8, No. 5, pp. 271–276, http://dx.doi.org/10.1023/A:1018504126866

Reddy B.J., Frost R.L., Weier M.L., Martens W.N. (2006) Ultraviolet-visible, near infrared and mid infrared reflectance spectroscopy of turquoise. *Journal of Near Infrared Spectroscopy*, Vol. 14, No. 4, pp. 241–250, http://dx.doi.org/10.1255/jnirs.641

Reiche I., Vignaud C., Champagnon B., Panczer G.R., Brouder C., Morin G., Solé V.A., Charlet L., Menu M. (2001) From mastodon ivory to gemstone: The origin of turquoise color in odontolite. *American Mineralogist*, Vol. 86, No. 11-12, pp. 1519–1524, http://dx.doi.org/10.2138/am-2001-11-1221

Rossi M., Rizzi R., Vergara A., Capitelli F., Altomare A., Bellatreccia F., Saviano M., Ghiara R.M. (2017) Compositional variation of turquoise-group minerals from the historical collection of the Real Museo Mineralogico of the University of Naples. *Mineralogical Magazine*, Vol. 81, No. 6, pp. 1405–1429, http://dx.doi.org/10.1180/minmag.2017.081.055

Schiffman P., Roeske S., Botto N. (2013) Electron microprobe analysis of minerals. In *Reference Module in Earth Systems and Environmental Sciences*, Elsevier, pp. 1–13, http://dx.doi.org/10.1016/B978-0-12-409548-9.05439-7

Schwarzinger B., Schwarzinger C. (2017) Investigation of turquoise imitations and treatment with analytical pyrolysis and infrared spectroscopy. *Journal of Analytical and Applied Pyrolysis*, Vol. 125, pp. 24–31, http://dx.doi.org/10.1016/j.jaap.2017.05.002

She L.Z., Qin Y., Luo W.G., Huang F.C., Li T.Y. (2009) Provenance-tracing of turquoise in northwest Hubei using rare earth elements. *Chinese Rare Earths*, Vol. 30, No. 5, pp. 59–65 [in Chinese].

Shi Z.R., Cai K.Q. (2008) A study of turquoise and secondary wood-houseite from Yuertan, Baihe County, Shaanxi Province. Vol. 27, No. 2, pp. 164–170, http://dx.doi.org/10.3969/j.issn.1000-6524.2008.02.009 [in Chinese].

Shirdam B., Aslani S. (2017) Origin determination of Iran excellent-quality turquoise based on trace element analysis using ICP-MS and micro XRF. *Proceedings of the 35th International Gemmological Conference, Windhoek, Namibia*, pp. 98–99.

Thibodeau A., Chesley J.T., Ruiz J., Killick D., Vokes A. (2012) An alternative approach to the prehispanic turquoise trade. In

J.C.H. King et al., Eds., *Turquoise in Mexico and North America: Science, Conservation, Culture and Collec*tions, Archetype Publications, London, pp. 63–72.

Thibodeau A.M., Killick D.J., Hedquist S.L., Chesley J.T., Ruiz J. (2015) Isotopic evidence for the provenance of turquoise in the southwestern United States. *GSA Bulletin*, Vol. 127, No. 11-12, pp. 1617–1631, http://dx.doi.org/10.1130/B31135.1

Thibodeau A.M., López Luján L., Killick D.J., Berdan F.F., Ruiz J. (2018) Was Aztec and Mixtec turquoise mined in the American Southwest? *Science Advances*, Vol. 4, No. 6, eaas9370, http://dx.doi.org/10.1126/sciadv.aas9370

Tian S.P. (1995) Formation of weathered phosphorite in Dianchi district of Yunnan Province and its model for mineralization. *Geology of Chemical Minerals*, Vol. 17, No. 1, pp. 29–36 [in Chinese].

Tu H.K. (1996) Geological characteristics of turquoise ore in the areas adjacent to Shaanxi and Hubei Province. *Geology of Shaanxi*, Vol. 14, No. 2, pp. 59–64 [in Chinese].

——— (1997a) Metallogenic characteristics of turquoise in the eastern Qinling Mountains. *Nonmetallic Geology*, No. 3, pp. 24–25 [in Chinese].

——— (1997b) Study on prospecting targets of turquois and uranium mineralization. *Acta Geologica Gansu*, Vol. 6, No. 1, pp. 74–79 [in Chinese].

Wang R., Wang C.S., Feng M., Pan W.B. (2007) Exploring the origin of turquoise with trace elements. *Cultural Relics of Central China*, No. 2, pp. 101–106 [in Chinese].

Wartewig S. (2003) *IR and Raman Spectroscopy: Fundamental Processing*. Wiley, https://onlinelibrary.wiley.com/doi/book/10.1002/3527601635

Weigand P.C., Harbottle G. (1993) The role of turquoises in the ancient Mesoamerican trade structure. In Ericson J.E., Baugh T.G., Eds., *The American Southwest and Mesoamerica: Systems of Prehistoric Exchange*, Springer US, Boston, pp. 159–177.

Xian Y.H., Fan J.Y., Li X.T., Li Y.X., Zhou X.Q., Gao Z.Y., Wu M.L. (2018) Research on the source characteristics of Luonan turquoise by using strontium isotopic method. *Northwestern Geology*, Vol. 51, No. 2, pp. 108–115, http://dx.doi.org/10.19751/j.cnki.61-1149/p.2018.02.015 [in Chinese].

Xu Y.F., Di J.R. (2018) Gemological identification of natural turquoise and treatment turquoise in Hubei. *Acta Petrologica et Mineralog-ica*, Vol. 37, No. 4, pp. 646–654 [in Chinese].

Yang X.Y., Zheng Y.F., Yang X.M., Liu X.H., Wang K.R. (2003) Mineralogical and geochemical studies on the different types of turquoise from Maanshan area, East China. *Neues Jahrbuch für Mineralogie—Monatshefte*, Vol. 2003, No. 3, pp. 97–112, http://dx.doi.org/10.1127/0028-3649/2003/2002-0097

Yang Y.Z., Zhang J.Z., Lan W.L., Cheng Z.J., Yuan Z.J., Zhu Z.F. (2017) 2013 excavation bulletin of Jiahu site, Wuyang County, Henan Province. *Archaeology*, No. 12, pp. 3–20 [in Chinese].

Ye X.H., Ren J., Xu H., Chen G.L., Zhao H.T. (2014) A preliminary study on geological provenance of turquoise artifacts from Er-litou site. *Quaternary Sciences*, Vol. 34, No. 1, pp. 212–223, http://dx.doi.org/10.3969/j.issn.1001-7410.2014.01.25 [in Chinese].

Yu F.W., Zhang J. (1994) Overview of Tang tri-color. *Cultural Relics of Central China*, No. 01, pp. 61–64, 100 [in Chinese].

Yue D.Y. (1995) A study of pseudomorphic turquoise from Maanshan area, Anhui Province. *Acta Petrologica et Mineralogica*, Vol. 14, No. 1, pp. 79–83 [in Chinese].

Zhang H.F., Lin C.Y., Ma Z.W., Yang Z.G. (1982) Magnetic properties, characteristic spectra and colour of turquoise. *Acta Mineralogica Sinica*, No. 4, pp. 254–261 [in Chinese].

Zhang J.Z., Pan W.B. (2002) Excavation at the Jiahu site in Wuyang, Henan, in the spring of 2001. *HuaXia Archaeology*, No. 2, pp. 14–30 [in Chinese].

Zhang Y. (2008) Tang Sancai's sinking and floating. *Journal of Hunan Industry Polytechnic*, Vol. 8, No. 4, pp. 69–72 [in Chinese].

Zhao X.K., Li J.L., Liu Y.L., Ren K. (2017) Resources and genesis of turquoise mineral in Baihe of Ankang city. *Geology of Shaanxi*, Vol. 35, No. 2, pp. 46–51, http://dx.doi.org/10.3969/j.issn.1001-6996.2017.02.008 [in Chinese].

Zhou S.Q., Jiang F.J. (2005) The research of the turquoise in Xichuan of Henan. *Journal of Nanyang Teachers' College*, Vol. 4, No. 3, pp. 63–65, http://dx.doi.org/10.3969/j.issn.1671-6132.2005.03.019 [in Chinese].

Zuo R., Dai H., Wang F., Jiang X.P., Yu L. (2018) Infrared spectrum characteristics and mineral composition of turquoise in Tongling. *Geology of Anhui*, Vol. 28, No. 4, pp. 316–320, http://dx.doi.org/10.3969/j.issn.1005-6157.2018.04.018 [in Chinese].

For online access to all issues of GEMS & GEMOLOGY from 1934 to the present, visit:

gia.edu/gems-gemology

GEMS & GEMOLOGY®

CONGRATULATIONS

This year, hundreds of readers participated in the 2020 *Gems & Gemology* Challenge. Entries arrived from around the world as readers tested their gemological knowledge by answering questions listed in the Spring 2020 issue. Those who earned a score of 75% or better received a GIA Certificate of Completion recognizing their achievement. Participants who scored a perfect 100% are listed below.

G&G Challenge Winners

Australia
Barbara Wodecki

Canada
Diane Gauthier

Czech Republic
Krystyna Samek

Italy
Chiara Piussi

Malaysia
Arnold Cheong

Ukraine
Nataliya Vovk

United Kingdom
Francesca Lawley-Hughes
Anu Manchanda
Ana Lucia Tres

United States
Robert Campbell
John Cason
Tameka Nicole Clark
Jessica Kramer
Jana Miyahira-Smith
Timothy Schuler
Geraldine Vest
Ryan Waddell
Heather Weishaar
Thomas Wendt

Answers
See pages 124–125 of the Spring 2020 issue for the questions.

1 (d), 2 (b), 3 (d), 4 (d), 5 (b), 6 (a), 7 (d), 8 (b), 9 (d), 10 (a), 11 (b), 12 (c), 13 (d), 14 (c), 15 (a), 16 (b), 17 (a), 18 (a), 19 (d), 20 (c), 21 (b), 22 (c), 23 (c), 24 (c), 25 (d)

VIETNAM: SHELL NUCLEI, PEARL HATCHERIES, AND PEARL FARMING

Nicholas Sturman, Kwanreun Lawanwong, Nuttapol Kitdee, and Devchand Chodhry

A field trip to Vietnam in late 2019 permitted team members from GIA's Bangkok laboratory access to a shell nucleus manufacturing factory and two pearl farms managed by Orient Pearls (Bangkok) Ltd. The team was able to see how high-quality bead nuclei used on the company's own farms, among others, are produced from the raw shells shipped to Vietnam. The end product is used on both farms to produce a range of attractive Vietnamese bead cultured pearls suitable for use in fine-quality jewelry on a commercial scale. The incredible attention to detail required to produce the bead nuclei, and the subsequent application of these nuclei in the culturing process, must be seen in person to be truly appreciated. This account will help explain the shell nucleus manufacturing process, as well as the pearl farming activities witnessed on two Vietnamese pearl farms.

Vietnam is a land of great diversity and beauty. From the hustle and bustle of Ho Chi Minh City to the beauty of Hạ Long Bay and Hoi An (both UNESCO World Heritage Sites), there are innumerable places of interest. Economically, Vietnam is beginning to see significant investment from a wide range of businesses, domestic and foreign. While still dependent on agriculture, the country is emerging as a major player in the electronics and oil/gas industries, among others. These factors, together with a robust tourism industry, are resulting in an expanding population with greater prosperity than ever before.

Jewelry, including pearl jewelry, ranks high on the list of luxury items, as there is a significant range of price points at which disposable wealth can be spent. From the costume jewelry sector to high-end offerings, there is something to suit all tastes. While cultured pearls, accounting for 99.9% of the market since the early 1900s, do not usually fall into the higher-end bracket, there remains a healthy demand from consumers (Shor, 2007; Heebner, 2015). The choice of bead cultured pearls in the marketplace is also diverse. Consumers may choose from the usual imported gray to black Tahitian bead cultured pearls, "golden" bead cultured pearls from the Philippines or Indonesia, and bead cultured pearls produced in China.

Hạ Long Bay (figures 1 and 2) in northern Vietnam is where most pearl farms, producing predominantly "akoya" (*Pinctada fucata martensii*) pearls, may be found. These farms are a mix of independent operations and joint ventures with the Vietnamese government. A prime example of the latter is Spica, a Vietnamese-Japanese joint venture that has produced bead cultured pearls for more than a decade. Some farming activity is also found in the waters off southern Vietnam at Nha Trang, as will be seen later, and Phu Quoc (Strack, 2006).

Vietnam has produced saltwater cultured pearls commercially since the 1990s. However, the first attempts reportedly began in the 1960s (Strack, 2006). Today, based on the 300–400 kg production from the two farms visited in this report, the country is estimated to produce approximately 2,000 kg per annum. The majority of the production is akoya, with a smaller quantity of *Pinctada maxima*, and much of the production is currently exported to China, Japan, India, and the United Sates. When the harvests are good, the quality tends to be higher, but the opposite also holds true.

SHELL BEAD NUCLEI

One of the most important aspects of the culturing process is the sourcing of suitable freshwater shell bead nuclei to insert into the host mollusks, which deposits nacre around them and ultimately produces cultured pearls (Taylor and Strack, 2008). While this may appear to be a simple matter of finding any type of shell and fashioning beads from it, the truth of the matter is more complex and demanding than most people realize. The use of saltwater bead nuclei fashioned from clamshell (*Tridacna*-species mollusks) has been known to result in their cracking during the

Figure 1. A Vietnamese pearl farm employee busy with his duties in Hạ Long Bay. Photo by Nuttapol Kitdee.

Figure 2. Hạ Long Bay in northern Vietnam is a site of great beauty. A select number of pearl farms operate among the limestone casts. Photo by Kwanreun Lawanwong.

drilling process. This is just one example of why nucleus selection is critical to the end product.

Ideally, any shell used for the process should be as white and free of colored banding as possible. This is especially true in akoya farming, since the nacre deposition is usually thinner and the culturing time is not as long as for other *Pinctada*-species mollusks. Plain white beads of high quality are preferred, and these are costlier for farmers to purchase. Any brown, yellow, or gray bands or blemishes present in the bead will impact the final product's color since they will be notable, to some degree, in the thinner-nacred samples. Of course this is not such a concern with beads used in the production of Tahitian (*Pinctada margaritifera*) or some "golden" (*Pinctada maxima*) pearls where the nacre is usually thicker, especially in the latter, and the naturally occurring pigments mask the underlying beads more effectively than white nacre.

Devchand Chodhry, who manages two pearl farms in Vietnam and oversees others in Indonesia, wanted to start his own nuclei production facility to ensure a ready supply of high-quality white nuclei. Chodhry asked his associate at Witco Co. Ltd. to dedicate part of his garment factory in Hai Phong, a port city in northeastern Vietnam, to the establishment of this operation in December 2018. The shells imported from the United States (mainly Kentucky Lake in the state of Tennessee) are the *Megalonaias nervosa* (washboard), *Fusconaia ebena* (ebony), *Amblema plicata* (three-ridge), *Quadrula fragosa* (maple leaf), and species within the genus Pleurobema (pig-toe)[1]. These shells are sealed in bags and shipped by sea in containers owing to their gross weight (20 tons of shell per container). Prior to shipping, the most suitable material is sourced on behalf of Witco by a contact at Cam-

---

[1]A GIA field trip to source freshwater mussels and pearls for research from Tennessee in the United States provides further details on the mollusks; visit https://www.gia.edu/gia-news-research/freshwater-pearling-tennessee

Figure 3. Photos from inside the factory showing the stages of nuclei production. Bags of imported shell (A), sawing each valve to separate the thickest section for the larger beads (B), placing pieces of shell into a machine to cut into cuboid pieces (C), grinding the corners off the larger cubes by hand (D), inserting preformed nuclei into a machine that perfects the rounding process (E), sieving preformed nuclei (F), checking a new group of spherical nuclei (G), and the metal ball bearings used to produce the grooves in the stone discs (H). Photos by Nuttapol Kitdee (A, C, E, F, G), Nick Sturman (B, D), and Kwanreun Lawanwong (H).

den Corporation in Tennessee who has a wealth of experience handling shell and pearls in the United States. The contact has a long-standing business relationship with many of the divers in the United States and can source the quantity and quality of shell required for the Vietnamese operation. While freshwater shell is also available in India, China, and some other countries, the quality produced by the United States is more prized by the trade.

Upon receipt at the facility, the staff remove the shells from the bags and sort them into separate piles according to species (figure 3A). Processing begins with each half (valve) of the whole shell being sawn into two pieces (figure 3B). The thickest portion, from which the largest beads can be fashioned, is separated for use in the next step, which involves cutting each new portion into strips. A machine containing evenly spaced blades then cuts the strips

into separate cube-like pieces (figure 3C). Staff use vertical blades to round the corners of the larger cubes (figure 3D) in preparation for the next step in the process, which is grinding the final spherical beads between two stone discs. The smaller cubes used for the small nuclei do not warrant such painstaking attention, so they move to another machine that automatically rounds them to the desired form (figure 3E). Next, the large and small preformed nuclei are sized by sieving (figure 3F) and then pass on to a grinding process that involves a series of stone discs of different grain sizes, from coarse to fine grain, to finalize the shaping (figure 3G). The discs arrive at the factory unscored, so another step in the process is to create the evenly spaced grooves in which the shell bead nuclei eventually sit. This is done by placing metal ball bearings onto the correctly sized ring-shaped template base. The new blank disc is lowered so that the ball bearings make contact with it, eventually creating grooves in the new disc. Water is applied throughout the process (figure 3H).

The equipment in the factory is designed and tested by the experienced Witco team to improve productivity and efficiency. In this way, they can apply any improvement to the process and machinery to see if it has the desired effect.

After the grinding work is complete, the nuclei pass on to a room where a staff of predominantly women sit with Perspex-based trays on their laps and another group sits at a table with closed-sided trays. The trays are gently rocked from side to side to make the nuclei with the most perfect symmetry (roundness) roll into a basket on the floor (figure 4A). Nuclei that do not make the grade—the ones that do not roll smoothly enough—are removed by hand and returned to the previous grinding step, where their size is sacrificed for the sake of a more precise shape. Roundness is then double-checked using the closed-sided trays (figure 4B), and once they pass this step, nuclei are transferred to two wooden barrels (figure 4C), where they are exposed to a weak acid treatment. The acid removes the powdery surface texture (figure 4D) and, in effect, polishes them into a final product (figure 4E). The proprietary acid bath step is very important. Too strong an acid will cause the shell to crack and etch too quickly, while too weak a solution will not effectively smooth the bead surface.

Next in the nuclei's journey comes a final check of the shape precision and color/imperfection grading so that they may be sorted into high-quality nuclei lots with matching grades for use in specific farms around the world depending on requirements (refer to earlier comment on color/imperfections and types of mollusks on farms). The shape is checked one final time using a machine (figure 4F) developed by the Chinese pearl industry that has been slightly modified and is manufactured in Vietnam. It consists of two stacked rotating glass discs with simple boundary walls that allow the beads, which gently drop from the hopper onto the outer surface of the first glass disc, to roll along. If the nuclei are perfectly spherical, they will follow the wall and drop into a basket and pass the test. If, on the other hand, there are any small flat or uneven surface areas, they will not roll smoothly and will travel away from the wall in keeping with the motion of the rotating glass. Those that fail eventually exit on the opposite side of the disc and are taken back to the grinding step. It was very evident that the speed of the glass discs was critical to this part of the process and had to be continuously monitored. The Witco team was working to make the speed more consistent or at least reduce the range of speed, for variability is sometimes needed depending on the bead size.

Color/imperfection sorting, the last step in the process, takes place in the same room as the machine with the stacked glass discs. Nuclei are examined and split into groups of varying degrees of whiteness (figure 4G). The whiter the nuclei, the better the quality and the higher the selling price. Discussions made it clear that the factory's work has just begun and they already supply nuclei to quite a few farms. Production will be increased as steps in the process allow, and different sized nuclei will continue to be produced, although all the smaller nuclei are destined for the farms operated by Orient Pearls (Bangkok) in Vietnam. The more banded or off-white nuclei are typically sent to existing clients for the production of Tahitian bead cultured pearls, where the whiteness is not as critical as in Japanese and Vietnamese akoya production. It was interesting to learn that the maple leaf mussel produces the purest white beads needed for akoya production, while the washboard mussel produces the more banded (figure 4H) and hence less expensive nuclei that are acceptable to the Tahitian pearl farmers and farms where golden *Pinctada maxima* are produced.

Witco produces beads from 1.5 mm (0.49 Bu)[2] to 6.0 mm (1.98 Bu) from the thinner areas of the shells

[2]"Bu" is an ancient Japanese unit of length. In metric terms, 1 bu is equivalent to 3.03 mm.

Figure 4. Photos from inside the factory show the stages of nuclei processing. Quality checks by the staff to remove any nuclei that need further processing (A and B), wooden tumblers for removing the powder from the surface and imparting a final finish (C), matte-surfaced nuclei prior to insertion into the drums (D), significantly improved surface luster after drum processing (E), the machine that checks the roundness of the fully processed nuclei (F), the final color grading/sorting step (G), and a selection of washboard mussel nuclei showing clear yellow banding (H). Photos by Nuttapol Kitdee (A, C, E), Nick Sturman (B, D), and Kwanreun Lawanwong (F).

and from 5.0 mm (1.65 Bu) to 12.0 mm (3.96 Bu) from the thicker areas of the shells. The production of very small nuclei is unique to Witco. Orient Pearls (Bangkok) Ltd. uses the production for its own farms in Vietnam to create a niche market for smaller bead cultured pearls of various attractive colors, as will be seen later when the Nha Trang farm visit is covered.

By the end of the visit to the factory, it was apparent that the roundest shape and whitest color were the paramount objectives in nuclei production. Obtaining these two goals, however, requires considerable experience, trial and error, investment, and adaptability. It was also very surprising to learn that only 3.5–4% of the imported shell leaves the factory as nuclei. The target is to produce 5% or more, but that still means that much of the original shell is not suitable for nuclei or is wasted, further underscoring the challenges of nuclei production.

Figure 5. A POL staff member working on a series of wheel grinders to knock off surface growth from each shell. Photo by Nuttapol Kitdee.

PEARL FARMING IN HẠ LONG BAY

Vietnam's long coastline extends from Hai Hoa in the north to Dat Mui in the south. There are also many islands along this coastline, the most famous of which are located in Hạ Long Bay, where Pearl Orient Limited (POL) has a farm. Located a short boat trip from Dong Xa, the island (21°03′12.5″ N, 107°28′09.3″ E) is perfectly positioned: close enough to the mainland for vital supplies, yet far enough away from any significant activity, such as shipping or tourism-related matters, to be of any concern to the production of pearls in a suitably clean environment.

Because the island is uninhabitable, the staff stay on the mainland. POL operates a shuttle service early each morning prior to sunrise and a return service in the late afternoon. Only six to seven staff stay on the island each night to guard the premises. When morning arrives and the guards head home to catch up on sleep, the employees brought by boat are left to work on the mollusks awaiting them.

The farm employs about 140 people. The staff are split into various groups with specific duties to perform. These responsibilities range from cleaning the shells, preparing the shells for operation, cutting and preparing the mantle tissue from the donor mollusks, and nucleating/seeding the host mollusks to collateral tasks such as preparing meals for the staff.

The day starts with selecting shells for the donor mantle tissue (*saibo*) and the hosts in which the nuclei are inserted. The chosen shells are removed from the holding area for preparation. These are stock previously transferred from the nursery area (see later in the report). The shells are cleaned in a number of ways, using hand tools for scraping and wheel grinders (figure 5) that remove most of the associated organic growth. A two-minute soak in a saturated salt bath helps to kill any parasites living on the shells. Once these steps are complete, the shells are selected and separated by size into groups of 80–150, which are then placed in black plastic containers and returned to the sea to be monitored. Those that are ready for the operation are also placed in an ozone tank for around eight hours to remove any

bacteria and byssus[3] prior to transfer to the nucleation room.

When the mantle donor shells are ready, the staff quickly and expertly cut the desired section of mantle from each shell and trim away the outer fringe from the inner whiter area. They are mindful to remove any colored areas from the final small pieces of mantle that will be used in the nucleating process, since these have been shown to have detrimental effects (discoloration, off-shape pearls, and surface blemishes) on the final product. The pieces of mantle destined for the host shells are quickly coated in antiseptic to ensure they remain as healthy as possible until insertion in the mollusks.

The next step is the nucleating or seeding itself. With the akoya shells, only one operation is ever performed, unlike in *Pinctada maxima* where two or more operations may take place depending on certain scenarios. This is because the shells are smaller and have a shorter life span of only 4–6 years, whereas the *P. maxima* can live for 20–30 years. On POL's farm, each akoya mollusk is nucleated with between one and four shell nuclei, depending on the size of the nucleus. If the smaller sizes below 3.03 mm (1 Bu) are used, three or four beads are inserted into the host. For nuclei measuring 3.6–4.8 mm (1.2–1.6 Bu), two shell bead nuclei are inserted, while larger beads of 5.7 mm (1.9 Bu) or above are inserted singly into each host. The skill of the operators is critical in performing this work quickly and effectively, for the quality of the end product depends on their talents. It was notable that all the employees performing this step were women owing to the belief that they are able to perform this delicate operation with better results.

When one looks at an unopened *Pinctada fucata* shell, one side shows a concave surface near the lip area. This is considered the right-hand side. It is in the gonad protected within this area of the pocket that nuclei are implanted during the seeding operation. The actual placement of the nuclei within the gonad is also of critical importance. With small beads, the placement of the two, three, or four nuclei together with the corresponding individual pieces of mantle become even more critical. Incorrect positioning may result in twin pearls, low-quality pearls, or no pearls at all.

After the operations are complete, the mollusks are placed into suitably sized nets with strips of plastic tubing that prevent the mollusks from moving around freely. The nets are subsequently taken to a holding area to be monitored for approximately two to three weeks, or until the piece of mantle forms a pearl sac around the shell bead. Then they are transported to the longlines in the waters within the farm limits, where nature takes its course and layers of nacre are deposited in the pearl sac to form pearls before their eventual harvest. At the time of the visit, the farm's stock consisted of approximately one million shells: 100,000 were seeded with one nucleus, 450,000 with two nuclei, and 450,000 with four nuclei.

Although we did not visit during a designated harvest period, POL was kind enough to remove some akoya from their nets and show us the results. This quality check is carried out every month to monitor the health and progress of the mollusks from the various operation dates. Shells with one, two, and four nuclei were chosen, and in almost all cases the number of pearls matched the number of nuclei inserted. In a few examples, however, no pearl was found—not an uncommon situation—and in some of the dual or quadruple operations, an uncoated nucleus was removed. This clearly shows that the process does not always work and that nature makes its own decisions.

After the mollusks have been in the water for a few months, their health is monitored, as we witnessed on the day we visited, by pulling up the nets and making a quick inspection of a random sample. Healthy mollusks tend to show "fingers" on the lip fringe that are intact and protruding, while those that are not so healthy show the opposite. Sadly, dead shells are lifeless and already open. This is something no pearl farmer wishes to see, but it is an inevitable part of the farming process, and the mortality rates are monitored closely. Detailed record keeping of every stage of the seeding process, post-operative care, and eventual placement of each group of operated mollusk allows the staff to check the shells' progress prior to the scheduled harvest date.

As with all pearl farms, the mollusks also need to undergo regular cleaning. The farm uses two specialized cleaning boats, each mounted with a conveyor-type cleaning unit. The fouled nets and shells are pulled up and fed into the unit, which uses high-pressure water jets. Afterward, the nets with their shells are returned to the water, and the remnants of the cleaning process may be seen as a cream to beige stain spreading behind the vessel as it continues its way down each longline, cleaning every net sus-

---

[3]The mass of strong threads ("sea silk") secreted by some mollusks at the hinge end by which they are able to attach themselves to rocks and other stable surfaces.

Figure 6. Staff at the nursery placing nets containing Pinctada radiata *mollusks into the waters of Hạ Long Bay. Photo by Nuttapol Kitdee.*

pended. This process is laborious but vital to the whole operation.

On the way back to the harbor, we detoured to another area of Hạ Long Bay (21°01′37.5″ N, 107°27′35.6″ E), a short distance from the main farm, where the spat are cared for. In this area, a separate team checks the spat received from the Nha Trang farm where Pearls Vietnam Limited (PVL) has its hatchery. Sizes are checked using a sieve before transfer to triangular blue nets (figure 6), which are suspended under wooden rafts for monitoring. Only when they reach the right age of around one year are they moved to the main farm for the team there to start working on them in the way described earlier.

It was very interesting to note that POL is experimenting with *Pinctada radiata* mollusks sourced from the Middle East but obtained via Japan and subsequently sent to Vietnam. This group has strong links with Japan and this was clearly visible in all steps of the operation. The use of this mollusk seems a good choice, as it is more suited to warmer waters than *Pinctada fucata martensii*, and its faster nacre

deposition means that the nacre coverage is ultimately thicker. The possibility of producing hybrids is also being considered. The future certainly looks promising, and we may start to see a greater variety of Vietnamese pearl products in the market.

PEARL FARMING IN NHA TRANG

The PVL pearl farm is located in southern Vietnam (12°40′02.4″ N, 109°12′36.8″ E) around one hour's drive from the city of Nha Trang, a popular tourist destination. It is far away from the main sources of pollution encountered from a concentrated area of humanity. Like the POL farm in Hạ Long Bay, it focuses on the production of akoya pearls from the *Pinctada fucata martensii* mollusk and follows the steps detailed previously for the northern farm. However, there are differences between the two. PVL produces the brood shell stock in its own hatchery for both farms, and the ratio of colored pearls to white and cream ones is higher in the northern farm since a greater percentage of silver, gray, and blue pearls are produced there.

However, the obvious difference between the two farms is the plentiful fresh water supply on this mainland farm, presumably part of the reason it is used as the hatchery location as well. Although the mollusks live and breed in the marine environment, fresh water plays a crucial role in the cleanliness needed to limit infection in the breeding and grafting steps. The use of fresh water is therefore more prominent in the hatchery and pre-operation mollusk preparation than on the northern farm. Some interesting facts about the care and pre-operation preparation of the *Pinctada fucata martensii* on the PVL and POL farms (noting that there are differences with other mollusks and farms) include:

- When moved from the hatchery to the sea, the mollusks need to be cleaned once a month.
- The age at which they are seeded ranges between 9 and 12 months. On the day of our visit, the shells being operated on were 10 months old.

- Prior to the grafting process, they are placed in a freshwater tank (figure 7) for two hours to kill the saltwater parasites and other guests living on or in the surface layers of the shells. The mollusks can tolerate the fresh water by closing tightly, while the other organisms cannot survive this long in fresh water.
- The shells are quickly dipped into a strong salt bath to kill any parasites or bacteria. Salt is used in the same way during the cleaning process. They are submerged for two minutes.
- The ozone process carried out in one tank helps remove the "legs" or byssus.
- The mollusks are immersed in an anesthetic bath to relax them prior to seeding. The time spent in the bath varies very slightly between the two farms and also depends on the size of the shells. It usually lasts around 10 minutes on the POL farm and around 14 minutes on the

Figure 7. The saltwater mollusks are placed in freshwater tanks for around two hours to kill any parasites or organic growth on or within the outer surface layers. The PVL farm manager, Mr. Kado (pictured), is the driving force behind the farm's success. Photo by Nuttapol Kitdee.

PVL farm. The concentration of the anesthetic also varies from 47% on the POL farm to 46% on the PVL farm.

- The fully anesthetized mollusks are easy to spot, as their shells are open. The ones that are not fully open need to be pegged in preparation for the next step. However, even the fully relaxed and open mollusks eventually need to be pegged before the anesthetic begins to wear off.

- After the operation, the mollusks are suspended in a tank. Numbers on the variously colored tags identify the technician who carried out the seeding. This information is valuable, as not all technicians share the same skill level; some may produce a pearl with better shape or a higher percentage of a specific shape.

- The operational head technician, who is from Japan, stated that from his experience, the pearl sac takes five to seven days to form post-operation.

- The mantle used was from donor shells that were a month younger than the host.

- Before being placed in the sea post-operation, the shells are inserted into pockets in nets, and then each one is further inserted into two fine green mesh covers for protection. After one week, the first green net is removed, and a week after that the last green net is removed. This ensures that the pearl sac forms and the newly formed byssus stick with other shells and the host net. The formation of the byssus limits the shells' movement within the nets.

Most hatcheries are set up in a similar way (Cartier at al., 2012). They depend on producing larvae from the eggs and sperm of suitable parents and then closely monitoring and feeding the larvae and spat as they develop from the former to the latter. The PVL farm is no different in this respect, but the use of fresh water during some steps of the process seems to differentiate the hatchery and farm from their peers.

In the hatchery, we noted the typical darkened conditions in the area where the tanks holding the larvae and spat are situated, though more lighting is provided when staff or visitors are in the area. Various tools such as nets with varying mesh sizes for different stages of larvae to spat formation were on hand, and the tanks were oxygenated to ensure the survival of the spat. The spat generally start to attach themselves to structures after 20 days (Otter et al.,

2017). This is when they transform from the larval stage, where they are free-swimming organisms, to spat form. On the day of our visit, the spat were 25 days old. Although small, they could clearly be seen attached to the black plastic screens suspended in the tanks. To keep the hatchery free of possible contamination, staff and guests must wash their hands and feet with fresh water and detergent before entry. Staff also wear hairnets and masks to prevent potential contamination of the tanks. In this way, the larvae and spat can reach a suitable age (usually 35–45 days), at which point they are taken out to the sea just a few meters away to be suspended from the rafts and longlines in the baskets and nets.

Before they are able to reach the sea, the spat and their larval stage have to be fed. The rest of the hatchery rooms are dedicated to producing the different phytoplankton required for three different age groups. The larvae are fed *Pavlova lutheri* and *Isochrysis galbana* from birth, and after five days *Chaetoceres gracilis* is added for further nutrition. Meticulous work goes into ensuring that the right nutrients are produced in the numerous glass vessels lining the shelves of the air-conditioned rooms. The stock is kept under optimum conditions so there is always a supply of food for the larvae or spat at any given time.

When they eventually make it to the sea, they are monitored to ensure the best possible conditions in which to continue developing. Mortality rates must be kept at a minimum for farmers to have any chance of producing enough pearls to turn a profit. When other overhead costs such as staffing and general operation are taken into account, this becomes even more challenging. Every step of the process is important. Weather is an additional factor, one that pearl farms have absolutely no control over. Extreme weather can wipe out farms and destroy the longlines and mollusks in some areas of the world (the Philippines being a prime example), yet this is less of a factor in Vietnam. Sea conditions also play a role in the way the farm is operated. The water is shallower and the seabed muddier in the Nha Trang farm than in the Hạ Long Bay farm, which results in more frequent cleaning as the baskets and nets quickly become clogged with sediment. The fouling in Hạ Long Bay is linked more to the marine life that attaches itself to the shells and structures in which they are housed. Thus, as in the northern farm, cleaning vessels are used to periodically move along the longlines and free the mollusks of any unwanted sediment or growth. PVL uses four cleaning vessels, one on floats, to do this work on a slightly more frequent basis.

Figure 8. Pinctada radiata *spat upon removal from the sea during a quick check of their health. The long and prominent "fingers" extending from the shells' lips indicated they were in good health, and no obvious mortality cases were evident. Photo by Kwanreun Lawanwong.*

During our brief visit, we took a boat trip out to the longlines to see the mollusks and nets used at the various stages of their growth cycle. Although the majority of the mollusks were *Pinctada fucata martensii*, we were shown some *Pinctada radiata* (figure 8) that had recently arrived from the northern farm via Japan and been sourced from the Middle East. They were being cared for in order to see whether they could be reproduced in the hatchery at a later date once suitable parent stock was identified. The mollusks were enclosed in a fine hemp bag that covered a three-tiered structure on which the shells were sitting. They all looked healthy, and the plan was to introduce them,

as previously noted in the section on the northern farm, to see whether they would produce better pearls with thicker nacre given that they are a species that better tolerates warmer waters. Other stages of the growth cycle where mollusks were kept in different nets were also observed, as were some mollusks that had already been operated upon on different dates. Some contained a single bead, while other mollusks from different operation dates grouped in other areas of the farm's waters contained two or four nuclei.

Back on dry land, we witnessed the opening of some shells to see the results of earlier operations. Ten mollusks operated on in December 2018 were

Figure 9. One of the many bags of pearls kept in the farm's office before being sent to Bangkok. The range of colors is very evident, and the white to yellow pearls are the most desirable range for Orient Pearls' end products. There is also a healthy demand for the silver, gray, and blue colors. Photo by Nuttapol Kitdee.

checked first, and the outcome of the eight-month formation period was the harvesting of ten pearls ranging from white to light yellow. The nacre condition looked good during the duration of growth permitted prior to their extraction. Ten mollusks from three other seeding operations were also opened in our presence, and we witnessed the removal of pearls from a two-nuclei operation and pearls from a couple of four-nuclei operations.

The final part of the day was spent in the office inspecting the bags of production (figure 9) from the safe and watching the sorting process. The quantity of pearls was impressive, and this was because the northern farm's production is sent to the southern pearl farm post-harvest for sorting. Here the staff check for the usual criteria—size, shape, color, luster, and surface imperfections—before grouping them into lots for further inspection during Chodhry's regular visits. After his inspection, they are shipped to Orient Pearls (Bangkok) for further sorting and pro-

cessing before ultimately being used in all types of jewelry for sale and distribution globally. Orient Pearls (Bangkok) is particularly proud of its range of uniquely small (1.5 to 5.0 mm) akoya cultured pearls ranging in color from white to yellow, as well as the greater quantities of similarly sized silver to light gray akoya with a bluish appearance produced at the northern farm. It is not very clear why there should be such a difference in colors when the mantle choices from the donors are similar, as are the hosts, and the techniques employed through the husbandry and farming processes are consistent. A visiting manager from the southern farm on the day of our visit suggested that the bluish color of the pearls results from the effects of bacteria in the northern farm's waters. Staff noted a greater variety of marine life and parasites in the waters of Hạ Long Bay than those of the southern farm. This is still a subject of discussion and could be an interesting case study going forward, since it is outside the scope of this field report.

SUMMARY

Vietnam is clearly a cultured pearl producer of note and, to a lesser degree, a source of shell bead nuclei. While there are a number of pearl farms in the north and a few in the south producing mainly akoya pearls, there is only one shell nucleus factory the authors are aware of today. The detail and commitment required to turn shell valves into high-quality bead nuclei on a consistent basis, and for the same nuclei to eventually end up in the center of bead cultured pearls, was evident from our time in Vietnam. All pearl farms operate along similar lines (Cartier et al., 2012; Sturman et al., 2016), yet it is also fair to say that they all have their own traits and quirks that differentiate them from one another. Whether it is the way the parents and spat are handled by hatcheries (which are not available at all farms), the subtle differences in the methods used to prepare the mollusks pre-operation, or the techniques employed in the grafting process itself, there is always something to learn from visiting a pearl farm.

The chance to witness this process close-up can be appreciated by anyone given such an educational and enjoyable opportunity. This report hopefully educates those unable to visit pearl-related sites in person, provides a valuable reference to those who have visited other farms, and proves how much dedication (financial and personal) is needed to run such ventures on a commercial basis. To this end, Chodhry noted that after 19 years, the Hạ Long Bay farm was only just starting to be cash-flow positive, illustrating this point. Pearl farming in particular is hard work, but all the farmers met by the lead author said, without exception, that the effort and expense are worth the results.

ABOUT THE AUTHORS
Mr. Sturman was formerly senior manager of pearl identification, Ms. Lawanwong is an analytical technician, and Mr. Kitdee is a digital imaging technician, at GIA in Bangkok. Mr. Chodhry is chairman of Orient Pearls (Bangkok) Ltd.

REFERENCES

Cartier L.E., Krzemnicki M.S., Ito M. (2012) Cultured pearl farming and production in the Federated States of Micronesia, *G&G*, Vol. 48, No. 2, pp. 108–122 http://dx.doi.org/10.5741/GEMS.48.2.108

Heebner J. (2015) Shell game. *Jewelers Circular Keystone*. Vol. 166, No. 9, pp. 100–103.

Otter L.M., Agbaje O.B.A., Huong L.T.-T., Häger T., Jacob D.E. (2017) Akoya cultured pearl farming in eastern Australia. *G&G*, Vol. 53, No. 4, pp. 423–437, http://dx.doi.org/10.5741/GEMS.53.4.423

Shor R. (2007) From single source to global free market: The transformation of the cultured pearl industry. *G&G*, Vol. 43, No. 3, pp. 200–226, http://dx.doi.org/10.5741/GEMS.43.3.200

Sturman N., Bergman J., Poli J., Homkrajae A., Manustrong A., Somsa-ard N. (2016) Bead-cultured and non-bead-cultured pearls from Lombok, Indonesia. *G&G*, Vol. 52, No. 3, pp. 288–297, http://dx.doi.org/10.5741/GEMS.52.3.288

Strack E. (2006) *Pearls*. Rühle-Diebener-Verlag GmbH, Stuttgart, Germany, 708 pp.

Taylor J., Strack E. (2008) Pearl production. In P.C. Southgate and J.S. Lucas, Eds., *The Pearl Oyster*. Elsevier, Oxford, UK, pp. 273–302.

Lab Notes

Editors
Thomas M. Moses | Shane F. McClure
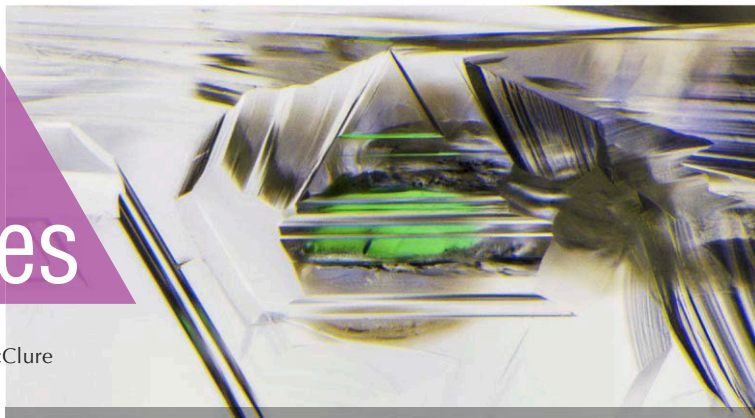
Dramatic Color Zoning in ALEXANDRITE

An 8.55 ct alexandrite was recently submitted to GIA's Bangkok laboratory. Standard gemological testing yielded a refractive index of 1.745–1.754 and a specific gravity of 3.73. The stone displayed a change of color from green in daylight to reddish purple in incandescent light (figure 1). All of these properties were consistent with alexandrite.

Microscopic examination revealed natural fingerprints, needles, zoned particles, and color zoning, along with internal growth features. Interestingly, the stone showed a thin color zone very close to some of the pavilion facets and culet when immersed in methylene iodide (figure 2).

Testing with a handheld spectroscope and ultraviolet-visible (UV-Vis) spectroscopy revealed chromium (Cr^{3+}) features. The absorption feature assigned to Cr^{3+} was located at 680 nm, with a broad band around 589 nm (figure 3). In contrast, when examined from the side (girdle to girdle), no Cr^{3+} feature was detected. This confirmed that color zoning at the culet strongly affected the color of this stone and its color-change effect.

The cutter designed the gem to contain the thin color zone along the pavilion facets and culet to display a
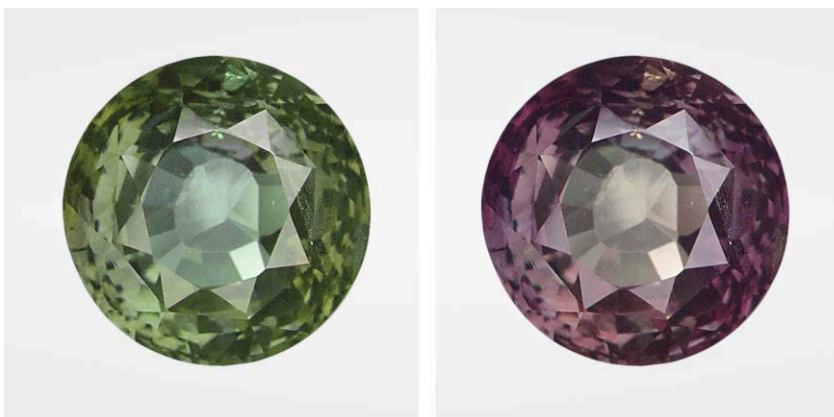
Figure 1. The 8.55 ct alexandrite in daylight (left) and incandescent light (right).

color change when viewed face-up. Without the Cr^{3+}-containing color zone, this stone would be chrysoberyl.

This example illustrates that orienting a color zone with the right trace elements combined with proper cutting can affect the variety designation of a gem.

Vararut Weeramongkhonlert

Novelty Cut DIAMOND with Remarkable "Fire and Ice" Fluorescence

A 0.37 ct Fancy yellowish brown diamond (figure 4, left) was recently submitted to the Carlsbad laboratory for Color Origin and Identification service. This novelty cut, faceted to resemble a dagger or sword, was

Figure 2. Viewed in immersion, the alexandrite displayed color zoning when viewed table-down (left) and from the side (right); field of view 12.5 mm.
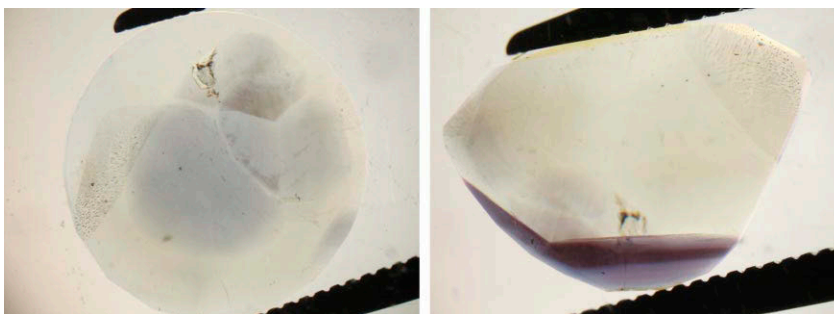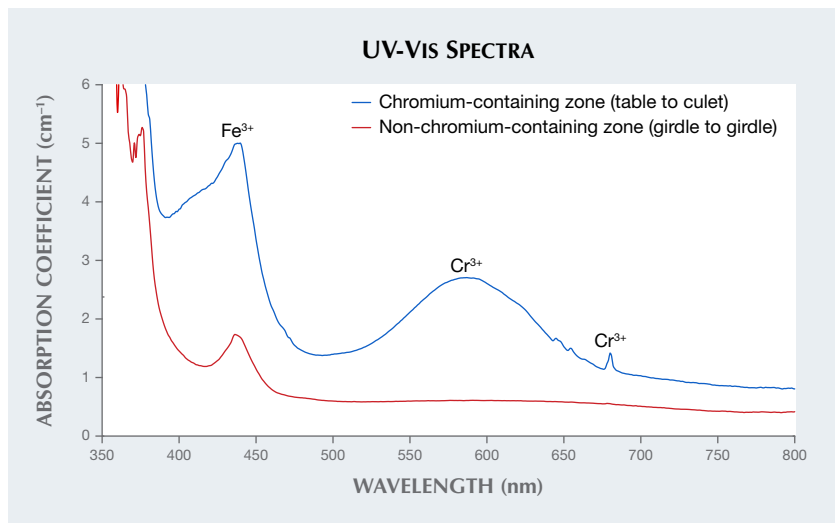
UV-VIS SPECTRA

Figure 3. UV-Vis absorption spectra of the alexandrite from table to culet (chromium-bearing color zone) and girdle to girdle (non-chromium-bearing color zone).
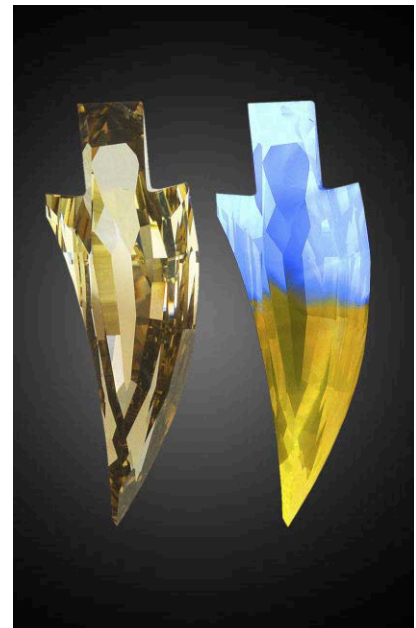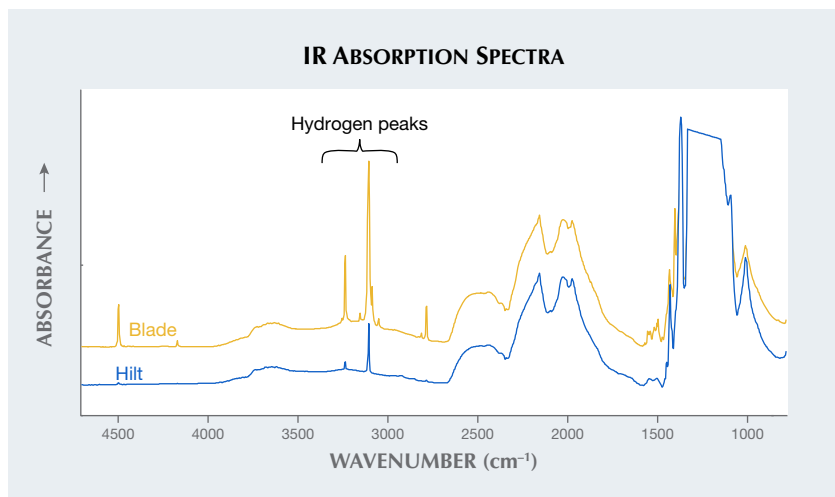

Figure 4. This 0.37 ct Fancy yellowish brown diamond (left) contained a remarkable hydrogen cloud in the "blade" and cape features in the "hilt." The stone showed corresponding areas of yellow and blue fluorescence in long-wave UV (right).

remarkable for its well-defined hydrogen-rich and cape regions, which created a distinctive fluorescence pattern. The "blade" section of the diamond fluoresced a strong yellow color, while the "hilt" fluoresced a strong blue (figure 4, right). As a result, we thought this diamond was an interesting interpretation of a lightsaber.

Microscopic examination showed that throughout the yellow-fluoresc-ing area were cloud inclusions, consisting of a high density of light-scattering micro-inclusions that correlate strongly with the presence of hydrogen. These are often called "hydrogen clouds" due to their coincidence with notable concentrations of hydrogen-related defects (W. Wang and W. Mayerson, "Symmetrical clouds in diamond—the hydrogen connection," *Journal of Gemmology*, Vol. 28, No. 3, 2002, pp. 143–152).

The infrared absorption spectra showed a type Ia diamond with saturated concentrations of nitrogen. Spectra recorded from the individual sectors were consistent with the gemological observations, as the yellow-fluorescing section containing the "hydrogen clouds" did show significantly more hydrogen than the blue-fluorescing area (figure 5).

To better understand the defects creating the dramatic difference in both the observable color in daylight and the fluorescence color under long-wave UV (figure 6), we performed photoluminescence (PL) mapping using 455 and 532 nm excitation at liquid nitrogen temperatures. The maps revealed distinct differences between the two areas. The yellow-fluorescing area showed peaks at 603 nm, a doublet at 641 and 645 nm, and a strong peak at 700.5 nm in the 532 nm PL spectra (figure 7). These peaks

Figure 5. The infrared absorption spectra of this type Ia diamond show weak hydrogen bands in the "hilt" (blue line) and high hydrogen content in the "blade" (yellow line). The spectra are stacked for clarity.
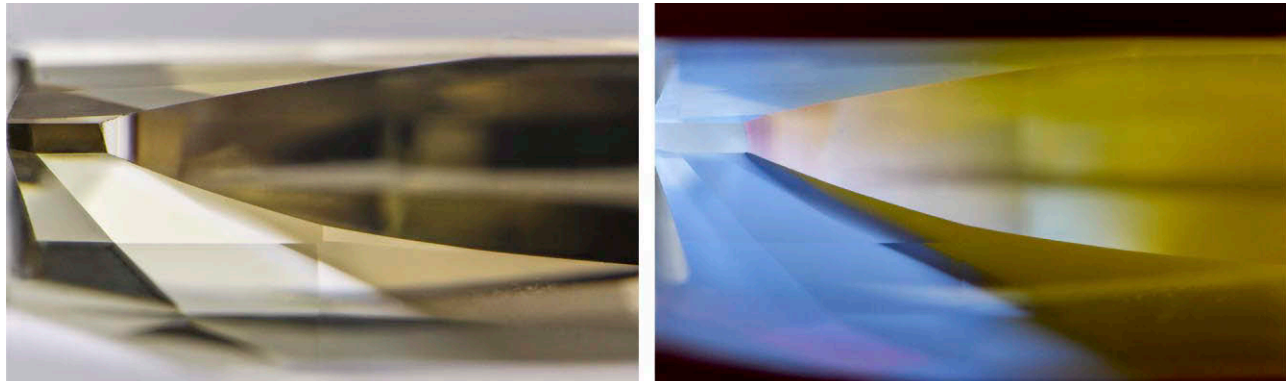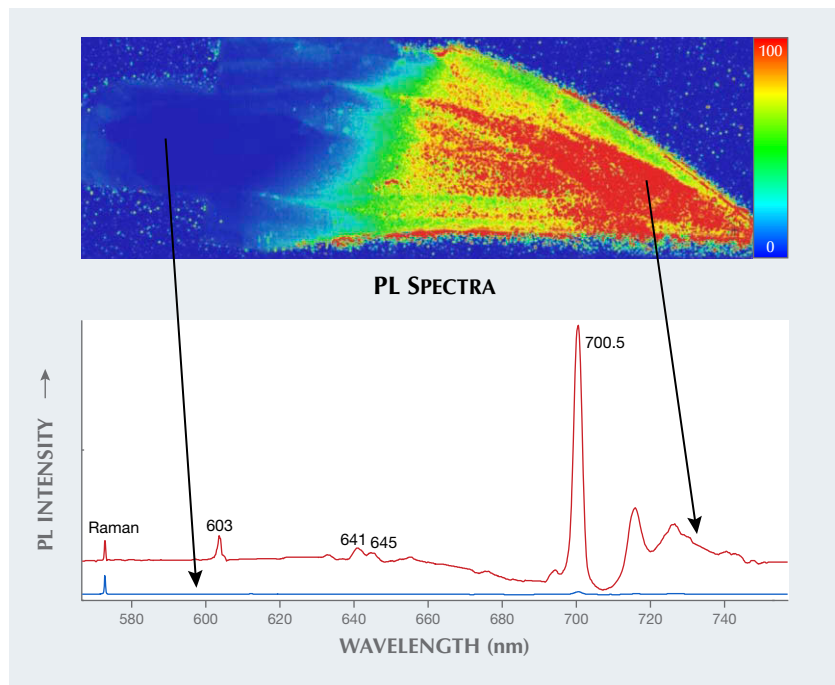
Figure 6. The distinctive separation line between the light yellowish brown cape section and the brown hydrogen section (left) matches the boundary between the blue and yellow fluorescence under long-wave UV (right); field of view 3.59 mm.

have all been ascribed to nickel and are often seen in hydrogen-rich diamonds (K. Iakoubovskii and G.J. Adriaenssens, "Optical characterization of natural Argyle diamonds," *Diamond and Related Materials*, Vol. 11, No. 1, 2002, pp. 125–131; S. Eaton-Magaña et al., "Inclusion and point defect characteristics of Marange graphite-bearing diamonds after high tempera-ture annealing," *Diamond and Related Materials*, Vol. 71, 2017, pp. 20–29). The blue-fluorescing area only shows a very small peak at 700.5 nm in the 532 nm PL map.

For PL spectra collected at 325 nm excitation, the N3 center is the major feature within the blue-fluorescing area, while a broad band centered at ~550 nm dominates the yellow-fluorescing area (figure 8). Also detected were peaks at 488 nm (ascribed to nickel; I.A. Dobrinets et al., *HPHT-Treated Diamonds*, Springer, 2013), 522 nm (unassigned), and the 603 and 700.5 nm peaks mentioned above. The yellow-fluorescing area also showed elevated intensities of the 490.7 nm peak (a natural feature in type Ia diamonds) in the 455 nm PL map and peaks at 926 and 948 nm (features also often seen in diamonds enriched with hydrogen and nickel; Eaton-Magaña et al., 2017) in the 830 nm excitation PL spectra.

Gemological and spectroscopic examination yielded interesting features such as this diamond's two distinct growth chemistries. The blue-fluorescing area had few inclusions and the typical fluorescence and PL spectroscopy of a cape diamond. The yellow-fluorescing side had higher hydrogen-related peaks in the infrared, hydrogen cloud inclusions, and pronounced nickel-related peaks in the PL spectra that are often seen in hydrogen-rich diamonds.

Figure 7. Top: This PL map shows the false-color intensity of the 700.5 nm peak area (ratioed to the diamond Raman peak) using 532 nm excitation at liquid nitrogen temperature; this feature ascribed to Ni is concentrated within the yellow-fluorescing area of the diamond. Field of view 9.2 mm. Bottom: Representative PL spectra from the "blue" and "red" regions of the 532 nm PL map. The lines are stacked for clarity, and the diamond Raman peak intensities (573 nm) are scaled equivalently.
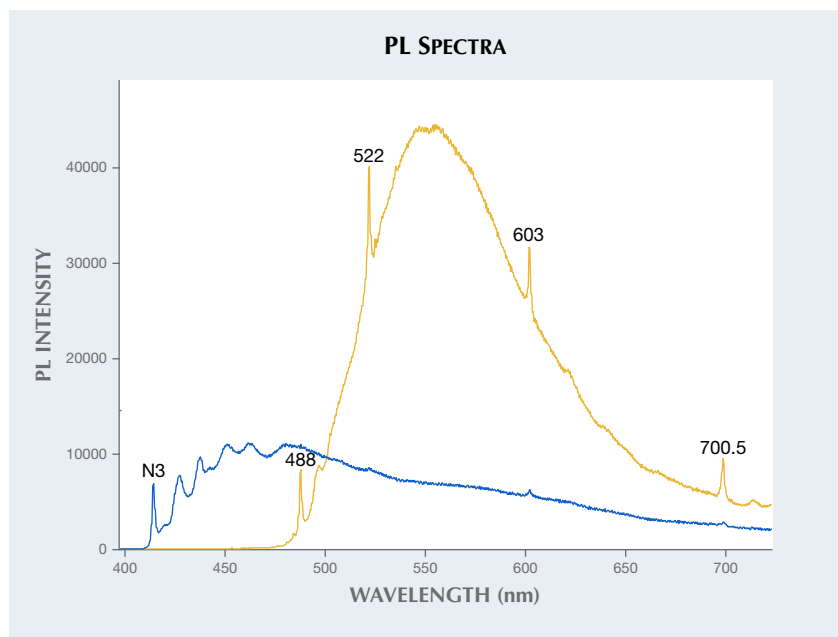
PL Spectra

Figure 8. These two PL spectra were collected with 325 nm excitation at liquid nitrogen temperature from the blue- and yellow-fluorescing regions. Due to limitations of the optics, we were unable to collect the diamond Raman peak along with the visible range luminescence; however, the two spectra were collected with the same laser power and plotted on the same scale.

Figure 9. The 60.71 ct diaspore displaying color change and chatoyancy under fluorescent light (left) and incandescent light (right).

The cutting style of this diamond, while unconventional, served to showcase the remarkable fluorescence scene illuminated within. The fluorescence differences allow this diamond to be imagined as a lightsaber or a sword of fire and ice.

Maryam Mastery Salimi and Sally Eaton-Magaña

Color-Change Cat's-Eye DIASPORE

A 60.71 ct cabochon was recently submitted to the Tokyo lab for identification (figure 9). Diaspore, α-AlO(OH), is one of the main aluminum minerals in bauxites, along with gibbsite, γ-Al(OH)$_3$, and boehmite, γ-AlO(OH). It is often observed as inclusions in rubies. Diaspore is also a gem in its own right, although it is very brittle and has perfect cleavage. The birefringence blink method revealed refractive indices of 1.69 and 1.74 and that the stone was biaxial. A dichroscope revealed strong trichroism: yellowish green, purple, and brown. The Raman spectrum was consistent with diaspore in the RRUFF reference database (R060287).

The hue of this stone changed from greenish yellow under daylight or fluorescent light to pinkish brown under incandescent light. Diaspore's color change can be caused by the chromophores Cr^{3+}, V^{3+}, and Fe^{2+}–Ti^{4+} pairs (C. Shen and R. Lu, "The color origin of gem diaspore: Correlation to corundum," Winter 2018 *G&G*, pp. 394–403). Color-change diaspores are sometimes known in the trade as "Zultanite" or "Csarite."

Chatoyant phenomena are usually the result of many long, thin, and closely spaced parallel needles or fibers, combined with cutting of a cabochon in the correct orientation to optimize the reflection of light off of these parallel inclusions. In this stone, the chatoyancy was caused not only by needles and/or tubes but also by the combination of iridescent reflective thin films or fissures in various shapes from ultrafine to wide, aligned along repeated cleavages (figure 10). Although some fissures reached the surface, no clarity

Figure 10. Needles and/or tubes with iridescent reflective thin films or fissures producing chatoyancy under brightfield and overhead illumination (left) and overhead illumination only (right); field of view 13.60 mm.
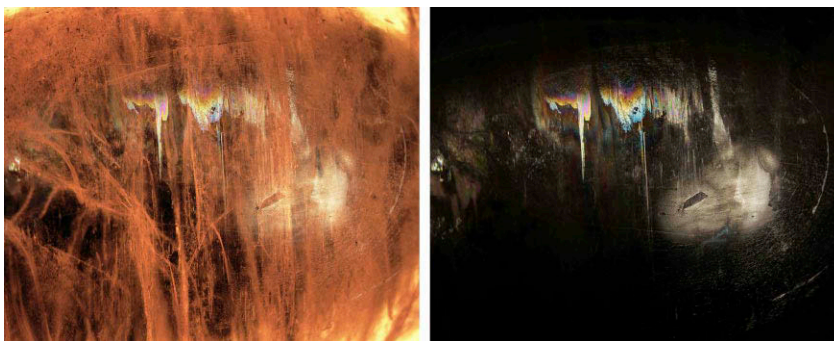
Figure 11. The red dashed line follows the edges of a large quartz crystal found breaking the surface of this 2.98 ct emerald.

enhancement was detected in this diaspore.

Taku Okada

EMERALD with Large Quartz Inclusion

A 2.98 ct emerald with a large, surface-reaching quartz inclusion was recently examined at the Carlsbad laboratory. The inclusion followed the red dashed outline shown in figure 11.

The discovery was made upon taking a refractive index reading on the table of the emerald. As the stone was rotated on the hemicylinder of the refractometer, the reading alternated between 1.581–1.590 and 1.545–1.550, typical refractive indexes for emerald and quartz, respectively. Upon microscopic inspection, a large colorless crystal was seen breaking the crown surface of the stone. This inclusion was further documented via photomicrography using both reflected and transmitted light (figure 12). The colorless crystal was conclusively identified by Raman spectroscopy as quartz. Raman spectroscopy also revealed the identity of the abundant acicular crystals seen throughout the emerald as actinolite.

Quartz inclusions within emerald are not commonly seen but have been reported in the gemological literature. In the *Photoatlas of Inclusions in Gemstones*, Volume 3, by E.J. Gübelin and J.I. Koivula (2008), they are listed as possible inclusions found in emeralds from Brazil, Colombia, Russia, and Tanzania. Quartz has also been seen within Madagascar emeralds. This example shows the value of simple standard gemological instruments, such as the refractometer and microscope, as a means to help identify unusual inclusions.

Britni LeCroy

15.53 ct PEARL Discovered in Edible Oyster from the Ostreidae Family

A white, non-nacreous baroque pearl weighing 15.53 ct and measuring 19.54 × 13.26 × 11.57 mm (figure 13) was recently submitted to GIA's Carlsbad laboratory for examination. Information from previously observed non-nacreous pearls submitted to GIA suggested the pearl was of scallop origin—a member of the Pectinidae family. The supporting evidence included a calcite peak seen at 280 cm^{-1} with associated peaks at 712, 1085, and 1437 cm^{-1} in the Raman spectrum, combined with a patchy surface appearance. Additionally, energy-dispersive X-ray fluorescence (EDXRF) chemical analysis showed low levels of manganese (Mn), confirming a saltwater growth environment. Real-time microradiography (RTX) revealed its natural formation, with a growth arc structure that followed the pearl's overall shape and a rounded, slightly less radio-opaque core (figure 14).

The client later informed the laboratory that the pearl had been found in an edible oyster while eating at a restaurant. Unfortunately, the host shell had not been retained and no photographs had been taken upon initial discovery. Despite this, the client

Figure 12. Left: The subtle luster difference reveals a relatively large quartz crystal inclusion and quartz veins breaking the table of the emerald host in reflected light. Right: The quartz crystal was also viewed in transmitted light, although less visible contrast was noted. Field of view (left and right) 7.19 mm.
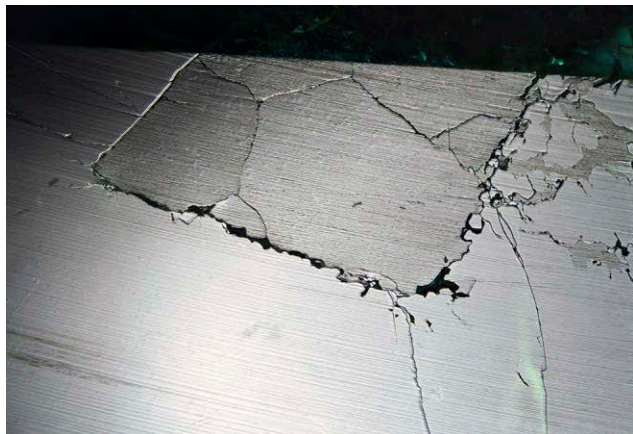
Figure 13. A white non-nacreous pearl weighing 15.53 ct and measuring 19.54 × 13.26 × 11.57 mm was found in an edible oyster, a member of the Ostreidae family.
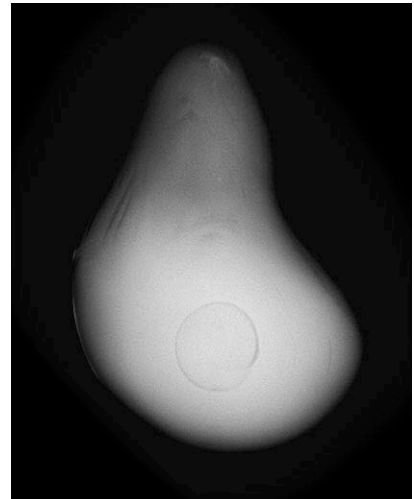

Figure 14. RTX imaging revealed a growth arc structure surrounding a rounded core of less radio-opacity, indicating the pearl formed naturally.

later returned to the restaurant to obtain shells from the two types of oysters served on their menu, the Pacific oyster (*Crassostrea gigas*) and the Atlantic oyster (*Crassostrea virginica*). Gemologists were able to use these shells to gather additional gemological information and compare the results to the submitted pearl.

Raman spectroscopic analysis verified that the shells were composed of calcite, and visual inspection showed nondirectional patches of a broad, mottled cellular structure bearing a striking resemblance to the pearl. However, these qualities are also seen in some white scallop pearls, as it is possible for them to contain a patchwork of directionless cells. A strong contrast, though, was seen in the microscopic surface appearance. The cellular structure within the oyster shells exhibited a slight reflective colored sheen in certain orientations when illuminated by a fiber-optic light, creating a faint iridescent phenomenon. This characteristic was nearly identical to the surface appearance of the pearl under examination (figure 15, left and center). Conversely, the individual cells of scallop pearls had a fibrous structure, and light reflected from them produced a shimmering sheen or silky appearance. This appearance has been noted to be a unique feature of scallop pearls in the literature (K. Scarratt and H.A. Hänni, "Pearls from the lion's paw scallop," *Journal of Gemmology*, Vol. 29, No. 4, 2004, pp. 193–203), and an example is shown in figure 15 (right). Such features were not observed on

Figure 15. Left: A microscopic view of the shell revealed a directionless patchwork of cells with an unstructured opaque white patch. The cells exhibited a faint iridescent phenomenon when illuminated by a fiber-optic light in certain orientations; field of view 9.87 mm. Center: A nearly identical appearance can be seen on the surface of the pearl; field of view 7.19 mm. Right: A differing mosaic pattern of non-oriented cells displayed on the surface of a white scallop pearl. Each cell contains a fibrous structure, and reflected light produced a unique shimmering sheen or silky appearance; field of view 5.08 mm.

Figure 16. Left: An overall patchy or mosaic pattern on the surface of the pearl; field of view 13.45 mm. Right: A similar appearance on the surface of a LaPearlite cabochon fashioned from an oyster shell; field of view 14.52 mm.

Figure 17. This 2.71 ct star peridot contained numerous magnetite inclusions.

the surface of the pearl under examination or the oyster shells.

The pearl and oyster shells also displayed translucency over most of their surfaces with randomly oriented opaque white patches. The cellular patchwork formation was faint or absent in these white patchy areas. This characteristic further supported their relationship (again, see figure 15, left and center).

Moreover, the angular mosaic-like appearance with areas of soft iridescence seen on the pearl closely resembled the surface of previously observed "LaPearlite" cabochons fashioned from oyster shells (figure 16; see also Summer 2018 Lab Notes, pp. 213–214). Lastly, it was also noted that the pearl, oyster shells, and LaPearlite samples all possessed layers of yellowish organic material covering part of their surfaces.

With supporting surface evidence from the oyster shells and the previously examined LaPearlite cabochon samples, gemologists were able to conclude that the pearl originated from the Ostreidae family, an edible oyster rather than a species of scallop, or member of the Pectinidae family. A few oyster pearls have been previously recorded in the literature (C.P. Idyll, "The pearls of Margarita," *Americas*, Vol. 19, No. 8, 1967, pp. 8–14; K. Scarratt et al., "A note on a pearl attached to the interior of *Crassostrea virginica* (Gmelin, 1791) (an edible oyster, common names, American or Eastern oyster)," *Journal of Gemmology*, Vol. 30, No. 1/2, 2006, pp. 43–50; Fall 2019 Gem News International, pp. 439–440).

Yet this is the first examination by GIA gemologists of a pearl known to have been produced from the Ostreidae family (true oyster) mollusk, as well as the first GIA pearl identification report for one. Additionally, the significant size and weight of this 15.53 ct pearl are noteworthy. Although oyster pearls are not of prime importance within the global pearl market, they are rare, curious novelties that can offer insight to the scientific pearl community.

Britni LeCroy and Artitaya Homkrajae

Magnetite Inclusions in Star PERIDOT

The Tokyo lab received a transparent yellow-green peridot displaying four-rayed asterism (figure 17). The 2.71 ct stone, measuring 9.94 × 7.88 × 4.08 mm, was reportedly from Myanmar. It had a spot refractive index of 1.64 and an SG of 3.29 and was identified as terrestrial peridot, which can be

Figure 18. The star peridot contained rectangular to needle-like magnetite inclusions responsible for the four-rayed asterism; field of view 2.50 mm.
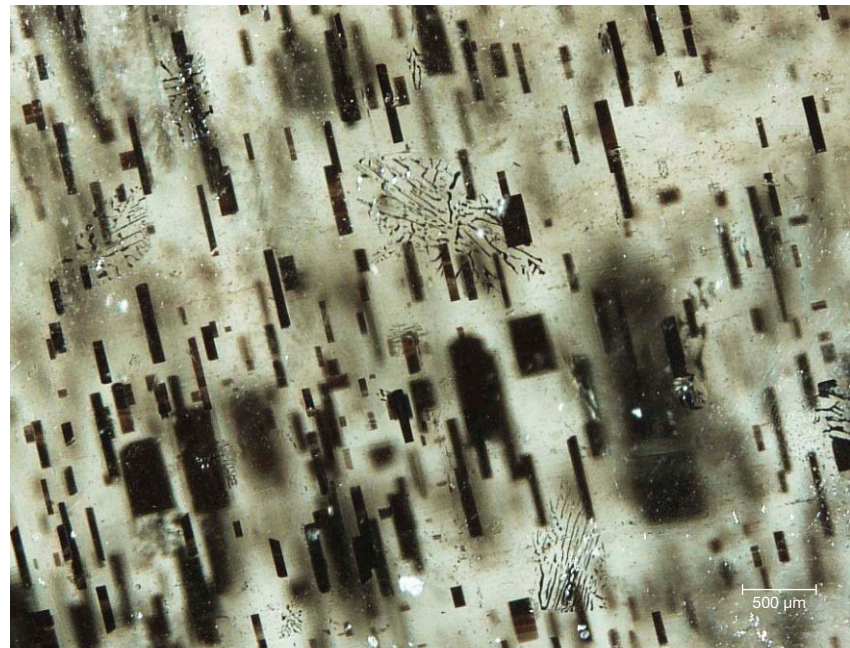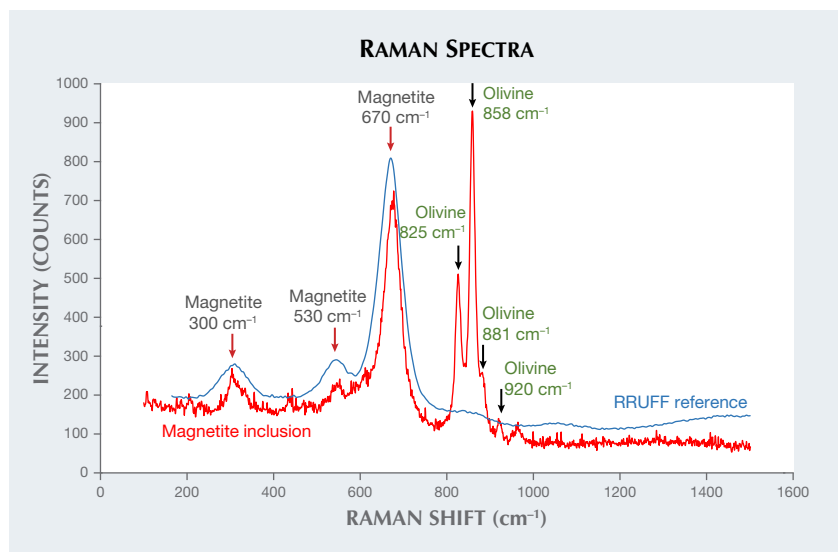
Figure 19. Raman spectrum of the magnetite platelet/needle inclusion in the star peridot, compared with a magnetite Raman spectrum (R080025) from the RRUFF database.

distinguished from pallasitic peridot by trace element concentrations.

The asterism of this stone was created by light reflecting from dark, rectangular platelets and needles (figure 18), which were visible without magnification. These were identified as magnetite by Raman spectroscopy (figure 19), namely the three broad bands at around 300, 530, and 670 cm⁻¹ (e.g., O.N. Shebanova and P. Lazor, "Raman spectroscopic study of magnetite ($FeFe_2O_4$): A new assignment for the vibrational spectrum," *Journal of Solid State Chemistry*, Vol. 174, No. 2, 2003, pp. 424–430), and its reaction to a magnet. These inclusions conforming to one crystallographic plane of the peridot were exsolution lamellae, which are interpreted to have formed by the exsolution of an iron-oxide component from the host peridot (olivine) by subsolidus reaction during cooling and/or decompression. (e.g., R.Y. Zhang et al., "Magnetite lamellae in olivine and clinohumite from Dabie UHP ultramafic rocks, central China," *American Mineralogist*, Vol. 84, No. 4, 1999, pp. 564–569). The inclusions in this peridot were larger and seemed to have a different shape from those in previously reported Burmese peridot (Spring 2020 Gems News International, pp. 159–160), which were more

acicular. Similar inclusions within a star peridot were also reported (Summer 2009 Lab Notes, pp. 138–139) but could not be identified by Raman spectroscopy due to interference from the host peridot. Although magnetite inclusions have been found in olivines (the mineralogical term for peridot) within some ultramafic and metamorphic rocks by petrological and mineralogical studies (e.g., Zhang

et al., 1999), it is notable that magnetite exsolution lamellae were identified in this star peridot using a Raman spectrometer. The difference in shape and size of the inclusions, however, could be due to the duration of the actual cooling and/or decompression time from the formation of the stone to its emplacement on the earth's surface. A longer emplacement time usually allows a longer time for the inclusions to grow larger.

Masumi Saito and Makoto Miura

Blue SPODUMENE

Recently this contributor received a light aqua blue stone that unexpectedly turned out to be spodumene. The following gemological properties were recorded for this 29.59 ct oval modified brilliant (figure 20): refractive indices of 1.661 and 1.676, birefringence of 0.015, a biaxial optic figure, and hydrostatic specific gravity of approximately 3.20. Pleochroism was observed using a linear polarizing filter, which revealed blue, yellowish green, and colorless trichroism. The RI and SG values were consistent with those reported for spodumene in the gemological literature. Magnification of this
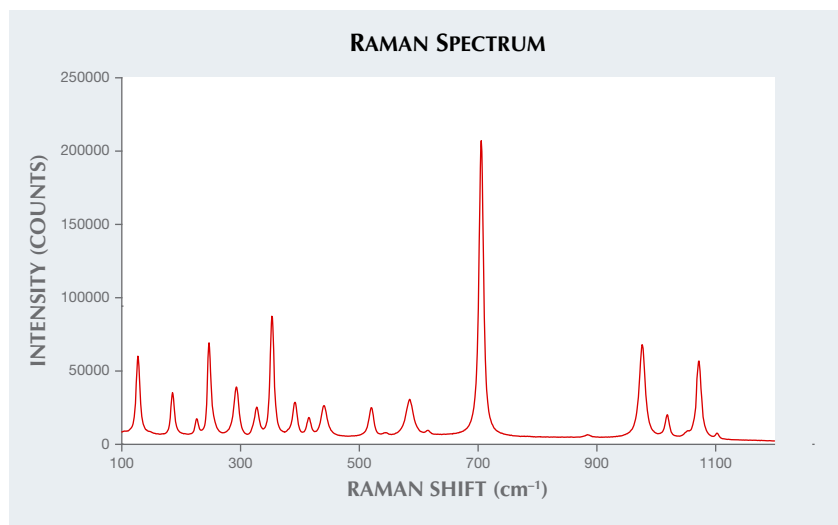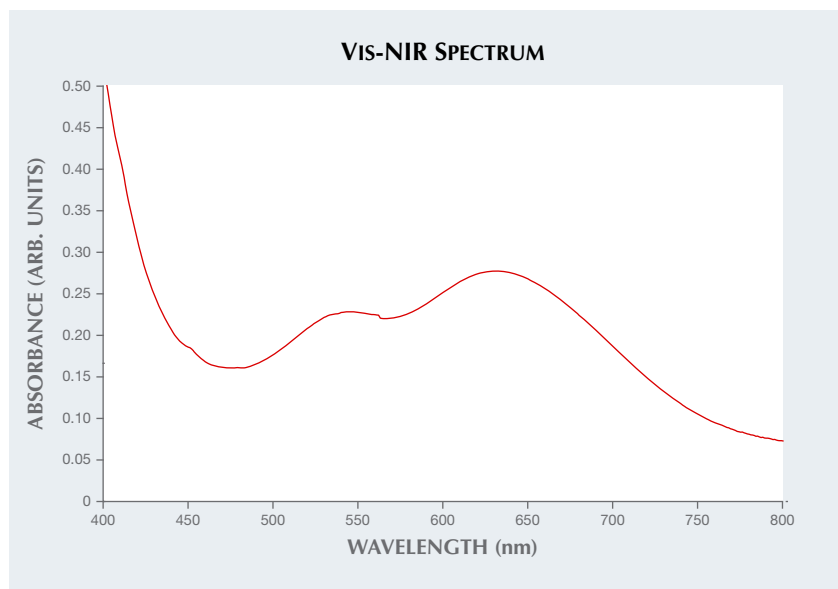
Figure 20. This 29.59 ct spodumene with light blue color is quite rare. It has been reported that exposure to sunlight changes this color to pink or purple.

RAMAN SPECTRUM

Figure 21. The light blue stone's Raman spectrum was consistent with that of spodumene published in the RRUFF database (R040050).

lithium aluminum silicate ($LiAlSi_2O_6$) showed parallel growth features, ripple-like internal graining, and most importantly two cleavage planes along the girdle edge. The identity of the stone was confirmed by further advanced testing. Its Raman spectrum (figure 21), with reference to the RRUFF database (R040050), proved that this stone was in fact spodumene.

Pure spodumene is colorless. Various colors may result from the presence of trace elements such as manganese, chromium, and iron, or sometimes from unstable color centers in its crystal structure. When mined, spodumene sometimes emerges from the ground with a blue-violet or green color that can be unstable in light and fade to pink in a relatively short time, sometimes in a matter of hours. This

suggests that the spodumene crystals have been exposed to some natural source of radiation (K. Nassau, *Gemstone Enhancement*, Butterworth-Heinemann, London, 1984, pp. 162–163). Blue spodumene has also been reported to result from artificial irradiation (G. Bosshart et al., "Colorimetric investigation of unstable and stable spodumene colours," *International Gemmological Conference 2011 Proceedings*, Interlaken, Switzerland, pp. 26–30). The Vis-NIR spectrum (figure 22) shows the bands at 543 and 637 nm, which are responsible for the blue color of the stone.

The main source of gem-quality spodumene is Afghanistan; other sources are Pakistan, Brazil, Madagascar, Mozambique, and the United States. While it is unknown whether the color of this blue spodumene was of natural or artificial origin, such stones are rarely seen as faceted gems, and this unusual large example would be of interest to any gem collector.

Forozan Zandi

SYNTHETIC MOISSANITE with Fraudulent GIA Inscription

GIA Johannesburg recently received a 1.02 ct round brilliant (figure 23) for a

Figure 22. The blue spodumene's Vis-NIR spectrum showed bands at 543 and 637 nm that are responsible for its color.

Figure 23. This 1.02 ct round brilliant with a fraudulent GIA inscription proved to be synthetic moissanite.
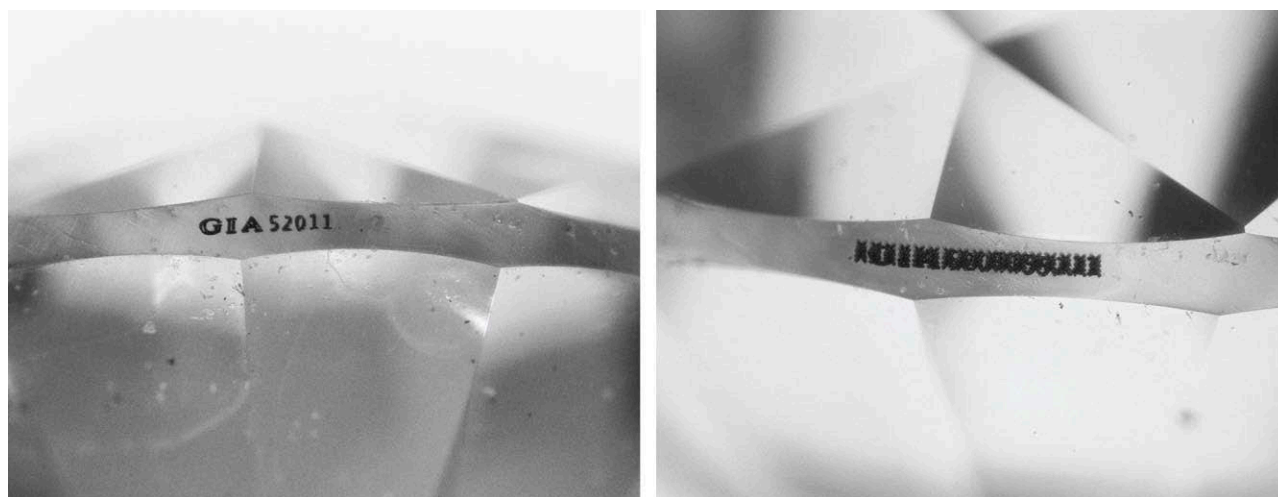
VIS-NIR SPECTRUM
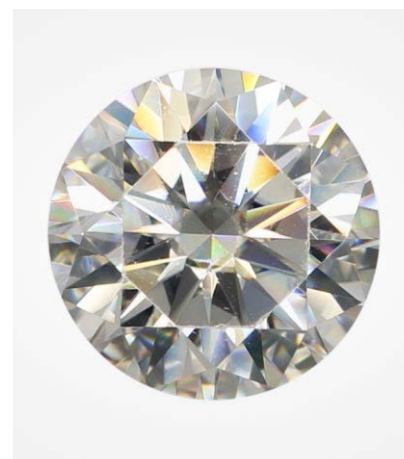
Figure 24. Left: The fraudulent inscription observed on the synthetic moissanite (the GIA report number is partially redacted in this photo for privacy). Right: GIA's standard procedure in these instances is to obscure the fraudulent inscription so it is no longer legible.

Diamond Grading report. Standard testing showed it was not a diamond, and subsequent spectroscopic and gemological analysis proved it to be synthetic moissanite. We often encounter simulants submitted for diamond grading, and they are easily detected through the standard grading process. This near-colorless synthetic moissanite was noteworthy because it had a fraudulent GIA inscription. GIA checks all stones with a preexisting inscription, and this one was obviously not inscribed by GIA. The report number does belong to an E-color natural diamond graded in 2019 with the same weight. But because of the dissimilar SGs of diamond and moissanite (3.52 and 3.22, respectively), their measurements were quite different.

Furthermore, the fraudulent inscription (figure 24, left) was distinctly different from GIA's standard inscription font. GIA's standard practice in such cases is to superimpose characters to obscure the original inscription (figure 24, right). The clarity would have been equivalent to VVS_2 (if such clarity grades were assigned to synthetic moissanite), while the clar-

ity of the graded natural diamond was VVS_1. The synthetic moissanite did not have any distinguishing inclusions, but it did show obvious double refraction in the microscope. Both IR absorption and Raman spectra confirmed the identification as synthetic moissanite.

In recent years, GIA has encountered similar instances of fraud. One was a synthetic moissanite that had been fashioned to resemble a natural rough diamond octahedron (Winter 2017 Lab Notes, pp. 462–463). That same year, an HPHT laboratory-grown diamond was submitted with a fraudulent inscription corresponding to a natural diamond (Fall 2017 Lab Notes, p. 366). However, this is our first instance of a fraudulent inscription on a diamond simulant.

Synthetic moissanite (SiC) is sometimes mistaken for diamond because some of its properties approach those of diamond, namely hardness and thermal conductivity (a trait measured in some instruments to distinguish diamond from many other simulants). However, several other properties are quite different from diamond, such as a much higher dispersion (leading to

more obvious fire) and double refraction. Nevertheless, the possibility exists that a consumer could purchase this simulant thinking it was a natural diamond, especially with a deliberately misleading inscription. In this case, careful examination protected the consumer against such attempted fraud.

Authors' note: Since the writing of this lab note, GIA Johannesburg has received and identified two more synthetic moissanites with fraudulent GIA inscriptions. They were handled in a similar manner.

Sicebiso Hlatshwayo and
Sally Eaton-Magaña

G&G Micro-World

Editor
Nathan Renfro

Contributing Editors
Elise A. Skalwold and John I. Koivula

Man-Made "Inclusion"?

Two important internal features in gemstones are inclusions and fissures. Inclusions are an important source of information in the gemological evaluation process. They can often provide indications about geographic origin (see, e.g., S. Saeseaw et al., "Three-phase inclusions in emerald and their impact on origin determination," Summer 2014 *G&G*, pp. 114–132); growth conditions (e.g., A. Cheilletz et al., "Time-pressure and temperature constraints on the formation of Colombian emeralds: An ^{40}Ar/^{39}Ar laser microprobe and fluid inclusion study," *Economic Geology*, Vol. 89, No. 2, 1994, pp. 361–380; J.G. Toloza et al., "Similarities and differences between fluid inclusions hosted by Colombian emeralds," *Special Issue on the 15th IAGOD Symposium*, 2018, pp. 166–167); natural or synthetic origin (e.g., N.D. Renfro et al., "Chart: Inclusions in natural, synthetic, and treated emerald," Winter 2016 *G&G*, pp. 402–403); and whether the stone has been treated to improve clarity.

Fissures are openings in the stones, and those "empty" spaces affect clarity in a negative way. Therefore, gemstones are treated to fill those gaps with different substances. Fillers can generate physical phenomena that resemble natural inclusions and may be misleading to the untrained eye.

Emeralds are most commonly enhanced with fissure filling. Fillers in emerald are identified by looking at the flash of color (blue, violet, orange, and yellowish) shown when the transmitted light of the microscope hits the inclusions or with the use of FTIR or Raman spectroscopy.

Recently the authors identified a man-made "inclusion" in a 1.15 ct cushion-cut Colombian emerald (figure 1) measuring 8.2 × 7.3 × 3.1 mm. It displayed a typical yellow flash most commonly seen in emeralds filled with liquid resin, which was later corroborated by FTIR spectroscopy. The "inclusion" was barely visible and almost transparent under regular microscope light sources (transmitted and reflected). Therefore, a 365 nm UV light was employed to check whether the foreign object fluoresced, and in fact it did (figure 2).

In the authors' opinion, the fiber could only have come from one of three sources: a cotton handkerchief, a microfiber jewelry cloth, or the net used during the immersion

Figure 1. Fiber inside a cavity filled with liquid resin in a cushion-cut emerald measuring 8.2 × 7.3 × 3.1 mm. Photomicrograph by Holman Alvarado.
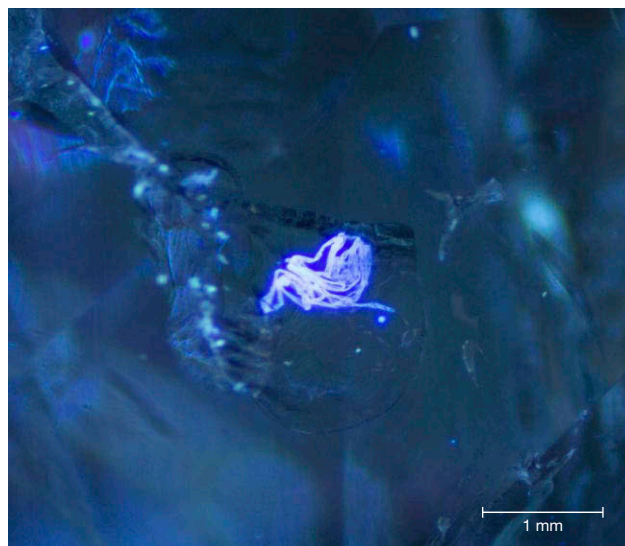
Figure 2. Fiber seen inside the cavity under 365 nm UV light at 50× magnification. Photomicrograph by Luis Gabriel Angarita.

of the stones in the enhancement container of the oiling machine. The first two would imply that a piece of fiber got stuck to the surface of the stone before the enhancement procedure took place, which is highly unlikely. The third source seemed the most plausible. In order to test that hypothesis, three strains of fibers were collected and compared using Raman spectroscopy with a Horiba HR Evolution with the laser operating at 532 nm. Although the spectra showed peaks in the 500 to 1500 cm^{-1} range, they were not specific for either of the fibers. Using the Olympus BX 41 microscope at 1000×, the diameter of the fiber was measured, and there was consistency with the diameter of the fiber collected from the net, about 50 μm. A

Figure 3. Three fibers under 365 nm UV light. A: Cotton handkerchief used to remove oil from the surface of the stone. B: Net fiber in which emeralds are placed for the enhancement process. C: Jewelry cleaning cloth also used to remove oil from the surface. Photomicrograph by Javier Toloza.
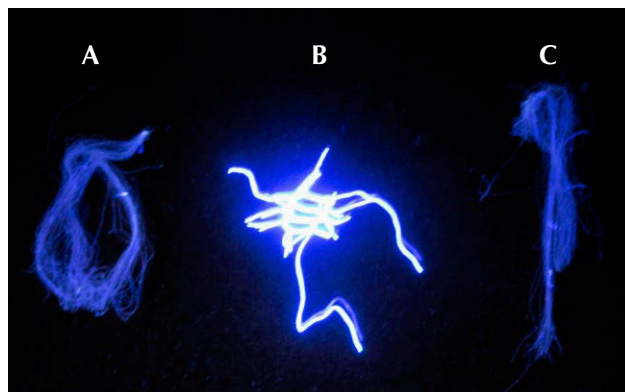
365 nm UV light source was also used to differentiate among them. A clear difference was evident between the nylon fiber from the net and the other two fibers (figure 3). This second test corroborated the authors' hypothesis.

Luis Gabriel Angarita, Holman Alvarado, and Javier Toloza
CDTEC Gemlab, Bogotá, Colombia

Manufactured Inclusions in Gem Materials

Inclusions in gems have gained popularity as social media has exposed collectors to a wide range of gem materials with interesting inclusions. As a result, there has been an increase in artificial inclusions in natural rock crystal quartz as predicted by E. Skalwold (Summer 2016 Micro-World, pp. 201–202). Recently, the authors had the opportunity to examine several unique gems with manufactured inclusions. Microscopic examination revealed that the main methods for manufacturing inclusions were carving, assembling, dyeing, three-dimensional internal laser engraving, or a combination of these methods.

A 47 ct rutilated quartz cabochon exhibits an eye-catching yellow and red floral-shaped inclusion produced by creative carving and filling with a colored composite material (figure 4). Microscopic examination revealed cir-

Figure 4. This 47 ct cabochon was creatively carved from the back, and the hollow cavity was then filled with a yellow and red composite material to highlight the floral inclusion. Photo by Robert Weldon; courtesy of Mike Bowers.
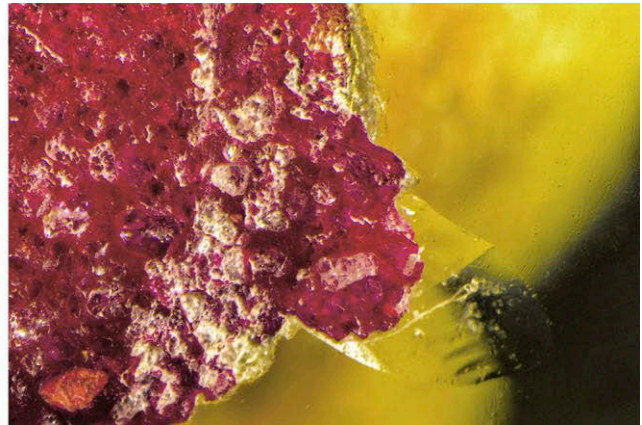
Figure 5. Tool marks from a rotary abrasive burr are clearly visible in this manufactured floral-shaped inclusion (left; field of view 9.72 mm). The cavity was subsequently filled with a yellow and red composite material consisting of sand grains and a colored binder or resin material (right; field of view 4.26 mm). Photomicrographs by Nathan Renfro; courtesy of Mike Bowers.

cular marks from a rotary abrasive tool used to create the intricate cavity (figure 5, left). The cavity was subsequently

Figure 6. This 226 ct round tablet of quartz contains an orange and yellow resin-filled fracture that convincingly imitates natural iron oxide mineral staining in quartz. Photo by Robert Weldon; courtesy of Mike Bowers.

filled with a yellow and red composite material of fine sand grains and a colored binder or resin (figure 5, right).

Another creatively manufactured inclusion in a quartz gem can be seen in a 226 ct round tablet containing a large fracture (figure 6). The fracture was filled with colored orange and yellow resin, which resembles natural iron oxide epigenetic staining sometimes seen in rock crystal quartz. A quick examination in the microscope revealed incomplete filling and trapped gas bubbles in the colored resin (figure 7), making the separation between this manufactured inclusion and its natural counterpart quite easy.

Creative dyeing also produced the manufactured inclusion in a 109 ct quartz with a completely enclosed green

Figure 7. A fracture in this rock crystal quartz has been filled with orange and yellow resin to give the appearance of natural iron oxide staining. Trapped gas bubbles make this manufactured inclusion readily identifiable. Photomicrograph by Nathan Renfro; field of view 8.94 mm. Courtesy of Mike Bowers.
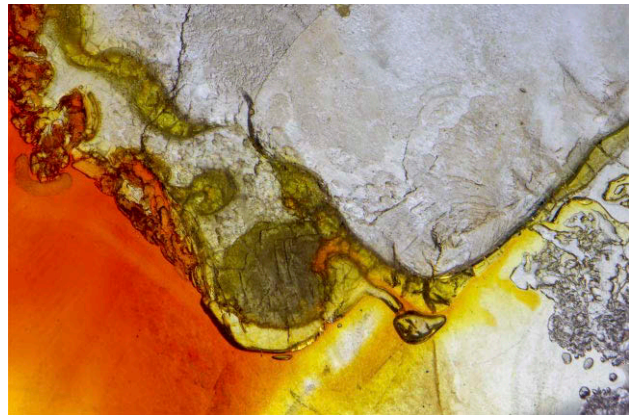
Figure 8. This 109 ct polished block of quartz has been assembled from two halves that contain numerous fractures filled with green resin. They have been glued together so that the moss-like inclusion is completely enclosed in the colorless quartz. Photo by Robert Weldon; courtesy of Mike Bowers.
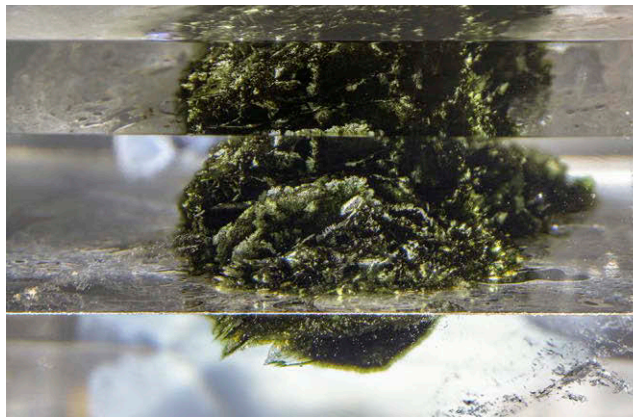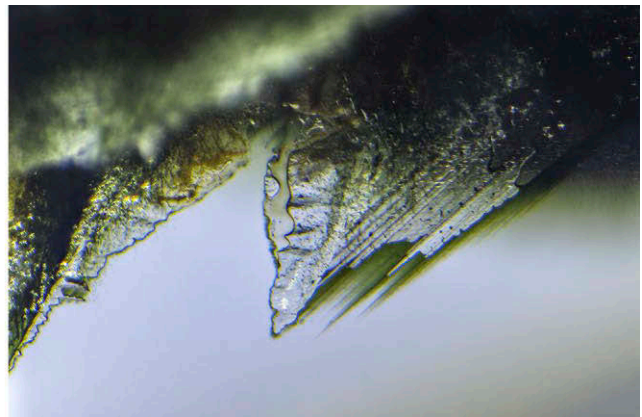

Figure 10. This 724 ct rock crystal quartz contains two manufactured inclusions induced by a 3D subsurface laser-engraving process. Photo by Robert Weldon; courtesy of Mike Bowers.

moss-like inclusion (figure 8). This stone consists of two pieces of rock crystal quartz, each with a centralized network of fine fractures that may have been artificially induced by laser, judging from their unnatural irregular pattern and striated appearance. The fracture network in each piece was subsequently filled with a dark green resin to give the appearance of a moss-like inclusion. The two halves were then glued together with colorless cement, completely enclosing the green moss-like inclusions in water clear rock crystal quartz. This left a somewhat obvious assembly plane (figure 9, left) when examined with the microscope, as well as trapped gas bubbles in the green resin-filled areas (figure 9, right).

The fourth example of manufactured inclusions recently examined is a 724 ct quartz crystal with a polished face that contains two white stellate inclusions consisting of numerous radial arms surrounding a spherical core structure (figure 10). Closer examination revealed a carefully layered series of micro-fractures consistent with 3D subsurface laser engraving (figure 11). This is by far the most technologically advanced example of a manufactured inclusion in a gem material examined by author NR.

While these four examples of manufactured inclusions may not be quite as sought after as gems with natural inclusions, they certainly can be appreciated for the efforts

Figure 9. This moss-like inclusion results from a fracture network in two pieces of rock crystal quartz filled with green resin and glued together to encapsulate the inclusion. The assembly plane of the two quartz halves is clearly visible on the side of the stone (left; field of view 18.80 mm). The green resin contained trapped gas bubbles, and the fractures displayed an unnatural striated appearance suggesting they were artificially induced (right; field of view 2.59 mm). Photomicrographs by Nathan Renfro; courtesy of Mike Bowers.
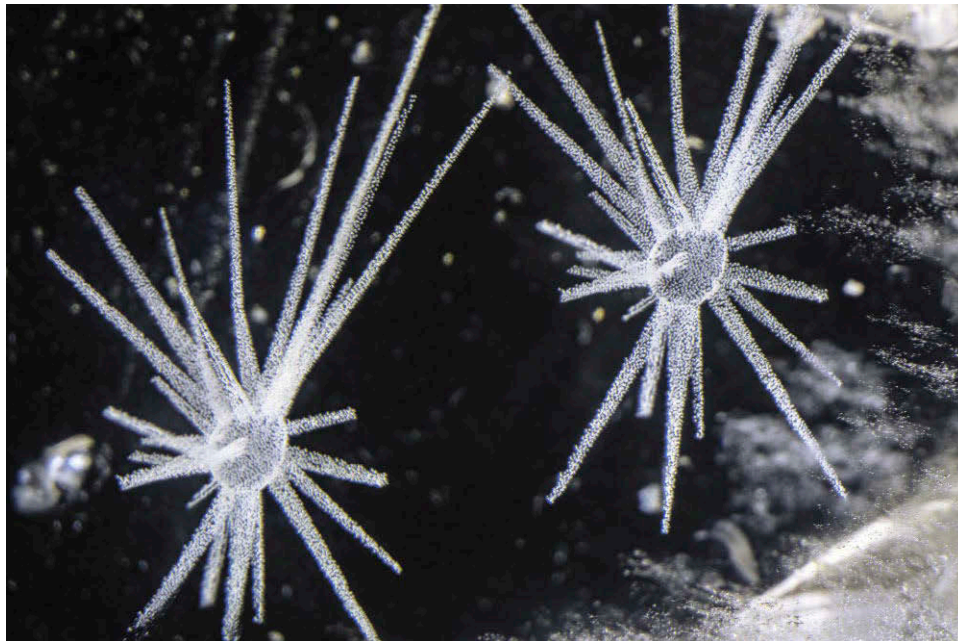
Figure 11. These stellate inclusions result from 3D subsurface laser engraving, which creates light scattering microfractures in a controlled pattern. These represent the latest advancement in manufactured inclusions within gem materials. Photomicrograph by Nathan Renfro; field of view 23.50 mm. Courtesy of Mike Bowers.

and techniques employed by the manufacturers. Obviously, collectors of gems that feature inclusions should be aware that manufactured inclusions such as those described here exist in the trade. While some manufactured inclusions may be intended purely as an artistic enhancement, others may be produced with the intention to deceive the consumer, and caution should be used if a manufactured origin is suspected.

Nathan Renfro and Robert Weldon
GIA, Carlsbad, California

Interesting "Egg" in Rock Crystal Quartz With Rutile

The micro-world of gemology is fascinating and often mimics scenery, landscapes, or, in this case, food. Recently the authors examined a natural rock crystal quartz that showed needles piercing a yellow and white circular inclusion (figure 12). The inclusion mimicked a fried egg and was seen during microscopic examination using fiber-optic lighting. The "egg" was actually an example of epigenetic residue surrounding a rutile needle trapped in a crack
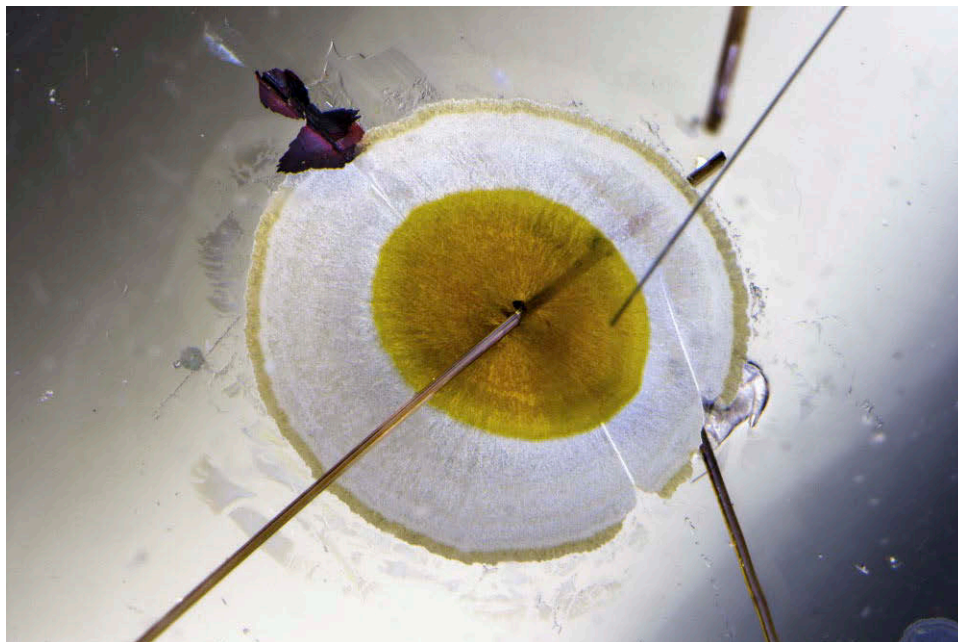

Figure 12. Rutile needles extending outward from epigenetic growth in rock crystal quartz. Photomicrograph by Nathan Renfro; field of view 8.81 mm. Courtesy of Mike Bowers.

within the host crystal. Here the rutile, a mineral composed primarily of titanium dioxide (TiO_2), is a syngenetic inclusion, having formed at the same time as the host quartz crystal, and the "egg" formed its circular shape after the rutile and quartz growth stopped. The epigenetic residue in this stone results from secondary fluids that enter surface-reaching fractures (see descriptions and images of inclusions in quartz in E.J. Gübelin and J.I. Koivula, *Photoatlas of Inclusions in Gemstones*, Vol. 2, 2005, Opinio Publishers, Basel, Switzerland, p. 541). Although quartz is relatively common as a host material, it is often an excellent source for unique mineral inclusions and, with this particular crystal, a fun novelty inclusion. Epigenetic residues in gems and crystals not only provide for interesting inclusion scenes, but they can also help determine growth phases and possible treatments.

Amy Cooper and Nathan Renfro
GIA, Carlsbad, California

Blue Inclusion in Rock Crystal Quartz

An interesting tuft of light blue needles was recently observed in a polished modified cube of rock crystal quartz (figure 13). The needles nucleated on a nearly invisible quartz crystal with the tuft tapering toward the opposite end (figure 14). When the tuft was examined looking parallel to the optic axis of the host quartz using cross-polarized light, the small included quartz crystal surrounded by

Figure 13. This 118.16 ct polished modified cube of rock crystal quartz contains an interesting tuft of blue needles, which may be tourmaline. Photo by Robert Weldon; courtesy of Mike Bowers.

Figure 14. This tuft of blue needles has nucleated on a quartz crystal and tapers toward the end opposite the core quartz crystal. Although too deep to be identified by Raman spectroscopy, the needles resemble light blue needles of tourmaline. Photomicrograph by Nathan Renfro; field of view 10.07 mm. Courtesy of Mike Bowers.

the blue needles stood out in high relief due to the crystallographic misalignment with the host quartz. It was also interesting to note that the included quartz was perched at the apex of a twinned sector of the host quartz (figure 15). While the needles were located too deep within the

Figure 15. When the host quartz is examined looking parallel to the optic axis, the core quartz crystal stands out in high relief and is interestingly located at the apex of a twinned sector of the host. Photomicrograph by Nathan Renfro; field of view 9.32 mm. Courtesy of Mike Bowers.
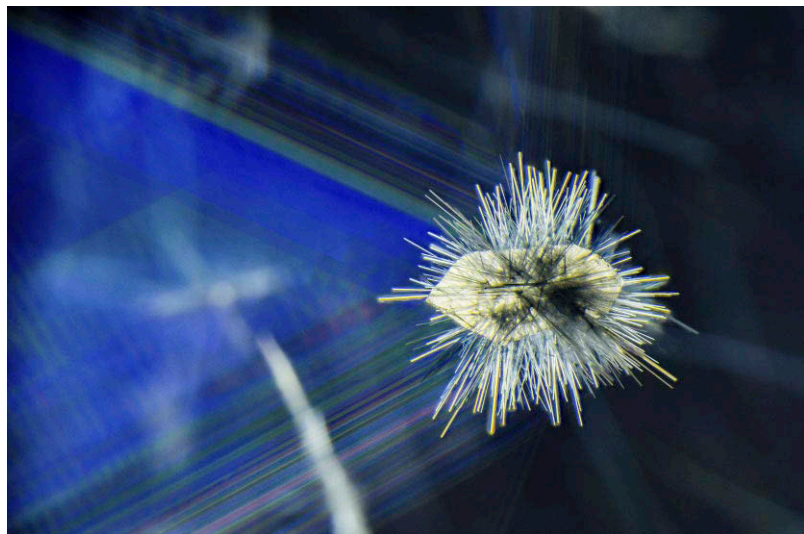
quartz to conclusively identify with Raman spectroscopy, their appearance (in the author's experience) suggests they may be pale blue tourmaline. This beautiful inclusion in rock crystal quartz is a striking example of a microfeature in a gem cut to showcase an inclusion.

Nathan Renfro

Tree in Rock Crystal Quartz

The unusual quartz cabochon shown in figure 16 displays visually appealing dendritic inclusions that resemble trees. This inclusion scene is an excellent example of pareidolia, the tendency to assign familiar shapes to abstract forms (see Winter 2007 Lab Notes, pp. 363–364). Combined with a unique illumination technique, the inclusions are reminiscent of trees with green grass and a blue sky (figure 17).

The dendritic "tree" patterns are metal sulfide inclusions, as evidenced by their brassy yellow metallic color and opaque nature. When viewed with diffused fiber-optic lighting, the metal sulfide inclusions show a crisp foil-like texture near a partially healed internal fracture. This is likely where the metal sulfides entered the quartz host. They were deposited as an epigenetic residue in the fracture near the base of the tree, which was later healed, leaving behind the metal sulfides and numerous minute fluid inclusions where the fracture once was.

Adding green and blue filters behind the stone, known as modified Rheinberg illumination (Fall 2015, pp. 328–229), helped complete the appearance of a micro-landscape contained in the rock crystal quartz. This lighting technique is characterized by using contrasting color filters to bring striking color contrast to scenes viewed with a microscope (N.D. Renfro, "Digital photomicrography for

Figure 16. This 80.60 ct rock crystal quartz cabochon contained an interesting tree-like metal sulfide inclusion. Photo by Robert Weldon.

gemologists," Summer 2015 *G&G*, pp. 144–159). This unique quartz gem can be appreciated for the beautiful inclusion scene it contains.
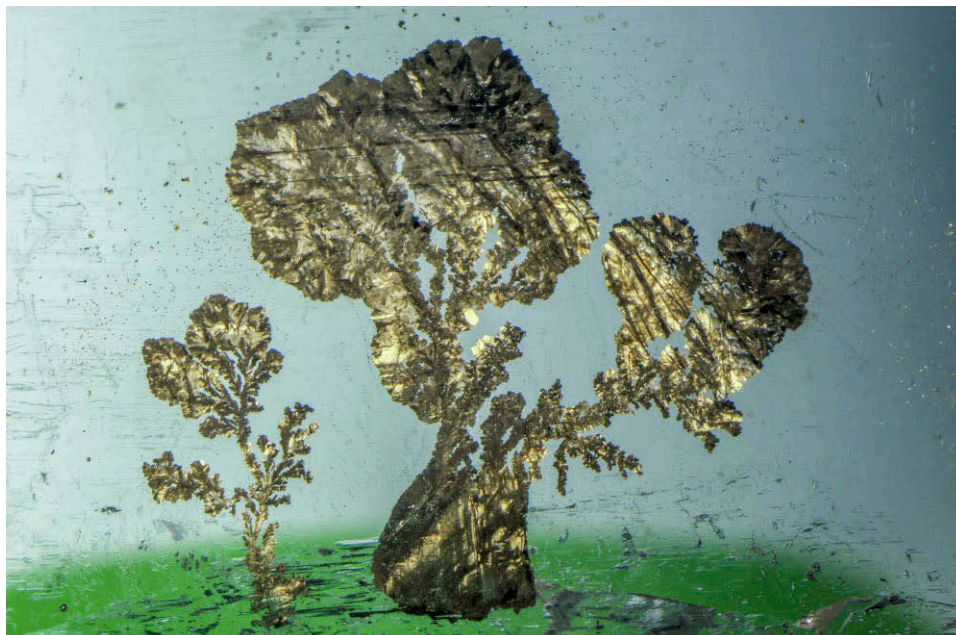
Amy Cooper and Nathan Renfro

Figure 17. Epigenetic metal sulfides are trapped in a partially healed fracture of rock crystal quartz. Modified Rheinberg illumination provides artificial blue and green color contrast reminiscent of grass and a sky. Photomicrograph by Nathan Renfro; field of view 20.14 mm. Courtesy of Mike Bowers.
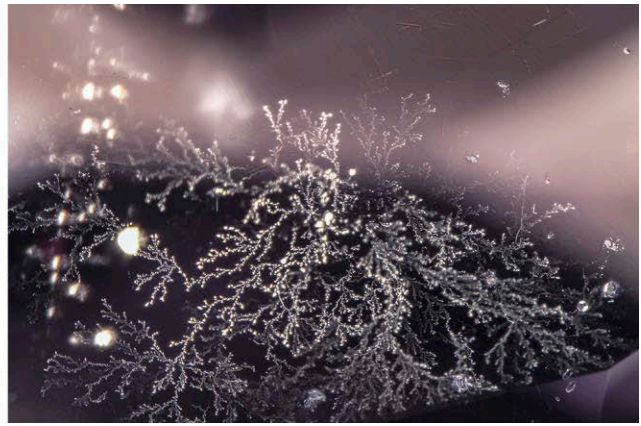
Figure 18. Left: When the pinkish purple sapphire was viewed under darkfield illumination, the only inclusions visible underneath the table were zircon crystals and rutile needles. Right: Examining the same area with fiber-optic light revealed unknown dendritic inclusions. Photomicrographs by Ezgi Kiyak; field of view 2.90 mm.

Unknown Dendritic Inclusions in Sapphire

The authors recently examined a 4.03 ct light pinkish purple unheated sapphire. When viewed under darkfield illumination, the inclusion scene at first seemed fairly vacant and occupied only by sparse zircon crystals and rutile needles (figure 18, left). However, microscopic observation with fiber-optic light revealed large, delicate dendritic inclusions underneath the table (figure 18, right) that resembled a fern frond. The dendritic inclusions seemed to be flat and parallel to each other and extended the entire length of the table. Small round platelets were associated with the "branches" of the inclusions.

Further examination with a polariscope and conoscope helped prove that the dendritic inclusions were oriented parallel to the basal plane of the host corundum. A distinct uniaxial interference pattern was observed when viewing these inclusions from a perpendicular angle. The thinness and relative distance to the surface of the stone made it difficult to identify the inclusions with Raman spectroscopy. This is the first example of such dendritic inclusions in sapphire the authors have observed. However, a similar inclusion has been observed previously in a heat-treated blue sapphire (see Spring 2007 Lab Notes, pp. 54–55).

Ezgi Kiyak and Augusto Castillo
GIA, New York

Spinel on Sapphire

Recently the authors examined a 4.8 cm tall pale blue sapphire crystal (figure 19) that featured numerous purple spinel crystals up to 8 mm in size on the surface (figure 20), a rather uncommon association. Steve Dubyk of Albuquerque, New Mexico, had acquired this specimen and doubted the accuracy of the accompanying label, indicating aquamarine from Tres Pozos in Baja California, Mexico. Raman spectroscopy confirmed Mr. Dubyk's suspicion that the specimen was in fact corundum and identified the associated purple crystals as spinel. LA-ICP-MS chemical

analysis suggested that the specimen was from Sri Lanka based on the trace elements present, which indicated an average of 130 ppma iron (Fe), 38 ppma titanium (Ti), and

Figure 19. This 4.8 cm pale blue sapphire crystal contained numerous purple spinel crystals on the surface. Photo by Angelica Sanchez; courtesy of Steve Dubyk.
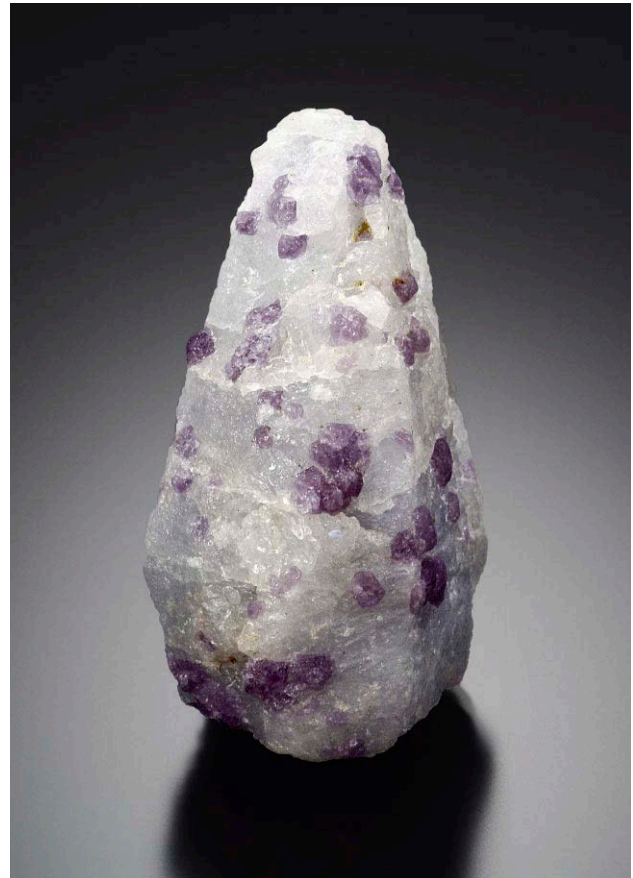
Figure 20. Purple spinel crystals were intergrown on the outermost layer of the sapphire crystal, which appears to be from Sri Lanka based on trace element chemistry. Photomicrograph by Nathan Renfro; field of view 13.42 mm.

37 ppma magnesium (Mg). The trace element chemistry is also notable, as the magnesium will preferentially charge compensate the titanium, leaving very little excess titanium to pair with iron to produce a blue color. The chemistry measurements were consistent with the very pale blue color observed in this stone. The chemistry of the spinel was also interesting in that its reasonably saturated purple color would indicate it was at least partially caused by chromium. However, the spinel was inert to long-wave UV light, suggesting no chromium was present. LA-ICP-MS testing confirmed the absence of chromium but showed relatively high iron (10,566 ppma) and some cobalt (2.75 ppma average) which together are likely responsible

for the purple color (A. Palke and Z. Sun, "What is cobalt spinel? Unraveling the causes of blue color in blue spinel," Fall 2018 *G&G*, p. 262). While spinel is uncommon in sapphire, a spinel inclusion has been previously reported in a Sri Lankan yellow sapphire (Winter 2015 Micro-World, p. 444). This sapphire is one of the more unusual examples the authors have encountered.

Ian Nicastro
San Diego, California

Nathan Renfro, Ziyin Sun, and Aaron Palke
GIA, Carlsbad, California

Staurolite in a Mozambique Ruby

Rubies from Mozambique have a well-known inclusion suite that can consist of particle clouds, planes of platelets, and negative crystals as well as sulfite and amphibole crystals. These inclusions and their trace element chemistry make the geographical origin of Mozambique rubies less difficult to decipher. Recently, a 1.11 ct unheated ruby was examined by the author for identification. Internally there were scattered silk with planes of thin films as well as negative crystals. These inclusions plus trace element chemistry collected by laser ablation–inductively coupled plasma–mass spectrometry (LA-ICP-MS) analyses confirmed the stone to be from Mozambique.

Mozambique rubies have a consistent suite of inclusions, and noting something out of the ordinary is quite uncommon. Alongside the negative crystals were clusters of a transparent orangy red crystal that the author had no prior knowledge of seeing in a Mozambique ruby (figure 21). Raman spectroscopy identified the unknown crystals
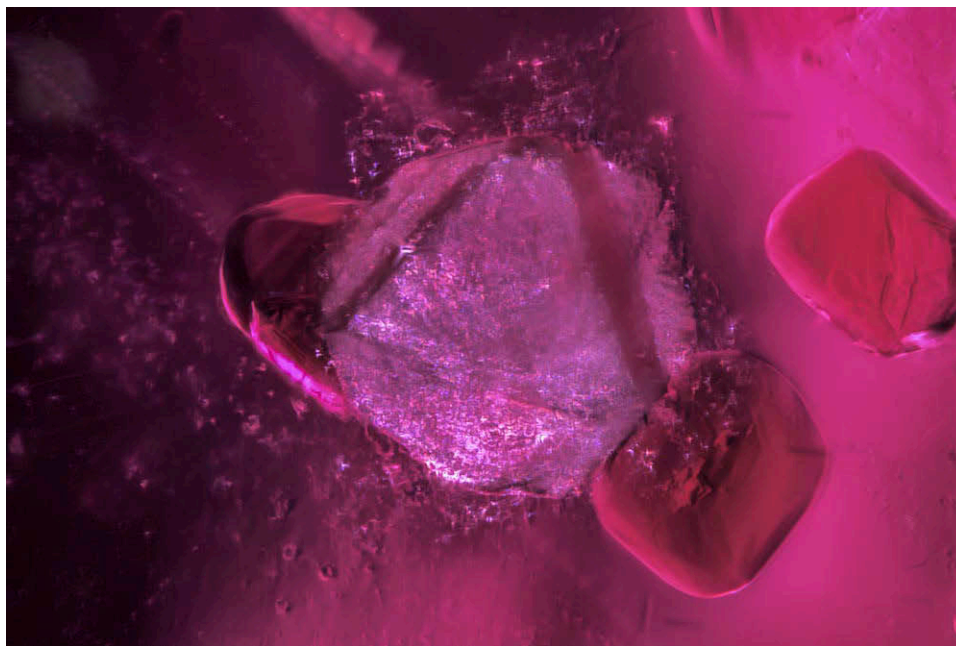

Figure 21. Orangy red staurolite crystals surround a negative crystal in a Mozambique ruby. Planes of thin films can be seen behind them. Photomicrograph by Nicole Ahline; field of view 1.42 mm.

as staurolite, a nesosilicate mineral known to occur in Mozambique. In a recent issue of *G&G*, staurolite was examined and documented for the first time as an inclusion in corundum, specifically in a Madagascar ruby (Spring 2020 Micro-World, pp. 144–145). The author believes that this staurolite is the first of its kind documented in a Mozambique ruby. Inclusions such as these will forever keep gemologists on the lookout for the next unknown.

Nicole Ahline
GIA, Carlsbad, California

Quarterly Crystal: Ferrocolumbite in Topaz

The author recently acquired a 239.25 ct transparent well-formed topaz crystal from the collection of Leon M. Agee. The crystal from the Shigar Valley in Pakistan, shown in figure 22, has a flat base formed by a cleavage plane. The termination appears to be a pyramid form. The crystal plays host to two prominent opaque black inclusions and one smaller similar-appearing inclusion that is close to the surface of the host (figure 23). The two larger inclusions were too deep in the topaz to analyze. However, the small inclusion was near the surface of one of the prism faces and could be reached by laser Raman microspectrometry. Testing showed a very close match to ferrocolumbite (columbite-Fe). Because of the resemblance between the smaller inclusion and the two larger ones, we concluded that the two larger inclusions were also ferrocolumbite. As an interesting aside, these inclusions are reminiscent of star cruisers in the Star Wars anthology.

John I. Koivula
GIA, Carlsbad, California

Figure 22. This 239.25 ct topaz crystal hosts some interesting inclusions of ferrocolumbite. Photo by Diego Sanchez.

Figure 23. Laser Raman microspectrometry identified the smallest of these inclusions as ferrocolumbite. Photomicrograph by Nathan Renfro; field of view 17.62 mm.

Gem News International

Contributing Editors

Emmanuel Fritsch, *University of Nantes, CNRS, Team 6502, Institut des Matériaux Jean Rouxel (IMN), Nantes, France* (fritsch@cnrs-imn.fr)

Gagan Choudhary, *Gem Testing Laboratory, Jaipur, India* (gagan@gjepcindia.com)

Christopher M. Breeding, *GIA, Carlsbad* (christopher.breeding@gia.edu)

## COLORED STONES AND ORGANIC MATERIALS

A near-field-communication (NFC) technology device embedded in bead cultured pearls. The Carlsbad laboratory received for examination two dark-colored bead cultured pearls embedded with an electronic device (figure 1) from Jeremy Shepherd, CEO of Pearl Paradise. The first sample had been cut in half by Mr. Shepherd in order to investigate the interior components; the smaller half weighed 2.56 ct and measured 10.63 × 9.73 × 3.88 mm (figure 1, left), and the larger half weighed 4.46 ct and measured 10.84 × 10.20 × 5.48 mm (figure 1, center). The second sample (figure 1, right) was intact and weighed 7.83 ct, measuring 10.84 × 10.20 × 5.48 mm. Both samples exhibited the typical external appearance of bead cultured pearls produced by the *Pinctada margaritifera* mollusk (referred to in the trade as "Tahitian" or "Black South Sea"). UV-Vis spectra of these samples showed the characteristic reflectance features typical of naturally colored pearls originating from this mollusk, with identifying features recorded at 405, 495, and 700 nm.

The cross-section surfaces of the two halves showed a straightforward bead cultured pearl structure. A round translucent white shell bead nucleus was clearly visible in the center. Its freshwater origin was subsequently verified with optical X-ray fluorescence imaging and EDXRF analysis. The alternating cream and brown concentric layers immediately overgrowing the bead were a combination of calcium carbonate and organic-rich materials (i.e., conchiolin) that are sometimes produced during the initial growth

stage prior to nacre (aragonite) deposition. The subsequently deposited layers are dark-colored nacre commonly produced by the *P. margaritifera* mollusk. An electronic device was very obvious within a large partial drill hole that ran through the bead and into the other side of nacre.

Real-time microradiography (RTX) revealed that the electronic devices embedded in the two halves and in the intact pearl samples were of the same kind. The device was composed of a high-density radio-opaque core (measuring approximately 5.10 × 3.26 mm) that appeared white in the RTX image and as an opaque black filler in the cross sections. An antenna could be seen wrapped around the core, and a circuit board was connected to the end of the antenna (figure 2). Chemical analysis of these components using laser ablation–inductively coupled plasma–mass spectrom-

Figure 1. An intact 7.83 ct Pinctada margaritifera *bead cultured pearl (right), together with a sectioned sample (2.56 ct left and 4.46 ct center), embedded with a near-field-communication (NFC) chip. Photo by Diego Sanchez.*
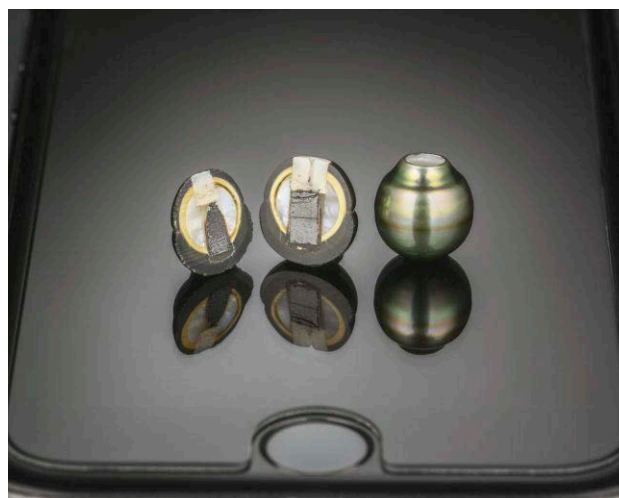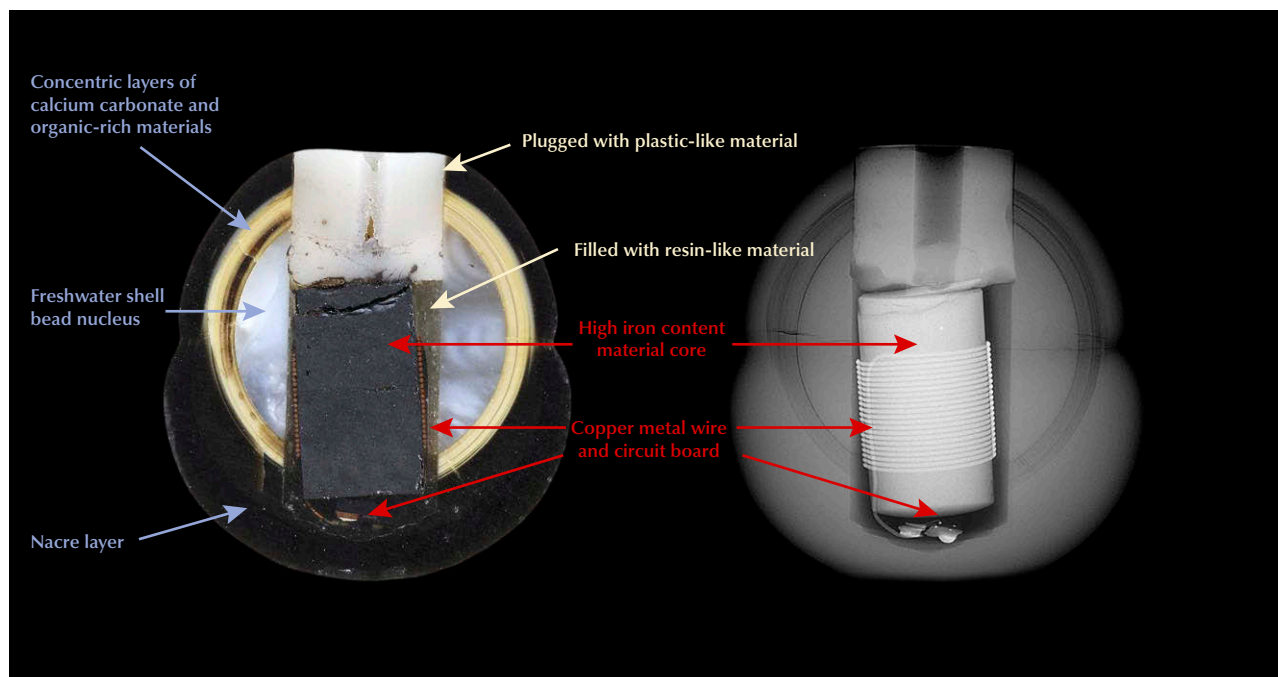
Figure 2. The cross section (left) and microradiograph (right) images of the same sample revealed the varied components of the bead cultured pearl and NFC chip. Photos by Diego Sanchez (left) and Artitaya Homkrajae (right).

etry (LA-ICP-MS) revealed that the black core was composed of a high-iron (Fe) material, which was confirmed using a magnet. The bronze-colored antenna and circuit board were identified as copper. The device was held in place in the large drill hole with a transparent near-colorless resin-like material containing numerous gas bubbles. The drill hole areas were worked (cut) to a flattened surface and plugged with a white plastic-like material, which was subsequently re-drilled with a smaller drill hole. Although the large drill hole was placed in the center, it did not affect the origin determination of the pearl. The shell bead nucleus and the device contained within could be observed using RTX, even for the intact sample. The pearl's shape was certainly impacted by the cut surface, and the classifications for color, overtone, luster, and surface would be based on the remaining nacreous surface.

The electronic device appeared to be a near-field-communication (NFC) chip, which is a short-range wireless connectivity technology based on traditional radio-frequency identification (RFID) (https://nfc-forum.org/what-is-nfc/about-the-technology). NFC technology allows data transfer between two NFC-enabled devices through electromagnetic radio fields within a very short distance, either by physically touching or being within a few centimeters of each other. NFC chips are passive and do not need to have a power source of their own, though the antenna can be coupled with an active device such as a smartphone via an electromagnetic field. The chip is used to store digital information such as images, video, text, and audio, which are accessed through an app due to limited memory. To the best of our knowledge, this technology was first incorpo-

rated within pearl jewelry by Galatea: Jewelry by Artist and marketed under the name "Momento" (https://www.momentogem.com). However, the NFC chip embedded in the intact pearl sample in this study was not compatible with the Galatea Momento smartphone application.

So far, GIA has observed three kinds of electronic devices in cultured pearls. The first device encountered was an RFID chip implanted inside a shell nucleus by Fukai Shell Nucleus prior to the culturing process ("ID nuclei add value to pearls," *Hong Kong Jewellery*, September 2013, pp. 62–64). The RFID technology is used to track and identify the pearl directly from farm to consumer. The second was a "capsule-like" feature found within an atypical *P. margaritifera* bead cultured pearl set in a ring that was submitted for identification at GIA Hong Kong, yet the reason for the device remains unknown (Spring 2020 Lab Notes, pp. 134–136). This NFC chip is the third kind and is used for wireless data transmission with an NFC-enabled device such as a mobile phone. The NFC chips were inserted into bead cultured pearls after they had been cultured, unlike the RFID chip. Therefore, the pearl is still classified as a bead cultured pearl on GIA's pearl identification report. The presence of the device is mentioned in the comments section.

Technology is pervasive in our daily lives and can even influence how pearl jewelry is produced. Since cultured pearls are opaque, the implementation of such micro-technologies within them is a viable option. These innovative wearable technologies retain the external appearance of pearls while performing a specific function.

Artitaya Homkrajae
GIA, Carlsbad

Trapiche-type emeralds from Pakistan. Numerous gem materials have been designated "trapiche" in the trade and in various publications. They generally describe a pattern consisting of a fixed non-transparent star in a transparent matrix, with the arms of the six-rayed star radiating from a central point or from a central core to the rim of the crystal. Only a limited number of mineral species show a clear trapiche pattern within crystal slices (i.e., a pattern with a clear separation of the crystal into distinct growth sectors). The boundaries of these growth sectors, running from the center to the edges between external prism or pyramidal faces, are normally sharp and contain mineral or fluid inclusions, separating different parts within the rim. These sector boundaries are also described as the arms of the fixed six-rayed star. The most prominent gem minerals showing a distinct trapiche pattern are Colombian emeralds and rubies from Myanmar.

Another group of gem materials is characterized by several areas of increased transparency and translucency that surround a central point or central core according to the symmetry of the host. The two types of areas are characterized by different concentrations of inclusions, which are trapped within specific parts of symmetry-equivalent growth sectors of the host. The arms of the fixed star are perpendicular to the external crystal faces. The most prominent gem materials of this second group are blue basaltic sapphires from different sources, but similar patterns also have been described for other gem varieties such as aquamarine from Namibia. This second group of crystals is designated "trapiche-type," and the emeralds from Pakistan described in this entry belong to this group of gem materials.

Trapiche-type emeralds originating from the Swat mining region in Pakistan have recently been described by Y. Gao et al. (Fall 2019 Gem News International, pp. 441–442) and H. Guo et al. ("Inclusion and trace element characteristics of emeralds from Swat Valley, Pakistan," pp. 336–355 of this issue). The samples showed an interesting growth pattern and color zoning with a colorless core, a lighter green intermediate zone, and a more intense green rim. The inclusions forming the trapiche-type pattern were restricted to the lighter green intermediate growth zone.

Recently, the author received six slices of similar material, reportedly from Swat, from the gem collector S. Hanken of Waldkraiburg, Germany; the samples had been purchased in 2020 from the U.S. gem trade. One of these samples, which were all cut perpendicular to the c-axis of the emerald crystals, showed an interesting growth pattern. The emerald slice measured from 4.6 to 4.8 mm (distances between different prism faces) with a thickness of 1.9 mm (figure 3). The sample revealed two colorless beryl cores of almost equal size. One of these colorless cores was surrounded by a large light green intermediate zone, which also contained the inclusions forming the trapiche-type pattern. The second core was surrounded by a lighter green intermediate zone, which was much smaller. Encompassing these two intermediate zones were intense green hexagonal growth boundaries with growth planes parallel to the external prism faces.

This intense green growth boundary surrounds both light green intermediate growth zones. Subsequent to this intense green boundary, an intense green outer rim without trapiche-type inclusions but with additional growth planes parallel to the prism faces was present.

As already described by Gao et al., the emerald was grown in three distinct steps with a colorless beryl core, a light green intermediate zone, and an intense green rim. All growth steps were separated by sharp boundaries, with a thin growth layer between the intermediate zone and the rim, which showed the most intense green coloration observed in the sample. The emerald formed with two cores, with a subsequent growth step, in which both parts were still separated from each other. Only in the last growth step, in which the intense green rim was formed, were the two parts of the final emerald crystal in contact with each other.
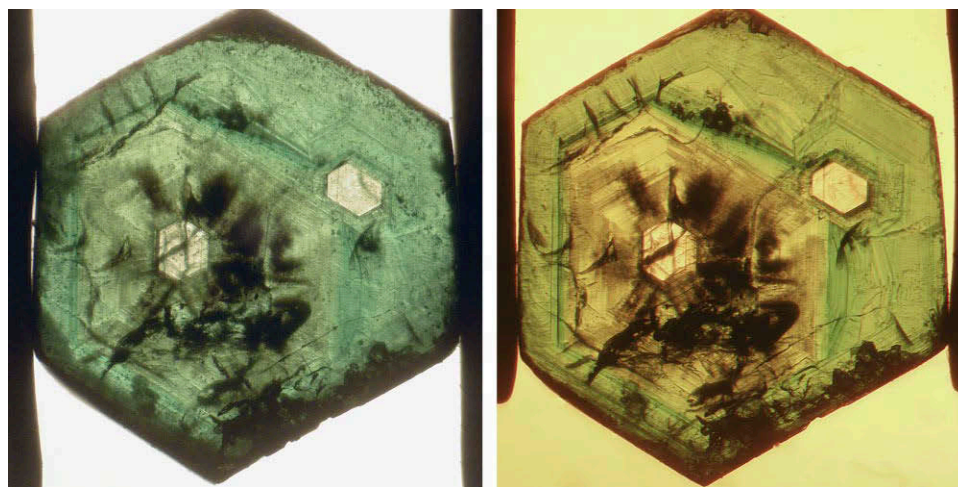
Karl Schmetzer
Petershausen, Germany

Figure 3. Growth pattern observed in a trapiche-type emerald from Swat, Pakistan. The slice shows two colorless cores and two intermediate lighter green zones surrounded by a more intense green rim. Viewed perpendicular to the c-axis, in air (left) and immersion (right); diameter of the sample from 4.6 to 4.8 mm. Photos by Karl Schmetzer.

Unusual violet Maxixe beryl. Recently examined in the Carlsbad laboratory was a 26.72 ct transparent violet modified cushion mixed-cut stone (figure 4). Standard gemological testing revealed a refractive index of 1.583–1.592 and a specific gravity of 2.78, both consistent with beryl. Using plane-polarized light, pale purple and saturated blue pleochroic colors were observed. A uniaxial optic figure was seen at the girdle, and the optical orientation of the stone showed the stronger blue pleochroic color down the optic axis direction. The stone was inert to long-wave UV light and fluoresced weak greenish yellow to short-wave UV. Viewed with fiber-optic light during microscopic examination, it displayed a few scattered blocky crystals, platelets, and needles, confirming natural growth origin. No coatings were seen on the surface under reflective light. Other than the unusual violet color, these properties were consistent with Maxixe beryl.

Advanced testing by LA-ICP-MS revealed that the stone lacked iron. This result was consistent with Maxixe beryl, in which iron is too low to be measured (I. Adamo et al., "Aquamarine, Maxixe-type beryl, and hydrothermal synthetic blue beryl: Analysis and identification," Fall 2008 *G&G*, pp. 214–226). Maxixe beryl normally has a blue to violet blue bodycolor, but this stone showed an unusual violet color. The UV-Vis-NIR spectrum (figure 5) showed absorption bands between 500 and 700 nm and a broad band near ~690 nm. This spectrum was consistent with Maxixe beryl (again, see Adamo et al., 2008). While Maxixe beryl

Figure 4. This 26.72 ct Maxixe beryl has an unusual violet color. Photo by Diego Sanchez.
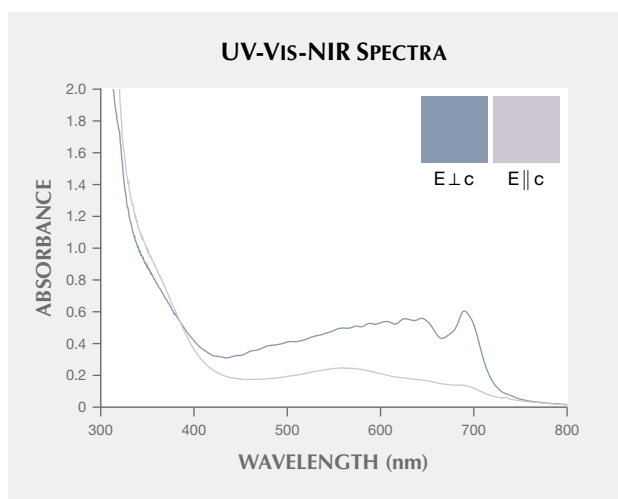

Figure 5. The violet beryl showed a typical UV-Vis-NIR spectrum for Maxixe beryl. Pleochroic colors were calculated from the spectra and revealed a blue (o-ray, dark blue trace and color swatch) and light violet (e-ray, pale purple trace and color swatch) pleochroism.

has been found to be colored by natural irradiation, it can also be produced by artificial irradiation. Some of these "Maxixe-type" beryls produced by artificial irradiation are known to fade when exposed to "mild heat or strong light" (see Winter 1997 Lab Notes, p. 293). However, there is no conclusive test to determine whether Maxixe color results from natural or artificial irradiation, and as such, beryl in the blue to violet color range that shows the type of visible spectrum previously mentioned is designated simply as the Maxixe variety of beryl by the GIA laboratory.

A small sample cut from the same rough as the 26.72 ct violet beryl was provided by lapidary Nolan Sponsler for destructive testing in order to evaluate the color stability of this material. An optically oriented wafer, 4.45 mm thick and normalized to a 25 mm path length in order to better observe the change in color, was fabricated from this sample with parallel polished windows that are parallel to the optic axis to allow measurement of the o- and e-rays. UV-Vis-NIR spectra were collected on the sample prior to fade testing and at four-hour intervals of exposure to a 150-watt halogen bulb at a distance of approximately four inches from the bulb to avoid any significant heating (figure 6). The results showed fading of the sample until its color was very pale (figure 7), confirming that this material may fade. One should avoid prolonged exposure to light and store it in a dark environment to preserve the color.

This violet Maxixe beryl was purported to be from Santa Maria de Itabira, Minas Gerais, Brazil. It is notable for its unusual color and its fantasy cut design. In addition to this violet Maxixe beryl, another violet beryl group mineral named "johnkoivulaite" was documented in 2019 (see Fall 2019 GNI, pp. 454–455); that new beryl is from the Mogok mining area in Myanmar. However, standard gemo-
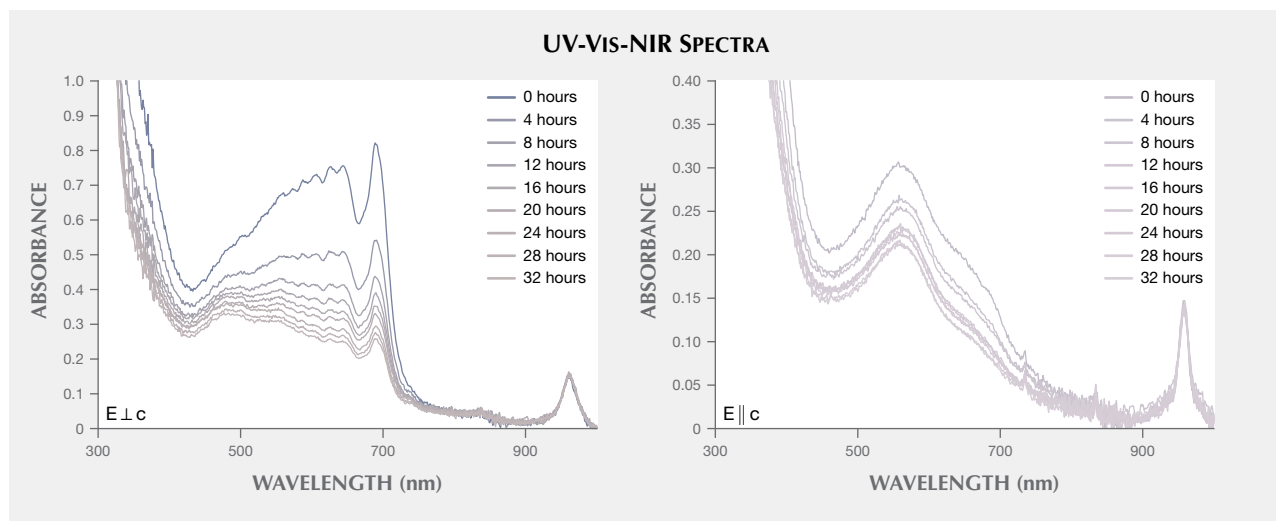
UV-VIS-NIR SPECTRA

Figure 6. From the violet beryl material provided for this study, a wafer was fabricated in order to directly measure the absorption spectra while conducting a fade test by placing the sample four inches away from an intense 150-watt halogen light source. The results, normalized to a 25 mm path length, confirmed that the color became less saturated over time with exposure to light. Most of the color loss came from the o-ray direction (left).

logical properties clearly separate the two violet beryl minerals. Even though this beryl owes its appealing violet hue to what would be considered an unstable color center, the color should remain intact if prolonged exposure to intense light sources is minimized.

Amy Cooper, Ziyin Sun, Dylan Hand, and
*Nathan Renfro*
GIA, Carlsbad, California

SYNTHETICS AND SIMULANTS

A new type of rutilated quartz composite product. Rutilated quartz, which refers to natural quartz with rutile needle inclusions, is very popular in Taiwan's mineral market.

Merchants carve rutilated quartz into spheres rather than pendants or cabochons to get higher prices. The value of such spheres depends on the size of quartz as well as the abundance or appearance of its rutile crystals. Since large and well-formed rutilated quartz is quite rare, it is possible to make those of lower quality into doublets with top covers of glass or synthetic quartz.

Recently, a rutilated quartz sphere was sent to Taiwan Union Lab of Gem Research (TULAB) for certification service. Half of the sphere was colorless and transparent, while the other half was brown and semitranslucent (figure 8). The supplier had informed the client that it was a rutilated quartz polished into a sphere together with its host rock in order to retain the maximum size and the striking rutile inclusions. The colorless and brown parts had refractive

Figure 7. The polarized visible spectra were used to produce color swatches of the ordinary-ray (E ⊥ c) and extraordinary-ray (E ‖ c) color normalized to a 25 mm path length to illustrate the change in color during fade testing over a period of 32 hours at four-hour intervals.
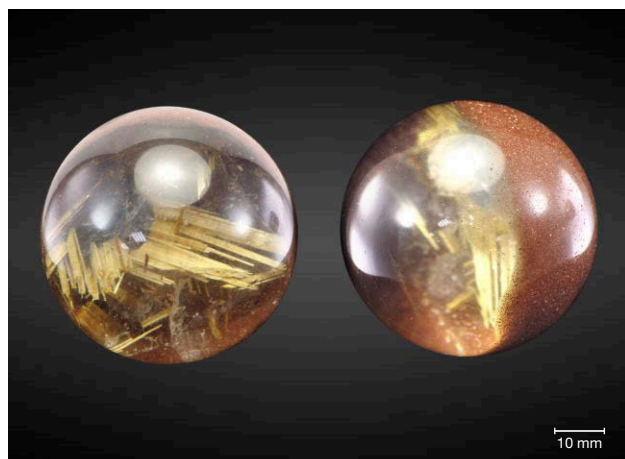

CIE Standard Illuminant D65
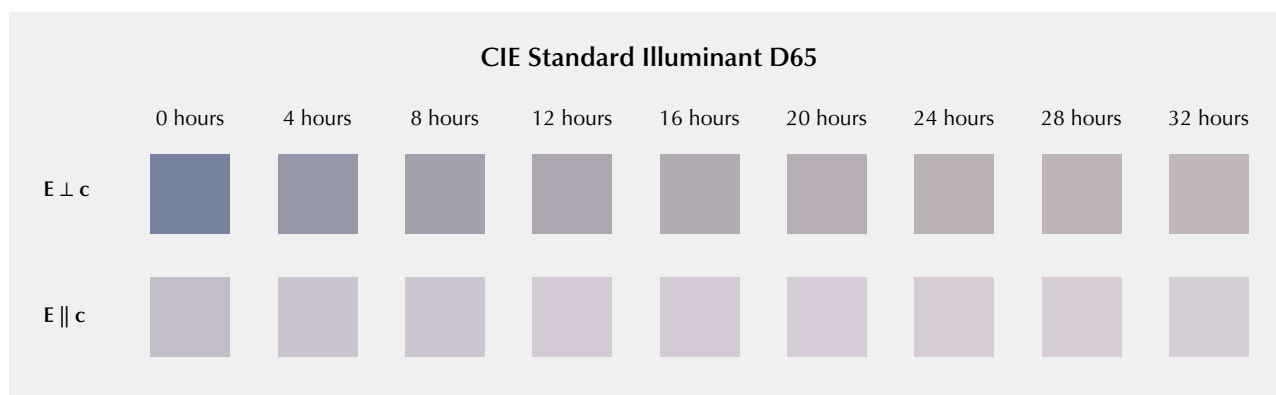
Figure 8. Photos of the rutilated quartz taken in different viewing directions (top view on the left and side view on the right) showed that the sphere was half colorless and half brown. Photos by Shu-Hong Lin.
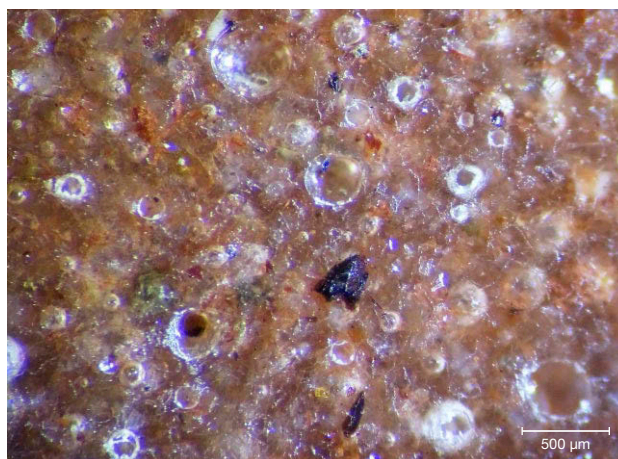

Figure 9. The microscopic image of the brown part of the rutilated quartz sphere showed yellow, brown, and black mineral particles with an abundance of bubbles. Photomicrograph by Shu-Hong Lin.

indices of 1.54 and 1.55, respectively, and the fluorescence was inert under an ultraviolet lamp. Microscopic observation revealed that the brown part contained yellow, brown, and black mineral particles with a large number of bubbles (figure 9). The specific gravity was 2.35, which is much lower than the specific gravity of quartz. To further confirm the material of the sphere, the colorless and brown parts were analyzed with a Raman spectrometer. The results showed that the former was quartz, and the latter was mainly composed of epoxy resin and quartz (figure 10).

After a series of gemological tests, we concluded that this sphere could be defined as a new type of doublet or composite material of rutilated quartz, in which the brown part mistaken for host rock was in fact epoxy resin mixed
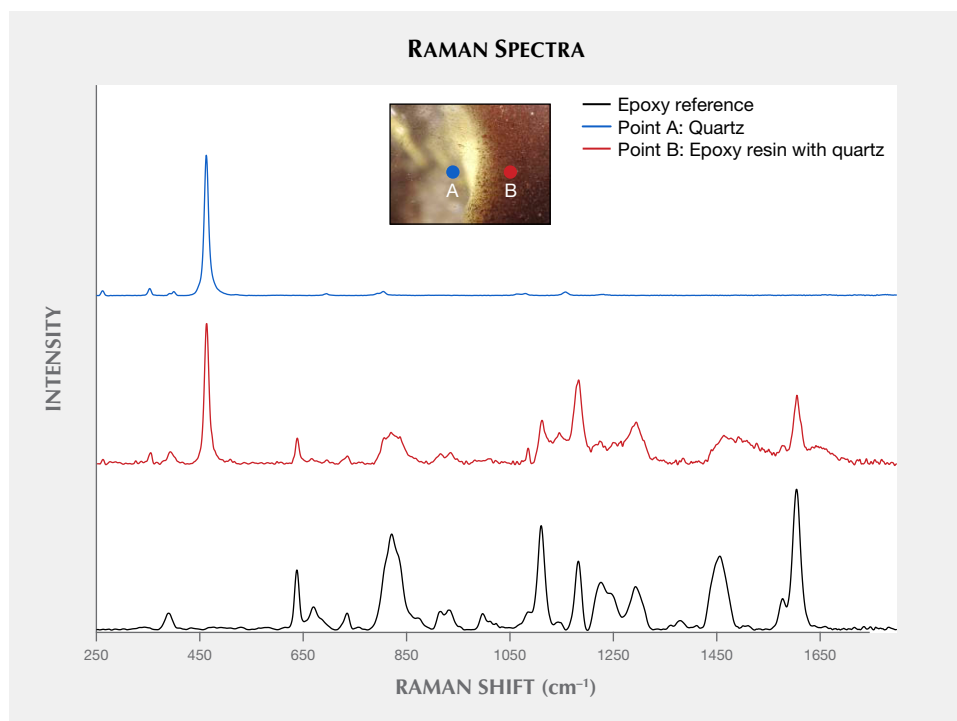

Figure 10. Stacked Raman spectra of the rutilated quartz sphere and epoxy resin revealed that the colorless part (A) was quartz (463 cm^{-1}) and the brown part (B) was mainly composed of epoxy resin (peaks at 637, 822, 1113, 1182, and 1606 cm^{-1}) and quartz. The spectra are baseline-corrected and normalized.

with mineral powders. Due to the increasing demand for rutilated quartz spheres in Taiwan, this composite material may not be merely an isolated case.

Shu-Hong Lin
Institute of Earth Sciences,
National Taiwan Ocean University
Taiwan Union Lab of Gem Research, Taipei

Yu-Ho Li
Institute of Earth Sciences,
National Taiwan Ocean University

Huei-Fen Chen
Institute of Earth Sciences and
Center of Excellence for Oceans
National Taiwan Ocean University, Keelung, Taiwan

Figure 11. The 75 ct black star sapphire that was brought in for testing. Photo by Wimon Manorotkul.

TREATMENTS

Black star sapphire with dual treatments. Black star sapphires primarily come from Kenya, Australia, and Thailand. Unlike other star sapphires and rubies, the asterism in these stones generally results from the exsolution of ilmenite ($FeTiO_3$) and/or hematite ($\alpha\text{-}Fe_2O_3$) instead of rutile (TiO_2). Rutile and ilmenite/hematite exsolve in different directions: rutile along the second-order hexagonal prism $\{11\overline{2}0\}$ and ilmenite along the first-order hexagonal prism $\{10\overline{1}0\}$. If both are present in the same stone, a 12-ray star results. The ilmenite/hematite crystals are far more "platy," and thus their layers tend to form planes of weakness. Breakage along those planes is termed parting. Parting differs from cleavage in that it results from structural planes of weakness due to imperfect growth rather than inherent weakness. There are often two different parting planes in the stones. One corresponds to the exsolution of ilmenite/hematite in the plane of the basal pinacoid $\{0001\}$. The other corresponds to planes of exsolved boehmite/diaspore along the rhombohedron $\{10\overline{1}1\}$.

In Thailand, one often sees cavities on the back of black star sapphires filled in with brown dopping varnish. It is onl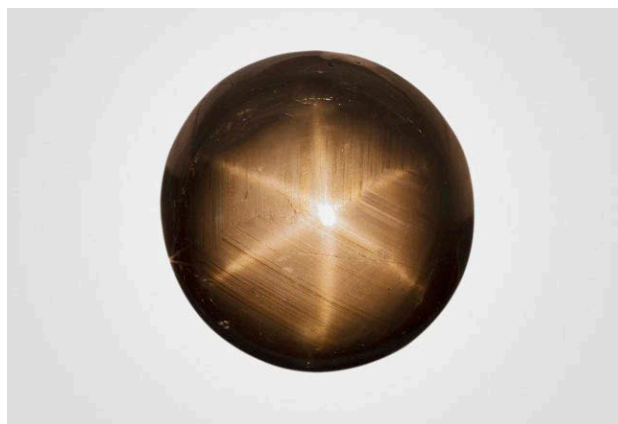y the basal parting that comes into play with black star sapphires, because the exsolved hematite that causes the lack of adhesion is only in the basal plane. It is because of this parting that the stones get filled with dopping varnish, to conceal large holes in the base. Note that the type of dopping varnish is of a color that matches the stone.

In May 2020, a client submitted a large 75 ct black star sapphire for testing (figure 11). The base of the stone contained two large pits filled with brown dopping shellac (figure 12, left). Interestingly enough, the shellac fluoresced bright orange under long-wave ultraviolet light (365 nm) (figure 12, right). Following the client's approval, we removed the shellac with alcohol and noticed a curved area exhibiting an unusual flow-like structure that looked suspiciously like glass. Unfortunately, attempting to get a Raman spectrum on the area was unsuccessful.

Careful microscopic examination showed what looked like gas bubbles trapped between the glassy material and the sapphire below (figure 13). Scratching the surface of the cavity with a number 7 hardness point confirmed that the area could not be corundum. Immersing the gem in methylene iodide showed the glassy area to cover roughly two-thirds of the base of the cabochon (figure 14). Energy-dispersive x-ray fluorescence (EDXRF) testing on the area suspected to be glass revealed a lead (Pb) component of over 3%.

Figure 12. Left: Two large pits on the base of the star sapphire contain brown dopping varnish (the white areas are adhesive from tape). Field of view 30 mm. Right: Under long-wave ultraviolet light (365 nm), the dopping shellac fluoresced bright orange. Field of view 27 mm. Photomicrographs by Richard W. Hughes.
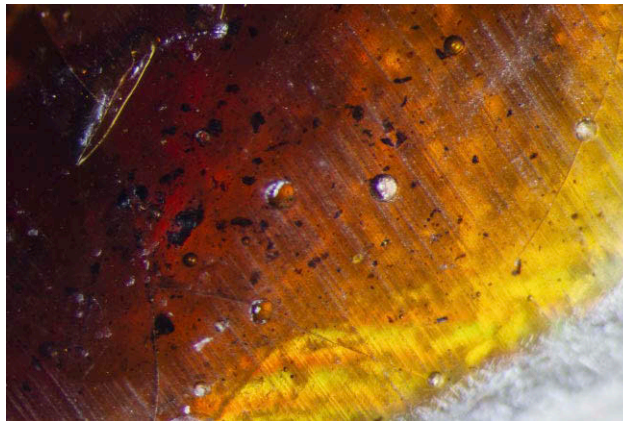
Figure 13. A close-up view of the shellac in the lower pit revealed trapped gas bubbles and black debris. Photomicrograph by Richard W. Hughes; field of view 5 mm.

Figure 14. Immersion in methylene diiodomethane (n = 1.741) reveals the extent of the glass filling on the base of the cabochon (the dark area that spreads across a large portion of the base). Photomicrograph by Richard W. Hughes; field of view 30 mm.

A variety of tests were brought to bear on this specimen, from the simple (hardness) to the high-tech (EDXRF). The results of these tests revealed a gem that had been treated by filling with two different substances: glass and dopping varnish.

Richard W. Hughes, E. Billie Hughes, and
Wimon Manorotkul
Lotus Gemology, Bangkok

Oiled spinel. When it comes to clarity enhancement with oils and resins, a common belief is that the refractive index of the host gem must match that of the filler. If one follows this logic, it would seem that using oils or resins to clarity enhance corundum (n = 1.76) or spinel (n = 1.72) would not be at all effective, since there is a yawning gap in RI between those gems and that of any oil or resin.

Certainly, Burmese gem traders have never bought into that idea, for we regularly encounter oiled rubies, sapphires, and spinels from Myanmar. In fact, Burmese traders have told us that it is common practice to immediately immerse rough into oil after it is unearthed (figure 15). Oiling rough not only makes viewing the interior easier but also significantly enhances the gem's clarity. In our experience, such treatment is almost never disclosed to buyers.

Figure 15. Bojan brand "King Ruby Red Oil" from Chanthaburi, Thailand, along with a parcel of rough Thai rubies purchased by the author in 2016. Note the red stain on the plastic bag. Photo by Wimon Manorotkul.

In 2013, while visiting various mines and markets in Myanmar's Mogok Stone Tract, we were taken to a small house where a man was heat-treating spinel. Gems were placed in a crucible and heated for a period of time. Then, while still relatively hot, they were dumped into a vessel containing red oil. It was a remarkable piece of performance art. After the oil was wiped off, we could discern no change in color from the heating.

Because of the prevalence of oiling, we now check every stone with fissures for oil, no matter the origin or type of gem. This is typically done with a hot point under the microscope. The hot point gently heats the gem until, with oiled stones, the oil leaks out of the fissure in beads on the surface of the stone. With the exception of emerald, customers purchasing colored gems are not expecting them to be clarity enhanced. As one major Bangkok trader told us several years ago, "I cannot sell an oiled spinel." For this reason, when we determine that a gem other than emerald has been fissure-filled with an oil or resin, we notify the client and allow them two opportunities to remove the filler before we issue the report.

In September 2020, Lotus Gemology received for identification a 3 ct spinel that originated from Mogok. We noticed a fissure on the pavilion running parallel to the girdle plane, and application of the hot point caused oil to leak out. After two rounds of oil removal by the client, the difference was truly remarkable. The gem was now disfigured by a highly reflective eye-visible fissure (figure 16).

This clearly demonstrates that oil can have a significant impact on the clarity of a gem even when there is a big difference in RI between the host and the oil. The greatest impact will be found in stones like this spinel, where fissures lie perpendicular to the viewing angle.

Richard W. Hughes
Lotus Gemology, Bangkok

CONFERENCE REPORTS

GSA Annual Meeting: Gem Research Session. The Geological Society of America held its 2020 annual meeting as a virtual conference October 26–30 (figure 17). The session on gemological research took place on Thursday, October 29, and featured presentations on various gemological topics.

Nelson Eby from the Department of Environmental, Earth, and Atmospheric Sciences of the University of Massachusetts in Lowell presented a chemical classification of emeralds from 24 deposits in 10 countries. Using data on major and minor chemical elements in emeralds obtained by the instrumental neutron activation analysis, he demonstrated how these emerald occurrences could be grouped into deposits related to igneous processes, to those related to low-to-moderate temperature solutions in sedimentary environments, and to metamorphic processes. **Rhiana Henry** of the Department of Earth, Ocean, and Atmospheric Sciences of the University of British Columbia in Vancouver described a method that could be used to calculate the water content of an emerald based on measured values of either Na^+ atoms per formula unit (apfu) or weight percent Na_2O. **Cisil Badur** of the Department of Geosciences at Auburn University in Alabama investigated plagioclase megacrysts containing macroscopic inclusions of native copper from the Dust Devil mine in south-central Oregon. She concluded that the homogeneous distribution of major and trace elements (including Cu) in the feldspar resulted from a rapid rate of cooling of the host basalt (which prevented substantial internal chemical diffusion following initial crystallization). The megacrysts display anomalously young argon-argon (or $^{40}Ar/^{39}Ar$) ages, which she attributed to the loss of radiogenic argon. **Shiyun Jin** of GIA in Carlsbad, California, investigated the thin, oriented, ribbon-like inclusions of magnetite and hematite whose presence cre-

Figure 16. On the left is the 3 ct spinel as initially submitted. At right is the same stone after removal of the oil. The difference is striking. Following cleaning, a large reflective fissure is visible parallel to the girdle plane. This demonstrates the ability of an oil/resin to mask fissures even when there is no close match in refractive index between the filler and host. Photos by Chanon Yimkeativong/Lotus Gemology.

Figure 17. The 2020 annual meeting of the Geological Society of America was held online this year due to the Covid-19 pandemic. Courtesy of GSA and Image AV/e-Attend.

ates an aventurescence effect in some rainbow lattice sunstone from Australia. The iron in these inclusions is thought to have been initially dissolved in the feldspar lattice and then expelled during exsolution of albite (as lamellae) and ordering of the crystal structure during cooling of the host orthoclase.

A study of zircon inclusions in unheated sapphires from four important commercial metamorphic deposits was carried out by **Wenxing Xu** from the Gübelin Gem Lab in Lucerne, Switzerland. She demonstrated how Raman spectroscopic features can help distinguish geologically younger sapphires from Kashmir and Myanmar from geologically older samples from Sri Lanka and Madagascar. **Wim Vertriest** of GIA in Bangkok discussed the identification of opaque sulfide inclusions in rubies. Inclusions in marble-hosted rubies from Mogok, Myanmar, proved to be pyrrhotite and sphalerite, while those from amphibole rocks in Montepuez, Mozambique, were complex mixtures of Fe-Cu-Ni sulfide minerals, which suggests differences in the geological conditions of ruby formation. **Evan Smith** from GIA in New York discussed the genetic relationship between type IIb and certain type IIa diamonds.

Both types appear to have formed in the sublithospheric mantle with the involvement of subducted serpentinized peridotite.

Ping Ma of the China University of Geosciences in Wuhan discussed the value of using three-dimensional fluorescence spectra to help differentiate untreated and various treated jadeite samples in the marketplace. **Di Cui** of the Engineering Research Center of Gems and Technological Materials of Tongji University in Shanghai described the chemical composition and crystal structure of both the emeralds from the Davdar deposit in Xinjiang Province of northwest China, and in a separate presentation, the high vanadium-content emeralds from the Dayakou deposit of Malipo County in southwestern China. **Elina Myagkaya** of GIA in New York described an unusual brownish yellow diamond that was found to be a IIa + IIb mixed-type diamond. Investigation using cathodoluminescence and photoluminescence hyperspectral imaging revealed a complex growth pattern distinguished by differences in luminescence colors and various optical defects.

James E. Shigley
GIA, Carlsbad, California